Conference Proceedings of the Society for Experimental Mechanics Series

Matthew Allen
Jason Blough
Michael Mains *Editors*

Special Topics in Structural Dynamics & Experimental Techniques, Volume 5

Proceedings of the 41st IMAC, A Conference and Exposition on Structural Dynamics 2023

SEM

Springer

Conference Proceedings of the Society for Experimental Mechanics Series

Series Editor

Kristin B. Zimmerman
Society for Experimental Mechanics, Inc.,
Bethel, CT, USA

The Conference Proceedings of the Society for Experimental Mechanics Series presents early findings and case studies from a wide range of fundamental and applied work across the broad range of fields that comprise Experimental Mechanics. Series volumes follow the principle tracks or focus topics featured in each of the Society's two annual conferences: IMAC, A Conference and Exposition on Structural Dynamics, and the Society's Annual Conference & Exposition and will address critical areas of interest to researchers and design engineers working in all areas of Structural Dynamics, Solid Mechanics and Materials Research.

Matthew Allen • Jason Blough • Michael Mains
Editors

Special Topics in Structural Dynamics & Experimental Techniques, Volume 5

Proceedings of the 41st IMAC, A Conference and Exposition on Structural Dynamics 2023

Springer

Editors
Matthew Allen
Brigham Young University
Provo, UT, USA

Jason Blough
Michigan Technological University
Houghton, MI, USA

Michael Mains
Modal Shop
Cincinnati, OH, USA

ISSN 2191-5644 ISSN 2191-5652 (electronic)
Conference Proceedings of the Society for Experimental Mechanics Series
ISBN 978-3-031-37006-9 ISBN 978-3-031-37007-6 (eBook)
https://doi.org/10.1007/978-3-031-37007-6

This Springer imprint is published by the registered company Springer Nature Switzerland AG
The registered company address is: Gewerbestrasse 11, 6330 Cham, Switzerland

Paper in this product is recyclable.

Preface

Special Topics in Structural Dynamics and Experimental Techniques represents one of ten volumes of technical papers presented at the 41st IMAC, A Conference and Exposition on Structural Dynamics, organized by the Society for Experimental Mechanics, and held February 13–16, 2023. The full proceedings also include volumes on Nonlinear Structures and Systems; Dynamics of Civil Structures; Model Validation and Uncertainty Quantification; Dynamic Substructures; Special Topics in Structural Dynamics and Experimental Techniques; Computer Vision and Laser Vibrometry; Dynamic Environments Testing; Sensors and Instrumentation and Aircraft/Aerospace Testing Techniques; Topics in Modal Analysis and Parameter Identification; and Data Science in Engineering.

Each collection presents early findings from experimental and computational investigations on an important area within Structural Dynamics. *Special Topics in Structural Dynamics and Experimental Techniques* represents papers highlighting new advances and enabling technologies in several areas, including Experimental Techniques, Finite Element Techniques, Active Controls, System Identification, Additive Manufacturing, and Rotating Machinery.

The organizers would like to thank the authors, presenters, session organizers, and session chairs for their participation in this track.

Provo, UT, USA — Matthew Allen
Houghton, MI, USA — Jason Blough
Cincinnati, OH, USA — Michael Mains

Contents

1 **Damage Identification for Beam-Like Structures Based on Physics-Informed Neural Networks** 1
Wei Zhou and Y. F. Xu

2 **On the Study of Fatigue on Vulcanized Rubber Using Vibration Testing** 13
Francesco Trainotti, T. Slimak, and D. J. Rixen

3 **The Astir Glider Wing Dataset for Population-Based SHM** 19
Marcus Haywood-Alexander, Keith Worden, Nikolaos Dervilis, Robin S. Mills, Lawrence A. Bull, and Tina A. Dardeno

4 **Experimental Characterization of Structural Traveling Wave-Induced Thrust** 27
Skriptyan Syuhri, Hossein Zare-Behtash, and Andrea Cammarano

5 **Low-Frequency Vibrothermography Using Lightweight Piezoelectric Actuators: The Location of Excitation and Application to Composite Materials** 37
Xintian Chi, Dario Di Maio, and Nicholas A. J. Lieven

6 **Damage Assessment with Laser Ultrasonics in 3D-Printed Plate** 51
Jeffrey Liu, Paweł H. Malinowski, Piotr Pawłowski, Zihan Wu, and Michael D. Todd

7 **Parameter Investigation of Sensor Fixation Methods Compared with High-Quality Laser Measurement Using a Scalable Automatic Modal Hammer** 57
Robin Pianowski, Robert Kamenzky, Stefan Wolter, Zeyun Song, and Peter Blaschke

8 **Iterative Learning Control Based on Force Measurements for Automatic Impulse Hammers** 65
Johannes Maierhofer and Daniel J. Rixen

9 **Experimental Slug Flow-Induced Fluid –Structure Interaction of a Pressurized Flexible Pipe** 79
Graeme Hunt, David Pickles, Andrea Cammarano, and Gioia Falcone

10 **Deep Learning-Based Pixel-Level Colonoscopy Analysis** 91
John Lewis and Young-Jin Cha

11 **Design and Integration of a Hydroelastic Solver in the Dynamic Model of a Scaled Marine Hydrokinetic Kite** 97
Carson M. McGuire and Matthew Bryant

12 **A Simplified Finite Element Joint Model Updated with Experimental Modal Features** 107
Jonathan K. Black, Skylar J. Callis, Aaron Feizy, Christopher Lin Johnson, Nicholas A. J. Lieven, and Manuel A. Vega

13 **Efficient Methods for Flexibility Based Meso-scale Dynamic Modeling** 125
Raj Pradip Khawale, Suparno Bhattacharyya, Dustin Bielecki, Rahul Rai, and Gary Dargush

14 **Micromechanics of Internal Frictions in Thermoplastic Composites Exposed to High-Frequency Vibrations** 129
Thijs Masmeijer, Ed Habtour, and Dario di Maio

15 Investigating Compressing Particle Damper Pockets in Beams Manufactured by Laser Powder Bed Fusion Additive Manufacturing 139
Yanzhou Fu, Satme Joud, Austin R. J. Downey, Lang Yuan, Tianyu Zhang, and Daniel Kiracofe

16 Additively Manufactured Component Characterization by Machine Learning from Resonance Inspection Techniques 145
Stephanie Gonzalez, Sierra D. Horangic, Joseph H. Lahmann, Timothy J. Ulrich, and Parisa Shokouhi

17 Experimental Modal Analysis of an Additively Manufactured Model 155
Aditya Panigrahi, Brianna Blocher, Marc Eitner, and Jayant Sirohi

18 Improving Dynamic Characteristics of Strain Gauge Load Cells Using Additive Manufacturing ... 163
M. Vanali, S. Pavoni, A. H. Lanthaler, and D. Vescovi

19 Niceclick: A New Frontier for Haptic Technologies 173
Elvio Bonisoli, Luca Dimauro, Simone Venturini, Salvatore Paolo Cavallaro, and Flavio Cerruti

20 Simultaneous Passive Vibration Attenuation and Energy Harvesting on a Fan-Folded Piezometaelastic Structure 185
Leticia H. Maki, Paulo S. Varoto, Elvio Bonisoli, Luca Dimauro, and Make S. V. Paredes

21 Induction Motor Diagnostics Using Vibration and Motor Current Signature Analysis 199
Suri Ganeriwala

22 Application of Synchronous Averaging for Detecting Defects of a Gearbox 207
Suri Ganeriwala

23 A Time-Variant/Invariant Equivalence for the Transient Response of Rotor Blades in Resonance Crossing 213
Vincent Denoël and Luigi Carassale

Chapter 1
Damage Identification for Beam-Like Structures Based on Physics-Informed Neural Networks

Wei Zhou and Y. F. Xu

Abstract Damage in a beam-like structure due to decreases in its stiffness and/or mass can cause local anomalies in its flexural guided wavefield at locations of damage. Usually, these local anomalies can be intensified by data-driven techniques such as the continuous wavelet transform, the gapped smoothing method, etc. However, the physics of beam-like structures are not considered in these data-driven techniques, leading to a lack of physical consistency in the damage identification results. In this paper, a baseline-free damage identification method is proposed to extract these local anomalies under the assumption that the pristine beam-like structures are homogeneous and isotropic. Flexural guided wavefield of a damaged beam-like structure is used to build a pseudo-pristine model of the beam-like structure by using physics-informed neural networks. When the pseudo-pristine model is built, the prediction of flexural guided wavefield can be generated, and those local anomalies can be approximated by the difference between the prediction of flexural guided wavefield and the corresponding measured flexural guided wavefield. The difference is used to yield an accumulative two-dimensional damage index for further damage identification. Effectiveness and noise-robustness of the proposed method are investigated in a numerical example. Results show that the proposed method is effective and noise-robust in identifying the location and extent of the damage.

Keywords Structural damage identification · Physics-informed neural networks · Pseudo-pristine model · Beam-like structures · Local anomalies

1.1 Introduction

Engineering structures in service suffer from long-term environmental effects and operational loads, which cause unexpected structural damage. Monitoring structural damage is important for preserving and sustaining the service life of engineering structures. It is necessary to monitor structural damage by developing noise-robust and accurate damage identification methods. Recently, machine learning and especially deep learning algorithms have been studied widely in damage identification methods, thanks to the rapid development of graphics processing units (GPUs) and sensing technology in the last decade, including acoustic emission-based methods [1], guided wavefield-based methods [2], vibration-based structural damage identification methods [3, 4], etc.

Guided wavefield-based methods have been studied widely for damage Identification, owing to the capability of scanning laser Doppler vibrometers (SLDVs), which can measure velocities of a structure on each point of a predefined grid. It allows the visualization and post-processing of a guided wavefield by reconstructing measured velocities [5]. Joseph et al. [6] proposed a guided wavefield-based method for damage detection in thin metal plates. It uses full wavefield data acquired by SLDV, half from the damaged state and another half from the undamaged state, to train a deep neural network with two convolutional layers and two fully connected layers. It was reported that their proposed method has a better performance than support vector machine-based methods. Abdalraheem et al. [2] proposed guided wavefield-based method for damage detection by using deep fully convolutional neural networks (CNNs) FCN-DenseNet. It was fed by a large dataset of guided wavefields, which contains 475 cases of guided wavefields resulting from interaction with delaminations of random shape, size, and location. The results reveal that their proposed method performs better than the adaptive wavenumber filtering method. Besides, the same dataset has been used in a comparative study for delamination identification by using several deep

W. Zhou · Y. F. Xu (✉)
Department of Mechanical and Materials Engineering, University of Cincinnati, Cincinnati, OH, USA
e-mail: zhouw6@mail.uc.edu; xu2yf@uc.edu

M. Allen et al. (eds.), *Special Topics in Structural Dynamics & Experimental Techniques, Volume 5*,
Conference Proceedings of the Society for Experimental Mechanics Series, https://doi.org/10.1007/978-3-031-37007-6_1

fully CNNs models, including VGG16 encoder-decoder, PSPNet, residual UNet, and FCN-DenseNet [7]. It was reported that GCN model has the highest identification accuracy among the five implemented models. Song et al. [8] proposed guided wavefield-based method for identifying sub-wavelength defects. It combines two distinct fully CNNs, including a global detection network and a local super-resolution network. It was reported that their proposed method can not only locate sub-wavelength defects but also estimate the shape and size of the identified sub-wavelength defects. The aforementioned methods require labeled dataset which not only contains guided wavefields but also contains corresponding information of damage. However, labels are usually unavailable in practice, or acquiring these datasets are very time-consuming. Hence, it is necessary for researchers to come up with innovative methods using guided wavefields without labels under machine learning or deep learning applications.

Physics-informed neural networks (PINNs) are a mesh-free scientific machine learning technique used to solve equations, like nonlinear partial differential equations [9]. PINNs approximate solutions of equations by training a multilayer perceptron neural network to minimize a loss function, which includes terms reflecting the equations residual at selected points in the spatial-temporal domain, and the initial as well as boundary conditions along boundaries of the domain [10]. PINNs have been applied in several works with the ability of incorporating data and their governing physics equation, especially solving inverse problems, where unknown parameters of equation are estimated. Shukla et al. [11] used a PINN to identify a surface breaking crack in a metal plate. Measured ultrasonic surface acoustic waves of the metal were target of the PINN, and a wave velocity field of the metal plate was estimated as a damage index. Rathod et al. [12] identified the change of a wave velocity in a rod by a trained PINN, where 50% reduction in Young's modulus in the mid part can be represented in the identified wave velocity along the rod, but the sharp variation in the wave velocity was not captured. Zhang et al. [13] presented a general framework based on PINNs for solving inverse problems involving unknown material properties and geometric in continuum solid mechanics. It was reported that the framework can accurately estimate the unknown material properties and geometric with a relative error in the order of 10^{-2}.

In this paper, a guided wavefields-based damage identification method based on PINNs is proposed for beam-like structures. In this proposed method, a pseudo-pristine beam model is constructed by a PINN from a measured flexural guided wavefield of a damaged beam-like structure. The residual of Euler–Bernoulli equation with an unknown parameter α, i.e., the ratio of bending stiffness and mass per unit length, is used in the PINN as a loss term. This parameter serves as a variable and is updated in each iteration of gradient descent during the training process of the pseudo-pristine beam model. A predicted flexural guided wavefield is obtained from the pseudo-pristine beam model when the PINN is trained. An accumulative two-dimensional damage index is calculated based on the difference between the measured flexural guided wavefield and the predicted flexural guided wavefield. The location and extent of damage can be identified by consistently high values of the damage index. Accuracy and noise-robustness of the proposed method are investigated in a numerical example of a damaged beam-like structure with different noise levels.

The rest of the paper is arranged as follows. In Sect. 1.2, the proposed damage identification method based on PINNs is presented. In Sect. 1.3, the numerical investigation is described. Conclusions of this work are presented in Sect. 1.4.

1.2 Methodology

1.2.1 Euler–Bernoulli Beam

Consider a narrow, long beam with a lateral load applied, and, consequently, its displacement is off the centerline. The type of dynamic behavior is called flexural motion [14]. In this study, the Euler–Bernoulli beam model is considered. It is a simplification of the linear theory of elasticity which governs the flexural motion of beams. Assuming a pristine beam-like structure is homogeneous undamped, hence its governing equation of flexural motion on a bounded spatial-temporal domain is defined by [15]

$$EI\frac{\partial^4 u\left(x,t\right)}{\partial x^4}+\mu\frac{\partial^2 u\left(x,t\right)}{\partial t^2}=p\left(x,t\right),\quad x\in[0,L],\ \text{and}\ t\in[0,T] \tag{1.1}$$

where $u\left(x,t\right)$ is the spatial-temporal flexural motion of the beam with L spatial lengths and T temporal lengths, E is the elastic modulus, I is the second moment of area of the beam's cross sections, μ is the mass per unit length of the beam, and

$p(x,t)$ is the external force. Divide by μ in each term of Eq. (1.1), and one has

$$\alpha \frac{\partial^4 u(x,t)}{\partial x^4} + \frac{\partial^2 u(x,t)}{\partial t^2} = \frac{p(x,t)}{\mu} \tag{1.2}$$

where

$$\alpha := \frac{EI}{\mu} \tag{1.3}$$

It is observed that Eqs. (1.1) and (1.2) are fourth-order partial differential equations in space, and second order in time.

1.2.2 PINNs for the Euler–Bernoulli Beam

Let $\mathcal{N}(\mathbf{s};\boldsymbol{\theta})$: $\mathbb{R}^{d_s} \rightarrow \mathbb{R}^{d_y}$ be a multilayer perceptron neural network with input vector $\mathbf{s}$, H hidden layers, an output vector $\mathbf{y}$, and trainable network parameters $\boldsymbol{\theta}$. In the h-th hidden layer, N_h number of neurons is present. Each hidden layer receives an input $\mathbf{s}^{h-1} \in \mathbb{R}^{N_{h-1}}$ from the output of the previous layer through the following nested transformations:

$$\mathcal{Q}_h := \sigma^h \left(\mathbf{w}^h \mathbf{s}^{h-1} + \mathbf{b}^h\right), \quad h = 1, \ldots, H \tag{1.4}$$

where σ^h is the nonlinear activation function in the h-th hidden layer, $\mathbf{w}^h \in \mathbb{R}^{N_h \times N_{h-1}}$ and $\mathbf{b}^h \in \mathbb{R}^{N_h}$ are weight matrices and bias vectors in the h-th hidden layer, respectively. Output layer has the similar transformations in Eq. (1.4) but without nonlinear activation. Hence, the final neural network representation can be expressed as

$$\mathcal{N}(\mathbf{s};\boldsymbol{\theta}) = \mathbf{w}^{H+1}\left(\mathcal{Q}_H \circ \mathcal{Q}_{H-1} \circ \cdots \circ \mathcal{Q}_1\right) + \mathbf{b}^{H+1} \tag{1.5}$$

where the operator $\circ$ is the composition operator, $\mathbf{w}^{H+1} \in \mathbb{R}^{N_H}$ and $\mathbf{b}^{H+1} \in \mathbb{R}$ are weight and bias parameters of the output layer, respectively. Hence, all trainable network parameters can be represented as $\boldsymbol{\theta} = \left\{\mathbf{w}^1, \mathbf{b}^1, ..., \mathbf{w}^{H+1}, \mathbf{b}^{H+1}\right\}$. With reference to the universal approximation theorem [16], $u(\mathbf{x},\mathbf{t})$ can be approximated by

$$u(\mathbf{x},\mathbf{t}) \approx \mathcal{N}(\mathbf{x},\mathbf{t};\boldsymbol{\theta}) \tag{1.6}$$

where $\mathbf{x} = \{x : x \in [0, L]\}$ and $\mathbf{t} = \{t : t \in [0, T]\}$ are input vectors of $\mathcal{N}(\mathbf{x},\mathbf{t};\boldsymbol{\theta})$. Based on the governing equation of the beam, i.e., Eq. (1.2), the partial differential equation residual $\mathcal{R}(\mathbf{x},\mathbf{t})$ is defined as

$$\mathcal{R}(\mathbf{x},\mathbf{t}) := \alpha \frac{\partial^4 \mathcal{N}(\mathbf{x},\mathbf{t};\boldsymbol{\theta})}{\partial \mathbf{x}^4} + \frac{\partial^2 \mathcal{N}(\mathbf{x},\mathbf{t};\boldsymbol{\theta})}{\partial \mathbf{t}^2} - \frac{p(\mathbf{x},\mathbf{t})}{\mu} \tag{1.7}$$

The value of α is unknown, which updates in each iteration of gradient descent in the training process. Note that $\boldsymbol{\theta}$ can be learned by minimizing the following composite loss function:

$$\mathcal{L}(\boldsymbol{\theta}) = \lambda \mathcal{L}_d(\boldsymbol{\theta}) + \mathcal{L}_r(\boldsymbol{\theta}) \tag{1.8}$$

where

$$\mathcal{L}_d(\boldsymbol{\theta}) = \frac{1}{N_d} \sum \left(\hat{u}(\mathbf{x}_d,\mathbf{t}_d) - \mathcal{N}(\mathbf{x}_d,\mathbf{t}_d;\boldsymbol{\theta})\right)^2 \tag{1.9}$$

$$\mathcal{L}_r(\boldsymbol{\theta}) = \frac{1}{N_d} \sum \left(\mathcal{R}(\mathbf{x}_d,\mathbf{t}_d)\right)^2 \tag{1.10}$$

are residual loss and data loss, respectively. Here, λ is a hyperparameter that is larger than 0, and N_d denotes the number of inputs $\{\mathbf{x}_d, \mathbf{t}_d\}$ in each channel, which can be randomly sampled from the spatial-temporal domain $[0, L] \times [0, T]$, and

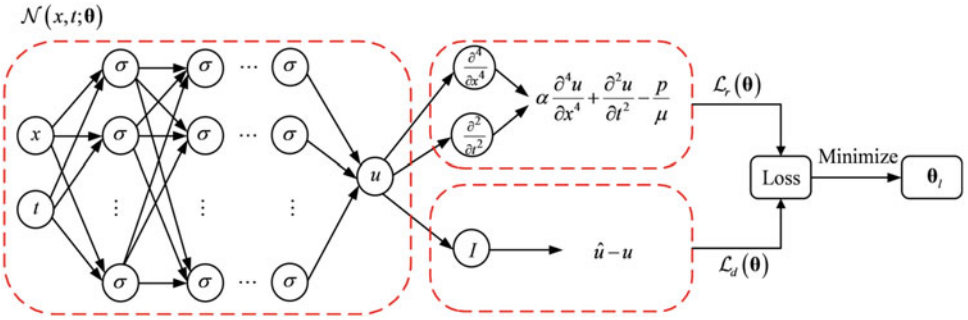

Fig. 1.1 Block diagram of the PINN model for the Euler–Bernoulli beam

$\hat{u}(\mathbf{x}_d, \mathbf{t}_d)$ is a sampled dataset from the measured flexural guided wavefield with corresponding coordinates $\{\mathbf{x}_d, \mathbf{t}_d\}$. The finally learned trainable network parameters are defined as $\boldsymbol{\theta}_l$. A block diagram describing the PINN model used in this study is shown in Fig. 1.1.

1.2.3 Damage Identification Process

Damage in a homogeneous beam-like structure can cause structural flexural motion anomalies at locations of damage although such local anomalies may not be apparent from the measured flexural motion [17]. In the piecewise form, $\hat{u}(x,t)$ can be written as a sum of three components, including the flexural motion for corresponding the pristine structure $\hat{u}_t(x,t)$, local anomalies $\hat{u}_p(x,t)$, if existing, and white noise $\hat{u}_n(x,t)$, if existing, and $\hat{u}(x,t)$ can be expressed by

$$\hat{u}(x,t) = \hat{u}_t(x,t) + \hat{u}_p(x,t) + \hat{u}_n(x,t) \tag{1.11}$$

When a surrogate model learned from $\hat{u}(x,t)$ by PINNs, $\mathcal{N}(x,t;\boldsymbol{\theta}_l)$ is close to $\hat{u}_t(x,t)$. Hence, the difference between $\hat{u}(x,t)$ and $\mathcal{N}(x,t;\boldsymbol{\theta}_l)$ can eliminate most effect from $\hat{u}_t(x,t)$:

$$\triangle u(x,t) = \hat{u}(x,t) - \mathcal{N}(x,t;\boldsymbol{\theta}_l) \tag{1.12}$$

When $\hat{u}(x,t)$ is measured from a pristine beam, $\triangle u(x,t)$ will contain errors of the surrogate model and $\hat{u}_n(x,t)$. On the other side, $\triangle u(x,t)$ will contain one more term, i.e., $\hat{u}_p(x,t)$, than the former one, when $\hat{u}(x,t)$ is measured from a damaged beam. Hence, unapparent local anomalies in $\hat{u}(x,t)$ will become dominated in $\triangle u(x,t)$ when damage exists.

An accumulative two-dimensional damage index can be constructed for damage identification for accumulating local anomalies, and alleviating the adverse effect of noise and errors in $\triangle u(x,t)$, which is defined as

$$\delta(x,m) = \left(\frac{\sum_{t=0}^{T} |\triangle u(x,t)|}{\max\left(\sum_{t=0}^{T} |\triangle u(x,t)|\right)} \right)^m, \quad m \in [1,\infty) \tag{1.13}$$

where $|\cdot|$ denotes the absolute value of a function and $\max(\cdot)$ is the maximum of a function. With increasing the value of m, the small values of $\delta(x,m)$ responding to noise and errors can be eliminated ultimately. While too large value of m can also lower the value of $\delta(x,m)$ in locations of damage. In this study, m is chosen in [1, 10] for all cases of $\delta(x,m)$. Note that $\delta(x,m) \in [0,1]$ and damage can be identified in neighborhoods with consistently high values of $\delta(x,m)$ with different values of m. A flowchart summarizing the proposed damage identification method is shown in Fig. 1.2.

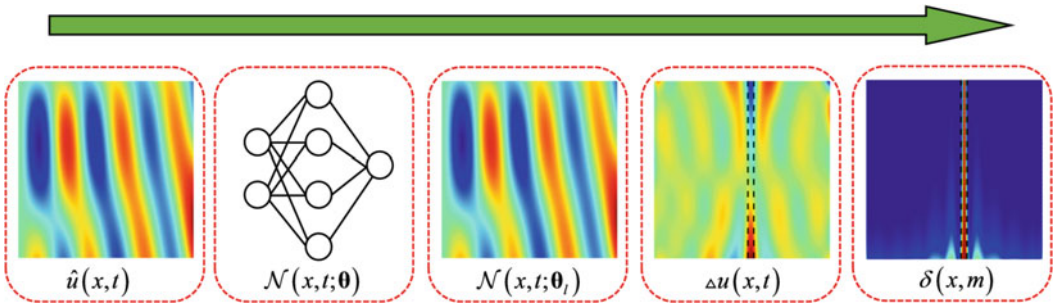

Fig. 1.2 Flowchart of the proposed damage identification method

1.3 Numerical Investigation

In this section, flexural guided wavefields obtained from numerical simulations of two cantilever beams: one is a pristine beam and the other is a damage beam which is generated from the pristine beam with damage in form of a thickness reduction area. The former one is used to study the capability of modeling by PINNs in constructing a surrogate model for the pristine beam. The latter one is used to study the effectiveness of the proposed damage identification method. Besides, the noise-robustness of the method is also investigated and discussed.

1.3.1 Numerical Models of Two Cantilever Beams

For the pristine cantilever beam, it has a height of 6 mm, a width of 3 mm, and a length of 300 mm. The damaged cantilever beam has the same dimensions as the pristine beam, and damage is introduced by a one-sided through-width thickness reduction area with a length of 10 mm and a depth of 0.3 mm. Dimensions of these two beams and the location of the damage are shown in Fig. 1.3. The pristine beam and damaged beam are made of aluminum 6061-T6 with a mass density of 2700 kg/m^3, Young's modulus of 68.9 GPa, and Poisson's ratio of 0.33. The ratio of bending stiffness and mass per unit length, i.e., α, is 19.1389 $\left(\mathrm{m}^4/\mathrm{s}^2\right)$ for the pristine beam. Their numerical model is modeled by the finite element method in finite element analysis software ABAQUS. The models of these two beams are built with the linear eight-node brick (C3D8R) elements. The size of elements is 0.3 mm so that a total of 1001 nodes are evenly distributed along the length of the intact side of each beam. These two cantilever beams are under zero initial conditions, and their free ends are subjected to a five-count wave packet force, which is expressed by

$$h(t) = A\left(H(t) - H\left(t - \frac{5}{f_c}\right)\right)\left(1 - \cos\left(\frac{2\pi f_c t}{5}\right)\right)\sin(2\pi f_c t) \tag{1.14}$$

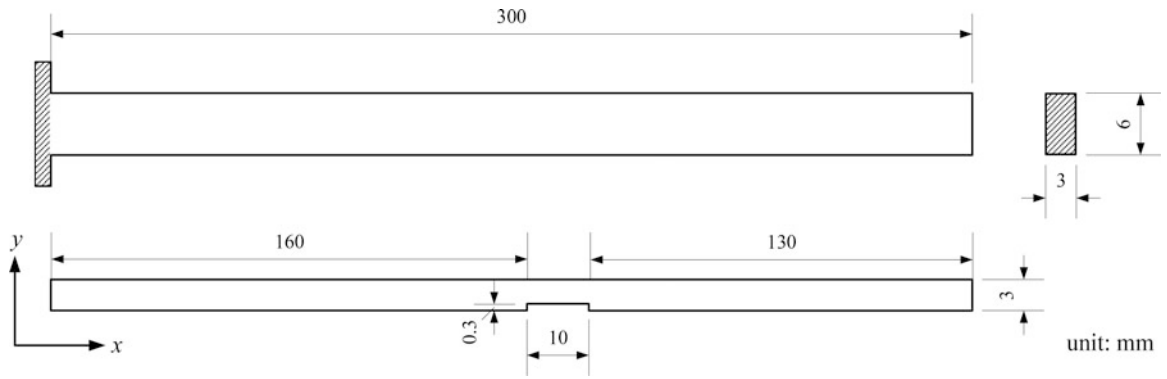

Fig. 1.3 Dimensions of the pristine beam and damaged beam, and the location of the damage on the damaged beam

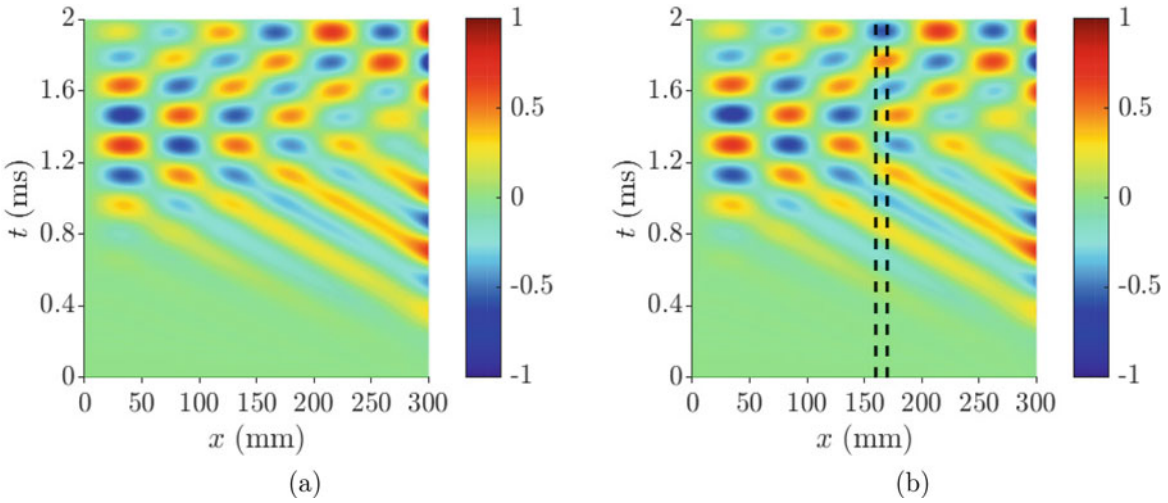

Fig. 1.4 Flexural guided wavefields for (**a**) the pristine beam and (**b**) the damaged beam. The amplitudes of the flexural guided wavefield shown in each figure are normalized for better comparison. Edges of the damage area are depicted by vertical dotted lines

where A defines the magnitude of the force, H is Heaviside function expressed by

$$H(t) = \begin{cases} 1, & t \geqslant 0 \\ 0, & t < 0 \end{cases} \tag{1.15}$$

and f_c is the central frequency of the force. The values of A and f_c are chosen to be 0.5 N and 3 kHz, respectively. The force is only applied in the free end nodes of two beams, and other nodes of beams are zeros. Hence, the force field, i.e., the rightmost item, is approximated by zeros in $\mathcal{R}(\mathbf{x}, \mathbf{t})$ of Eq. (1.7).

Two flexural guided wavefields for the pristine beam and damaged beam are obtained on a grid with 1001 nodes that are evenly distributed along the length of the intact side of each beam and 2501 steps in 2 ms after the excitation force is applied. These flexural guided wavefields are shown in Fig. 1.4. Figure 1.4a shows the flexural guided wavefield consists of a wave packet that is generated from the excitation point and propagating toward the fixed end, and reflecting back to the free end. In Fig. 1.4b, similar observations can be made regarding the resulted flexural guided wavefield for the damaged beam. Besides, reflections and/or local anomalies cannot be directly observed near the damage area.

1.3.2 Numerical Verification Process

The capability of modeling by PINNs is first investigated based on the flexural guided wavefield obtained from the pristine beam. PINNs are notoriously hard to train especially when high-frequency or multi-scale behavior exists [18]. In this study, the spatial-domain frequency is lowered by scaling $\mathbf{x} = \{x : x \in [0, 0.3]\}$ with unit of meter to $\bar{\mathbf{x}} = \{\bar{x} : \bar{x} \in [0, 1]\}$. In the temporal domain, only part of ranges are used and then scale $\mathbf{t} = \{t : t \in [t_1, t_2]\}$ with unit of second to $\bar{\mathbf{t}} = \left\{\bar{t} : \bar{t} \in [t_1/t_2, 1]\right\}$. Besides, the amplitudes of corresponding flexural motion are scaled to the interval $[-1, 1] \in \mathbb{R}$ as follows

$$\bar{u}(x, t) = -1 + 2 \times \frac{\hat{u}(x, t) - \min\left(\hat{u}(x, t)\right)}{\max\left(\hat{u}(x, t)\right) - \min\left(\hat{u}(x, t)\right)}, \quad t \in [t_1, t_2] \tag{1.16}$$

where $\min(\cdot)$ is the minimum of a function. Two models, i.e., model #1 and #2, are built based on two different ranges of the temporal domain to verify the consistence of modeling by PINNs, and they are $t \in [0.5, 0.7] \times 10^{-3}$ s and $t \in [1, 1.2] \times 10^{-3}$ s, respectively. A three-layer fully connected neural network with 100 neurons per hidden layer is used in each model. Two input channels exist in the neural network and number of $N_d = 20{,}000$ points $\left\{\bar{x}_i, \bar{t}_i\right\}_{i=1}^{N_d}$ which are randomly sampled from the selected spatial-temporal domain. The corresponding $\left\{\bar{u}\left(\bar{x}_i, \bar{t}_i\right)\right\}_{i=1}^{N_d}$ are sampled from the scaled flexural guided

wavefield $\bar{u}\left(\bar{\mathbf{x}}, \bar{\mathbf{t}}\right)$. The target function is used as the nonlinear activation function in the two models. The hyperparameter λ in the loss function Eq. (1.8) is set to 10^5. A two-phase optimizer is used to minimize the loss function. In the first phase, the Adam optimizer [19] with a learning rate of 10^{-3} and a weight decay of 10^{-5} is used via 50,000 iterations of gradient descent. In the second phase, the L-BFGS optimizer [20] with a learning rate of 10^{-1} is used until the two models are converged.

The capability of the proposed damage identification method is investigated based on the flexural guided wavefield from the damaged beam. Two pseudo-pristine beam models, i.e., model #3 and #4, are trained under the same setups as the model #1 and #2 with different $\left\{\bar{u}\left(\bar{x}_i, \bar{t}_i\right)\right\}_{i=1}^{N_d}$ sampled from the damaged beam, respectively. When the model #3 and #4 are trained, a damage index is calculated based on Eq. (1.13) for damage identification. Besides, the noise robustness of the proposed damage identification method is investigated. Model #5 is trained under the same setups as the model #4 with noise-contaminated $\left\{\bar{u}\left(\bar{x}_i, \bar{t}_i\right)\right\}_{i=1}^{N_d}$, which is sampled from noise-contaminated flexural guided wavefield. It is generated by adding a Gaussian noise with a signal-to-noise ratio of 30 dB to the flexural guided wavefield obtained from the damaged beam.

1.3.3 Numerical Verification Results

The model #1 is trained after 50,200 iterations of gradient descent, and its results are shown in Fig. 1.5. It can be seen that $\mathcal{L}_r$ is smaller than $\mathcal{L}_d$ at the initial iterations, but $\mathcal{L}_r$ increases radially under the effect of λ and then generally decreases

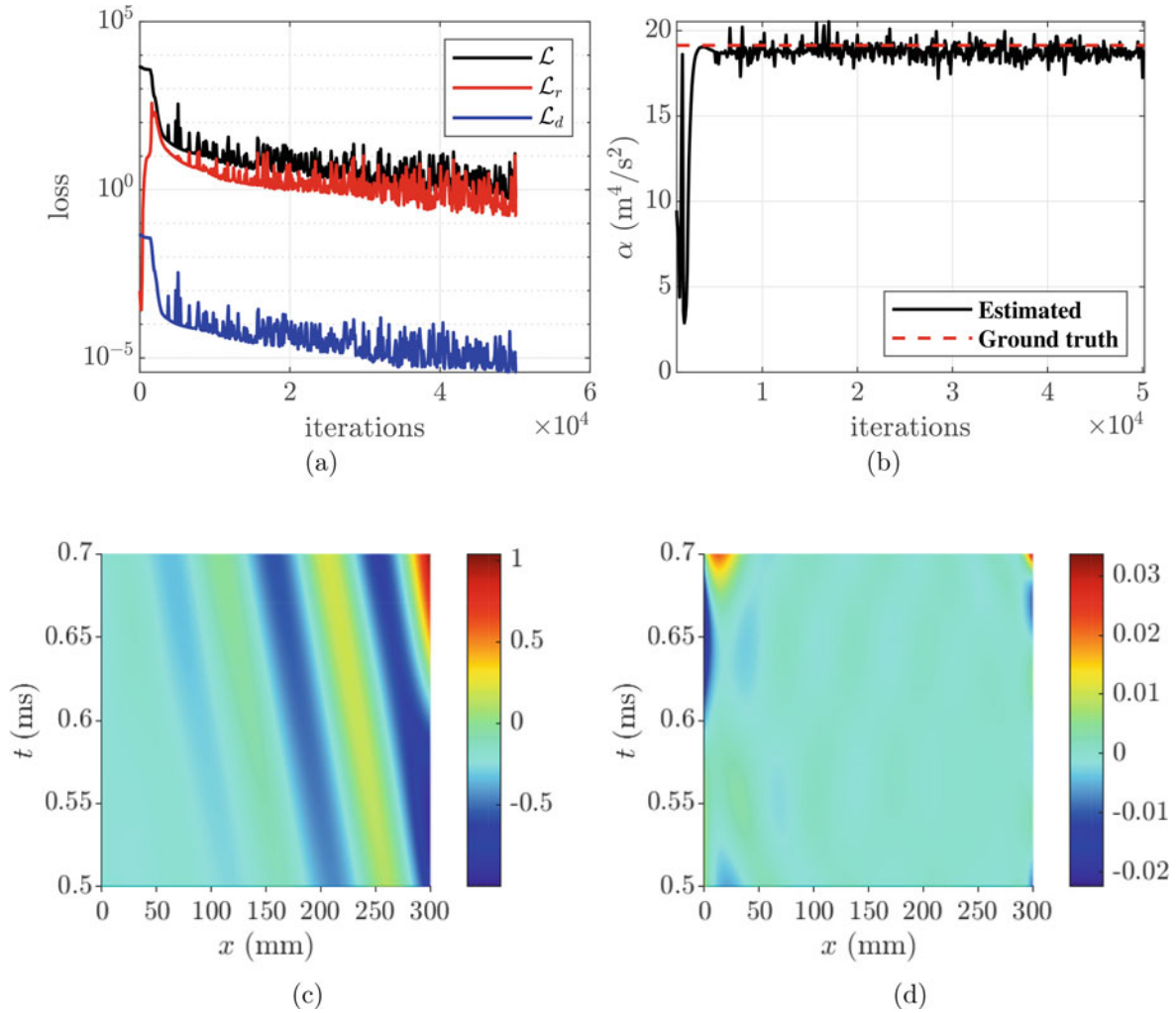

Fig. 1.5 Results for the model #1: (**a**) the composite loss $\mathcal{L}$, the residual loss $\mathcal{L}_r$, and the data loss $\mathcal{L}_d$ with iterations; (**b**) comparison of the estimated value of α and the ground truth of α; (**c**) the prediction of flexural guided wavefield; and (**d**) the difference between the predicted wavefield and the corresponding measured wavefield

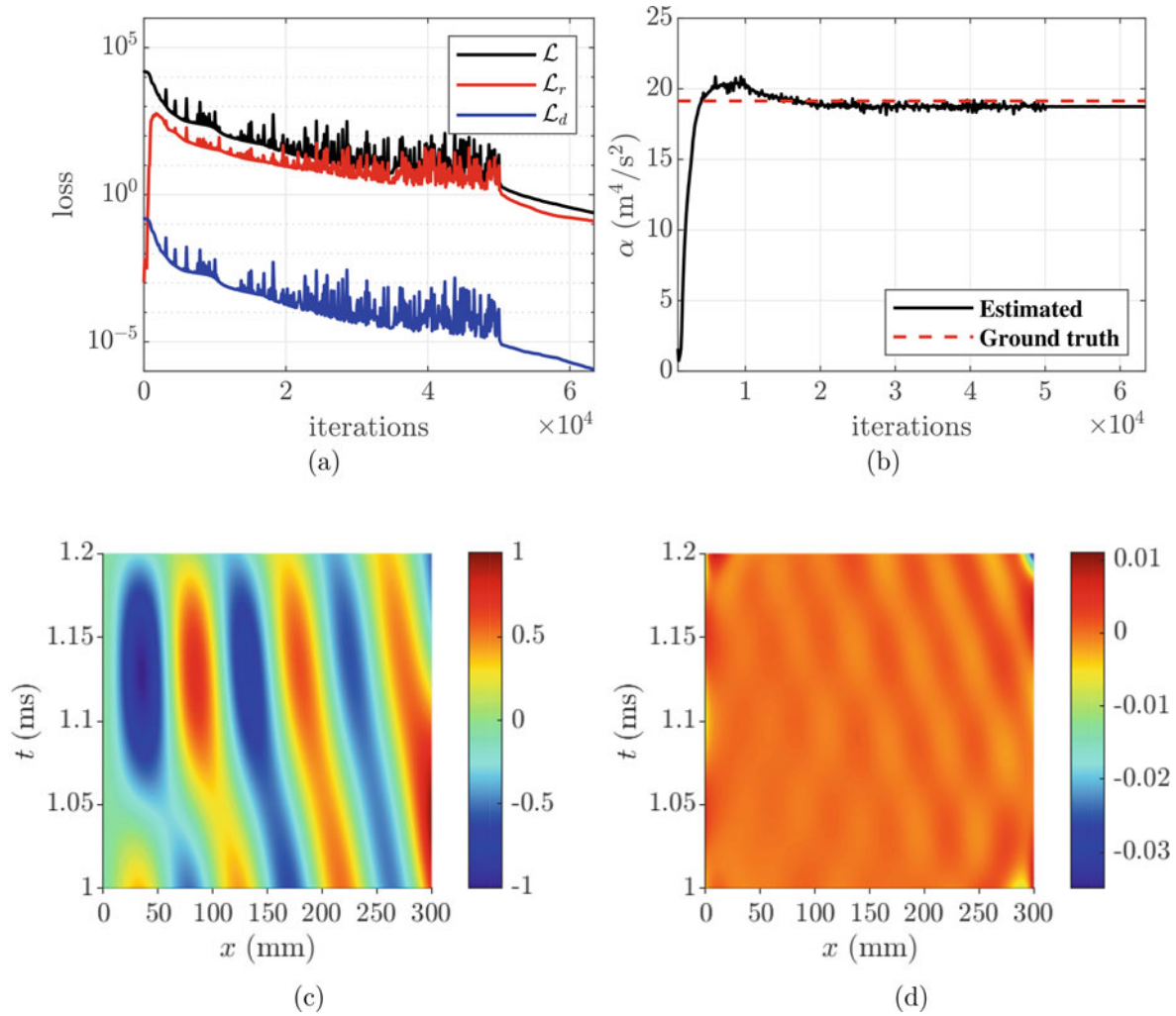

Fig. 1.6 Results for the model #2: (**a**) the composite loss $\mathcal{L}$, the residual loss $\mathcal{L}_r$, and the data loss $\mathcal{L}_d$ with iterations; (**b**) comparison of the estimated value of α and the ground truth of α; (**c**) the prediction of flexural guided wavefield; and (**d**) the difference between the predicted wavefield and the corresponding measured wavefield

as same to $\mathcal{L}_d$ as shown in Fig. 1.5a. The estimated α needs to be divided by a factor of $\left(L^4/t_2^2\right)$ with $L = 0.3$ m and $t_2 = 0.7 \times 10^{-3}$ s due to the scaling in spatial and temporal coordinates in the model #1. The estimated α with iterations is shown in Fig. 1.5b. It can be seen that the estimated α is always nearby the ground truth after approximately 0.5×10^4 iterations. The final estimated α is 18.7446 $\left(\mathrm{m}^4/\mathrm{s}^2\right)$, and the relative error to the ground truth is 2.06%. The prediction of flexural guided wavefield by the model #1 is shown in Fig. 1.5c, and the difference between the predicted wavefield and the corresponding measured wavefield is shown in Fig. 1.5d. Small magnitudes are dominated in the majority ranges, and only relative large magnitudes exist in boundaries of the spatial-temporal domain of the model #1.

The model #2 is trained after 63,400 iterations of gradient descent, and its results are shown in Fig. 1.6. The loss and estimated α have the similar trend as that of model #1, and their values become stable in iterations of gradient descent by the L-BFGS optimizer. The final estimated α is 18.7399 $\left(\mathrm{m}^4/\mathrm{s}^2\right)$, and the relative error to the ground truth is 2.09%. The prediction of flexural guided wavefield by the model #2 is shown in Fig. 1.6c, and the difference between the predicted wavefield and the corresponding measured wavefield is shown in Fig. 1.6d. It can be seen that the prediction wavefield is close to the corresponding measured one. The results for model #1 and model #2 show that PINNs can model the pristine beam with high accuracy and consistency.

The model #3 and #4 are trained after 51,400 and 55,100 iterations of gradient descent, respectively. The difference between the predicted wavefield and the corresponding measured wavefield for the model #3 is shown in Fig. 1.7a. Large magnitudes of the difference mainly exist in the areas of damage, but others exist nearly by the areas of damage and boundaries. The difference is used to calculate $\delta(x, m)$ in a domain $(x, m) \in [5, 295] \times [1, 10]$ with a step of 0.01 for

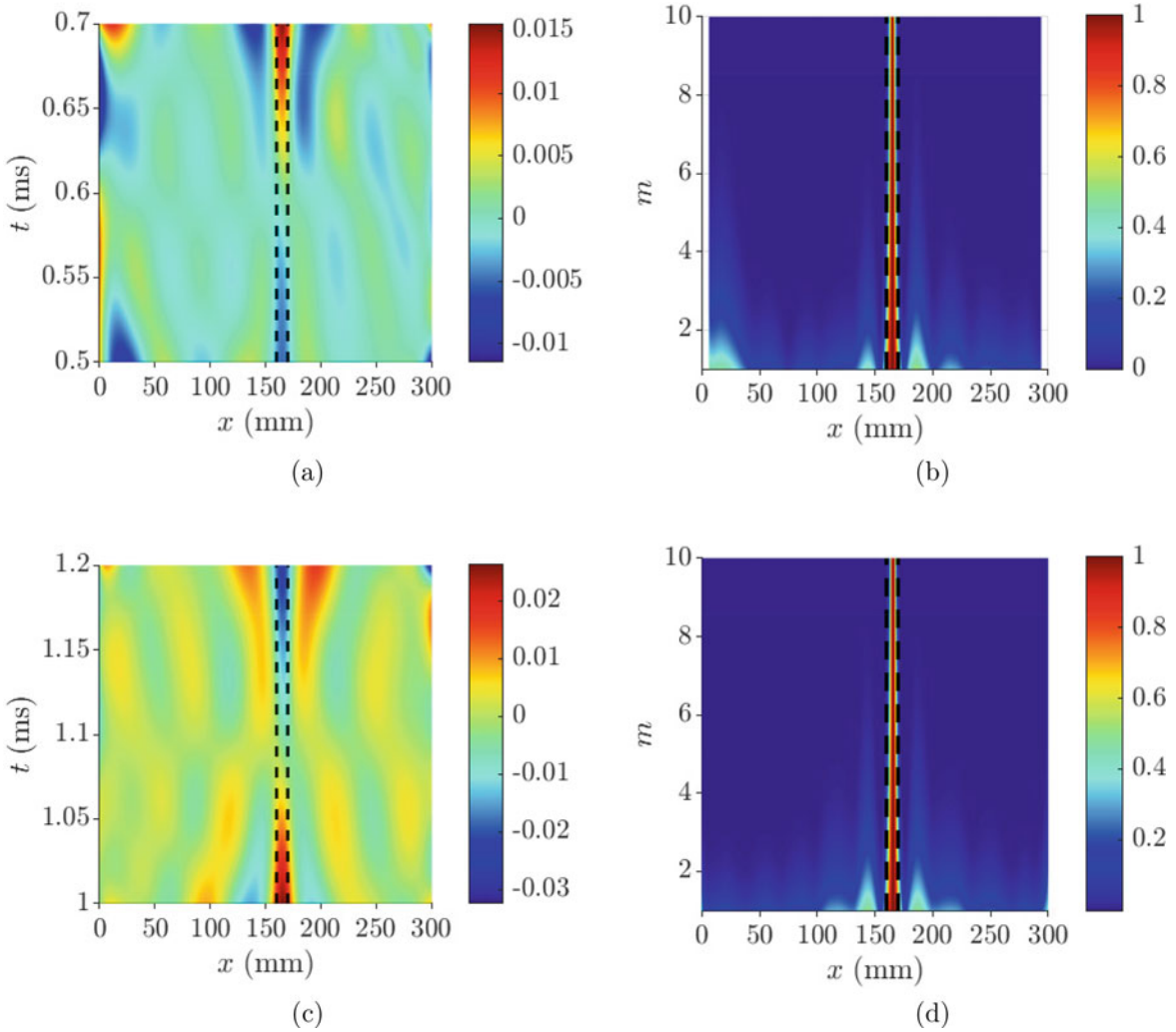

Fig. 1.7 (**a**) The difference between the predicted wavefield and the corresponding measured wavefield for model #3, (**b**) the damage identification result $\delta(x, m)$ for model #3, (**c**) the difference between the predicted wavefield and the corresponding measured wavefield for model #4, and (**d**) damage identification results $\delta(x, m)$ for model #4. Edges of the damage area are depicted by vertical dotted lines

m, which is shown in Fig. 1.7b. It can be seen that high $\delta(x, m)$ values mainly exist in the damage area so that the locations and extent of the damage can be accurately identified by the consistently high $\delta(x, m)$ values. Large magnitudes of the difference between the predicted wavefield and the corresponding measured wavefield for the model #4 also mainly exist in the areas of damage as shown in Fig. 1.7c. The difference is used to calculate $\delta(x, m)$ in a domain $(x, m) \in [0, 300] \times [1, 10]$ with a step of 0.01 for m, which is shown in Fig. 1.7d. Similarly, consistently high $\delta(x, m)$ values mainly exist in the damage area. The damage identification results for model #3 and model #4 show that the proposed method can identify the locations and extent of the damage with high accuracy and consistency.

It takes 50,700 iterations of gradient descent to train the model #5. The difference between the predicted wavefield and the corresponding measured wavefield for the model #5 is shown in Fig. 1.8a. Gaussian noise can be clearly detected in the difference, and large magnitudes of the difference exist in the damage area, boundaries, as well as nearby the damage area. The difference is used to calculate $\delta(x, m)$ in a domain $(x, m) \in [5, 295] \times [1, 10]$ with a step of 0.01 for m, which is shown in Fig. 1.8b. It can be seen that high $\delta(x, m)$ values mainly exist in the damage area, and Gaussian noise is alleviated with increasing the value of m.

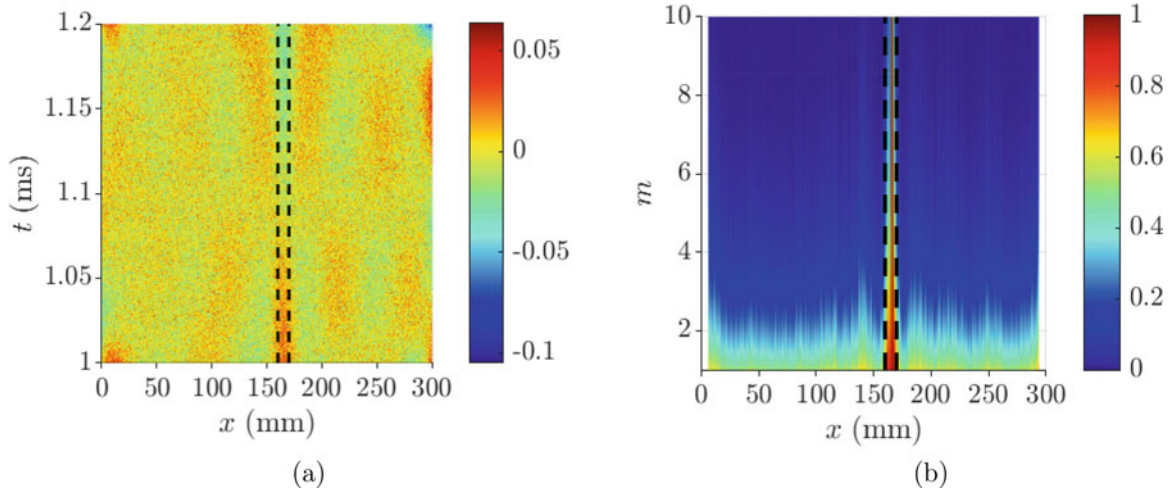

Fig. 1.8 (**a**) The difference between the predicted wavefield and the corresponding measured wavefield for model #5 and (**b**) the damage identification result $\delta(x, m)$ for model #5. Edges of the damage area are depicted by vertical dotted lines

1.4 Concluding Remarks

In this paper, a baseline-free structural damage identification method is developed for beam-like structures based on PINNs. Pseudo-pristine beam models are built by PINNs from measured flexural guided wavefields of damaged beam-like structures. A two-dimensional damage index is calculated based on the difference of the predicted flexural guided wavefields by pseudo-pristine beams and their corresponding measured flexural guided wavefields. Damage can be identified in neighborhoods with consistently high values of the damage index. The capability of modeling by PINNs is studied on the pristine beam. The results demonstrate that PINNs can accurately model the pristine beam, providing highly accurate and consistent estimates of the ratio of bending stiffness to mass per unit length. The effectiveness of the proposed damage identification method is investigated in a damage cantilever beam. It was found that (1) the proposed method can accurately identify the location and extent of damage, and (2) the proposed method is robust for measurement noise. In future works, it is worthwhile to conduct investigations on experiments by the proposed method. Besides, segmentation is only used in the temporal domain of flexural guided wavefields for better training PINNs in this study. Segmentation in the spatial-temporal domain for flexural guided wavefields can be studied when higher excitation frequencies are applied to structures.

Acknowledgments The authors are grateful for the financial support from the National Science Foundation through Grant No. CMMI-1762917.

Conflicts of Interest The authors declare no conflict of interest.

References

1. Ai, L., Soltangharaei, V., Ziehl, P.: Developing a heterogeneous ensemble learning framework to evaluate Alkali-silica reaction damage in concrete using acoustic emission signals. Mech. Syst. Signal Process. **172**, 108981 (2022)
2. Ijjeh, A.A., Ullah, S., Kudela, P.: Full wavefield processing by using FCN for delamination detection. Mech. Syst. Signal Process. **153**, 107537 (2021)
3. Abdeljaber, O., Avci, O., Kiranyaz, S., Gabbouj, M., Inman, D.J.: Real-time vibration-based structural damage detection using one-dimensional convolutional neural networks. J. Sound Vib. **388**, 154–170 (2017)
4. Yu, Y., Wang, C., Gu, X., Li, J.: A novel deep learning-based method for damage identification of smart building structures. Struct. Health Monitor. **18**(1), 143–163 (2019)
5. Ruzzene, M.: Frequency–wavenumber domain filtering for improved damage visualization. Smart Mater. Struct. **16**(6), 2116 (2007)
6. Melville, J., Alguri, K.S., Deemer, C., Harley, J.B.: Structural damage detection using deep learning of ultrasonic guided waves. In: AIP Conference Proceedings, vol. 1949, p. 230004. AIP Publishing LLC (2018)
7. Ijjeh, A.A., Kudela, P.: Deep learning based segmentation using full wavefield processing for delamination identification: A comparative study. Mech. Syst. Signal Process. **168**, 108671 (2022)
8. Song, H., Yang, Y.: Noncontact super-resolution guided wave array imaging of subwavelength defects using a multiscale deep learning approach. Struct. Health Monitor. **20**(4), 1904–1923 (2021)

9. Raissi, M., Perdikaris, P., Karniadakis, G.E.: Physics-informed neural networks: A deep learning framework for solving forward and inverse problems involving nonlinear partial differential equations. J. Comput. Phys. **378**, 686–707 (2019)
10. Cuomo, S., Di Cola, V.S., Giampaolo, F., Rozza, G., Raissi, M., Piccialli, F.: Scientific machine learning through physics-informed neural networks: where we are and what's next. Preprint (2022). arXiv:2201.05624
11. Shukla, K., Di Leoni, P.C., Blackshire, J., Sparkman, D., Karniadakis, G.E.: Physics-informed neural network for ultrasound nondestructive quantification of surface breaking cracks. J. Nondestruct. Eval. **39**(3), 1–20 (2020)
12. Rathod, V., Ramuhalli, P.: Physics-informed neural networks for identification of material properties using standing waves. In: Nondestructive Characterization and Monitoring of Advanced Materials, Aerospace, Civil Infrastructure, and Transportation XVI, vol. 12047, pp. 179–188. SPIE (2022)
13. Zhang, E., Dao, M., Karniadakis, G.E., Suresh, S.: Analyses of internal structures and defects in materials using physics-informed neural networks. Sci. Adv. **8**(7), eabk0644 (2022)
14. Hagedorn, P., DasGupta, A.: Vibrations and Waves in Continuous Mechanical Systems. Wiley (2007)
15. Doyle, J.F.: Wave Propagation in Structures: Spectral Analysis Using Fast Discrete Fourier Transforms. Springer (1997)
16. Hornik, K.: Approximation capabilities of multilayer feedforward networks. Neural Networks **4**(2), 251–257 (1991)
17. Wang, Q., Deng, X.: Damage detection with spatial wavelets. Int. J. Solids Struct. **36**(23), 3443–3468 (1999)
18. Wang, S., Wang, H., Perdikaris, P.: On the eigenvector bias of Fourier feature networks: From regression to solving multi-scale PDEs with physics-informed neural networks. Comput. Methods Appl. Mech. Eng. **384**, 113938 (2021)
19. Kingma, D.P., Ba, J.: Adam: A method for stochastic optimization. Preprint (2014). arXiv:1412.6980
20. Liu, D.C., Nocedal, J.: On the limited memory BFGS method for large scale optimization. Math. Programm. **45**(1), 503–528 (1989)

Chapter 2
On the Study of Fatigue on Vulcanized Rubber Using Vibration Testing

Francesco Trainotti, T. Slimak, and D. J. Rixen

Abstract Thanks to the unique properties of high elongation, reversibility, incompressibility, and energy dissipation, rubber materials are employed in numerous engineering applications in industrial practice. The rheological behavior of rubbers depends on chemical composition, presence of additives, and curing process. As a consequence, a large variety of materials may be encountered with a rich phenomenological description of their static and dynamic characteristics. Rate, amplitude, and temperature, among others, are operational parameters that affect rubber's stiffness and damping properties. On top of that, to ensure the long-term performance and reliability of a rubber component, aging effects and fatigue life assessments are paramount. Existing laboratory vibrational techniques, based on uni-axial displacement-controlled cyclic tests, are capable of extracting storage and loss properties of the rubber under study as a function of frequency and amplitude of the oscillation. This paper investigates the robustness of a transmissibility-based shaker setup for the dynamic characterization of a rubber component extended to long-run operational loading. A preliminary analysis shows the influence of the adhesive substance used to hold the rubber in place in a variety of testing scenarios.

Keywords Rubber · Characterization · Testing · Shaker · Fatigue

2.1 Introduction

Rubber materials are widely adopted in engineering practice due to their high versatility and mechanical properties such as high strength, high elongation, and energy dissipation. Synthetic rubbers are commonly used in aerospace and automotive applications to produce mounts that act as vibration isolation interfaces. The rheological behavior of the polymeric compound will mostly depend on its chemical composition, the presence of additives, and the vulcanization process. As a result, a wide range of characteristics and sensitivity to mechanical loads and environmental conditions can be realized. On a macro-scale, for a mechanical engineer, the stiffness and damping properties along the principal deformation axes might show dependence on rate/frequency, temperature, state/amplitude, static pre-load, etc. [1, 2]. In addition, change in properties due to long operational loading cycles or exposure to extreme environmental conditions can lead to non-functioning and non-robust design solutions. An appropriate understanding of their characteristics via an experimental characterization process is therefore needed. Different strategies might be adopted depending on the level of detail desired/required, e.g., material or component level, phenomenological or constitutive approach, type of dependencies, inclusion of inertia contribution, single or multi-axial, etc. Material-level identification using standard(-ized) machines (e.g., dynamic mechanical analyzer) provides the most accurate, extensive, though expensive, characterization results [3]. A cheaper and faster option is commonly adopted in NVH analysis which consists in identifying the transfer of vibration of the rubber mount considered as a structural component. Standard single-DoF shaker- and impact-based laboratory testing may be adopted [4, 5]. Recently, multi-DoF substructuring identification based on frequency response measurements has gained popularity, thanks to the capability of handling complex rubber mounts and the versatility of the identified experimental model [6]. A comparison between the two mentioned component-based testing strategies has been offered by the authors in [7]. There, a transmissibility-based setup is presented to extract stiffness and damping characteristics as a function of frequency and amplitude in a uni-axial cyclic testing mode. Prior to extending the test capabilities to study long-term loading behavior (e.g., fatigue and/or aging), the

F. Trainotti (✉) · T. Slimak · D. J. Rixen
Chair of Applied Mechanics, Department of Mechanical Engineering, TUM School of Engineering and Design, Technical University of Munich, Garching, Germany
e-mail: francesco.trainotti@tum.de; tomas.slimak@tum.de; rixen@tum.de

M. Allen et al. (eds.), *Special Topics in Structural Dynamics & Experimental Techniques, Volume 5*,
Conference Proceedings of the Society for Experimental Mechanics Series, https://doi.org/10.1007/978-3-031-37007-6_2

reliability and robustness of the workflow must be assessed. This preliminary analysis focuses on the effect of the adhesive used to fix the rubber specimen in place and point out accuracy and repeatability of the experimental identification.

The characterization strategy along with the testing setup is outlined in Sect. 2.2. The processed results of the measurement campaigns are presented in Sect. 2.3. Conclusive remarks are collected in Sect. 2.4.

2.2 Transmissibility-Based Uni-axial Shaker Characterization

The transmissibility setup is briefly summarized in the following. A more comprehensive derivation can be found in [7].

The measurement configuration is shown in Fig. 2.1. The idea is to approximate a single-DoF oscillator with the rubber acting as a (complex) spring, a moving mass on the top of it, and a uni-axial base excitation via an electrodynamic shaker. By measuring the motion on either side of the rubber specimen while performing a dynamic excitation, the dynamic equilibrium of the system can be written as:

$$m\ddot{y} + k^*(y - x) = 0 \tag{2.1}$$

where k^* is the complex stiffness including both stiffness and damping contributions and y, x are the displacements above and below the rubber, respectively. Note that the single-DoF assumption in Eq. (2.1) holds for an ideal uni-axial motion and as long as the "excitation" mass underneath the rubber is significantly larger than the moving mass $m\ddot{y}$.

The rubber properties are identified by isolating the complex stiffness k^* and using the parametrization following the linear viscoelastic theory such that $k^* = k' + ik''$ where k', k'', $k^\star = |k^*|$, $\eta = \dfrac{k''}{k'}$ represent the storage stiffness, loss stiffness, dynamic stiffness, and loss factor, respectively.

Depending on the excitation signal, different analyses can be conducted:

- Linearized sweeps: a linear sweep excites the system. The frequency-based counterparts of the top and bottom responses are estimated, and the transmissibility ratio is computed as $T(\omega) = \dfrac{Y(\omega)}{X(\omega)}$. The complex stiffness is then computed by solving Eq. (2.1), and the stiffness and damping terms identified. The change of properties due to deformation amplitude is neglected so that equivalent linearized frequency-dependent characteristics are retrieved. Temperature is assumed to be constant.
- Amplitude-frequency maps: a cyclic displacement-controlled dynamic excitation is performed. The controlled quantity is the relative displacement $y - x$. Per each controlled operating point defined by an oscillation frequency and peak amplitude, the stationary time responses are stored, and Eq. (2.1) is used to determine stiffness and damping via an averaged peak fitting and zero crossing strategy. The linearized values can be expressed as a function of the operating frequency and dynamic amplitude/strain, such that a 2D map is generated. Temperature is assumed to be constant.

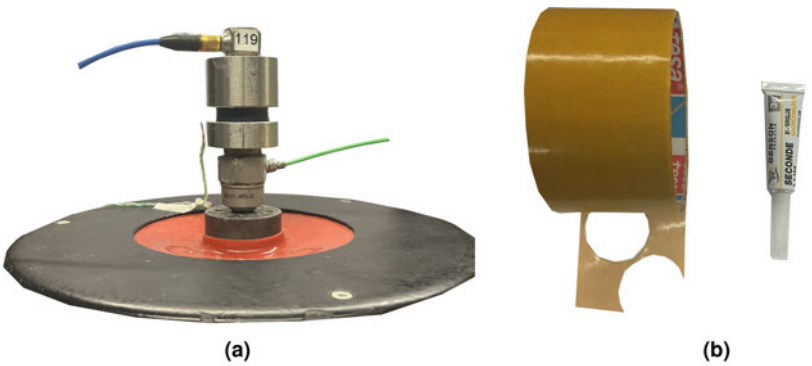

Fig. 2.1 Experimental setup used to characterize the rubber component. (**a**) Transmissibility shaker setup with an accelerometer attached to either side of the rubber sample and excitation from the bottom. (**b**) Adhesive substances used to fix the rubber sample. Left: double-sided adhesive tape. Right: cyanoacrylate glue

- Long-time runs: a cyclic displacement-controlled dynamic excitation is performed for a large number of measurement cycles. The processing is analogous to that of the amplitude-frequency map type of analysis, with the difference being the possible reversible or non-reversible fatigue effects affecting the behavior of the rubber.

The current setup uses an accelerometer on the moving mass and an impedance sensor (measuring force and acceleration) on the base. An additional sensor close to the rig is used to monitor the room temperature (assumed constant) during the testing. Two types of adhesive substances are investigated: a double-sided tape and a cyanoacrylate glue (see Fig. 2.1). A rubber disc with diameter 22 mm and thickness 6 mm is used as sample. To assess the robustness of the workflow, two different materials are tested, referred to as "MAT 1" and "MAT 2."

2.3 Testing Results

Tests are conducted as follows. First, a linearized sweep analysis is performed in the range 20–1000 Hz. This allows a quick evaluation of stiffness and damping trends as frequency-based curves and serves as a basis to choose reasonable operating points for the subsequent analysis. Then, a fully automated testing workflow is adopted as described below:

1. Amplitude-frequency map in the controllable/observable range 300–700 Hz and 0.03–0.25 % strain.
2. Pause 30 min.
3. Long-lasting run consisting of repeated cyclic loads at 500 Hz with 0.25 % peak strain. Time schedule: run 60 min—pause 30 min—run 60 min.
4. Pause 30 min.
5. Amplitude-frequency map in the controllable/observable range 300–700 Hz and 0.03–0.25 % strain.

The results of the sweep analysis are grouped in Fig. 2.2. Some considerations are as follows:

- The two materials present clearly distinguishable frequency trends. This indicates an appropriate/robust identification process.
- The repeatability of the attachment process for tape is significantly higher than that for glue.
- The frequency trends between tape and glue are similar, while there is a bias in the absolute value. Tape results present higher levels of damping and lower levels of stiffness. This might be due to the effect of tape acting as an additional viscoelastic layer.

The amplitude-frequency maps are shown in Fig. 2.3. All considerations regarding the comparison between the materials and between the adhesives made for the sweep are confirmed by the plots and readily extended to the amplitude/strain dependence. As additional information, no clear difference exists between maps before and after the long-lasting runs, thus suggesting a fully reversible behavior.

Finally, the preliminary fatigue study is provided in Fig. 2.4. A very repeatable change in stiffness and damping properties is observed with increasing number of cycles (and time) for all combination of materials and adhesives. The change occurs

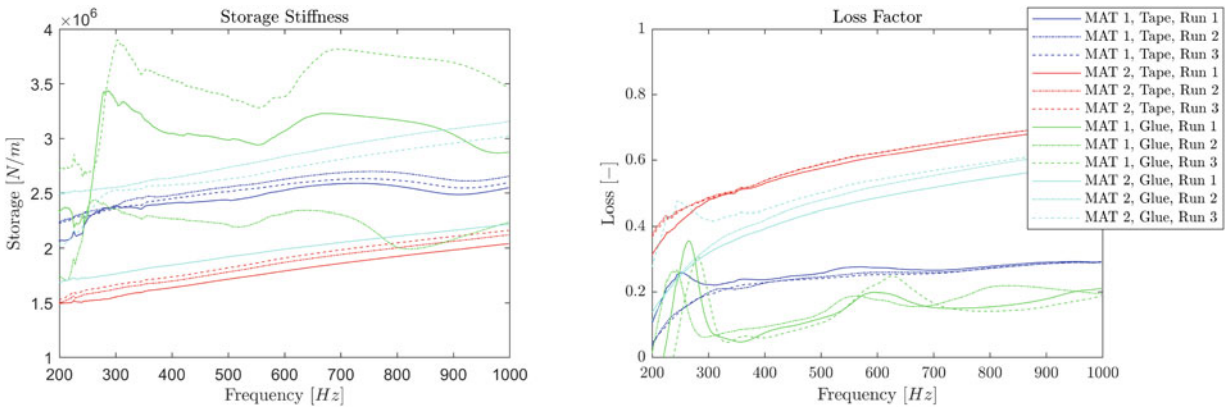

Fig. 2.2 Linearized sweep analysis on the rubber samples of MAT 1 and MAT 2 with both Tape and Glue. Three repetitions (Runs) are provided for each combination tested. Left: storage stiffness. Right: loss factor

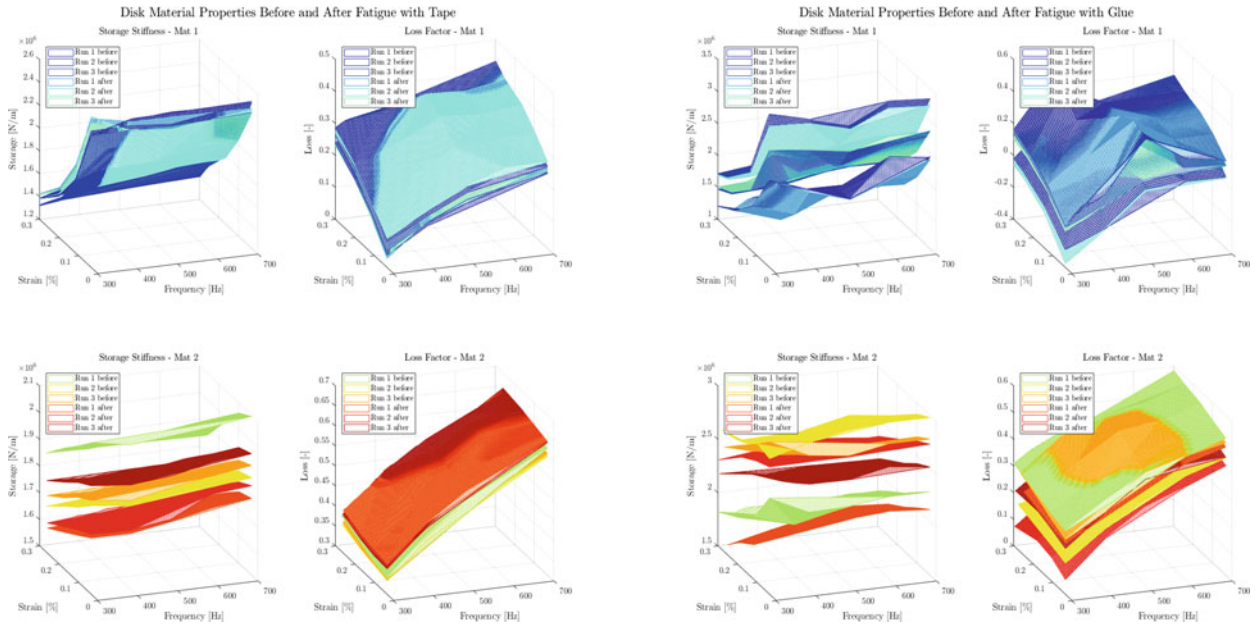

Fig. 2.3 Amplitude-frequency maps analysis on the rubber samples of MAT 1 and MAT 2 with both Tape and Glue. Three repetitions (Runs) are provided for each combination tested. Results before and after fatigue are shown. Left: storage stiffness and loss factor of MAT1 (top) and MAT2 (bottom) for Tape. Right: storage stiffness and loss factor of MAT1 (top) and MAT2 (bottom) for Glue

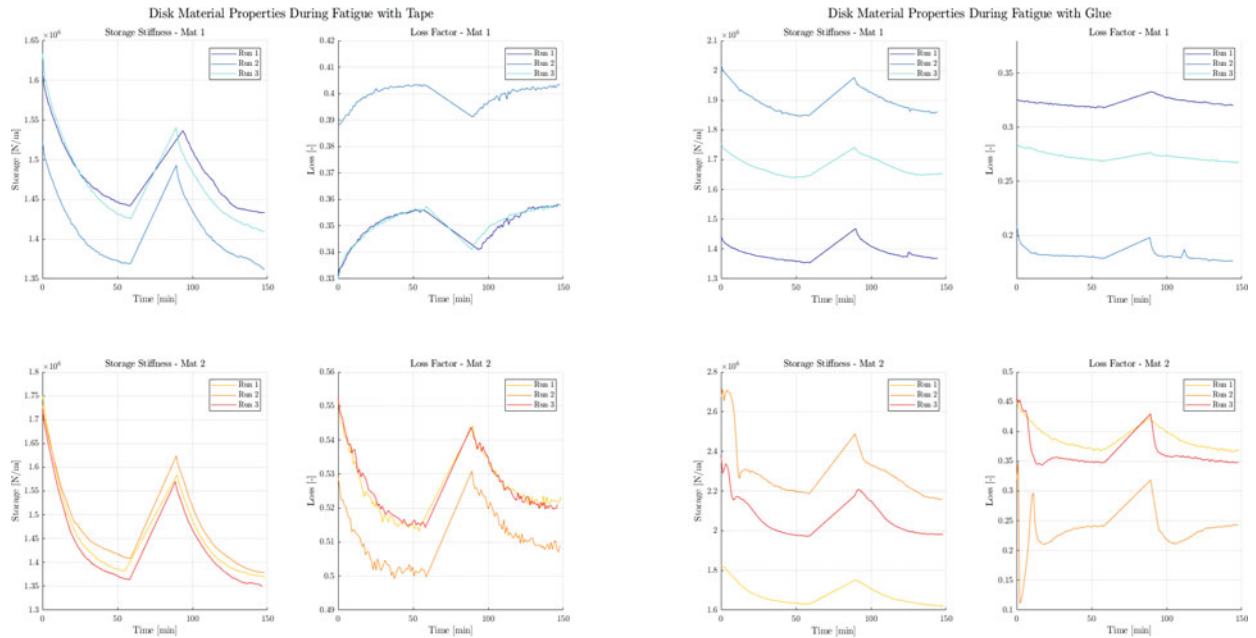

Fig. 2.4 Long-lasting runs (Fatigue) analysis on the rubber samples of MAT 1 and MAT 2 with both Tape and Glue. Three repetitions (Runs) are provided for each combination tested. Left: storage stiffness and loss factor of MAT1 (top) and MAT2 (bottom) for Tape. Right: storage stiffness and loss factor of MAT1 (Top) and MAT2 (bottom) for Glue

as a decrease in storage and loss properties for most cases analyzed, except for the loss factor of the combined tape and MAT 1, which shows the opposite trend. Further investigation is needed in this regard. Overall, the source of the long-lasting effect is unknown, but it seems to be fully reversible within the tests conducted (as also supported by Fig. 2.3).

2.4 Conclusion

Experimental testing is paramount for an adequate understanding of the mechanical properties of rubber components, which are widely spread in engineering applications.

A transmissibility-based uni-axial shaker configuration enables a cheap and automated testing chain to extract stiffness and damping properties of a rubber on a component level. This strategy is capable of identifying the frequency and (dynamic) amplitude dependence of the rubber characteristics by using a linearized equivalent viscoelastic (and steady-state) approach. In a first stage, the robustness of the methodology is investigated by comparing the results arising from repeated sweep and map data for different material compositions and adhesive types. The outcome revealed a significantly greater repeatability of the double-sided tape adhesive process in comparison with the glue. Nonetheless, although frequency and amplitude trends were successfully estimated in all scenarios, a non-negligible bias in absolute value seems to negatively affect the tape results. In a second stage, a preliminary study of fatigue is conducted. Overall, the results showed fully reversible time-dependent changes in both stiffness and damping.

A more extensive testing campaign is needed to assess the role of adhesive in long-lasting loading scenarios and comprehend the reasons behind the observed changes in rubber mechanical properties. Ultimately, a reliable and repeatable design solution is sought.

References

1. Per-Erik, A.: Modeling of elasticity and damping for filled elastomers. PhD thesis. Lund University, Lund Institute of Technology, Division of Structural Mechanics (1997)
2. Sjöberg, M.: On dynamic properties of rubber isolators. PhD thesis. KTH, Royal Institute of Technology, Department of Vehicle Engineering (2002)
3. Rouleau, L., et al.: Application of Kramers-Kronig relations to time-temperature superposition for viscoelastic materials. Mech. Mater. **65**, 66–75 (2013). ISSN: 01676636. https://doi.org/10.1016/j.mechmat.2013.06.001
4. Ramorino, G., et al.: Developments in dynamic testing of rubber compounds: assessment of non-linear effects. Polym. Test. **22**(6), 681–687 (2003). ISSN: 01429418. https://doi.org/10.1016/S0142-9418(02)00176-9
5. Roncen, T., Sinou, J.J., Lambelin, J.P.: Experiments and nonlinear simulations of a rubber isolator subjected to harmonic and random vibrations. J. Sound Vibr. **451**, 71–83 (2019). ISSN: 10958568. https://doi.org/10.1016/j.jsv.2019.03.017
6. Haeussler, M., Klaassen, S.W.B., Rixen, D.J.: Experimental twelve degree of freedom rubber isolator models for use in substructuring assemblies. J. Sound Vibr. **474**, 2020 (2020). ISSN:10958568. https://doi.org/10.1016/j.jsv.2020.115253
7. Trainotti, F., Slimak, T., Rixen, D.: Vibration testing for industrial rubber characterization. In Submission (2023)

Chapter 3
The Astir Glider Wing Dataset for Population-Based SHM

Marcus Haywood-Alexander, Keith Worden, Nikolaos Dervilis, Robin S. Mills, Lawrence A. Bull, and Tina A. Dardeno

Abstract Applications of structural health monitoring (SHM) often use vibration data to detect when damage occurs in structures, by detecting changes in the modal properties. Damage causes changes in material/structural properties which affect the modal characteristics; however, inconsequential changes in environment can reduce the capability of the damage detector, as they also affect the modal characteristics. Furthermore, small differences between nominally identical structures may also manifest as changes in the modal characteristics, thus making fully enveloping baselines difficult to obtain for an entire *population* of structures. This challenge provides the motivation for the field of *population-based SHM* (PBSHM), where the population is considered as a whole, in order to generate a more robust damage detection strategy. An experimental campaign was conducted to collect vibration data on four nominally identical Grob G102 Astir glider wings, three of which were "healthy" and one of which was damaged; this was done to generate a dataset which can be used to develop and test PBSHM methods. The experimental campaign included testing over a range of temperatures, and included a variety "pseudo-damage" states, where masses were added to the structures. This paper highlights the challenges faced, which motivate PBSHM by showing some examples of the data collected, including frequency response data and estimated modal characteristics. In addition, the paper shows some preliminary work which aims to separate out data of individual structures or states, from data of the full population.

Keywords Environmental envelope · Structural health monitoring · Population-based · Dataset · Aerospace structures

3.1 Introduction

When damage occurs in structures, this often causes changes in local material properties, such as Young's modulus. This change in material properties can manifest via changes in modal properties, such as natural frequencies, damping, mode shapes, etc. Inverting this principle, vibration testing has long been used to monitor the structural health of aerospace structures, by use of measuring modal characteristics. However, aerospace structures also undergo a wide variety of environmental conditions, which can affect the structural properties and/or modal characteristics. For example, temperature can cause changes in stiffness of the material [1], or thermal expansion can alter boundary conditions [2]. This can lead to two possible issues in vibration-based health monitoring; false-positives may occur when environmental conditions are not taken into account, or expected changes from environmental conditions may conceal changes resulting from damage.

Distinguishing between patterns in data within the expected environmental envelope and damage can be a difficult task, and it can affect practical implementation of structural health monitoring (SHM) [3–6]. This challenge drives the motivation for developing *population-based structural health monitoring* (PBSHM), which allows the transfer of valuable information—such as normal operating conditions and damage states—across a population of structures. Much like expected changes within the operational envelope, there will be small changes in material properties, internal structure, and manufacturing

M. Haywood-Alexander (✉) · K. Worden · N. Dervilis · T. A. Dardeno
Dynamics Research Group, Department of Mechanical Engineering, University of Sheffield, Sheffield, UK
e-mail: m.haywood@sheffield.ac.uk

R. S. Mills
Dynamics Research Group, Laboratory for Verification and Validation, University of Sheffield, Sheffield, UK

L. A. Bull
Department of Engineering, University of Cambridge, Cambridge, UK

M. Allen et al. (eds.), *Special Topics in Structural Dynamics & Experimental Techniques, Volume 5*,
Conference Proceedings of the Society for Experimental Mechanics Series, https://doi.org/10.1007/978-3-031-37007-6_3

details between nominally identical structures within a population. These discrepancies can manifest as differences in the modal characteristics, making generalizing between structures difficult.

In this work, vibration data were collected on four nominally identical glider wings, three of which were healthy and one of which had several damages over the wing. To cover the environmental envelope, the wings were tested at a range of temperatures, and were tested with masses fixed at specific locations to "simulate" damage [7]. Frequency response (FRF) data were then passed through two post-processing methods: the PolyMAX algorithm [8] and the overlapping mixture of Gaussian processes (OMGP) method [9]. The PolyMAX algorithm returns estimated modal characteristics from an FRF, which are often used as damage indicators in SHM techniques. PolyMAX was applied to first check any variations of these characteristics between structures and across the environmental envelope, for studying applications of SHM on the structures. Here, they are shown and studied to discuss aspects of PBSHM using modal characteristics, considering how these characteristics can change within the expected "healthy" envelope. The OMGP method is a useful method to separate out data of individual structures from a set of population data, or data from different environmental and operational conditions. In particular, it can separate out data that lies within the same envelope, making this a useful method for application in PBSHM.

This paper aims to showcase the new dataset collected, which has been collected with the motivation for development of the field of PBSHM. Firstly, the experimental campaign is explained, including the experimental setup and the structure population. This section is followed by a brief explanation of the abovementioned post-processing techniques applied. The results section shows an example of FRFs from the dataset, followed by the results from each of the methods. These results are a preliminary example, and are included to show and discuss the motivation of PBSHM techniques, as well as highlighting how this dataset is a useful resource for researchers in the field.

3.2 The Glider Wings and Experimental Setup

The purpose of this experimental campaign was to create a dataset which can be used as a benchmark in the field of PBSHM. As will be shown in this work, these structures return consistent vibration data results, though changes resulting from the structural and environmental envelope can mask those due to damage. Previously, it was shown how the temperature affects the modal characteristics of the wings, and how these can be modelled in order to aid SHM applications [10].

The structures in this campaign are four nominally identical Grob G102 Astir glider wings, with two symmetric pairs from two gliders, an image of one under test is shown in Fig. 3.1. Each of the pairs is labelled as A & B, where the starboard

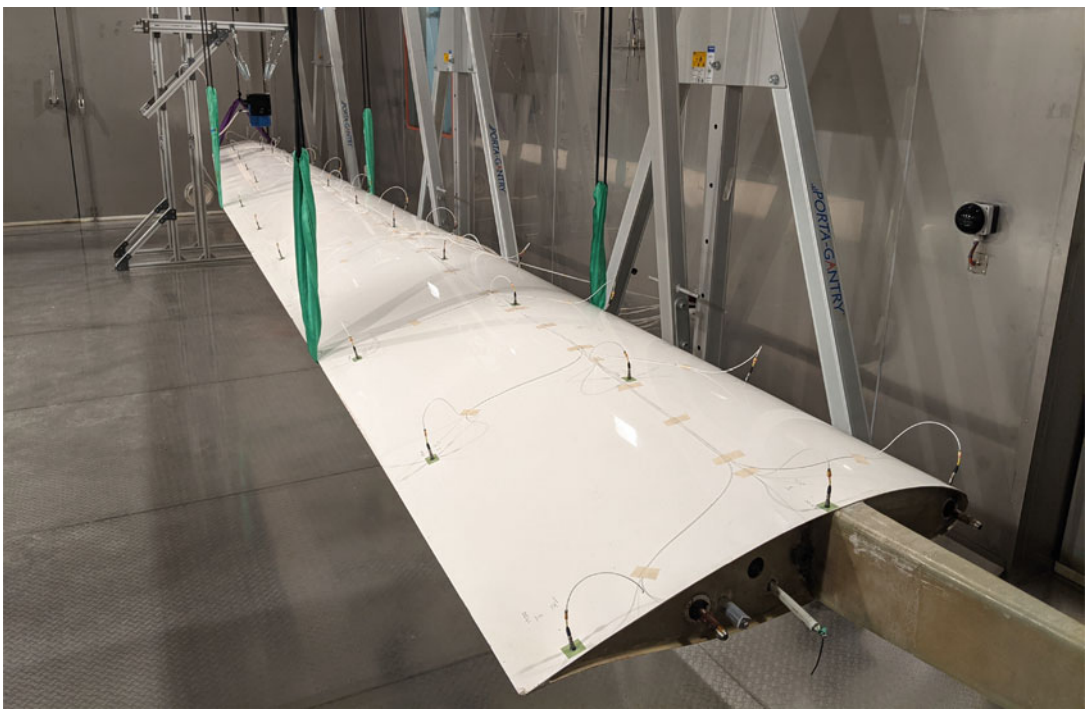

Fig. 3.1 Image of glider wing A2 in the environmental chamber

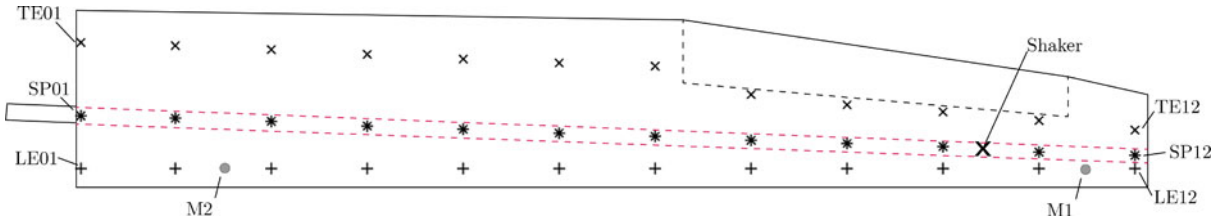

Fig. 3.2 Experiment layout, including location of sensors, shaker and masses. The sensor labels are split into three 'lines' of sensors; along the leading edge 'LE', spar 'SP', and trailing edge 'TE', and are then numbered in order starting from the root

and port wings are suffixed as 1 and 2, respectively (e.g., the port wing from the second glider is labelled B2). Three wings were healthy, i.e., no visible damage was present (A1, B1, and B2), and one had multiple damages over the wing (A2). To approximate free-free boundary conditions, the wings were suspended from gantries using elastic slings.

For this series of data, 36 uniaxial accelerometers were placed over the upper surface of the wings; their layout is shown in Fig. 3.2; each had a nominal sensitivity of 10 mV/g. Acceleration data were recorded from the wing using Siemens PLM LMS SCADAS hardware and software, where the individual sensitivities of each accelerometer were used to an accuracy of 0.01 mV/g. The accelerometers were placed in the same locations on all wings, using a datum at the trailing edge-root corner. Electrodynamic shakers were suspended from a gantry using elastic slings, attached to the upper surface of the wings, and used to excite the glider wings with a white-noise signal. The force applied to the wing measured using a PCB Piezotronics Force Transducer.

A continuous random excitation was generated in the LMS system up to 1024 Hz, and supplied to the shaker, where the amplitude was kept consistent throughout the campaign by controlling the voltage amplitude of the supply signal. During excitation, data from the accelerometers and force transducer were acquired simultaneously, recording 20 averages, with a 1% overlap between averages. The target bandwidth and number of spectral lines of the frequency data output were selected to be 1024Hz and 8192, respectively, resulting in an acquisition time and sample rate of 8 s and 2048 Hz, respectively. A Hanning window was applied to each of the recorded time signals before calculating the amplitude spectra, frequency response relative to the forcing, coherence, and autopower, all averaged in the frequency domain.

For the experimental campaign, two influencing variables were controlled: additional localized masses and temperature. On all wings except for the damaged wing A2, masses were added in three setups: a 64g mass towards the tip (labelled M1), a 63g mass towards the root (labelled M2), and both masses in their designated location simultaneously (labelled M3). As shown in [7], the addition of masses to a structure can "simulate" the appearance of damage, as they affect modal characteristics in a similar manner as a reduction in stiffness. In addition to the added masses, the wings were tested at seven different temperatures, from 0°C to 30°C in 5°C increments, at the Laboratory for Verification and Validation (LVV). The wings were soaked at each temperature for a minimum of 8 hours before testing. This results in a total of 28 frequency-domain datasets for each of the healthy wings, and seven datasets for the unhealthy wing, giving a total of 91 datasets, spanning a variety of wings, temperatures, and pseudo-damage states.

3.3 Preliminary Analysis Methods

From the frequency response data, the poly-reference least-squares complex frequency domain method [11, 12] was then used to estimate the modal parameters for the first 12 modes. These parameters included the resonance frequency, the viscous damping ratio, and the mode shape, for each mode. Specifically, the commercially available PolyMAX algorithm was used, a detailed background on which can be found in [8, 13]. This algorithm was implemented with a maximum model order of 50, a bandwidth of 3–64 Hz, and tolerances of 1% and 5% for the frequency and damping ratio, respectively. The chosen solutions (poles) selected were those that were fully stable (i.e., had only stable poles at higher ranks) and had a rank greater than 12. For brevity, this paper looks at the modal parameters for all four wings, and all mass states, but at a fixed temperature of 20°C.

As well as methods on individual modal parameters, the OMGP method was applied to the full frequency response data, for different subsets of the data. A detailed definition and overview of the method can be found in [9, 14, 15]. The OMGP is a flexible method for developing the population form without the need for labelling into operational, environmental, and health conditions. This method aims to separate out overlapping functions, or in the context of PBSHM, to separate out

different operational/environmental states from a known set of structures. A particular advantage of the OMGP method is its capability to accommodate for multiple tasks that occur between structures within the population.

An OMGP assumes that the number of classes is known *a priori*, but does not assume which data belongs to each class. For the first case, an OMGP was fit to the real and imaginary components of the FRF data from all healthy wings at a fixed temperature of 20°C. As such, it was assumed that three FRFs from three glider wings contributed to the data ($K = 3$). Likewise, for the second case, an OMGP was fit to the real and imaginary components of the FRF data from wing A1 at temperatures between 0 and 30°C, at 10°C increments ($K = 4$). In this paper, the FRFs obtained from sensor SP03 were considered for analysis, and a narrow frequency band was selected between 35 and 47 Hz, as the third bending mode dominated in that band, at that particular measurement location.

The OMGP [9, 14–16] describes a dataset by evaluating each observation using one of K latent functions plus additive noise. In the method, a binary indicator matrix $\mathbf{Z}$ is applied to the function space, the non-zero entries of which indicate observation i was generated by function k. The likelihood of the OMGP is therefore written as [9, 15],

$$p(\mathbf{y} \mid \{\mathbf{f}^{(k)}\}_{k=1}^{K}, \mathbf{Z}, \mathbf{x}) = \prod_{i,k=1}^{N,K} p(y_i \mid f^{(k)}(x_i))^{\mathbf{Z}[i,k]} \tag{3.1}$$

Like the conventional GP, the OMGP is a flexible regression technique that allows for inclusion of physics-based knowledge via the mean and kernel functions (which are encoded in the prior). Here, a squared exponential kernel was used in order to embed smoothness of the function. To incorporate knowledge of the dynamic properties of the wings, a non-zero mean function was introduced, via an estimation of the accelerance FRF,

$$\mathbf{H}_{ij}(\omega) = -\omega^2 \sum_{k=1}^{n} \frac{\mathrm{A}_{ij}^{(k)}}{\omega_{nk}^2 - \omega^2 + 2i\zeta_k \omega \omega_{nk}} \tag{3.2}$$

where $\mathrm{A}_{ij}^{(k)}$ is the residue for mode k, defined as the product of the mass-normalized mode shapes at locations i and j ($\mathrm{A}_{ij}^{(k)} = \psi_{ik}\psi_{jk}$) [17]. The natural frequency associated with mode k is ω_{nk}, and the modal damping associated with mode k is ζ_k [17]. Modal damping, residue, and natural frequency provide the mean-function hyperparameters.

Exact computation of the posterior distribution is intractable; therefore, a variational inference [18] and Expectation Maximization (EM) scheme was used to determine a suitable approximation for the posterior. In this work, the data were classified and fit by approximating the intractable posterior distribution $p(\{\mathbf{f}^{(k)}\}_{k=1}^{K}, \mathbf{Z} \mid \mathbf{x}, \mathbf{y})$ via the OMGP approach described in [9], using the variational inference and EM scheme presented in [9].

3.4 Results

Some examples of FRFs extracted from the experiment are shown in Fig. 3.3, showing the results from two sensors. These figures show that the nominally identical structures within the population still have discrepancies in their frequency response. Importantly, it is apparent that the expected discrepancies within the population may mask the changes in a specific structure from damage, as wing A2 is not obviously different from the undamaged wings.

Modal Parameter Estimation This section studies the estimated modal parameters, by comparing those between wings and those at different mass states. These comparisons are displayed in Fig. 3.4, with the damaged wing highlighted using a diamond-shaped marker. In Fig. 3.4a, the population is separated into individual structures by color, with all mass states included. In Fig. 3.4b, the grouping is made into mass states, to compare the effect of pseudo-damage on the entire population.

The first observation from Fig. 3.4a is that with the change in pseudo-damage states, the individual modal characteristics of the wing appear to remain similar, when compared to changes over the population. This observation indicates that simply using the modal parameters as a means of detecting small-scale damage, such as this, may be inadequate when applying to a population of structures. Furthermore, there is no discernible pattern or scaling between the individual structures, meaning that it is not simple to transfer knowledge from one structure to another.

When looking at Fig. 3.4b, there appears to be no grouping in terms of pseudo-damage states, specifically much less so than the clear grouping of structures in Fig. 3.4a. Furthermore, in both figures, the modal characteristics of the damaged wing are within the envelope covered by both the population and the pseudo-damage states. Both of these observations indicate

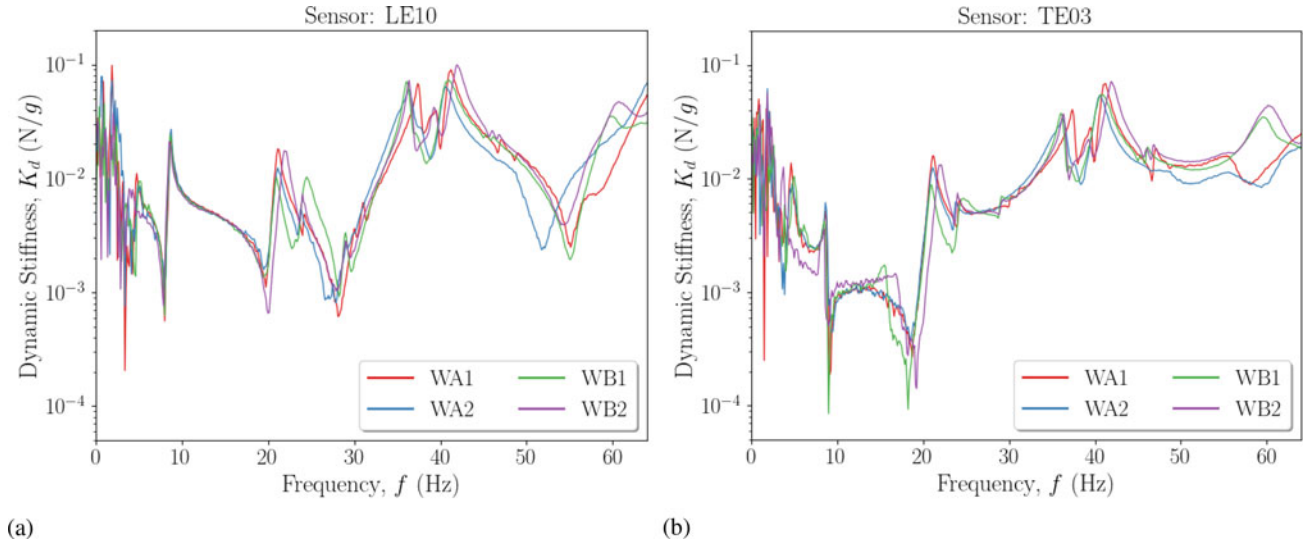

Fig. 3.3 Example frequency response data from sensors (**a**) LE10 and (**b**) TE03. All data are shown for a fixed temperature of 20°C and with no mass additions

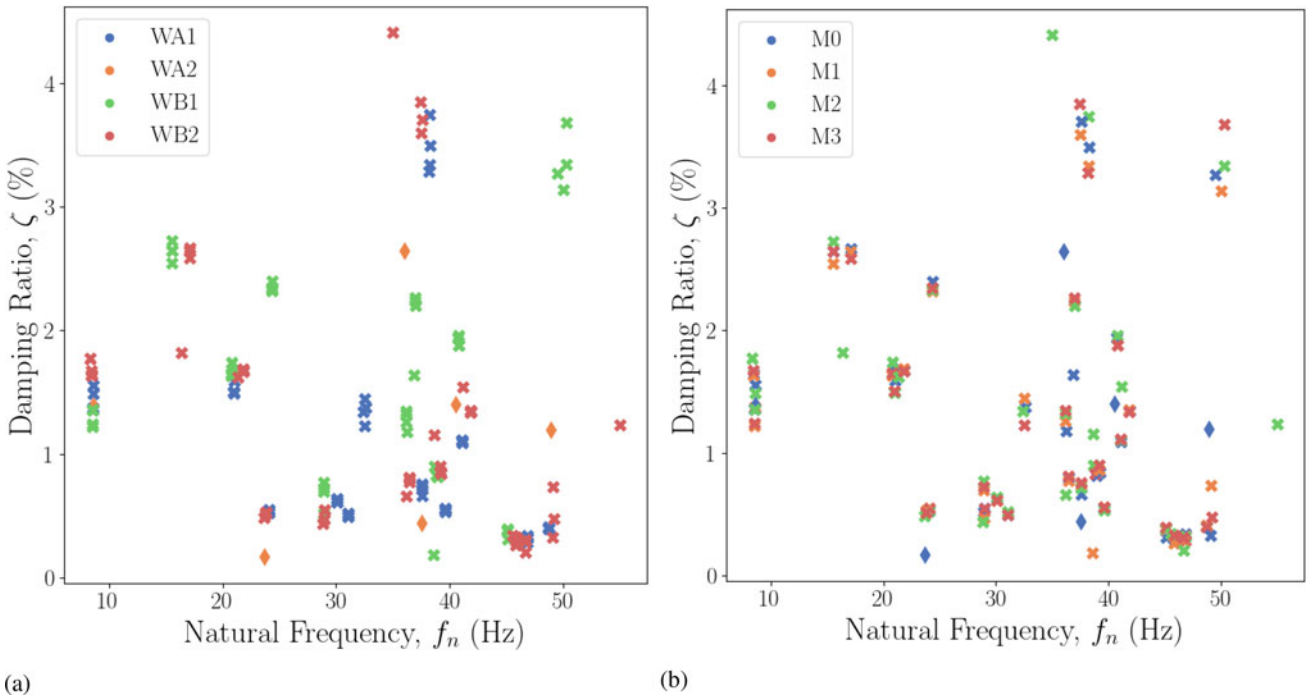

Fig. 3.4 Estimated modal characteristics of the population at a fixed temperature of 20°C, grouped by (**a**) individual structures and (**b**) added mass. The diamond marker shows the damaged wing (WA2)

once more that the expected change in structural properties throughout the population can easily mask changes that may occur because of damage, when considering only the unique modal characteristics.

OMGP-Based Population Forms Before discussing the results of the method, first it is important to note some considerations made during the application of the method. Because the real part of the FRF was more separable than the imaginary part, the OMGP performed better for a variety of initializations on the real data. As such, the real data were fit first, and an optimal solution was found by randomly initializing the hyperparameters ten times, keeping the training set fixed, and choosing the solution with the maximum lower bound, and, therefore, the highest marginal likelihood. The initialization parameters were chosen randomly, but restricted to reasonable intervals in the same manner as the hyperparameters were bounded during the optimization. Once learnt, the optimized hyperparameters for the real data were used to initialize the OMGP for the imaginary data. The results from applying the OMGP method to data of separate wings at a fixed temperature are shown in Fig. 3.5, and the results of applying the method to wing A2 at various temperatures are shown in Fig. 3.6.

In both cases, the FRF model from Eq. (3.2) was used to generate a mean function, with the modal damping, residue, and natural frequency used as mean-function hyperparameters. The sign of the data ($\pm$) was assumed to be known *a priori*, and can easily be determined via data inspection. For the first case, the posterior predictive mean of the OMGP is plotted with the mean function, variance (99% confidence interval), and training data for the real and imaginary FRFs in Figs. 3.5a and b. Likewise, for the second case, the posterior predictive mean of the OMGP is plotted with the mean function, variance (99% confidence interval), and training data for the real and imaginary FRFs in Figs. 3.6a and b, respectively.

It is also worth noting the non-smoothness of one of the estimated functions in Fig. 3.6, which may be a result of the data not being distinct enough. This could be improved by enforcing smoothness in the hyperparameter choice, though constricting the learner may arguably go against the purpose of such a method. Figures 3.5a to 3.6b show that for both cases, the OMGPs provided a reasonable fit for the FRF data, and the majority of the training data were enclosed by the variance bounds. The *form* developed using the OMGP approach provides a unified model for a population of structures, despite slight changes in boundary conditions, differences among the nominally identical members, and variations in temperature.

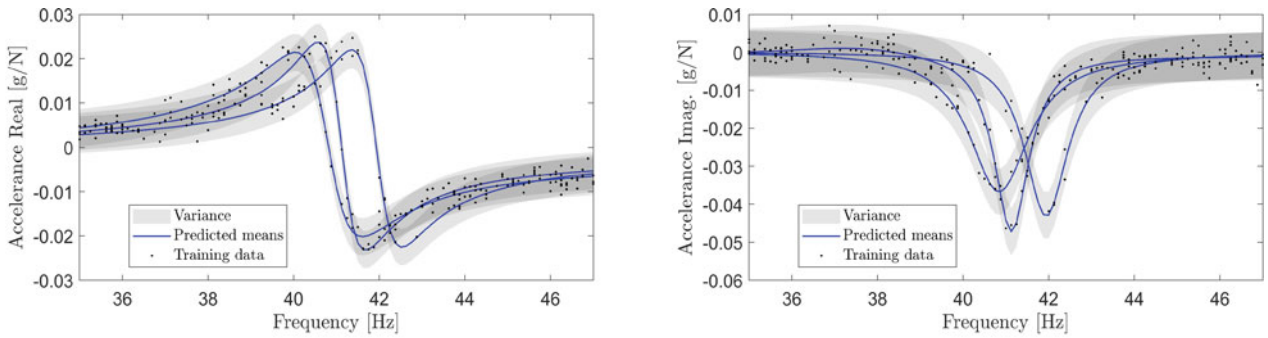

Fig. 3.5 OMGP predictions using (**a**) real and (**b**) imaginary FRF data, for the healthy glider wings (WA1, WB1, and WB2) at 20°C

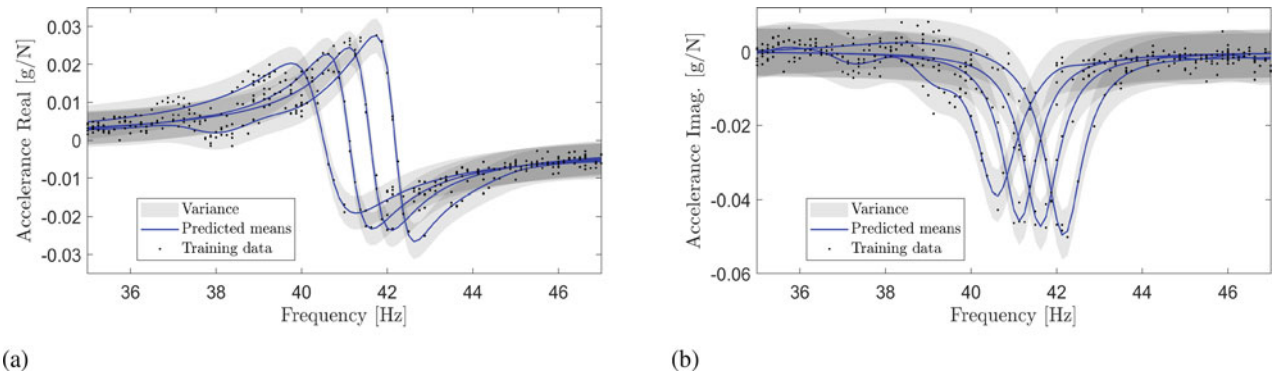

Fig. 3.6 OMGP predictions using (**a**) real and (**b**) imaginary FRF data, for WA1 at various temperatures

3.5 Conclusions

This paper showed the development of a new dataset which was collected for the purposes of research and development in PBSHM techniques, and displayed some preliminary results from the dataset. The data collected highlights the challenges that the field of PBSHM aims to address, importantly, how discrepancies between structures within a population, and changes because of the environmental conditions, can mask those that appear from damage. Estimates of the modal properties were shown, which were similarly difficult to extract from the envelope of conditions and structure differences. Using the OMGP method, preliminary results were shown on how the dataset can be separated into the individual structures, highlighting the datasets use for PBSHM method development. This dataset is being developed to include further data, including a complete set of frequency-domain data and modal characteristics—it aims to provide a benchmark for PBSHM.

Acknowledgments The authors gratefully acknowledge the support of the UK Engineering and Physical Sciences Research Council (EPSRC), via grant references EP/R003645/1, EP/R004900/1, and EP/W005816/1. L.A. Bull was supported by Wave 1 of the UKRI Strategic Priorities Fund under the EPSRC grant EP/W006022/1, particularly the Ecosystems of Digital Twins theme within that grant and the Alan Turing Institute.

This research made use of the Laboratory for Verification and Validation (LVV), which was funded by the EPSRC (grant numbers EP/J103714/1 and EP/N010884/1), the European Regional Development Fund (ERDF), and the University of Sheffield. The authors would like to extend special thanks to Michael Dutchman, for assisting with experimental setup.

References

1. Yu, B., Kodur, V.: Effect of temperature on strength and stiffness properties of near-surface mounted frp reinforcement. Compos. Part B Eng. **58**, 510–517 (2014)
2. Santiuste, C., Barbero, E., Henar Miguelez, M.: Computational analysis of temperature effect in composite bolted joints for aeronautical applications. J. Reinf. Plast. Compos. **30**(1), 3–11 (2011)
3. Worden, K., Sohn, H., Farrar, C.R.: Novelty detection in a changing environment: regression and interpolation approaches. J. Sound Vib. **258**(4), 741–761 (2002)
4. Alampalli, S.: Influence of in-service environment on modal parameters, In: Proceedings-SPIE the International Society for Optical Engineering, vol. 1, pp. 111–116. Citeseer (1998)
5. Cawley, P.: Long range inspection of structures using low frequency ultrasound. Structural Damage Assessment Using Advanced Signal Processing Procedures, pp. 1–17 (1997)
6. Sohn, H.: Effects of environmental and operational variability on structural health monitoring. Philos. Trans. R. Soc. A Math. Phys. Eng. Sci. **365**(1851), 539–560 (2007)
7. Papatheou, E., Manson, G., Barthorpe, R.J., Worden, K.: The use of pseudo-faults for novelty detection in SHM. J. Sound Vib. **329**(12), 2349–2366 (2010)
8. Peeters, B., Van der Auweraer, H., Guillaume, P., Leuridan, J.: The polymax frequency-domain method: a new standard for modal parameter estimation? Shock Vib. **11**(3–4), 395–409 (2004)
9. Lázaro-Gredilla, M., Van Vaerenbergh, S., Lawrence, N.D.: Overlapping mixtures of Gaussian processes for the data association problem. Pattern Recognit. **45**(4), 1386–1395 (2012)
10. Dardeno, T.A., Haywood-Alexander, M., Mills, R.S., Bull, L.A., Dervilis, N., Worden, K.: Investigating the effects of ambient temperature on feature consistency in vibration-based SHM. In: Proceedings of the 13th International Workshop on Structural Health Monitoring (IWSHM) (2022)
11. N.M.M. Maia, J.M. Montalvao e Silva, Theoretical and Experimental Modal Analysis. Research Studies Press, Boston (1997)
12. Guillaume, P., Verboven, P., Vanlanduit, S., Van Der Auweraer, H., Peeters, B.: A poly-reference implementation of the least-squares complex frequency-domain estimator. In: Proceedings of IMAC, vol. 21, pp. 183–192. A Conference & Exposition on Structural Dynamics, Society for Experimental Mechanics (2003)
13. Peeters, B., Lowet, G., Van der Auweraer, H., Leuridan, J.: A new procedure for modal parameter estimation. J. Sound Vib. **38**(1), 24–29 (2004)
14. Bull, L.A., Gardner, P.A., Gosliga, J., Rogers, T.J., Dervilis, N., Cross, E.J., Papatheou, E., Maquire, A.E., Campos, C., Worden, K.: Foundations of population-based SHM, Part I: homogeneous populations and forms. Mech. Syst. Signal Process. **148**, 107141 (2021)
15. Bull, L.A., Gardner, P.A., Rogers, T.J., Dervilis, N., Cross, E.J., Papatheou, E., Maquire, A.E., Campos, C., Worden, K.: Bayesian modelling of multivalued power curves from an operational wind farm. Mech. Syst. Signal Process., 108530 (2021)
16. Tay, M.C.K., Laugier, C.: Modelling smooth paths using Gaussian processes. In: Proceedings of the International Conference on Field and Service Robotics (FSR07), pp. 381–390. Springer, Chamonix, France (2007)
17. Worden, K., Tomlinson, G.R.: Nonlinearity in Structural Dynamics: Detection, Identification and Modelling. Institute of Physics Publishing, Bristol, UK (2001)
18. Blei, D.M., Kucukelbir, A., McAuliffe, J.D.: Variational inference: A review for statisticians. J. Am. Stat. Assoc. **112**(518), 859–877 (2017)

Chapter 4
Experimental Characterization of Structural Traveling Wave-Induced Thrust

Skriptyan Syuhri, Hossein Zare-Behtash, and Andrea Cammarano

Abstract Using nature-inspired solutions for propulsion, this work investigates the use of traveling waves to generate thrust in water. A design based on a slender cantilever beam similar to flagella in bacteria is submerged in water and excited with a sinusoidal motion to study the impact of frequency and amplitude of the oscillation on the thrust generation. Structural measurements combined with advanced flow diagnostic techniques are used to characterize the behavior of the fluid–structure system.

The structural response and the induced traveling waves are first studied in air and characterized through laser vibrometry and high-speed digital image correlation. This demonstrated the possibility of inducing traveling waves in the structure and permitted to identify the conditions that maximize the traveling versus the standing wave contribution.

The characterization of the fluid–structure interaction has been done using Laser Doppler Anemometry (LDA). LDA measurement was carried out downstream from the beam at a fixed distance to measure the velocity of the induced flow at different excitation conditions (amplitude and frequency).

The results showed that the coupling between the structural motion and the thrust generated is nonlinear in nature and depends on the tip displacement of the beam. Empirical laws that relate the amplitude and frequency of excitation to the generated thrust are here proposed.

Keywords Traveling waves · Fluid · Structure interactions · Experimental structural dynamics · Thrust · Laser experimental measurements

4.1 Introduction

The arrangement of a beam submerged in liquid can provide many advantages in engineering applications by offering an ability to generate thrust. This is achieved via traveling waves that propagate through the beam and, interacting with the surrounding fluid, generate thrust. Numerous concepts and implementations have been proposed differing in general arrangements that lead to different structural and fluid characteristics. Ramananarivo et al. [1], for instance, reproduced undulatory swimming by using an elastic beam with a permanent magnet attached to one tip as an actuator that was achieved by inducing electromagnetic fields around the structure. Subsequently, such studies have been carried out numerically and experimentally by many researchers to further the understanding of the dynamic characteristics and propulsive phenomena of beam structures submerged in viscous fluid [2–7].

Similar configurations can be used as micropumps capable of delivering tiny volume of fluid and transporting different type of fluid viscosity and temperature. Ogawa et al. [8] first introduced a liquid pumping device by utilizing a clamped–clamped beam configuration actuated with nine piezoelectric patches distributed evenly along the beam length. Traveling waves are induced by applying sinusoidal voltages with a phase difference of 120° for each piezoelectric. The bending traveling waves on the beam surface are then used to carry the liquid. Following this investigation, the performance of traveling wave-based pumping devices is further improved in references [9, 10] by using magnetic-based actuators to replace the piezoelectric patches. This actuator generates more force for the beam, which, in turn, produces higher flow rate than the piezoelectric-based actuator [9–11].

S. Syuhri · H. Zare-Behtash · A. Cammarano (✉)
James Watt School of Engineering, University of Glasgow, Glasgow, UK
e-mail: andrea.cammarano@glasgow.ac.uk

M. Allen et al. (eds.), *Special Topics in Structural Dynamics & Experimental Techniques, Volume 5*,
Conference Proceedings of the Society for Experimental Mechanics Series, https://doi.org/10.1007/978-3-031-37007-6_4

Researchers [4, 12–14] have also attempted to create robotic fish, devices that use oscillatory motion to generate propulsion using slender beam structures. This is due to similar characteristics of the first and second mode shape of cantilever beam models to the swimming motion of thunniform fish. Subsequently, fluid dynamics of the beam tip have been thoroughly investigated [4, 14–17]. A parametric study has been conducted to address the influence of beam geometries to the propulsive performance of the beam [12, 13]. The use of smart materials to actuate and mimic the fin and tail characteristics of a fish has been attempted in recent times [12, 18–21].

In cases of beam submerged in a viscous fluid, strong damping induced from fluid loading can generate phase delay along the beam length that leads to traveling wave phenomena in the vibration pattern. Accordingly, passive traveling waves can be produced by implementing single excitation such as a cantilever beam configuration subjected to base motion. Some researchers have attempted to improve the traveling wave generation on the beam structures. Loh and Ro [22] introduced a two-mode excitation where two forces arranged in a symmetrical form along the beam length are set at the same amplitude and frequency with a phase difference of 90°. This technique is considered easy to be implemented in the real engineering applications and has been expanded in many successive works [23–30]. Another method to produce the traveling wave was developed by Kuribayashi et al. [31] based on the principle of impedance matching. This actuation also utilizes two actuators: one actuator is functioned as the source of excitation and the other is used to prevent the reflection wave when the propagating wave collides with boundaries. Furthermore, Tanaka and Kikushima [32] proposed an active sink method, which is based on the elimination of the reflecting wave at the other boundary utilizing damping mechanisms. However, study in reference [33] suggested that generating maximum traveling waves in a particular frequency does not necessarily promote maximum generated thrust. The relationship between traveling waves and their capacity to generate propulsion is not well understood. Therefore, the purpose of this study is to provide insight into the understanding of the contribution of traveling waves to the characteristics of fluid velocity.

4.2 Beam FRF in Different Fluid Media

The study of the induced fluid flow due to traveling waves requires a thorough investigation of the dynamics of the structure in which the traveling waves propagate. Since the phenomenon is quite complex in its nature, some simplifications are necessary to highlight the fundamental physics of this interaction. For this reason, the experimental design is based on a base-excited cantilever beam, a structure which is well characterized and easy to model. This choice is prompted by the need to limit the complexity in the dynamics of the structure in isolation, so that a system of system approach could be used to identify the effect of the fluid dynamics on the behavior of the beam.

In this experiment, the base of the cantilever beam is mounted directly to the base of an LDS V201 shaker via a rigid extension plate: the motion of the base of the shaker, as well as the tip of the extension plate, has been measured using a PCB Piezotronics accelerometer, model 352C22. The signal from the accelerometers was amplified with a PCB Piezotronics amplifier, model 428C. The extension plate is necessary to permit full immersion of the beam in the liquid while conveying the excitation to the beam. The extension plate has been designed so that its first natural frequency does not interfere with the dynamics of the cantilever beam. The deflection of the beam has been measured at its free tip using a Polytech laser vibrometer PDV-100. A spectrum analyzer Quattro DataPhysics has been used to estimate the transfer function between the acceleration at the free tip with respect to the acceleration of the base. The transfer function is estimated by measuring the amplitude and phase delay between two signals, one from the accelerometer placed on the extension plate and the other from the laser vibrometer. The transfer function obtained in this manner is the form of a voltage ratio between the laser vibrometer signal (proportional to the tip velocity) and that of the accelerometer (proportional to acceleration) across a range of frequencies. SigCalc, the software interface for Quattro, has been used to convert the velocity measured from the laser vibrometer into accelerations. The input signals used to obtain the FRF in this study are random and stepped-sine input signals. Since the structure behaves linearly, using a random signal to drive the shaker is a very effective way to obtain a good estimation of the FRF of the structure within minutes. The stepped-sine signals, on the other hand, generate constant amplitudes at a single frequency per time with the driving frequency varying discretely across a range of frequencies: this method is more time demanding, but is more suitable in the presence of nonlinear behavior (Fig. 4.1).

The beam used in the fluid investigation had a thickness of 0.6 mm. The mass of the beam was 8.718×10^{-3} kg, resulting in the beam density of 8442 kg/m^3. The flexural rigidity of the beam was undetermined and will be estimated from the FRF using random input signals. The accelerometer was located at the clamped section of the beam to monitor the base input acceleration, while the laser vibrometer was pointed to the free tip of the beam to acquire the velocity responses. Figure 4.2 presents the FRF of the beam vibrating in air and water for various input amplitudes. To generate those data, the frequency span was limited to 600 Hz with the maximum random amplitude varied arbitrarily at 400 mV, 600 mV, and 800 mV. The gain

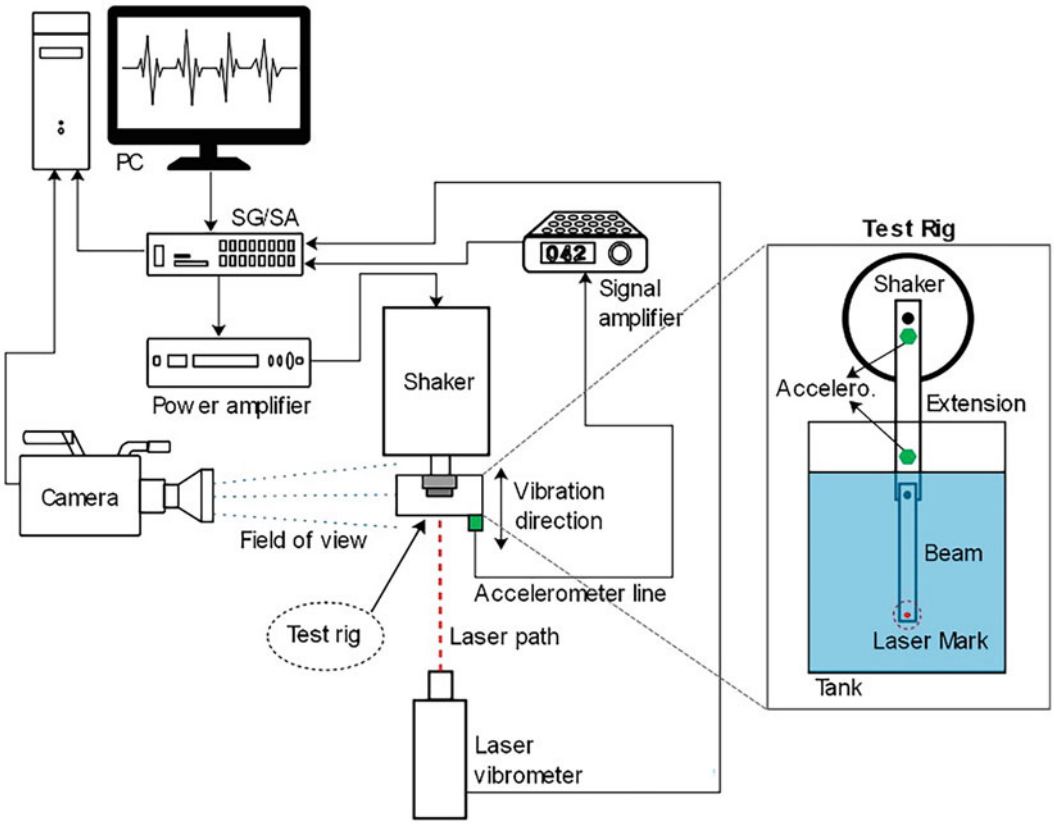

Fig. 4.1 Schematics of the setup for the measurement of the FRF of the beam

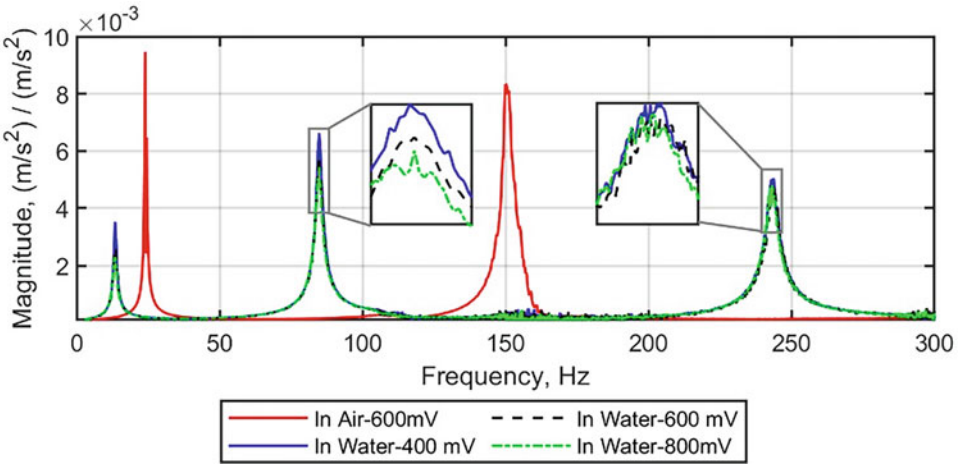

Fig. 4.2 FRF of the beam with the thickness of 0.6 mm

for the power amplifier was set around 4.6 V. Note that the signal analyzer automatically converted the velocity responses of the beam tip to the acceleration responses, resulting in dimensionless FRF magnitudes. This process might include filtering procedures that could underestimate the magnitude values. However, this should not influence the location of peaks with respect to frequency.

It is observed from the FRF of the beam vibrating in air shown in Fig. 4.2 that the beam is rigid indicated with the first resonant frequency located at 24 Hz. There is also a notch (discontinuity) in the first peak, which can be associated with the interaction of the beam and the supporting plate. The damping ratios for the first three resonant frequencies obtained from

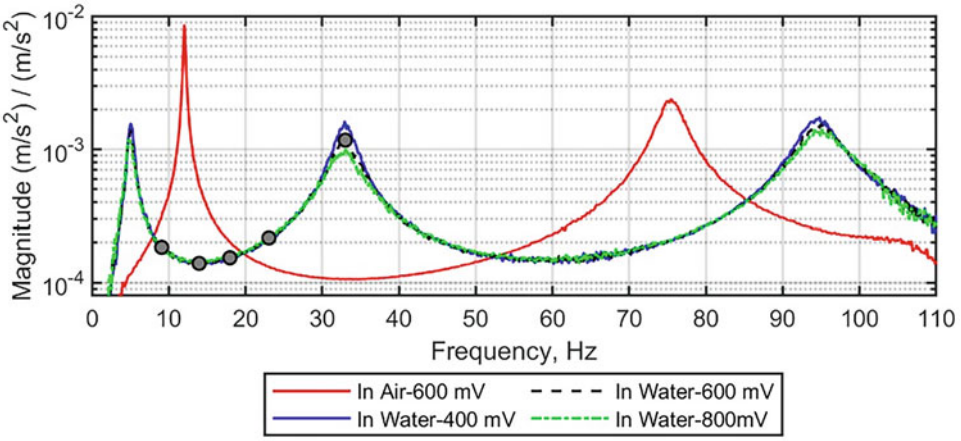

Fig. 4.3 FRF of the beam with the thickness of 0.3 mm

the signal analyzer are 2.8%, 1%, and 0.148%, respectively. It is noticed that the first damping ratio is considerably high. This might be caused by the nonlinearity due to the beam acting as dynamic absorbers of the supporting plate. The first three natural frequencies from the FRF can be utilized to obtain the flexural rigidity of the cantilever beam model using an equation in reference [34]. This gives the flexural rigidity value of 0.0395 N.m^2, 0.0392 N.m^2, and 0.04 N.m^2 for the first three resonant frequencies, respectively. The mean flexural rigidity is 0.0396 N.m^2, rounded to the nearest integer.

For the case of beams vibrating in water, there is a small deviation in the FRF magnitudes due to the variation of input amplitudes shown in Fig. 4.2. The first three damping ratios extracted from the signal analyzer with the amplitude of 600 mV are 4.496%, 1.272%, and 0.841%. Using the same equation in reference [34], the first three natural frequencies of 13.48 Hz, 84.77 Hz, and 243 Hz can result in the mean flexural rigidity of 0.0379 N/m^2. The relative error of the mean flexural rigidity value for the beam vibrating in air and water is 4.6%.

A metal beam with the thickness of 0.3 mm was used to examine the fluid flow between the first and two resonant frequencies. The mass of the beam is 4.457×10^{-3} kg, which leads to the estimated density of 8631 kg/m^3. The same procedures were applied to obtain the beam FRF. The time and frequency span for the signal analyzer were set to 10.24 s and 312.5 Hz, respectively, resulting in the frequency resolution of 0.09766 Hz. Figure 4.3 displays the beam FRF in two different media for various forcing amplitudes. It is observed that the first natural frequency for the beam vibrating in air drops to 12 Hz due to the thickness reduction. There is no nonlinearity observed in the peak of the first resonant. Using the quadrature pick picking method, the damping ratio is estimated to be 1.22%. The second resonant frequency is located at 75.5 Hz with the estimated damping ratio of 2.070%. The second damping ratio may be influenced by the interaction of the beam and the supporting plate. These natural frequencies can result in the mean flexural rigidity of 0.0051 N.m^2. For the beam vibrating in water, it is observed that the variation in the base amplitude can significantly change the magnitude at the peaks. The first three natural frequencies are obtained at 4.98 Hz, 32.90 Hz, and 94.80 Hz, respectively. The first three damping ratio values at the amplitude of 600 mV are estimated about 8.654%, 5.473%, and 2.775%, respectively. The mean flexural rigidity of the beam vibrating in water is 0.0046 N.m^2. Accordingly, the relative error of the flexural rigidity for the beam vibrating in air and water is 9.6%. The error increases due to thickness reduction, which makes the beam more flexible than the previous beam with the thickness of 0.6 mm. This agrees with the presumption in reference [5] stating that the approximation of fluid forces works well for estimating the dynamic behavior of a rigid (solid) structure and tends to break down for flexible structure.

4.3 Fluid Velocity Measurements

The schematic diagram for investigating fluid flow produced by a cantilever beam vibrating in water is illustrated in Fig. 4.4a. The mechanism to induce vibration in the submerged beam is the same as in previous section. The PicoScope 2405A USB oscilloscope was used to generate sine wave signals for the LDS V201 shaker and record the voltage readings from accelerometer sensors. The beam was submerged into a rectangular glass tank with the size of a $40 \times 25 \times 25$ cm filled with approximately 23.5 L of water. Note that the y- and z-axis direction shown in Fig. 4.4a are for the projection of the test rig including the tank, extension plate, and beam. Accordingly, the beam vibrates in the y-axis. The more detailed view of the

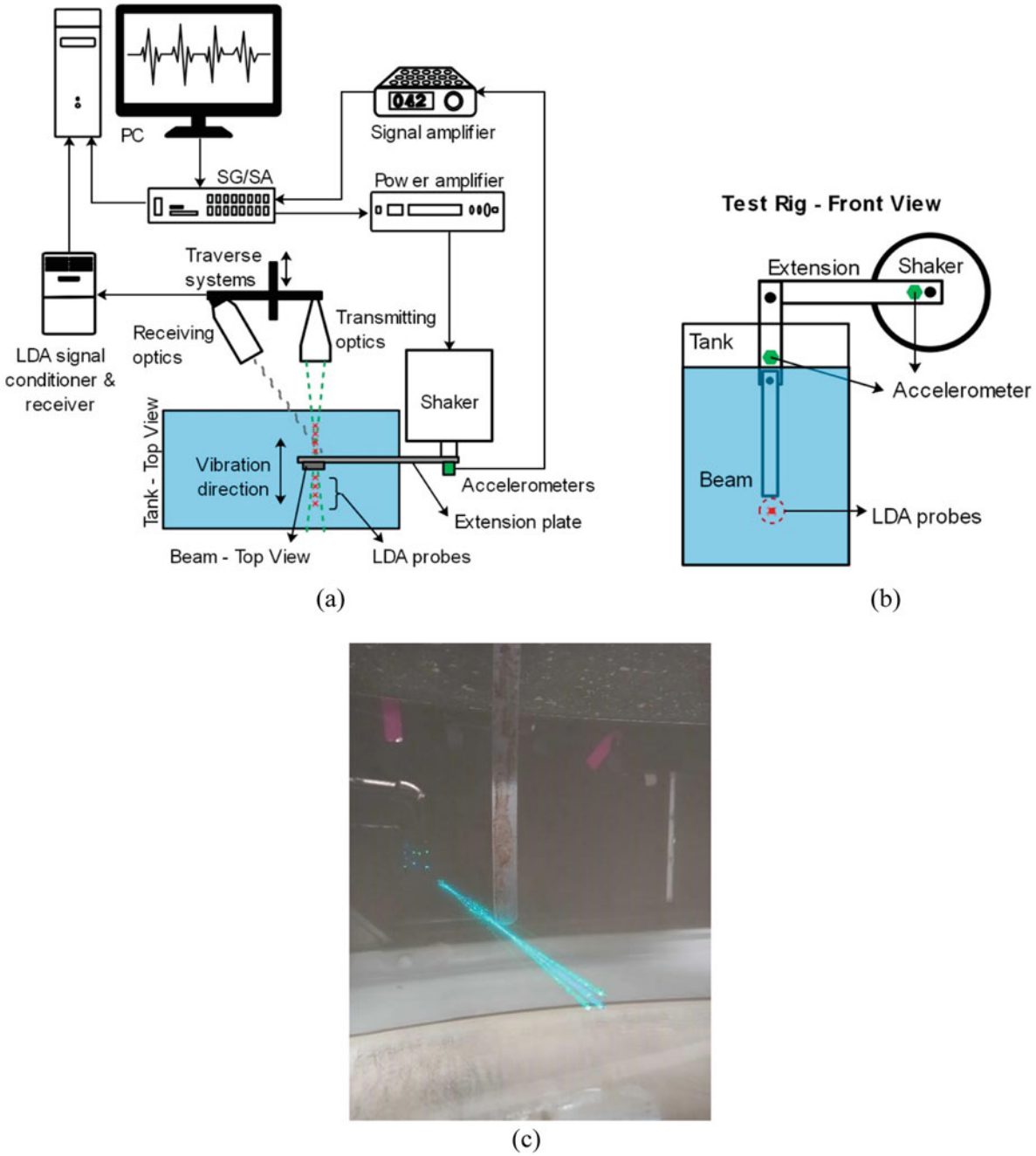

Fig. 4.4 Schematic diagram of fluid velocity measurement: top view (**a**) and lateral view (**b**). Picture of the LDA laser beam at the base of the cantilever beam

test rig is depicted in the *XZ*-plane displayed in Fig. 4.4b. Two accelerometers were used to monitor the input signal for the beam: one accelerometer was mounted close to the shaker, and the other accelerometer was attached to the clamped section of the beam. The vibration of the beam in the *y*-direction was expected to generate thrust in the *x*-direction. Therefore, the fluid measurement points were located below the free tip of the beam indicated with the red cross marker shown in Fig. 4.4b.

The fluid velocity around the beam was measured by a Dantec Dynamics two-component Laser Doppler Anemometry (LDA) system. This non-intrusive fluid measurement system mainly consists of laser, transmitting optics, receiving optics, and traverse systems. Two diode-pumped solid-state 1W lasers with wavelengths of 488 nm and 514 nm were used to facilitate continuous wave lasers. The transmitting optics, which includes laser beam splitters and focusing lenses, was used to diffract laser beams and shift their frequencies. The outputs of the beam splitters were directed with the focusing lens to

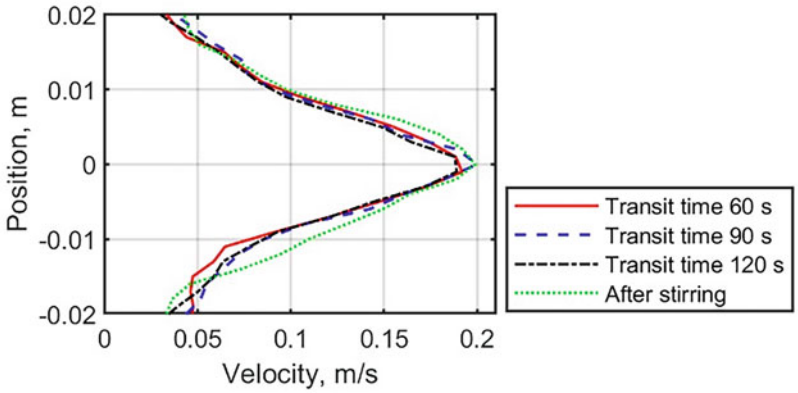

Fig. 4.5 Influence of the transit time on the fluid velocity profiles

intersect in the measurement point. Figure 4.4c displays four laser beams that coincide at one point below the beam. All laser beams were oriented at an angle of 2.5°, creating a volume measurement of 2.62 × 0.12 × 0.12 mm. The receiving optics, consisting of the lenses, filters, and photodiodes, would detect the scattered light due to seeding particles that pass through the probe. The optical lenses for the transmitting and receiving optics were mounted on a Dantec 9041T3332 2D traverse system capable of generating a linear motion with an accuracy of ± 0.01 mm. Moreover, the seeding particles used to scatter the light were silver-coated hollow glass spheres with the mean size of particles 10 μm.

Although the 2D traverse system is capable of scanning the measurement points on the *xy*-plane, the probe locations were kept at constant distance of 0.140 m below the tip of the cantilever beam for safety reasons (see Fig. 4.4b for a schematic representation). This was mostly done to prevent possible reflection of the laser lights from the beam surface that could damage the receiving optics. The traverse system was operated to acquire measurement points in the direction orthogonal to the axis of the beam and in the same direction of deflection from −0.025 to 0.025 m (see Fig. 4.4a for a schematic representation). This location was defined on the basis where strong fluid flow occurred. Before starting the LDA measurement, the water was stirred gently to distribute the seeding particles. This procedure was performed only if the experiment was suspended for a long time. Then, the beam was actuated with a particular forcing amplitude and frequency for some time not only to ensure the beam reaching steady states, but also to remove the influence of the water circulation due to the stirring process. The laser power was set to 110 mW. The laser intensity was regularly calibrated with a Thorlab S121C standard photodiode sensor in conjunction with a Thorlab PM100USB power and energy meter. The LDA system began to measure fluid flow at the *y*-coordinate of −0.025 m, which was set as the origin of the traverse system. The two velocity components of the LDA system detect instantaneous velocities of particles in the *x*- and *z*-direction. In an ideal case, the fluid movement in the *z*-axis is negligible and is not the interest of this study. Therefore, only the *x*-velocity component will be used in the analysis.

It has been mentioned that the transit time of the traverse system is paramount in the LDA measurement. To examine the appropriate transit time for the measurement, the beam was arbitrarily actuated with the frequency of 18 Hz and the base amplitude of 1.8 mm. The transit time was subjectively extended from 60 s, 90 s, to 120 s. Figure 4.5 presents the average velocities in the *x*-direction obtained from the LDA measurement for various transit times. Note that the fluctuation in the velocity profiles was filtered with the *smoothdata* built-in function available in MATLAB. It is observed that all transit time values generate consistent results. Accordingly, the transit time 120 s was chosen to investigate the fluid flow for different forcing amplitudes and frequencies to facilitate adequate data samples, particularly at lower frequencies. Furthermore, the effect of water circulation due to stirring the water in the beginning process was also investigated. The dotted green line shown in Fig. 4.5 presents the mean fluid velocity measured directly after stirring the water. It is observed that there is no notable discrepancy particularly at the peak with the coordinate of $y = 0$. The deviation occurs on the side of the velocity profile where the flow induced by the beam is minimum. Based on this measurement, it is believed that the fluid flow around the tip is only influenced by the beam and is not affected by water circulation due to the stirring process or reflection from the walls.

Due to the limitation of the rig, the maximum forcing frequency was constrained to 35 Hz to prevent cavitation or bubble induced by vibrating beam, which might affect to the fluid characteristics. At 9 Hz, increasing the base velocity from 0.07 to 0.11 m/s can increase the maximum mean velocity by about 2.5 times. On the contrary, increasing the base velocity at the resonant, $f = 14$ Hz, from 0.11 to 0.18 m/s only improves the maximum fluid velocity about 1.5 times. Moreover, the maximum fluid velocity at $f = 18$ Hz also increases approximately 1.5 times when the base input velocity rises about 1.4

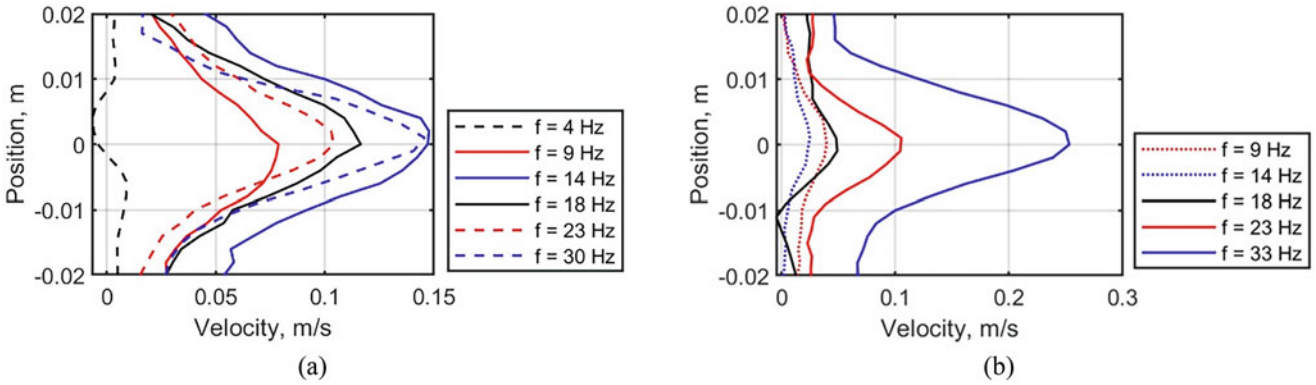

Fig. 4.6 Comparison of the fluid velocity profiles for various forcing frequencies induced by (**a**) the 0.6 mm beam and (**b**) 0.3 mm beam

times, from 0.14 to 0.20 m/s. These nonlinear relationships between the base input velocity and the maximum mean fluid velocity can be related to the beam FRF presented in Fig. 4.2. At the resonant, the beam tip velocity decreases with increasing the base amplitude due to increasing the damping force. Conversely, the FRF magnitudes at 9 Hz and 18 Hz are unchanged due to the variation in the base amplitude. Finally, these findings support the previous analysis for the constant amplitude with variation of forcing frequency where the fluid velocities highly depend on the beam FRF.

To further study the fluid flow, the base amplitude was maintained constant at 1.2 mm. This value was chosen to significantly generate fluid flow at low frequencies. The forcing frequencies were varied at 4 Hz, 9 Hz, 14 Hz, 18 Hz, 23 Hz, and 30 Hz. The first three values are to demonstrate the characteristics of mean fluid velocities due to the first mode shape. The other values are to signify the influence of the first and second mode shapes when the beam is developing nodes and the beam tips have 180° phase shift. Figure 4.6a displays the mean velocity from LDA measurements for various forcing frequencies. It is noticed at $f = 4$ Hz that the mean fluid velocity oscillates around zero. The fluctuation might be caused by very low velocities produced by the vibrating beam, creating uncertainties in the measurement. The base amplitude at this frequency is estimated to be approximately 0.03 m/s. At 9 Hz, the velocity of the base amplitude and the maximum mean fluid is equal which is about 0.07 m/s. At the first resonant frequency, $f = 14$ Hz, the maximum mean fluid velocity is higher than the base amplitude velocity. It is noticed that the characteristics of the mean fluid velocity follow the trend line of the FRF. This trend line continues to the next regime where the phase shift of the beam tips is about 180 degrees. At $f = 18$ Hz, the maximum fluid velocity decreases to 0.12 m/s, while the base input velocity increases to 0.14 m/s. The decrease in the maximum fluid velocity is observed until $f = 23$ Hz where the base velocity increases to approximately 0.23 m/s. At this frequency, the amplitude at the nodal point in the beam envelope becomes minimum and the phase delay between the two tips is nearly 180 degrees due to lack of damping contribution in the beam equation. However, the maximum fluid velocity rises from 0.1 to 0.14 m/s at $f = 30$ Hz. This phenomenon will be further investigated with the beam with the thickness of 0.3 mm to reveal the fluid characteristics until the second resonant.

The same LDA setup was used to investigate the fluid characteristics in between the first and second resonant frequencies. The forcing frequencies were varied at 9 Hz, 14 Hz, 23 Hz, and 33 Hz. The first three values are intended to obtain the fluid characteristics when the beam is in lack of traveling waves due to the minimum contribution of the damping. The last two values are to investigate the fluid flow around the second resonant frequency. In addition, these forcing frequencies are also aimed to provide a fair comparison between the beam with thickness of 0.3 mm and 0.6 mm. Figure 4.6b presents the mean fluid velocity obtained from the LDA measurement for various forcing frequencies. As expected, the maximum mean fluid velocities follow the trend line of the FRF. The least fluid velocity is obtained at 14 Hz where this frequency is located at the trough of the first and second peaks of the FRF. At 9 Hz, the maximum mean fluid velocity is 0.04 m/s. At 18 Hz, the vibration of the beam only induces the maximum fluid velocity of 0.05 m/s. This value is far lower than the beam with the thickness 0.6 mm. At $f = 23$ Hz, the maximum mean fluid velocity increases to 0.11 m/s, which is comparable to the 0.6 mm beam. In addition, the fluid velocity value doubles when the beam is actuated at the resonant, $f = 33$ Hz. To conclude, the experimental results show that the characteristics of the maximum fluid velocity induced by the submerged cantilever beam have a linear relationship to the beam FRF. On the basis of these data, further investigations utilizing numerical simulation will be carried out to obtain the influence of the node in the beam envelope, phase delay between two tips, beam mode shapes, and vibration pattern of the beam on the fluid flow.

4.4 Conclusions

In this chapter, an investigation on the fluid dynamics of cantilever beams submerged in liquid has been presented, to examine the propulsion capabilities of a slender structure vibrating in a fluidic media. An experimental rig capable of measuring the mean fluid velocity for various locations has been developed. The experimental tests consider two different beam configurations to explore the characteristics for the first two resonant frequencies. Particular attention was given to the variation of the forcing amplitude and frequency of the beam in correspondence to the first two resonant frequencies in which the mean fluid velocities are determined by the trend line of the FRF magnitude of the beam.

As expected, the dynamics of the structure is heavily influenced by the presence of the fluidic media, as demonstrated by the FRF obtained in air and in water. The surrounding media have two main effects: it increases the moving mass (hence lowering the frequencies at which resonances are encountered) and harvests energy from the vibrating structure (decreasing the peak amplitudes of the FRF). The second effect is of particular interest for this study because it is through this mechanism that energy is transferred to the fluid. The geometrical characteristics of the beam heavily change the fluid structure interaction between the beam and the surrounding water: not only they change the modal response, but they also change the capability of the surrounding media to influence the motion of the beam. This has a profound implication on the velocity induced by beams of different thicknesses on the fluid at different frequencies. While the velocity pattern changes considerably when the frequency of excitation of the slender beam varies, this effect is less visible in the 0.6 mm beam.

These experiments have provided a unique experimental benchmark for the study and the analysis of fluid structure interactions induced by vibrating structures surrounded by fluidic media. Some initial conclusions have been drawn here, but further analysis will be undertaken as a continuation of this work. In particular, these data can support the development of numerical data that can augment the measurements taken in the experimental campaign and shed some more insight in this complex phenomenon.

References

1. Ramananarivo, S., Godoy-Diana, R., Thiria, B.: Passive elastic mechanism to mimic fish-muscle action in anguilliform swimming. J. R. Soc. Interface. **10**(88) (2013). https://doi.org/10.1098/rsif.2013.0667
2. Godoy-Diana, R., Thiria, B.: On the diverse roles of fluid dynamic drag in animal swimming and flying. J. R. Soc. Interface. **15**(139) (2018). https://doi.org/10.1098/rsif.2017.0715
3. Piñeirua, M., Godoy-Diana, R., Thiria, B.: Resistive thrust production can be as crucial as added mass mechanisms for inertial undulatory swimmers. Phys. Rev. E. **92**(2) (2015). https://doi.org/10.1103/PhysRevE.92.021001
4. Piñeirua, M., Thiria, B., Godoy-Diana, R.: Modelling of an actuated elastic swimmer. J. Fluid Mech. **829**, 731–750 (2017). https://doi.org/10.1017/jfm.2017.570
5. Ramananarivo, S., Godoy-Diana, R., Thiria, B.: Propagating waves in bounded elastic media: transition from standing waves to anguilliform kinematics. EPL (Europhys.Lett.). **105**(5) (2014). https://doi.org/10.1209/0295-5075/105/54003
6. Ramananarivo, S., Thiria, B., Godoy-Diana, R.: Elastic swimmer on a free surface. Phys. Fluids. **26**(9) (2014). https://doi.org/10.1063/1.4893539
7. Raspa, V., et al.: Vortex-induced drag and the role of aspect ratio in undulatory swimmers. Phys. Fluids. **26**(4) (2014). https://doi.org/10.1063/1.4870254
8. Ogawa, J., et al.: Development of liquid pumping devices using vibrating microchannel walls. Sensors Actuators A Phys. **152**(2), 211–218 (2009). https://doi.org/10.1016/j.sna.2009.04.004
9. Ye, W., et al.: Travelling wave magnetic valveless micropump driven by rotating integrated magnetic arrays. Micro & Nano Lett. **9**(4), 232–234 (2014). https://doi.org/10.1049/mnl.2014.0022
10. Yu, H., et al.: Design, fabrication, and characterization of a valveless magnetic travelling-wave micropump. J. Micromech. Microeng. **25**(6) (2015). https://doi.org/10.1088/0960-1317/25/6/065019
11. Liu, G., Zhang, W.: Travelling-wave micropumps. In: Microbial Toxins, pp. 1–19 (2017). https://doi.org/10.1007/978-981-10-2798-7_29-1
12. Erturk, A., Delporte, G.: Underwater thrust and power generation using flexible piezoelectric composites: an experimental investigation toward self-powered swimmer-sensor platforms. Smart Mater. Struct. **20**(12) (2011). https://doi.org/10.1088/0964-1726/20/12/125013
13. Shahab, S., Tan, D., Erturk, A.: Hydrodynamic thrust generation and power consumption investigations for piezoelectric fins with different aspect ratios. Euro. Phys. J. Spec. Top. **224**(17–18), 3419–3434 (2015). https://doi.org/10.1140/epjst/e2015-50180-1
14. Fernández-Prats, R., et al.: Large-amplitude undulatory swimming near a wall. Bioinspir. Biomim. **10**(1) (2015). https://doi.org/10.1088/1748-3190/10/1/016003
15. Demirer, E.: Bio-Inspired Locomotion Using Oscillating Elastic Plates. Georgia Institute of Technology, Georgia, Atlanta, USA (2021)
16. Shelton, R.M., Thornycroft, P., Lauder, G.V.: Undulatory locomotion of flexible foils as biomimetic models for understanding fish propulsion. J. Exp. Biol. (2014). https://doi.org/10.1242/jeb.098046
17. Yeh, P.D.: Fast and Efficient Locomotion Using Oscillating Flexible Plates. Georgia Institute of Technology, Georgia, Atlanta, USA (2016)
18. Cen, L., Erturk, A.: Bio-inspired aquatic robotics by untethered piezohydroelastic actuation. Bioinspir. Biomim. **8**(1) (2013). https://doi.org/10.1088/1748-3182/8/1/016006

19. Shahab, S., Erturk, A.: Underwater dynamic actuation of macro-fiber composite flaps with different aspect ratios: Electrohydroelastic modeling, testing, and characterization. In: Volume 2: Mechanics and Behavior of Active Materials; Integrated System Design and Implementation; Bioinspired Smart Materials and Systems; Energy Harvesting. American Society of Mechanical Engineers (ASME); Newport, Rhode Island, USA (2014)
20. Shahab, S., Erturk, A.: Experimentally validated nonlinear electrohydroelastic Euler-Bernoulli-Morison model for macro-fiber composites with different aspect ratios. In: Volume 8: 27th Conference on Mechanical Vibration and Noise. American Society of Mechanical Engineers (ASME); Boston, Massachuse's, USA (2015)
21. Shahab, S., Erturk, A.: Coupling of experimentally validated electroelastic dynamics and mixing rules formulation for macro-fiber composite piezoelectric structures. J. Intell. Mater. Syst. Struct. **28**(12), 1575–1588 (2016). https://doi.org/10.1177/1045389x16672732
22. Byoung-Gook, L., Ro, P.I.: An object transport system using flexural ultrasonic progressive waves generated by two-mode excitation. IEEE Trans. Ultrason. Ferroelectr. Freq. Control. **47**(4), 994999 (2000). https://doi.org/10.1109/58.852083
23. Bucher, I., et al.: Experimental travelling waves identification in mechanical structures. Math. Mech. Solids. American Society of Mechanical Engineers (ASME); Haifa, Israel **24**(1), 152–167 (2017). https://doi.org/10.1177/1081286517732825
24. Gabai, R., Bucher, I.: Generating traveling vibration waves in finite structures. In: Volume 2: Automotive Systems; Bioengineering and Biomedical Technology; Computational Mechanics; Controls; Dynamical Systems. American Society of Mechanical Engineers (ASME); Haifa, Israel, pp. 761–770 (2008)
25. Hariri, H., Bernard, Y., Razek, A.: A traveling wave piezoelectric beam robot. Smart Mater. Struct. **23**(2) (2014). https://doi.org/10.1088/0964-1726/23/2/025013
26. Hariri, H., Bernard, Y., Razek, A.: Dual piezoelectric beam robot: the effect of piezoelectric patches' positions. J. Intell. Mater. Syst. Struct. **26**(18), 2577–2590 (2015). https://doi.org/10.1177/1045389x15572013
27. Malladi, V.V.N.S.: Continual Traveling Waves in Finite Structures: Theory, Simulations, and Experiments. Virginia Polytechnic Institute and State University, Blacksburg (2016)
28. Musgrave, P.F.: Electro-hydro-elastic modeling of structure-borne traveling waves and their application to aquatic swimming motions. J. Fluids Struct. **102** (2021). https://doi.org/10.1016/j.jfluidstructs.2021.103230
29. Musgrave, P.F., Albakri, M.I., Phoenix, A.A.: Guidelines and procedure for tailoring high-performance, steadystate traveling waves for propulsion and solid-state motion. Smart Mater. Struct. **30**(2) (2021). https://doi.org/10.1088/1361-665X/abd3d7
30. Musgrave, P.F., et al.: Generating structure-borne traveling waves favorable for applications. In: ASME 2020 Conference on Smart Materials, Adaptive Structures and Intelligent Systems, American Society of Mechanical Engineers (ASME); Virtual, Online (2020)
31. Kuribayashi, M., Ueha, S., Mori, E.: Excitation conditions of flexural traveling waves for a reversible ultrasonic linear motor. J. Acoust. Soc. Am. **77**(4), 1431–1435 (1985). https://doi.org/10.1121/1.392037
32. Tanaka, N., Kikushima, Y.: Active wave control of a flexible beam. Proposition of the active sink method. JSME Int. J. Ser. 3, Vibr. Cont. Eng. Eng. Ind. **34**(2), 159–167 (1991). https://doi.org/10.1299/jsmec1988.34.159
33. Malladi, V.V.N.S., et al.: Investigation of propulsive characteristics due to traveling waves in continuous finite media. In: Bioinspiration, Biomimetics, and Bioreplication, Society of Photo-Optical Instrumentation Engineers (SPIE); Portland, Oregon, USA (2017)
34. Inman, D.J.: Engineering Vibrations, Fourth edn. Pearson, Upper Saddle River, New Jersey, USA (2013)

Chapter 5
Low-Frequency Vibrothermography Using Lightweight Piezoelectric Actuators: The Location of Excitation and Application to Composite Materials

Xintian Chi, Dario Di Maio, and Nicholas A. J. Lieven

Abstract This article presents a novel infrared thermographic approach for damage detection by utilizing the heat generated around damage sites during vibrations below 1000 Hz induced by lightweight piezoelectric actuators. In this research, the optimal location of excitation was first investigated through finite element analyses, where two generalized equations were obtained to describe the relationship between the excitation and the resulting displacement response. These observations were then verified experimentally on an aerospace-grade composite plate, followed by vibrothermographic tests conducted on the same structure to demonstrate the effectiveness of the proposed damage detection process employing only a single lightweight piezoelectric disk as the actuator.

Keywords Structural health monitoring · Vibrothermography · Modal testing · Finite element analysis · Piezoelectric actuator

5.1 Introduction

Vibrothermography is a multi-physics technology that can be applied to non-destructive testing and evaluation, structural health monitoring, and characterization of dynamic behavior under long-timescale vibratory motion by exploiting the heat generated between interfaces [1]. When an object is subjected to vibratory excitation, heat will be generated internally through mechanisms such as frictional heating, viscoelastic heating, plasticity-induced heat generation, and sometimes thermoelastic effect [2]. The heat generated inside is often caused by damage, defects, or other issues and can be conducted to the surfaces and detected by infrared cameras, which can then be used to identify and locate these issues [3–7]. In some literature, this approach is less commonly known by other names such as (ultra)sonic infrared thermography, thermosonics, or ultrasonic vibrothermography when acoustic or ultrasonic transducers are used as the excitation sources [7].

For this reason, in vibrothermography, temperature measurement is utilized to read across the mechanics of contact and tribology of interfaces, which can change over time because of damage or altered contact conditions. Because of the unique heat generation mechanisms, vibrothermography is especially powerful for detecting a wide variety of problems. In addition, as the damage and defects act as the internal heat sources, the travel distances of heat waves are shortened compared to the case with externally applied heat in conventional active thermography [8], which suggests that vibrothermography is faster and can be particularly helpful for detecting issues at greater depth.

To ensure detectable heat generation, there must be adequate strain energy in relevant regions such as the damage sites [2, 4, 6, 9–26]. For any structure subjected to vibratory excitation, its operating deflection shape (ODS) is a combination of the mode shapes of all the excited modes [27], so obtaining the modal parameters of the structure can provide critical information for understanding its dynamic behaviors, including the strain distributions around the potential damage sites. Based on this comment, to perform vibrothermographic tests effectively, the dynamic properties—specifically modal parameters—of the inspected objects must be analyzed so that the behaviors—in particular the distributions of strain—can be revealed, interpreted, and utilized to control the vibrations of the structures [3, 4], which can be achieved through modal analysis.

X. Chi (✉) · N. A. J. Lieven
Department of Aerospace Engineering, University of Bristol, Bristol, UK
e-mail: xintian.chi@bristol.ac.uk

D. Di Maio
Faculty of Engineering Technology, University of Twente, Enschede, The Netherlands

M. Allen et al. (eds.), *Special Topics in Structural Dynamics & Experimental Techniques, Volume 5*,
Conference Proceedings of the Society for Experimental Mechanics Series, https://doi.org/10.1007/978-3-031-37007-6_5

In analogy to conventional infrared thermography [28], external excitation might or might not be required in order to perform vibrothermographic testing. In most situations, vibrothermography refers to the processes with external excitation provided. Typical examples involve utilizing external excitation in the forms of mechanical forces or ultrasonic waves created by sources such as electrodynamic shakers [29–33] and ultrasonic transducers, where the latter usually include ultrasonic welders [9–11, 34–36] and piezoelectric actuators [11–20, 36–47].

When external excitation is required, to optimize the parameters of a vibrothermographic test, a target mode—or modes—of vibration should be chosen first. After this, parameters related to the excitation of the structure need to be carefully selected to ensure that the right resonance—or resonances—can be excited effectively, which can exhibit a viable strain distribution across the structure. The dynamic response with the correct modal distribution will increase the strain in damaged regions so that the heat generation can be increased as well, which enhances the chance of successful detection of damage and defects.

When a single mode of vibration is considered, to excite the target mode effectively, sinusoidal excitation whose frequency matches the corresponding natural frequency should be used. In this case, the structure will exhibit a greater dynamic response and so the heat generation will be increased as well [4, 9–13, 16, 18–22, 26, 37–42, 45–47]. Due to the relationship between heat generation and strain energy, a mode in which the potential damage sites possess high strain energy is preferred.

In vibrothermographic testing, damage and defects often generate more heat in higher-order modes of vibration due to the increased frequencies [21, 22, 33, 47]. However, for high-order modes, issues such as transverse shear and rotary inertia can become more significant, which correspondingly add complexity to the analytical modeling process [47]. In vibrothermographic tests, vibrations in higher-order modes are also usually more localized, so the coverage of strain energy in the test structure can be relatively limited, which reduces the effective area of detection. From a practical point of view, more specialized amplifiers are also required for excitation at high frequencies, which may limit the general applicability of this approach. These high-frequency excitation forces may bring other concerns to the test structures because of the high strain rates, with which additional damage may be generated. This last issue is especially problematic for structures made of laminated composite materials, such as the structure studied in this research, which are intrinsically vulnerable to impact or high strain rate loading [48–53]. As a comparison, vibrothermographic tests targeting lower-order modes may suffer from issues caused by insufficient heat generation. However, these tests are often easier to apply with fewer practical concerns such as the factors stated above.

In comparison with the frequency of excitation, selecting the optimal location of excitation is not as straightforward and is almost always omitted in relevant research activities. The optimal location of excitation depends on the type of actuator and the method of excitation used. The actuators available for vibrothermographic testing can be approximately grouped into three categories based on the mode of excitation that is provided.

The first category is linear actuators such as electrodynamic shakers [29–33] and longitudinal piezoelectric actuators that can then be subdivided into piezoelectric stack actuators [11, 13, 20, 37–39, 46], bolt-clamped Langevin transducers [17, 19, 44], and piezoelectric shakers [16, 40, 41, 47]. Some other ultrasonic transducers such as ultrasonic welders, when used in vertical alignment, are also examples of this category [54], which have been proven useful for vibrothermographic testing [9–11, 34–36]. To summarize, thanks to the simple mode of excitation, convenient setup, and high amplitudes of the produced forces, linear actuators have been widely utilized in vibration tests, including vibrothermographic inspections.

Alternatively, piezoelectric materials may also be applied as shear actuators. Despite having equally wide frequency ranges, the shear loads achievable are usually significantly lower than the forces produced by the linear actuators. Separately, ultrasonic welders can also be placed parallel to the weld surfaces to induce shear forces into the structures. However, tests using shear actuators are often more difficult to plan and set up while the efficiency of energy transfer is also lower, which limits their practical use in relevant tests.

The third category is the contracting actuators, which typically include lightweight piezoelectric actuators such as piezoelectric disks. These contracting actuators may also be attached to substrates, which can be another piezoelectric material or a passive material such as metal or ceramic, to act as bending actuators [55, 56]. There have been research activities demonstrating the effectiveness of these actuators for vibrothermography [12, 14, 15, 18, 42, 43]. Due to the mode of displacement and the fact that such actuators are often relatively thin and lightweight, the amplitudes of the excitation are often among the lowest compared to alternative options. However, piezoelectric disks and patches can be permanently bonded to or embedded in a structure [14, 15, 42, 43] without causing noticeable modifications to the structure's physical properties. This attribute enables the possibility of easier in situ damage detection and structural health monitoring. In addition, because of the small size and low weight of these actuators, multiple piezoelectric disks or patches can be attached to a single structure. Activating the actuators simultaneously can increase the response level of the test structure during the induced vibration, which compensates for the low-power output of such actuators to some extent.

In this paper, a successful vibrothermographic test was conducted on an aerospace-grade composite plate containing subsurface damage with low-frequency excitation (<1000 Hz) generated using a single lightweight piezoelectric disk, which would provide a high level of convenience and flexibility as explained above. This approach has seldom been applied in

either modal tests or vibrothermographic experiments due to the low level of dynamic response. However, in the test to be presented, detectable heat was still able to be generated with carefully selected parameters of excitation.

5.2 Location of Excitation

For contracting or bending actuators such as the piezoelectric disks, the selection of the optimal location for excitation in vibrothermography is rarely considered. However, because of the low amplitudes of vibration achievable with these actuators, determining the optimal location of excitation should be optimized to achieve viable dynamic response.

In principle, the analogy to linear actuators can still be applied [55]. In detail, both surface-bonded and embedded piezoelectric actuators should be placed in regions of higher strain to induce greater dynamic responses of the structure [55, 57]. This observation is equally relevant for vibration suppression and control [58]. For a specific mode of vibration, they should be located in regions of high modal strain (energy) to control the vibrations more effectively [59, 60], which means that strain nodal lines should be avoided [61]. When utilized as sensors, these conclusions would still apply [60, 62].

To verify these statements, finite element (FE) analyses were conducted, during which multiple piezoelectric disks were created and attached to a free-free plate. The dynamic responses of the plate when different disks were used to provide the excitation were calculated using direct solution steady-state dynamic analyses, then recorded and compared so that the relationship between the dynamic response of the structure and the location of excitation could be investigated. The details of the modeling process are thoroughly explained in a separate publication [1].

As shown in Fig. 5.1, the free-free plate model created in Abaqus was composed of a cuboid base and 45 identical piezoelectric disks. Due to the symmetry of the model, the 15 disks in the bottom-left region could be used to represent the behaviors in the other three quarters. For future reference, the 15 disks were named *Ai-j*, where *i* represented the row number while *j* represented the column number. The disk A1–1 corresponded to the disk closest to the bottom-left corner, while the disk A3–5 corresponded to the disk at the center of the top surface of the plate.

A natural frequency extraction step was performed first to calculate the modal parameters of the free-free plate model. The natural frequencies and mode shapes of the first four modes of vibration were calculated and recorded. For quantitative data collection, the magnitude of deformation ϕ_{mag} and its three components ϕ_{X}, ϕ_{Y}, and ϕ_{Z}, in addition to the six strain components ε_{XX}, ε_{YY}, ε_{ZZ}, ε_{XY}, ε_{XZ}, and ε_{YZ}, were extracted at 19 nodes as shown in Fig. 5.2.

To be more specific, the first 15 nodes were located on the top surface of the plate where the centers of the bottom surfaces of the 15 aforementioned disks were attached, which made them the locations of excitation in the subsequent direct solution steady-state dynamic analyses. Besides these 15 nodes, the four corner nodes of the top surface of the plate were also included. These extracted data would be utilized later to analyze the relationship between the location of excitation and the dynamic response of the model.

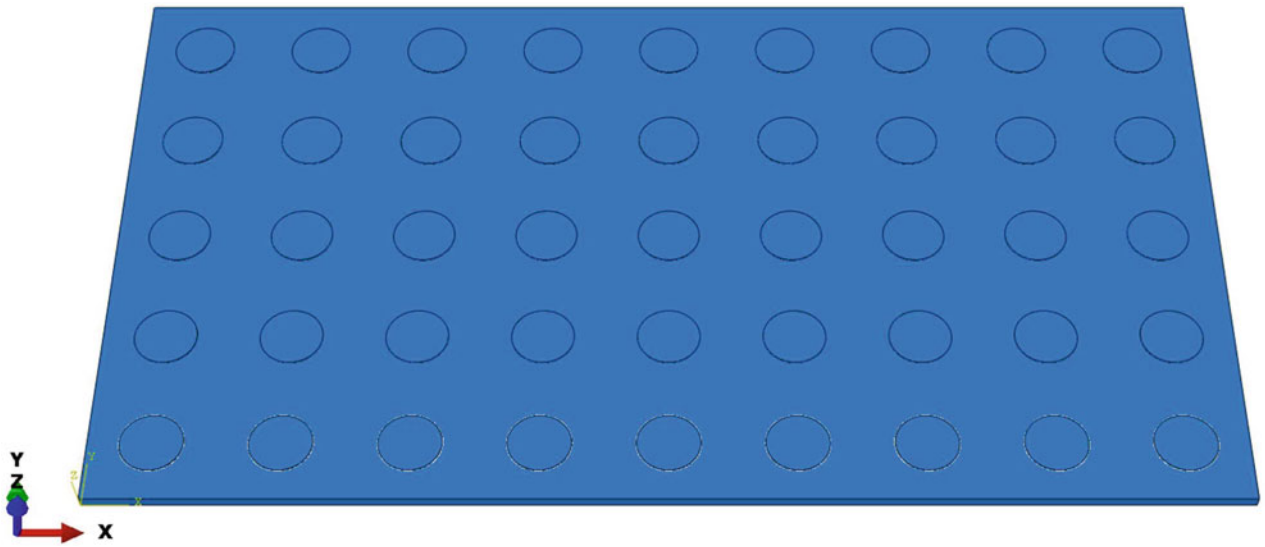

Fig. 5.1 Free-free plate model created in Abaqus

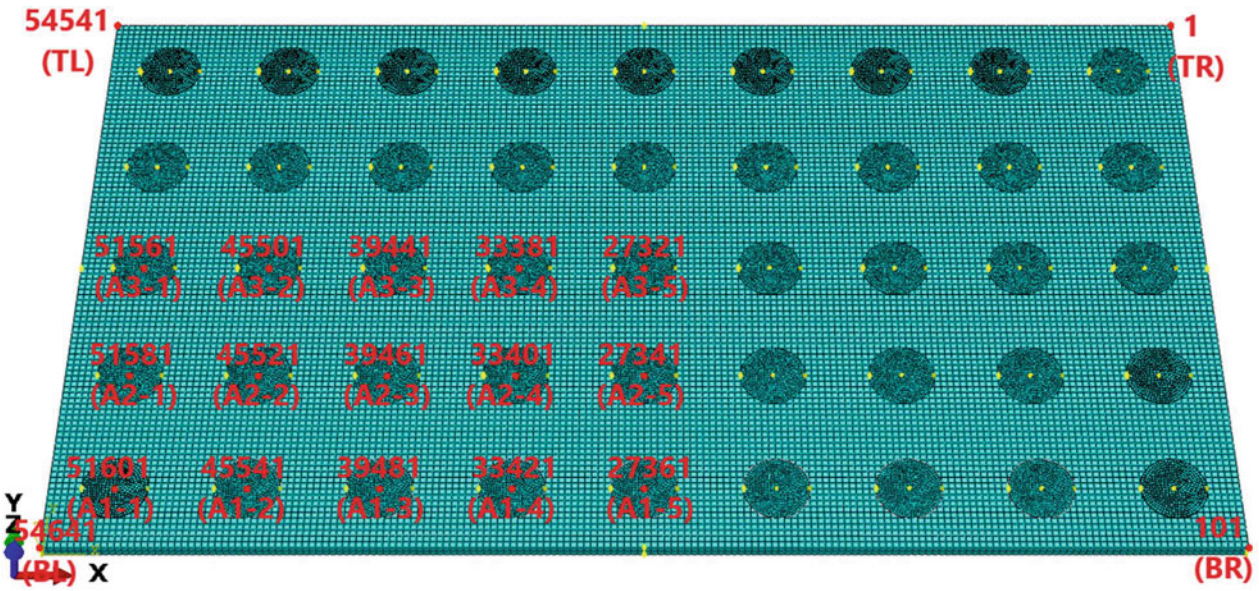

Fig. 5.2 Locations of the excitation and measurement points on the free-free plate

Following the completion of the natural frequency extraction step, 24 direct solution steady-state dynamic analyses were completed to obtain the dynamic responses of the free-free plate model. In the first 15 analyses, each of the 15 disks was subjected to a voltage of 10 V in its direction of polarization. In the next two analyses, disks A2–2 and A2–4 were provided with voltages of 5 V instead, followed by three analyses where disks A3–1, A3–3, and A3–5 were supplied with voltages of 20 V. In the 21st analysis, three different voltages, namely 10 V, 5 V, and 20 V, were applied to disks A1–1, A2–2, and A3–3, respectively. In the 22nd analysis, the same voltages were applied to disks A1–3, A2–2, and A3–1. Similarly, disks A1–3, A2–4, and A3–5 were used for the 23rd analysis, while disks A1–5, A2–4, and A3–3 were used for the 24th analysis. During the analyses, boundary conditions were applied to maintain the electric potentials at the remaining disks at zero.

In each analysis, the steady-state responses of the free-free plate when the frequency (or frequencies) of the voltage (or voltages) matched each of the four natural frequencies of interest were obtained. To demonstrate the results, the deformed shapes of the free-free plate when a voltage of 10 V was applied to disk A1–1 are shown in Fig. 5.3.

To record the data, the same 19 nodes were used for quantitative data collection, at which the displacement values were probed to represent the dynamic responses after the direct solution steady-state dynamic analyses. By analyzing the extracted dynamic response levels with the previously recorded modal parameters, the following relationship was obtained:

$$\mathbf{U}_{\text{resp}} \propto \sum_{j}^{M} A V_{\text{Z}}^{j} \left(\varepsilon_{\text{XX}}^{j} + \varepsilon_{\text{YY}}^{j} \right) \mathbf{\Phi} \tag{5.1}$$

where $\mathbf{U}_{\text{resp}}$ is the displacement response of the structure, M is the number of excitation forces (number of disks in this case), A is a scale factor related to both the properties of the structure, such as damping, and the parameters of the piezoelectric actuator, such as the piezoelectric coefficients, and V_{Z}^{j} is the voltage applied in the direction of polarization of the jth actuator, while $\varepsilon_{\text{XX}}^{j}$ and $\varepsilon_{\text{YY}}^{j}$ are the first two components of modal strain at the location of excitation.

When several modes of vibration would be excitation, the induced dynamic response of the structure should still be the sum of the individual cases, so Eq. (5.1) may be generalized to:

$$\mathbf{U}_{\text{resp}} \propto \sum_{i}^{N} \sum_{j}^{M} A_i V_{\text{Z}}^{j} \left(\varepsilon_{\text{XX}}^{ij} + \varepsilon_{\text{YY}}^{ij} \right) \mathbf{\Phi}^{\boldsymbol{i}} \tag{5.2}$$

where A_i now also depends on the difference between the frequency of the voltages and the natural frequency of the ith excited mode. For completeness, the derivation of the equations above is thoroughly explained in a separate publication, together with

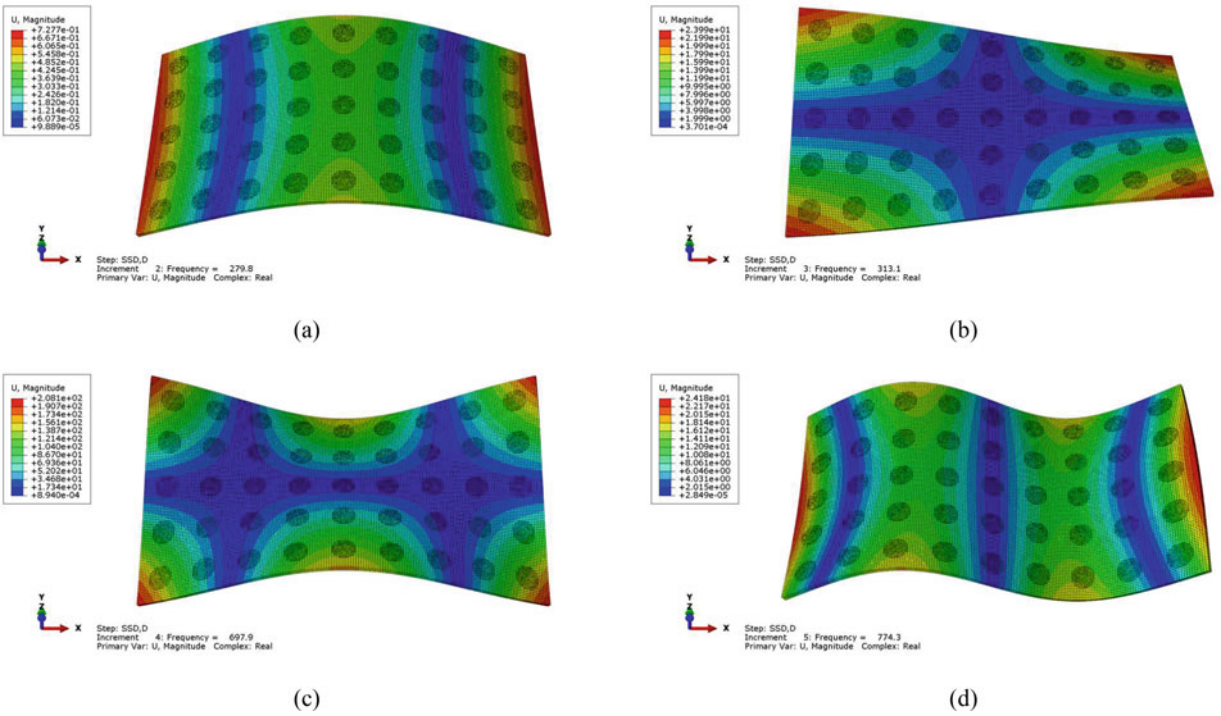

Fig. 5.3 Deformed shapes of the free-free plate excited by the piezoelectric disk closest to its bottom-left corner when the frequency of the voltage matched the natural frequencies of the (**a**)–(**d**) first to fourth modes of vibration

the recorded quantitative data mentioned above. Similar research was also conducted for electrodynamic shakers representing linear actuators, where generalized equations were also obtained [1].

Based on this research, especially the two generalized equations above, it may be concluded that for contracting or bending actuators, the level of the dynamic response is proportional to the weighted sum of the first two modal strain components at the node where the actuator is attached. When multiple actuators are used, the weighted sum of the modal strain components at all excitation locations should be considered, where the weight is determined by the amplitude of the voltage supplied to each actuator, given that the actuators are all identical.

For more complicated situations that were not discussed in this research, such as when multiple actuators of different types are used together, or when excitation forces no longer have equal frequencies, the proposed relationship will undoubtedly become more complex. However, the observations and conclusions obtained in this research should still be able to act as general guidelines on selecting proper locations of excitation to increase the overall dynamic response of a structure, which is crucial for both conventional vibration testing and vibrothermography.

5.3 Experimental Verification with Modal Testing

To reiterate, as introduced previously, although there have been research outputs showing the utilization of these piezoelectric actuators in vibrothermography [12, 14, 15, 18, 42, 43], the optimal location of excitation is rarely considered, especially experimentally. This omission can be particularly critical for vibrothermographic tests using piezoelectric disks or patches due to their low-power output. In addition, in previous research activities using piezoelectric actuators, high-frequency (ultrasonic) excitation has been predominantly employed. For these reasons, this research was conducted focusing on vibrothermographic testing with lightweight low-power piezoelectric disks using low excitation frequency.

The specimen to be studied was an aerospace-grade composite plate as shown in Fig. 5.4a. The plate was made of HexPly® 8552 epoxy matrix AS4 fiber woven carbon prepregs containing delamination along the vertical centerline of the plate created artificially through dynamic fatigue. Ply drops were added during the manufacturing phase to help create the damage. The damage was subsurface and barely visible from visual inspection. Due to the subtlety of the damage and the potential lack of energy because of the low-power actuators, the parameters of excitation must be carefully considered. For this reason,

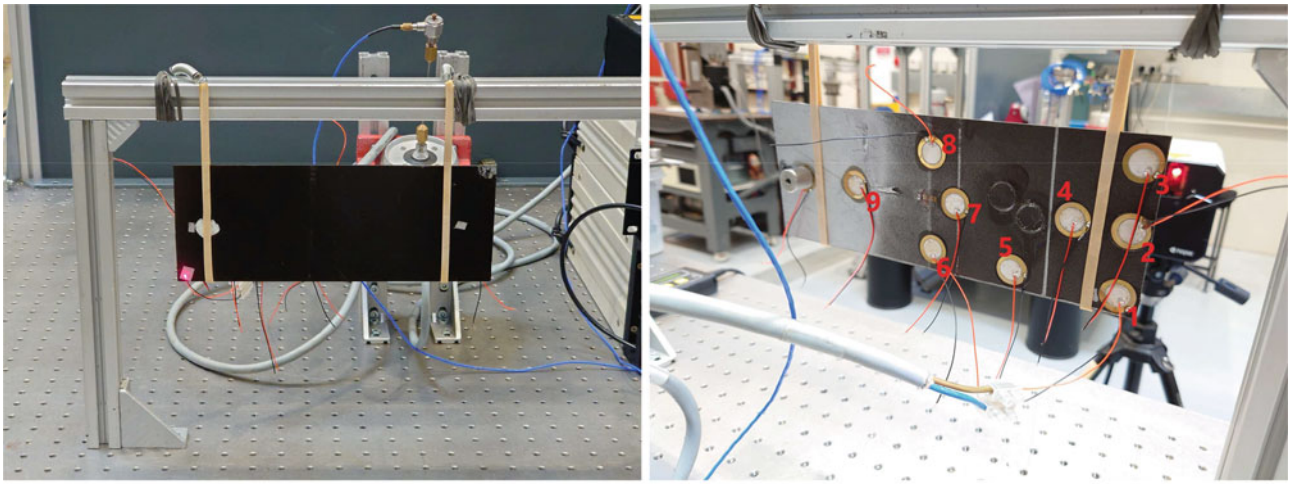

(a) (b)

Fig. 5.4 (**a**) Rig setup for the experimental tests on the composite plate and (**b**) locations of the piezoelectric disks

preliminary modal tests were completed first, during which piezoelectric disks were attached at different locations of the plate. These disks were utilized individually to provide separate excitation so that the levels of dynamic response could be compared, which would also verify the findings in the previous section. After this, the modal parameters were analyzed so that the frequency and location of excitation could be more properly selected for the subsequent vibrothermographic testing, increasing the possibility of successful damage detection.

In the experimental tests, the plate was suspended using two elastic bands connected to springs to simulate a free–free condition to avoid unnecessary external forces and constraints. In total, there were nine disks attached to the plate using superglue. However, only seven disks would be studied, which were disks D1, D3, D4, D5, D6, D7, and D8 in Fig. 5.4b. Disks D2 and D9 were installed in a previous study for different purposes, so they were not related to this research.

As shown in Fig. 5.4b, the piezoelectric disks were glued to brass substrates to form bending actuators. The diameters of the piezoelectric disks and the substrates were 15 mm and 20 mm, respectively. The thickness was 0.2 mm each. The resonant frequency was around 6.8 kHz, while the capacitance was 15,000 pF (picofarad) ±30%. Because of the amplitude and the frequency of excitation to be applied, an LDS PA100E power amplifier could be employed without needing more specialized equipment. As for data collection, a scanning laser Doppler vibrometer (SLDV) system was used to measure the vibration data, while a Nippon Avionics TH9100MR infrared camera was employed to measure the temperature values.

Before the experimental tests, an FE analysis was performed to predict the modal parameters of the plate, which would provide results at much higher resolutions. To achieve this, the composite plate was modeled as a 3D deformable shell using Abaqus built-in composite layup function based on the measured dimensions and the material properties provided by Hexcel and other sources [63, 64]. Zero boundary conditions were added in order to simulate the suspension of the plate in the experimental tests. A natural frequency extraction step was then performed, which yielded natural frequencies of 118.34 Hz, 374.32 Hz, 390.00 Hz, 746.44 Hz, 800.13 Hz, and 1141.2 Hz for the first six modes of vibration. The mode shape and the distribution of strain energy of the first mode are presented in Fig. 5.5 as examples.

To start the experimental tests, modal testing of the composite plate was conducted first to validate the FE model and to investigate the optimal location of excitation to increase the dynamic response level. In total, seven experimental modal tests were completed, each using a piezoelectric disk at a different location supplied with an input voltage of 30 V.

During the modal tests, a chirp signal sweeping from 20 to 1000 Hz over 2 s was created to control the excitation. In each test, ten cycles of measurement were completed, while the root-mean-square method was utilized to increase the signal-to-noise ratio. The frequency response functions (FRFs) were measured at the location indicated by the reflective tape with the red dot from the SLDV at the corner of the plate, as shown in Fig. 5.4a. Based on the FRFs, the levels of dynamic response with different excitation locations could be compared.

After the modal tests, four modes of vibration were successfully discovered. However, the measured FRFs were heavily corrupted by noise, which was a consequence of the low-power output of the piezoelectric disks. As demonstrations, the FRFs measured when disks D3 and D7 were used to excite the plate are shown in Fig. 5.6a, b.

With the FRFs, the natural frequencies and the dynamic response levels were determined using peak picking. Due to the noise in the data, the values summarized in Table 5.1 were only approximate representations of the actual dynamic behaviors.

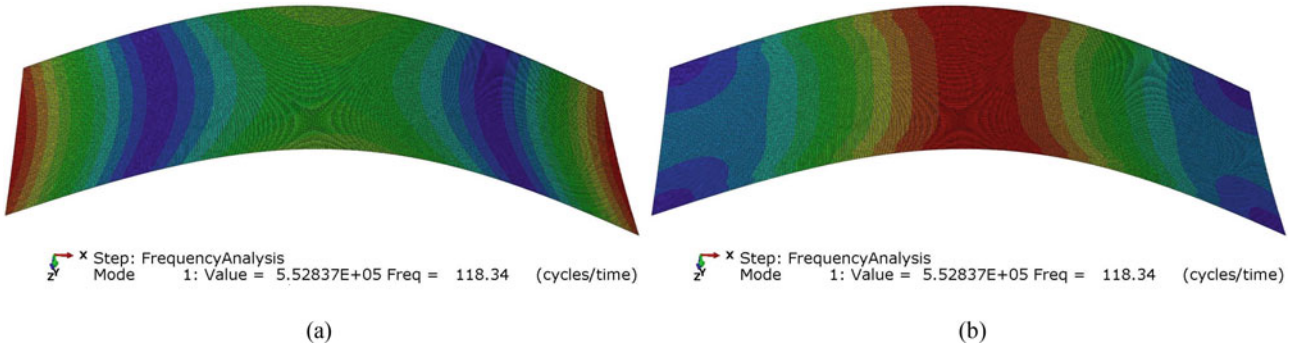

Fig. 5.5 (**a**) Mode shape and (**b**) distribution of strain energy of the first mode of the FE composite plate

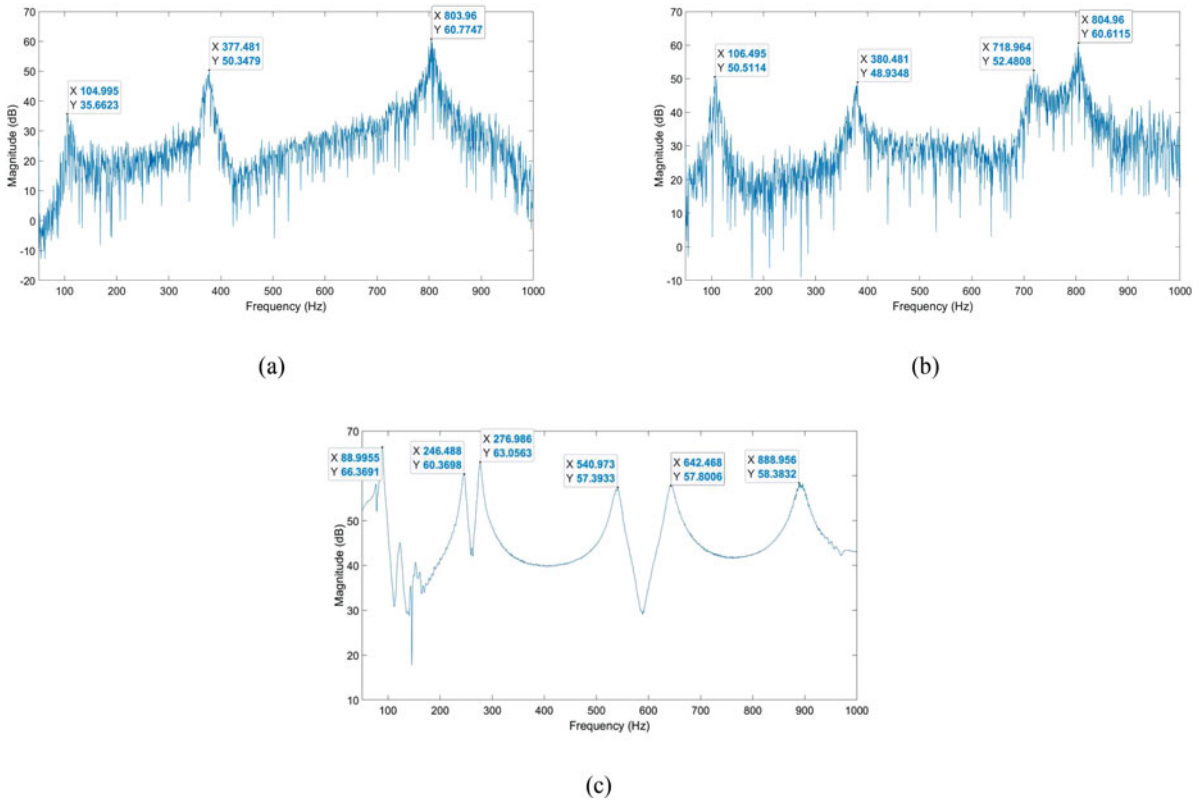

Fig. 5.6 Mobility plots when (**a**) piezoelectric disk D3, (**b**) piezoelectric disk D7, and (**c**) the LDS V201 shaker were utilized as the actuators

From the results in Table 5.1, it could be observed first that the natural frequencies measured here were close to those calculated from the FE analysis. However, the third mode of vibration observed in the FE analysis was unable to be detected here. Considering the quality of the data, it might be possible that it was mixed with the second mode and became indistinguishable. Based on the current data, it would be difficult to determine the exact reason behind its disappearance. It could also be assumed that this mode was not excited from the outset. Nevertheless, this phenomenon was relatively unimportant for the subsequent vibrothermographic testing as long as another mode with sufficient strain energy in the damaged region would exist and could be excited favorably.

To demonstrate the relationship between the level of dynamic response and the local strain energy at the location of excitation, the first mode of vibration, which was the first vertical bending mode, could be studied because of its simple deflection shape. According to the distribution of strain energy shown in Fig. 5.5b, locations closer to the center of the plate should have higher local strain energy. As marked in Fig. 5.4b, this would correspond to disks with larger indices. From Table 5.1, it could be observed clearly that, for piezoelectric disks closer to the center of the plate, the levels of dynamic response were significantly greater when the first mode was targeted.

Table 5.1 Natural frequencies (Hz) of the first five modes obtained through FE analysis and natural frequencies (Hz) and magnitude of dynamic response (dB) of the composite plate measured experimentally with each of the seven piezoelectric disks used as the actuator

Actuator	M. 1 freq. (mag.)	M. 2 freq. (mag.)	M. 3 freq. (mag.)	M. 4 freq. (mag.)	M. 5 freq. (mag.)
FE	118.34	374.32	390.00	746.44	800.13
D1	104.0 (32.3)	377.5 (48.8)	N/A	N/A	803.0 (55.4)
D3	105.0 (35.7)	377.5 (50.3)	N/A	N/A	804.0 (60.8)
D4	105.0 (32.3)	373.5 (59.5)	N/A	713.0 (52.8)	800.5 (54.3)
D5	109.5 (44.7)	379.0 (55.3)	N/A	717.0 (47.8)	807.0 (48.9)
D6	107.0 (47.7)	378.0 (59.9)	N/A	719.5 (54.5)	805.0 (48.0)
D7	106.5 (50.5)	380.5 (48.9)	N/A	719.0 (52.5)	805.0 (60.6)
D8	107.5 (51.3)	378.0 (64.7)	N/A	717.0 (54.2)	811.5 (62.8)

As a comparison, a final test was conducted using an LDS V201 permanent magnet shaker supplied with a 2 V voltage. The shaker was attached to the plate at the location marked by the metal connector in Fig. 5.4b through a drive rod. In contrast to the results with the piezoelectric disks, the FRF shown in Fig. 5.6c appeared significantly less noisy. The second and third modes of vibration, which were possibly mixed previously in Fig. 5.6a, b due to noise, were able to be distinguished. Quantitatively, the natural frequencies of the modes underwent noticeable decreases. This observation demonstrated the changes to the system's dynamic properties caused by the attachment of the drive rod and the shaker, which could be avoided by employing the lightweight piezoelectric disks as actuators instead.

By comparing Fig. 5.6a–c, the dynamic response levels of the first three modes were significantly higher using the shaker. For higher-order modes with natural frequencies greater than 500 Hz, the differences became smaller, and eventually, a higher dynamic response level could be achieved with a piezoelectric disk. This phenomenon was able to corroborate that electrodynamic shakers are usually more suitable in low- to medium-frequency ranges, while piezoelectric actuators often excel at higher frequencies.

5.4 Vibrothermographic Testing

With the previous findings about the optimal location of excitation verified, the vibrothermographic tests could be initiated. From Table 5.1, regardless of the location of excitation, the level of dynamic response tended to be greater for higher-order modes of vibration, which was comprehensible due to the frequency response of the piezoelectric disks. Based on this observation, a relatively higher-order mode could be a more suitable target for vibrothermographic testing because of the higher heat generation caused by the greater dynamic response, in addition to the fact that a higher frequency of vibration itself would also accelerate the local heating.

Among the observed modes, the final mode had the highest natural frequency, which was around 800–810 Hz. In this mode, there existed high local strain energy near the center of the plate, which was where the damage was created, which was supported by the high dynamic response levels of this mode when disks D7 and D8 were used to excite the plate. This finding provided justification for the choice of using this mode for the vibrothermographic test. Despite the mode number, this frequency was still far from the typical high-frequency range that has been commonly applied in vibrothermography—which is often ultrasonic—so that the relevant issues discussed previously would not be encountered.

As for the location of excitation, although using disk D8 yielded the greatest dynamic response level as shown in Table 5.1, it was decided to employ disk D7 instead to avoid overlapping the location of excitation and the damage. To elaborate, during the vibrothermographic test, heat would be emitted from the piezoelectric disk, so placing the disk at the location of the damage may cause the heat of the disk to be superimposed onto the heat generated due to the subsurface damage, complicating the analysis of the sources of the heat and hindering the detection of the damage.

To set up the test, a sinusoidal signal was generated at 810 Hz. The amplitude of the input voltage was set again to 30 V. During the vibrothermographic test, the TH9100MR infrared camera was set to capture one frame every 5 s. The test lasted for 22 min, so 265 frames of temperature data were recorded. The exact timeline of events is summarized in Table 5.2. The temperature recording began before the excitation started to measure the background data, which then continued after the excitation was stopped to capture the heat dissipation process. To present the results, eight representative images are shown in Fig. 5.7, in which a constant temperature scale from 24.7 to 25.7 °C was applied.

Table 5.2 Timeline of the events in the vibrothermographic test on the composite plate using the piezoelectric disk

Time (min:s)	Event
0:00	Data recording started
0:30	Infrared image displayed in Fig. 5.7a taken
2:00	Excitation turned onInfrared image displayed in Fig. 5.7b taken
3:00	Infrared image displayed in Fig. 5.7c taken
5:00	Infrared image displayed in Fig. 5.7d taken
7:00	Infrared image displayed in Fig. 5.7e taken
12:00	Excitation turned offInfrared image displayed in Fig. 5.7f taken
14:15	Infrared image displayed in Fig. 5.7g taken
22:00	Data recording stoppedInfrared image displayed in Fig. 5.7h taken

The image in Fig. 5.7a was taken at 30 s after the recording began, showing the initial temperature distribution. It could be observed that the spatial temperature variation on the composite plate was relatively small, mostly within the range of <0.2 °C. This temperature variation should be attributed to the difference caused by the angle of view [65, 66].

The image in Fig. 5.7b was taken 2 min after the recording began, which was the moment when the excitation was started. By comparing it with Fig. 5.7a, the temperature distribution was generally unchanged, showing that no unexpected behaviors had happened.

The image in Fig. 5.7c was taken 1 min after the excitation was turned on, which was approximately the moment when the first visible local hot spot at the damage site was detected. As a comparison, this time—1 min—was significantly longer than its counterpart—which was only 4 s—in another test on the same plate using an LDS V201 permanent magnet shaker [1, 29]. For these reasons, it was evidenced that the heat generation was considerably lower using the piezoelectric disk.

The temperature and the corresponding thermal contrast of the hot spot continued to increase as more heat was generated. The continuous increase then gradually slowed, and eventually, the characteristics of the hot spot were stabilized after approximately another 2 min, as shown in Fig. 5.7d. In Fig. 5.7d, the majority of the hot spot was only less than 0.5 °C hotter than the rest of the plate, noticeably lower than the values in the test using the shaker [1, 29].

After this event, the amplitude and size of the hot spot remained approximately unchanged. To support this observation, the images recorded at 7:00 and 12:00 of the test are displayed in Fig. 5.7e, f. Visually, the overall temperature distributions and the characteristics of the hot spots looked almost identical. Only small discrepancies existed from Fig. 5.7d–f, which should be attributed to the fluctuations caused by the slight inaccuracy of the infrared camera.

The input voltage was stopped at 12:00 of the test. It took approximately another 135 s for the local heat concentration to fully dissipate, as presented in Fig. 5.7g. The final image taken before the recording was stopped, which was at 22:00 of the vibrothermographic test is shown in Fig. 5.7h. The similarity between Fig. 5.7g, h indicated that no unexpected behaviors had happened after the excitation was stopped.

With the completion of this vibrothermographic test showing the successful detection of the subsurface damage, additional tests were completed with different locations and frequencies of excitation. In these cases, the vibrothermographic tests were unable to yield equally positive results. Equally detectable heat could not be generated with these less optimal parameters.

Separately, an ultrasonic C-scan test was performed on this plate as additional verification (Fig. 5.8) [1, 29], showing that the vibrothermographic approach was able to identify and locate the damage successfully while having significant advantages in terms of measurement time. However, slight discrepancies were observed in terms of the size of the damage, which should be attributed to the low amplitude of excitation force that was unable to introduce sufficient relative movement and friction for the thermal pattern to reach its maximum potential size in the edge areas.

5.5 Conclusion

In the first part of the research, the optimal location of excitation using piezoelectric disks as actuators to increase the dynamic responses of structures was studied. Based on the results from the FE analyses, two generalized equations have been created to summarize the relationship between the excitation and the induced displacement response of the structure.

In the second part of the research, experimental modal analyses and vibrothermographic testing were completed on a composite plate using piezoelectric disks as actuators. During the modal tests, the conclusions made previously regarding the optimal location of excitation were verified experimentally. It was demonstrated that, despite the noise, the level of dynamic

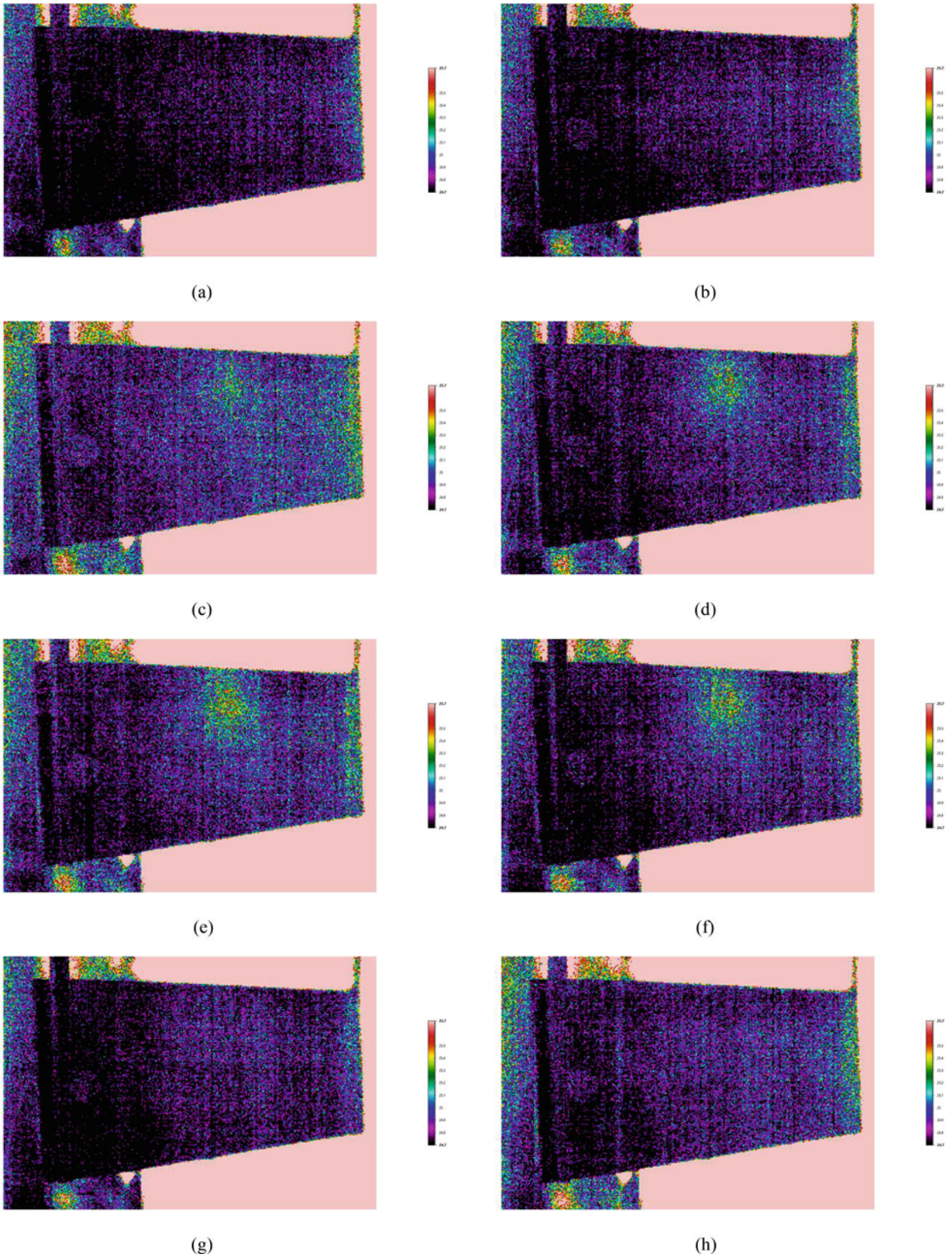

Fig. 5.7 Infrared images taken at (**a**) 0:30, (**b**) 2:00, (**c**) 3:00, (**d**) 5:00, (**e**) 7:00, (**f**) 12:00, (**g**) 14:15, and (**h**) 22:00 of the vibrothermographic test on the composite plate using the piezoelectric disk

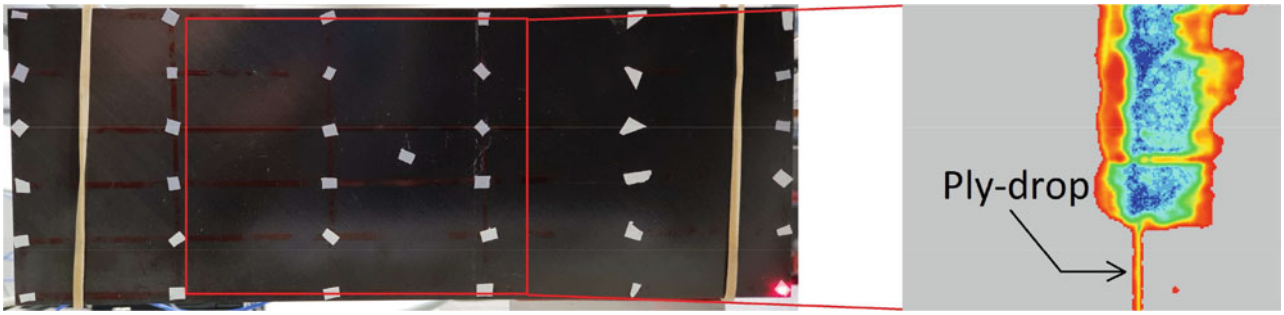

Fig. 5.8 Ultrasonic C-scan result of the central region of the composite plate

response was positively correlated with the local strain energy at the location of excitation. Based on this observation, the frequency and location of excitation could be selected for the subsequent vibrothermographic test.

In the vibrothermographic test, a visible hot spot was generated at the damage site under the vibration induced by a piezoelectric disk with carefully selected parameters of excitation. These results verified that low-power actuators such as the piezoelectric disks could be employed in vibrothermographic tests, providing benefits such as greater flexibility and less interference with the dynamic properties of the test structures. However, the parameters regarding the excitation of the structures must be more carefully selected to ensure sufficient levels of dynamic response and heat generation.

References

1. Chi, X.: Modal-based vibrothermography for damage detection and structural health monitoring. PhD thesis, University of Bristol (2022)
2. Renshaw, J., Chen, J.C., Holland, S.D., Bruce Thompson, R.: The sources of heat generation in vibrothermography. NDT & E Int. **44**(8), 736–739 (2011)
3. Stinchcomb, W.W.: Mechanics of Nondestructive Testing. Springer New York, NY, USA (1980)
4. Henneke II, E.G., Reifsnider, K.L., Stinchcomb, W.W.: Vibrothermography: investigation, development, and application of a new nondestructive evaluation technique. Engineering Science and Mechanics Department, Virginia Polytechnic Institute and State University, Blacksburg, Tech report (1986)
5. Henneke II, E.G., Jones, T.S.: Detection of damage in composite materials by vibrothermography. In: Nondestructive Evaluation and Flaw Criticality for Composite Materials (1979)
6. Henneke II, E.G., Reifsnider, K.L., Stinchcomb, W.W.: Thermography — an NDI method for damage detection. JOM. **31**(9), 11–15 (1979)
7. Stepinski, T., Uhl, T., Staszewski, W.: Advanced Structural Damage Detection: From Theory to Engineering Applications. John Wiley & Sons, Ltd, Chichester, West Sussex, UK (2013)
8. Ibarra-Castanedo, C., Genest, M., Guibert, S., Piau, J.-M., Maldague, X.P.V., Bendada, A.: Inspection of aerospace materials by pulsed thermography, lock-in thermography, and vibrothermography: a comparative study. Thermosense XXIX. **6541**, 321–329 (2007)
9. Mignogna, R.B., Green, R.E., Duke, J.C., Henneke II, E.G., Reifsnider, K.L.: Thermographic investigation of high-power ultrasonic heating in materials. Ultrasonics. **19**(4), 159–163 (1981)
10. Montanini, R., Freni, F.: Correlation between vibrational mode shapes and viscoelastic heat generation in vibrothermography. NDT & E Int. **58**, 43–48 (2013)
11. Holland, S.D., Uhl, C., Ouyang, Z., Bantel, T., Li, M., Meeker, W.Q., Lively, J., Brasche, L., Eisenmann, D.: Quantifying the vibrothermographic effect. NDT & E Int. **44**(8), 775–782 (2011)
12. Morbidini, M., Cawley, P., Barden, T., Almond, D., Duffour, P.: Prediction of the thermosonic signal from fatigue cracks in metals using vibration damping measurements. J. Appl. Phys. **100**(10), 104905 (2006)
13. Holland, S.D., Uhl, C., Renshaw, J.: Vibrothermographic crack heating: a function of vibration and crack size. AIP Conf. Proc. **1096**(1), 489–494 (2009)
14. Krapez, J.-C., Taillade, F., Balageas, D.: Ultrasound-lockin-thermography NDE of composite plates with low power actuators. Experimental investigation of the influence of the lamb wave frequency. Quant. InfraRed Thermogr. J. **2**(2), 191–206 (2005)
15. Solodov, I., Rahammer, M., Derusova, D., Busse, G.: Highly-efficient and noncontact vibro-thermography via local defect resonance. Quant. InfraRed Thermogr. J. **12**(1), 98–111 (2015)
16. Bai, G., Lamboul, B., Roche, J.-M., Baste, S.: Investigation of multiple cracking in glass/epoxy 2D woven composites by vibrothermography. Quant. InfraRed Thermogr. J. **13**(1), 35–49 (2016)
17. Kang, B., Cawley, P.: Low power PZT exciter for thermosonics. AIP Conf. Proc. **894**(1), 484–491 (2007)
18. Kang, B., Cawley, P.: Multi-mode excitation system for thermosonic testing of turbine blades. AIP Conf. Proc. **975**(1), 520–527 (2008)
19. Kang, B., Lee, H., Lee, C.: Performance of a small PZT exciter for thermosonic non-destructive testing. In: INTELEC 2009 – 31st International Telecommunications Energy Conference, pp. 1–4 (2009, October)
20. Renshaw, J., Holland, S.D., Barnard, D.J.: Viscous material-filled synthetic defects for vibrothermography. NDT & E Int. **42**(8), 753–756 (2009)

21. Pye, C.J., Adams, R.D.: Heat emission from damaged composite materials and its use in nondestructive testing. J. Phys. D. Appl. Phys. **14**(5), 927–941 (1981)
22. Pye, C.J., Adams, R.D.: Detection of damage in fibre reinforced plastics using thermal fields generated during resonant vibration. NDT Int. **14**(3), 111–118 (1981)
23. Homma, C., Rothenfusser, M., Baumann, J., Shannon, R., Thompson, D.O., Chimenti, D.E.: Study of the heat generation mechanism in acoustic thermography. AIP Conf. Proc. **820**(1), 566–573 (2006)
24. Rantala, J., Wu, D., Busse, G.: Amplitude-modulated lock-in vibrothermography for NDE of polymers and composites. Res. Nondestruct. Eval. **7**(4), 215–228 (1996)
25. Harwood, N., Cummings, W.M.: Thermoelastic Stress Analysis. CRC Press, Boca Raton, FL, USA (1991)
26. Morbidini, M., Cawley, P., Barden, T.J., Almond, D.P., Duffour, P.: A new approach for the prediction of the thermosonic signal from vibration records. AIP Conf. Proc. **820**(1), 558–565 (2006)
27. Ewins, D.J.: Modal Testing: Theory, Practice and Application, 2nd edn. Research Studies Press Ltd., Baldock, Hertfordshire, UK (2000)
28. Meola, C., Boccardi, S., Carlomagno, G.M.: Infrared Thermography in the Evaluation of Aerospace Composite Materials. Woodhead Publishing, Duxford, UK (2015)
29. Chi, X., Di Maio, D., Lieven, N.A.J.: Modal-based vibrothermography using feature extraction with application to composite materials. Struct. Health Monit. **19**(4), 967–986 (2020)
30. Chi, X., Di Maio, D., Lieven, N.A.J.: Health monitoring of bolted joints using modal-based vibrothermography. SN Appl. Sci. **2**(8), 1446 (2020)
31. Chi, X., Zhang, Y., Di Maio, D., Lieven, N.A.J.: Viability of image compression in vibrothermography. Exp. Tech. **45**(3), 345–362 (2021)
32. Chi, X., Di Maio, D., Lieven, N.A.J.: Frictional heating as an estimator of modal damping and structural degradation: a vibrothermographic approach. In: 12th Defence Science and Technology International Conference on Health and Usage Monitoring (2021)
33. Talai, S.M., Desai, D.A., Heyns, P.S.: Infrared thermography applied to the prediction of structural vibration behaviour. Alex. Eng. J. **58**(2), 603–610 (2019)
34. Han, X., Zeng, Z., Li, W., Islam, M.S., Lu, J., Loggins, V., Yitamben, E., Favro, L.D., Newaz, G., Thomas, R.L.: Acoustic chaos for enhanced detectability of cracks by sonic infrared imaging. J. Appl. Phys. **95**(7), 3792–3797 (2004)
35. Favro, L.D., Han, X., Ouyang, Z., Sun, G., Sui, H., Thomas, R.L.: Infrared imaging of defects heated by a sonic pulse. Rev. Sci. Instrum. **71**(6), 2418–2421 (2000)
36. Li, M., Holland, S.D., Meeker, W.Q.: Quantitative multi-inspection-site comparison of probability of detection for vibrothermography nondestructive evaluation data. J. Nondestruct. Eval. **30**(3), 172–178 (2011)
37. Vaddi, J., Reusser, R., Holland, S.D.: Characterization of piezoelectric stack actuators for vibrothermography. AIP Conf. Proc. **1335**(1), 423–429 (2011)
38. Vaddi, J., Holland, S.D., Reusser, R.: Transducer degradation and high amplitude behavior of broadband piezoelectric stack transducer for vibrothermography. AIP Conf. Proc. **1430**(1), 552–558 (2012)
39. Vaddi, J.S., Holland, S.D., Kessler, M.R.: Absorptive viscoelastic coatings for full field vibration coverage measurement in vibrothermography. NDT & E Int. **82**, 56–61 (2016)
40. Demy, P., Golinval, J.-C., Simon, D.: Damage detection in composites by vibrothermography and local resonances. Mech. Ind. **14**(2), 137–143 (2013)
41. Holland, S.D.: First measurements from a new broadband vibrothermography measurement system. AIP Conf. Proc. **894**(1), 478–483 (2007)
42. Lamboul, B., Passilly, F., Roche, J.-M., Balageas, D.: Ultrasonic vibrothermography using low-power actuators: an impact damage detection case study. AIP Conf. Proc. **1650**(1), 319–326 (2015)
43. Solodov, I., Bai, J., Bekgulyan, S., Busse, G.: A local defect resonance to enhance acoustic wave-defect interaction in ultrasonic nondestructive evaluation. Appl. Phys. Lett. **99**(21), 211911 (2011)
44. Parvasi, S.M., Xu, C., Kong, Q., Song, G.: Detection of multiple thin surface cracks using vibrothermography with low-power piezoceramic-based ultrasonic actuator—a numerical study with experimental verification. Smart Mater. Struct. **25**(5), 055042 (2016)
45. Zhu, L., Guo, X.: Vibro-thermography of debonding defects in composite plates. In: Conference on Quantitative Infrared Thermography – QIRT Asia 2017, Daejeon (2017)
46. Renshaw, J., Holland, S.D., Bruce Thompson, R.: Measurement of crack opening stresses and crack closure stress profiles from heat generation in vibrating cracks. Appl. Phys. Lett. **93**(8), 081914 (2008)
47. Russell, S.S., Henneke II, E.G.: Dynamic effects during vibrothermographic NDE of composites. NDT Int. **17**(1), 19–25 (1984)
48. Wang, C.-Y., Yew, C.H.: Impact damage in composite laminates. Comput. Struct. **37**(6), 967–982 (1990)
49. Bull, D.J., Spearing, S.M., Sinclair, I., Helfen, L.: Three-dimensional assessment of low velocity impact damage in particle toughened composite laminates using micro-focus X-ray computed tomography and synchrotron radiation laminography. Compos. A: Appl. Sci. Manuf. **52**, 62–69 (2013)
50. Yang, F.J., Cantwell, W.J.: Impact damage initiation in composite materials. Compos. Sci. Technol. **70**(2), 336–342 (2010)
51. Richardson, M.O.W., Wisheart, M.J.: Review of low-velocity impact properties of composite materials. Compos. A: Appl. Sci. Manuf. **27**(12), 1123–1131 (1996)
52. Tai, N.H., Yip, M.C., Lin, J.L.: Effects of low-energy impact on the fatigue behavior of carbon/epoxy composites. Compos. Sci. Technol. **58**(1), 1–8 (1998)
53. Sjoblom, P.O., Hartness, J.T., Cordell, T.M.: On low-velocity impact testing of composite materials. J. Compos. Mater. **22**(1), 30–52 (1988)
54. de Vries, E.: Mechanics and mechanisms of ultrasonic metal welding. PhD thesis, The Ohio State University (2004)
55. Crawley, E.F., de Luis, J.: Use of piezoelectric actuators as elements of intelligent structures. AIAA J. **25**(10), 1373–1385 (1987)
56. PI Ceramic: Displacement modes of piezoelectric actuators. https://www.piceramic.com/en/piezo-technology/properties-piezo-actuators/displacement-modes. Accessed 16 Sept 2022
57. Dimitriadis, E.K., Fuller, C.R., Rogers, C.A.: Piezoelectric actuators for distributed vibration excitation of thin plates. J. Vib. Acoust. **113**(1), 100–107 (1991)

58. Kim, T.-W., Kim, J.-H.: Optimal distribution of an active layer for transient vibration control of a flexible plate. Smart Mater. Struct. **14**(5), 904–916 (2005)
59. Ramesh Kumar, K., Narayanan, S.: The optimal location of piezoelectric actuators and sensors for vibration control of plates. Smart Mater. Struct. **16**(6), 2680–2691 (2007)
60. Aldraihem, O.J., Singh, T., Wetherhold, R.C.: Optimal size and location of piezoelectric actuator/sensors: practical considerations. J. Guid. Control. Dyn. **23**(3), 509–515 (2000)
61. Sadri, A.M., Wright, J.R., Wynne, R.J.: Modelling and optimal placement of piezoelectric actuators in isotropic plates using genetic algorithms. Smart Mater. Struct. **8**(4), 490–498 (1999)
62. Swann, C., Chattopadhyay, A.: Optimization of piezoelectric sensor location for delamination detection in composite laminates. Eng. Optim. **38**(5), 511–528 (2006)
63. Hexcel Corporation: HexPly® 8552 epoxy matrix product data sheet (2020)
64. Marlett, K.: Hexcel 8552S AS4 plain weave fabric Prepreg 193 gsm & 38% RC qualification material property data report. National Institute for Aviation Research, Wichita State University, Tech report (2011)
65. Speakman, J.R., Ward, S.: Infrared thermography: principles and applications. Zoology. **101**, 224–232 (1998)
66. Nicodemus, F.E.: Directional reflectance and emissivity of an opaque surface. Appl. Opt. **4**(7), 767–775 (1965)

Chapter 6
Damage Assessment with Laser Ultrasonics in 3D-Printed Plate

Jeffrey Liu, Paweł H. Malinowski, Piotr Pawłowski, Zihan Wu, and Michael D. Todd

Abstract The growing use of 3D-printed (additively manufactured) structural components implies the need to develop effective methods of damage assessment. This study focuses on guided wave propagation and its interaction with structural damage. The waves were excited using a laser scanning system which allows for easy excitation of the waves at various points at the surface. Also, the excitation is broadband, giving the ability to excite more guided wave modes at once. The combined laser scanning with a single piezoelectric measurement transducer takes advantage of reciprocity to reconstruct the full propagating wavefield. The investigated sample was printed from an aluminum alloy. The first set of measurements was realized for an intact (healthy) sample. Next, an artificial damage was introduced in order to study the wave interaction with it. Machine learning-based signal process algorithms were developed to analyze the wave interaction with the damaged plate. The obtained results show a good potential of guided wave-based techniques for the structural health monitoring of 3D-printed structures.

Keywords Guided waves · Laser ultrasonics · 3D printing · Nondestructive evaluation · k-means clustering · Principal component analysis

6.1 Introduction

The growing use of 3D-printed (additively manufactured) structural components implies the need to develop effective methods of damage assessment. Structural health monitoring (SHM) and nondestructive evaluation (NDE) approaches are focusing on the evaluation of structural elements without causing any permanent alterations, and there is a need to develop tailored approaches to inspect additively manufactured structures. NDE is most prominent in industries requiring very detailed inspections of structures that survive long past the manufacturing process such as in aircraft [1] and nuclear power plants [2]. Such complex structures such as aircraft undergo a variety of loads continuously over time that may lead to structural deterioration and damage development. That may be often hidden or barely visible [3]. One prominent technique within NDE is the usage of laser ultrasonics to determine and estimate the structural health of materials [4]. Laser ultrasonics takes advantage of laser excitation of the guided waves, and the resulting data are analogous to that obtained by laser vibrometry, which was successfully applied to the inspection of printed samples in the past. The 3D-printed and traditionally manufactured aluminum plates were studied employing ultrasonic transducers and laser vibrometers with second-harmonic Lamb wave propagation [5]. The laser ultrasonic and laser vibrometry provide valuable insight into structural health monitoring due to scanning abilities providing high-resolution images produced from the wavefield data collected from its propagation throughout the material. Although this technique proves its value from the high spatial resolution data that it collects, the analysis of laser ultrasonics data requires specialized skills from knowledgeable experts to

J. Liu
Computer Science & Engineering Department, University of California San Diego, San Diego, CA, USA

P. H. Malinowski (✉)
Institute of Fluid Flow Machinery, Polish Academy of Sciences, Gdańsk, Poland
e-mail: pmalinowski@imp.gda.pl

P. Pawłowski
Institute of Fundamental Technological Research, Polish Academy of Sciences, Warsaw, Poland

Z. Wu · M. D. Todd
Structural Engineering Department, University of California San Diego, San Diego, CA, USA

M. Allen et al. (eds.), *Special Topics in Structural Dynamics & Experimental Techniques, Volume 5*,
Conference Proceedings of the Society for Experimental Mechanics Series, https://doi.org/10.1007/978-3-031-37007-6_6

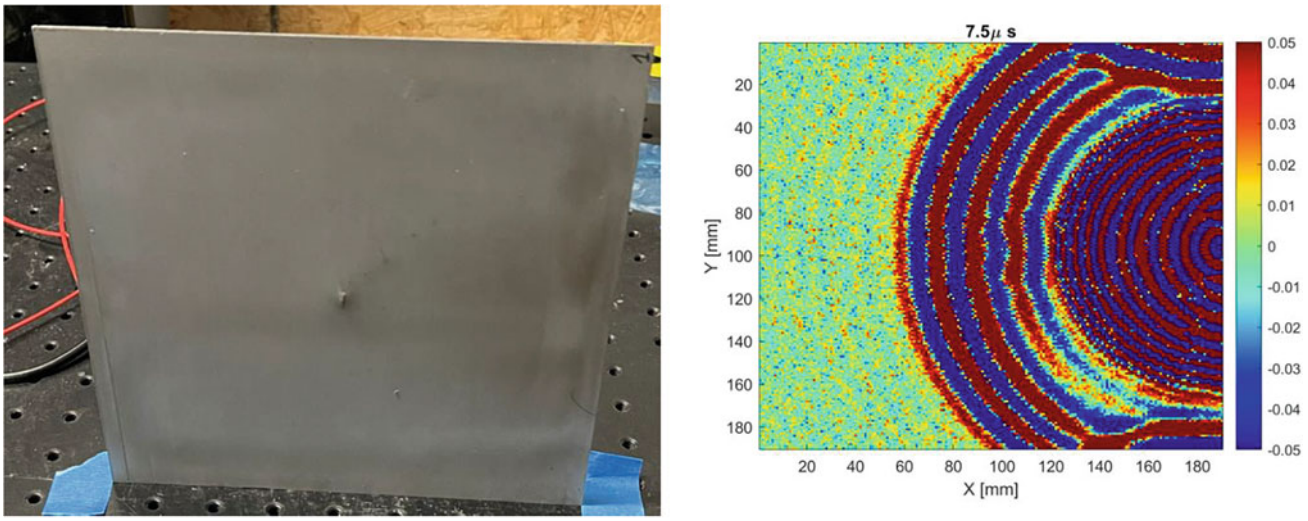

Fig. 6.1 (**a**) View of the samples from the laser scanned side; (**b**) the registered guided wave propagation: Two wave modes are visible with different wavelengths

interpret them; in fact, this not only applies to laser ultrasonics but many advanced techniques in NDE as well where machine learning is currently being utilized to automate such processes [6]. In this paper, we propose a data handling procedure to improve the automatization of the damage assessment process in the printed aluminum plate with simulated damage. The gathered data are transformed using principal component analysis (PCA) to perform k-means clustering for the classification.

6.2 Experimental Setup

The study was performed using a laser ultrasonic integration system (LUIS) which comprises a laser scanning system, a data acquisition system, and a piezoelectric sensor. The laser scanning system incorporates a diode-pumped solid-state Q-switched Nd:YAG laser that was used for the wave excitation and a 2D laser mirror scanner to move the laser beam along a defined grid of points allowing for multiple excitation points. The investigated specimen (200 mm × 200 mm × 1 mm) was additively manufactured out of AlSi10Mg alloy. To collect the wavefield data from the surface of the plate, the contact sensor is mounted at its edge center using cyanoacrylate adhesive. The plate was firstly measured in a healthy state (intact), and later, a 10 mm × 1 mm notch was introduced to simulate damage that was next deepened (Fig. 6.1a). It was located in the middle of the plate with a longer edge parallel to the edge with the piezoelectric sensor. With this specimen, a raster scan across the surface was performed with the LUIS. At each designated scan point of the aluminum plate, the laser pulses, causing an ultrasonic wave to propagate symmetrically throughout the plate. The mounted piezoelectric transducer senses the energy from the surface of the plate and sends the measurements to the oscilloscope, where the data are digitized and read for a single point until every scan point is covered by the laser. The data that are collected by the oscilloscope are read as an $N \times M$ grid of points. Each of these points contains the time series data collected for that scan point. The entire wavefield data read in is represented as a three-dimensional image of the ultrasonic wave propagation with two spatial dimensions and one temporal dimension described as $N \times M \times T$. The registered data at one time moment are presented in (Fig. 6.1b).

6.3 Methodology

From the three-dimensional image that is collected from the LUIS, it is necessary to clean the data such that only the incident wave is visible; i.e., ambient noise from the start of the sensor recording and images including feedback from reflected waves after the incident wave has propagated throughout are discarded. This reduces the dimensions of collected LUIS data from $N \times M \times T$ to $N \times M \times T_\mathrm{r}$. From the time-reduced dataset, every spatial point (n, m), where $n \in N$, $m \in M$, is Fourier transformed such that the original dataset is transformed from $N \times M \times T_\mathrm{r}$ to $N \times M \times Lf$ where L_f is the corresponding

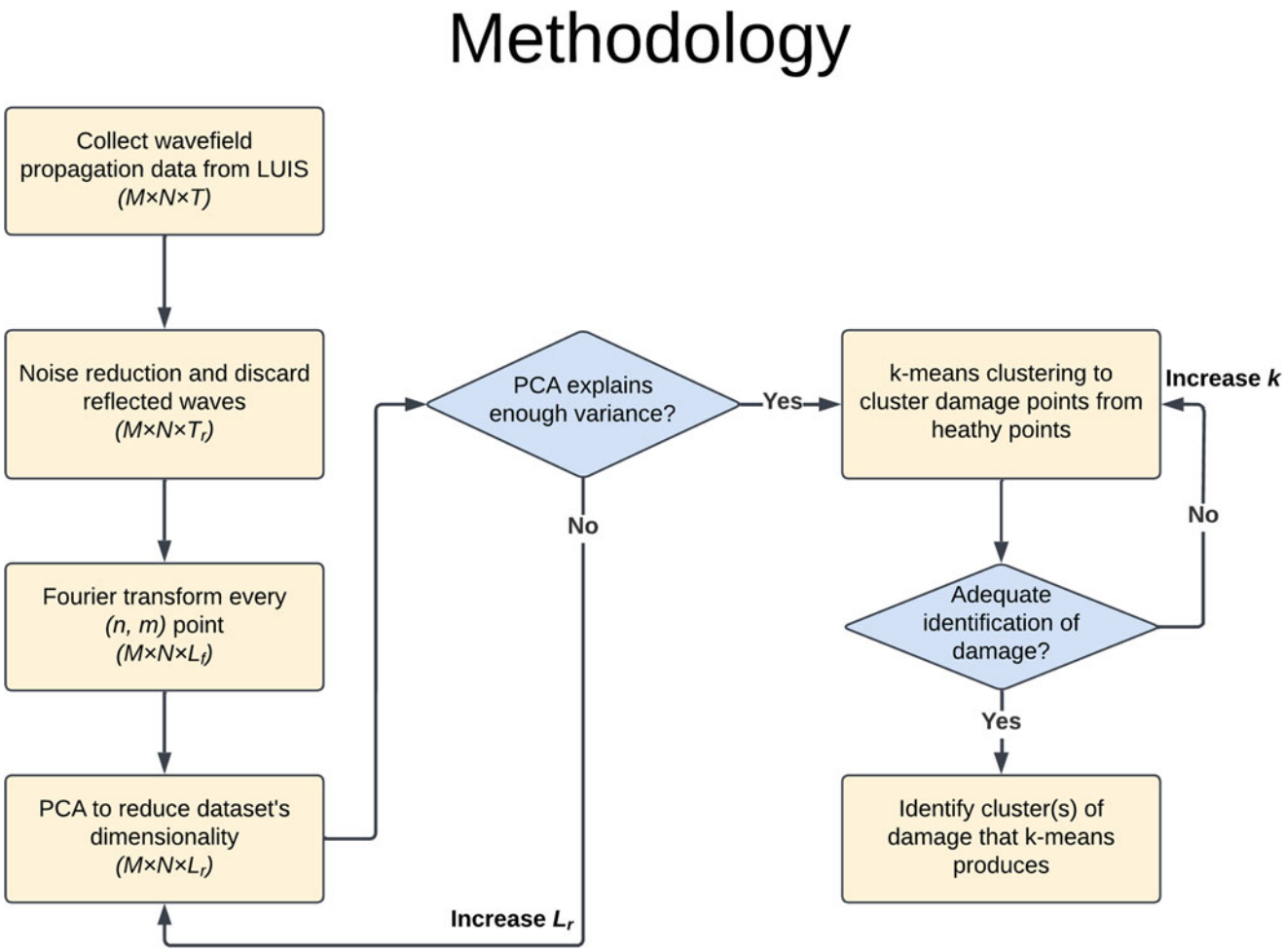

Fig. 6.2 Flowchart of the given methodology above

frequency space for each (n, m). To utilize the $N \times M \times L_f$ dataset of spectra that were generated from the Fourier transform of each (n, m), it is necessary to reduce the dimensionality of our dataset to increase the efficiency of any machine learning model using this dataset. This is the case since the clustering technique scales with the number of data points within the dataset, so reducing the dimensionality and losing information is the tradeoff for computational efficiency. To preserve the most information from the dataset while reducing many variables, principal component analysis (PCA) is used. In general, the $N \times M$ grid of scan points would be very large to maintain high spatial resolution data and L_f would vary depending on sampling frequency and speed of the wave propagation, so PCA will be very helpful in saving computational resources and runtime. PCA was used to compress the original Fourier transformed dataset such that $N \times M \times L_f \rightarrow N \times M \times L_r$, where L_r is the space of principal components used to explain L_f. Using the PCA-reduced dataset of size $N \times M \times L_r$, k-means clustering was performed. K-means clustering is an unsupervised machine learning algorithm that forms k clusters based on x number of observations in the dataset where x is $N \times M$ number of points scanned by the LUIS. Analyzing all k clusters, it is feasible to automate searching for the cluster that maintains the shape and information of the specimen's damage since, in general, $k \ll N \times M$. The workflow of the entire methodology is given in Fig. 6.2.

6.4 Results

After performing a scan of the aluminum plate, the dataset for both the deeper and shallow cuts obtained was a $190 \times 190 \times 500$ matrix. The reference, deeper, and shallow cut datasets are then reduced to $190 \times 190 \times 211$, $190 \times 190 \times 211$, and $190 \times 190 \times 231$, respectively, after cleaning the dataset of ambient noise and reflected waves. After computing the Fourier transform of every scan point, PCA is performed. Performing PCA on the dataset was able to reduce

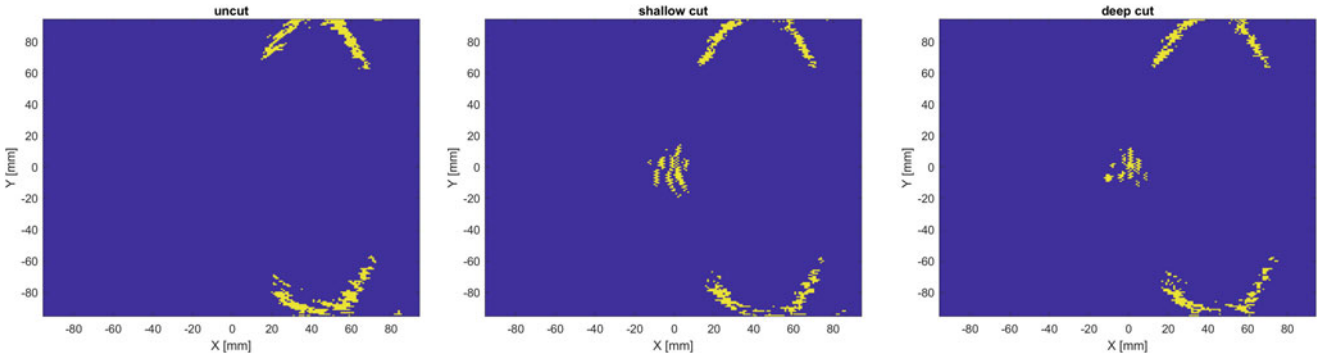

Fig. 6.3 Results of clustering; clusters indicating: (**a**) edges reflection (reference measurement); (**b**) damage reflection and edges reflection (measurement for shallow cut); and (**c**) damage reflection and edges reflection (measurement for deep cut)

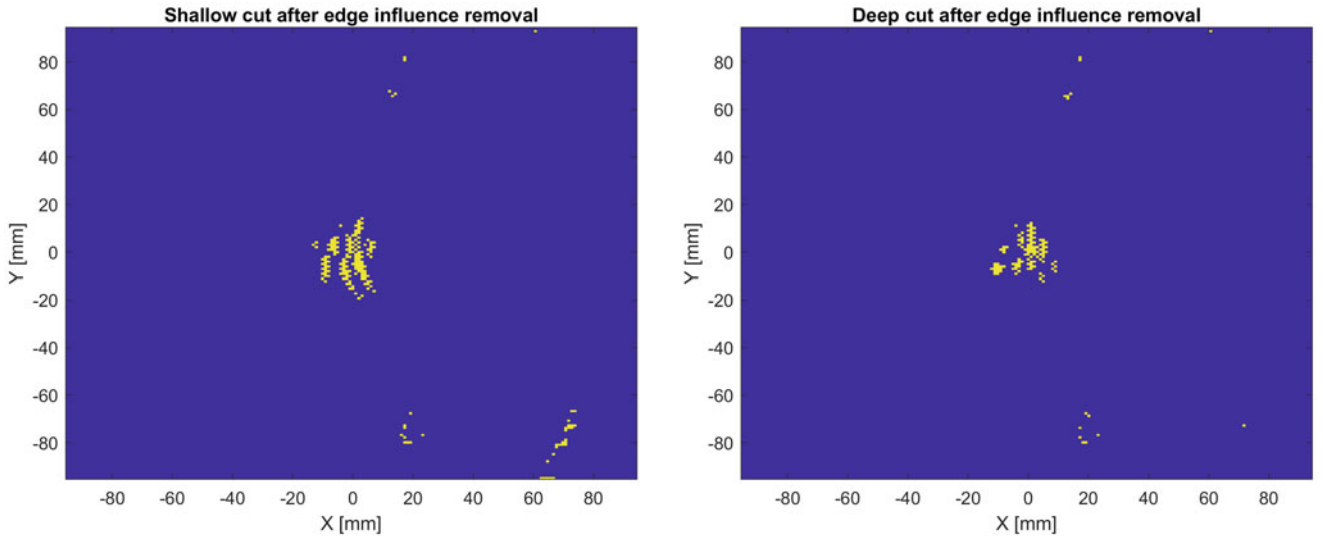

Fig. 6.4 Results after edge influence removal: (**a**) shallow cut case; (**b**) deep cut case

the dimensions of both datasets to merely $190 \times 190 \times 3$. Here, three principal components explained approximately 92.79%, 92.86%, and 92.52% of the variance in the time-reduced datasets for the reference, shallow, and deeper cut, respectively.

With the PCA-reduced datasets, k-means clustering is performed. Naturally, as the number of principal components and number of clusters rise, computational workload increases and takes much longer to compute. However, since PCA was so efficient in reducing the dimensionality of the dataset, the result is a very efficient pipeline that clusters damaged points from healthy points. Experimentally, we determined that the optimal number of clusters to choose using three principal components for these datasets is $k = 50$ clusters.

We were able to highlight the cluster containing the damaged points in the scatter plot by manually plotting and visualizing every point. Cluster no. 36 indicated the damage location for the data for shallow and deep cuts (Fig. 6.3b, c), while the data used for reference were obtained from the 31st cluster (Fig. 6.3a). There is a large improvement in identifying the damage location on the aluminum plate. As opposed to analyzing 500 images per measurement, this procedure ensures that a clear image of the damage is guaranteed by searching through only 50 images.

Although the location of the damage is clearly indicated in both cases (shallow and deep cut), there is still an indication related to wave reflection from the top and bottom sample edges. It is the same as visible in the undamaged plate (Fig. 6.3a). Simple direct subtraction cannot remove this since the pixel locations representing edge reflection are a bit different in each of the cases, although the shape is similar. In order to facilitate the background subtraction, a numerical procedure was developed that assumes a ± 3 mm margin (for X and Y) for subtraction and allows the removal of the edge influence almost completely (Fig. 6.4).

6.5 Conclusion

In this paper, a machine learning-based damage assessment of laser ultrasonic imaging data was proposed. The damage search is performed in steps, where the data undergo filtering, Fourier transform, PCA decomposition, and then k-means clustering to find the damage location. Although the identification of clusters for reference and with damage information was done manually, these steps may be automated. In the future, this procedure may be modified to work also for other materials (both printed and standard).

Acknowledgements Pawel Malinowski acknowledges the funding support provided by the National Science Center, Poland, under the OPUS project (2019/35/B/ST8/00691) and the Polish National Agency for Academic Exchange for funding the research stay at the University of California San Diego under the Bekker NAWA Programme (BPN/BEK/2021/2/00005). The UC San Diego researchers were funded by the National Science Foundation REU Program, Award #1757994.q.

References

1. Kostroun, T., Milan, D.: Application of the pulse infrared thermography method for nondestructive evaluation of composite aircraft adhesive joints. Materials. **14**(3), 533 (2021)
2. Glass, S.W., Fifield, L.S., Jones, A.M., Hartman, T.S.: Frequency domain reflectometry modeling for nondestructive evaluation of nuclear power plant cables. AIP Conf. Proc. **1949**, 110005 (2018)
3. Wronkowicz-Katunin, A., Katunin, A., Dragan, K.: Reconstruction of barely visible impact damage in composite structures based on non-destructive evaluation results. Sensors. **19**(21), 4629 (2019)
4. Wu, Z., Chong, S.Y., Todd, M.D.: Laser ultrasonic imaging of wavefield spatial gradients for damage detection. Struct. Health Monit. **3**, 960–977 (2021)
5. Vien, B., Chiu, W., Rose, R.F.: Experimental investigation of second-harmonic lamb wave generation in additively manufactured aluminum. J. Nondestruct. Eval. Diagn. Progn. Eng. Syst. **1**, 041003 (2018). https://doi.org/10.1115/1.4040390
6. Kot, P., Muradov, M., Michaela Gkantou, M., Kamaris, G.S., Hashim, K., Yeboah, D.: Recent advancements in non-destructive testing techniques for structural health monitoring. Appl. Sci. **11**(6), 2750 (2021)

Chapter 7
Parameter Investigation of Sensor Fixation Methods Compared with High-Quality Laser Measurement Using a Scalable Automatic Modal Hammer

Robin Pianowski, Robert Kamenzky, Stefan Wolter, Zeyun Song, and Peter Blaschke

Abstract The need to measure complex mechanical structures has grown in importance for efficiency in the design process and for structural monitoring. Despite the convenience of using a 3D scanning laser Doppler vibrometer (LDV), fixed acceleration sensors are still widely used for industrial applications. However, the effects of sensor attachments cannot be disregarded for lightweight structures. This paper provides a thorough description of how various sensor attachment techniques affect vibration measurements over a wide frequency range (up to 16 kHz). Frequency response function (FRF) measurements were conducted on an aluminum plate using both the LDV and an accelerometer simultaneously, excited by a scalable automatic modal hammer (SAM). For particular frequency ranges of interest, recommendations for fixation methods are proposed. Recommendations for fixation techniques are proposed for certain frequency ranges. The study's findings offer practical advice for industrial structure measurement evaluations.

An important outcome of this study is how the fixation method influences the experimental results of the modal properties. The research reveals that the fixation, the contact area, the sensor, and the test specimen built a dynamic system that influences the results especially at higher frequencies and should be considered for precise measurements.

Keywords Sensor fixation · Scalable automatic modal hammer · Modal damping · High-quality FRF

7.1 Introduction

Accelerometers are still widely used for vibration measurements and experimental modal analysis, although LDV enables contactless and fast measurements. It is common knowledge that the transducer and attached sensor will add mass to the system. This mass loading effect is even more significant for lightweight structures. Numerous attempts have been made to study and eliminate the mass loading effect [1–2]. In addition, the sensor mounting can contribute to additional relative motion and alter the stiffness and damping, affecting the structural dynamics and the accuracy of acceleration measurements. Marscher et al. [3] studied the FRF measurement fidelity for several fixation methods and found that all fixation methods exhibit good agreement up to 5 kHz, while the fidelity is related to the adhesive layer thickness at higher frequencies. Shokrollahi et al. [4] examined the response amplification and transmissibility for modal wax, magnetic, and screw fixation, which revealed that rigid bonding reproduces the input acceleration more accurately, especially at higher frequencies. Maierhofer et al. [5] compared the FRFs of an aluminum beam under various fixation conditions, finding that in the frequency range of interest (up to 2 kHz), there is no significant difference in FRFs between fixation methods in normal direction, whereas tangential vibrations are more sensitive. Colombo et al. [6] investigated the performance of different adhesive materials based on a set of weighted assessment criteria, delivering a helpful guideline for adhesive selection. This paper deals with the influence of sensor fixation methods on two-dimensional structures, whereas most of the previous research has focused on beam structures. Despite this, few studies have been conducted on sensor performance at even higher frequencies (above 5 kHz), where the vibration characteristic becomes increasingly relevant to sensor dynamic properties. In this work, frequencies up to 16 kHz are considered, providing precise insights into different frequency ranges.

R. Pianowski · R. Kamenzky · S. Wolter · Z. Song · P. Blaschke (✉)
Laboratory for Machine Dynamics and Acoustics, Technical University of Applied Science Wildau, Wildau, Germany
e-mail: pblaschke@th-wildau.de

M. Allen et al. (eds.), *Special Topics in Structural Dynamics & Experimental Techniques, Volume 5*,
Conference Proceedings of the Society for Experimental Mechanics Series, https://doi.org/10.1007/978-3-031-37007-6_7

7.2 Materials and Methods

The experimental setup is shown in Fig. 7.1a. The specimen is a 210 × 150 × 5 mm aluminum plate weighting 418 g, which was suspended on acoustic foam to approximate free-free boundary condition. For repeatable measurements and constant contact points between the plate and foam, the specimen position was marked on the foam. A Polytec PSV-500-3D-H 3D scanning laser Doppler vibrometer (LDV) was utilized to take contactless vibration measurements. For an optimal incidence angle of 90°, the laser beams were redirected over a mirror onto the plate surface. A precise measurement is a crucial basis for further analysis. Therefore, a scalable automatic modal hammer (SAM) (NV-TECH-Design, Steinheim a.d. Murr, Germany), shown in Fig. 7.1b separately, was used to exert accurate, repeatable, and precisely adjustable force impacts on the specimen [7]. The SAM was instrumented with a light impact hammer (model 086E80 from PCB Piezotronics), enabling a non-mass loaded broadband excitation with constant force and location, eliminating the transducer's mass effect when using a shaker as well.

A detailed depiction of the test specimen is shown in Fig. 7.2a with the marked excitation point, which remains the same for all measurements. 20 × 20 mm from the bottom left corner is a 3.5 mm through hole to bolt a piezoelectric acceleration sensor. For a comprehensive evaluation of the specimen's deflection shapes, a modal test was conducted using the LDV in a roving sensor setup before the sensor was put in place. The specimen was scanned with a 15 × 15 mm grid of degree of freedom (DOF) points. A total number of 116 DOFs were measured with a measurement time of 4 s and a sampling rate 125 kHz. Impact force was 40 N, and for each frequency response function (FRF) of every DOF, the average of three measurements was calculated.

To make an investigation into the influence of sensor mounting method on vibration measurements, subsequent measurements were conducted with a different test range. A triaxial piezoelectric acceleration sensor (356B21 from PCB Piezotronics) with a mass of 4 g was fixed at the hole's center on the opposite side of the excitation. Figure 7.2b gives an illustrative schematic of the sensor alignment. To obtain single-point FRFs between the excitation point and sensor point,

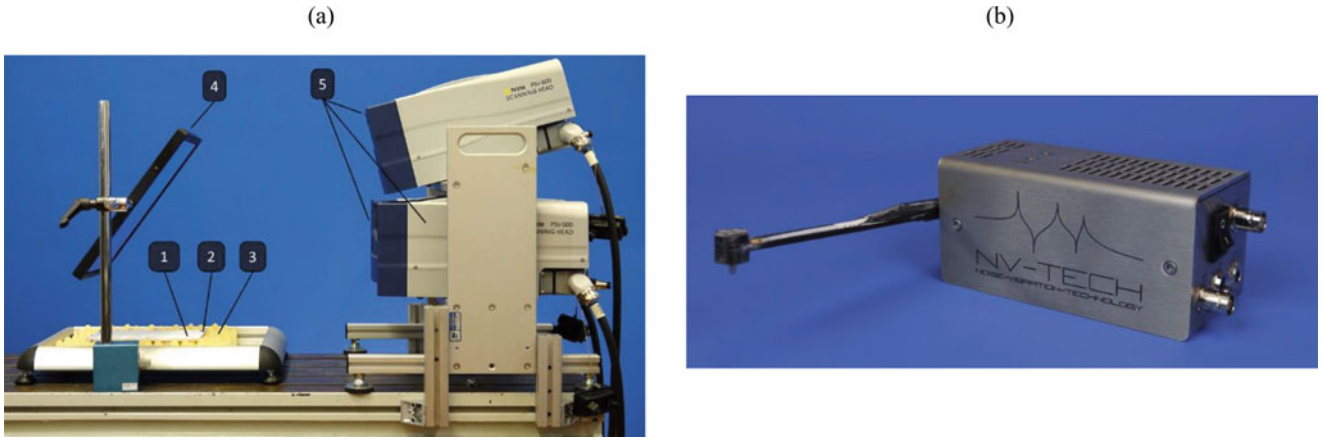

Fig. 7.1 Photographs of (**a**) the experimental setup: 1—aluminum plate, 2—accelerometer, 3—acoustic foam, 4—mirror, 5—LDV and (**b**) the scalable automatic modal hammer (SAM)

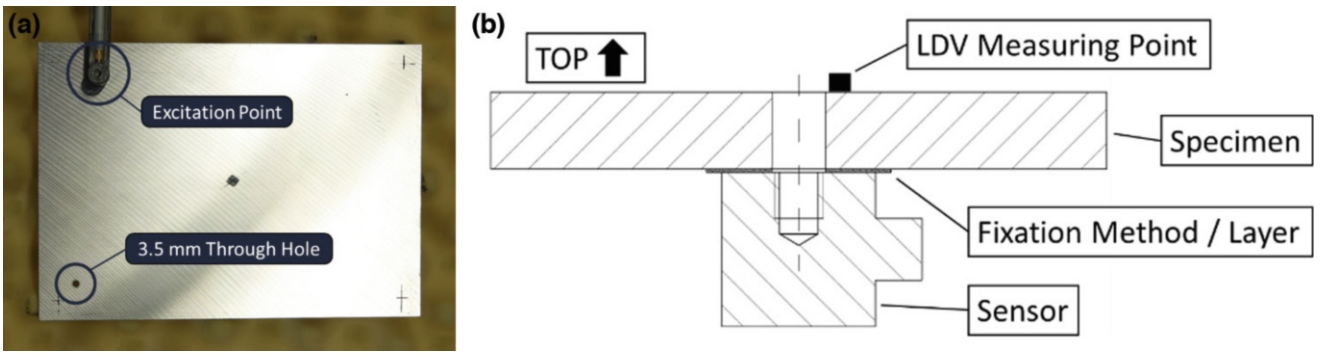

Fig. 7.2 A detailed view of (**a**) the tested specimen and (**b**) the sensor alignment

measurements were performed with the accelerometer with a measurement time of 4 s and 125 kHz sampling rate, averaged from ten measurements. Simultaneously, LDV measurements were conducted for comparison. Hence, it is desirable that the laser beam of the LDV is focused on the nearest possible location from the sensor on the upper side of the plate.

For the following measurements, different mounting methods for the sensor were tested:

1. Super glue: This investigation used cyanoacrylate-based Loctite 454, which enables rapid bonding and strong adhesive force [5] with only a thin layer of glue, leading to the assumption that it is highly rigid and only slightly dampens materials. However, removing the sensor and cleaning the surface can be challenging, as no damage should be done to the sensor or the specimen.
2. Modal wax: Modal wax is often used for sensor attachment because installing and removing the sensor are easy, and there is no hardening effect. Furthermore, the stiffness of the bonding contact is sensitive to the thickness of the wax and shows relatively high energy loss in viscous damping. At the same time, high damping is anticipated; a study by Colombo et al. [6] compared the use of superglue and modal wax, implying that FRFs measured with the waxed sensor showed notably reduced amplitude and accuracy. Therefore, a high damping is expected.
3. Ceramic glue: This study uses X60 adhesive, which uses a methacrylate mixture as the base material. The lowest possible usable temperature is −200 °C. Compared to cyanoacrylate-based glue, X60 adhesive provides stiffer bonding [6] better operational capabilities for rough surfaces [8]. It is assumed to have the lowest internal friction in the glue layer.
4. Hot glue: A hot glue gun was used to apply Bosch Glue Stick Set Ultra Power to the surface. Care has to be taken to achieve a thin adhesive layer between specimen and sensor. Due to its low bonding stiffness, it is assumed to have similar modal material properties to modal wax.
5. Screw fixation: A N 5–40 UNC B screw with a length of 11 mm was used to assemble the sensor. Consequently, a slightly higher additional mass and a shifted center of gravity of the attached sensor occur and a significant stiffening effect in the contact zone is assumed. In contrast to all other mounting methods, energy losses caused by relative motion between sensor and specimen occur because of contact friction instead of material damping. However, the requirements to drill a hole in the structure make this application less practical.

7.3 Experimental Results and Analysis

The vibrations of the sensor mounting point of the plate were measured by LDV with and without an attached accelerometer and then compared to the FRFs measured with an attached accelerometer to determine the difference between accelerometer and LDV measurements. Figure 7.3 illustrates the z-direction FRFs under three distinct fixation conditions: superglue (top), modal wax (middle), and ceramic glue (bottom). The FRFs measured by the LDV at the sensor position without the mounted sensor are plotted as blue-dashed curves. The solid red curves represent the FRFs measured by the LDV with the sensor attached to the plate. The solid blue curves show the FRFs directly measured by the installed accelerometer. The plots reveal that the mass affects all obtained eigenmodes of the plate, as a decrease at each natural frequency can be observed by the LDV and the accelerometer as well. The LDV tests and accelerometer tests produce similar FRFs in a frequency band of 300 Hz to 3.3 kHz and from 5.4 to 10 kHz. However, some deviations are evident in the mid-frequency range from 3.3 to 6 kHz. There the vibration amplitudes become smaller, and the LDV tests exhibit a smaller signal-to-noise ratio (SNR). So specific modes are no longer identifiable by the LDV. This is observable for all three fixation cases. Compared to the FRFs measured by the LDV, accelerometer tests produce signals with a better SNR, revealing more information about the eigenmodes where the sensor is located at a nodal point and specific anti-resonances. Therefore, accelerometer data are utilized for analysis in the scope of this work.

In the remainder of this section, two alternative fixation methods are considered, i.e., hot glue and screw. The FRFs at the location of the installed accelerometer are evaluated step by step in several frequency ranges marked by gray bands, as shown in Figs. 7.4, 7.5, 7.6, and 7.7. The blue-dashed curves represent data collected before sensor installation as reference signals; super glue, ceramic glue, and screw mounting are represented by red, black, and green solid curves, respectively. The modal wax and hot glue fixation are represented by red-dashed and black-dashed curves, which indicate less rigid connections.

Figure 7.4a demonstrates that measurements for all five fixation methods agree well at low frequencies, with the additional mass having the only discernible effect on the dynamic properties of the structure. From 1000 Hz, the attachment method's effect is observed, with all measurements exhibiting different damping and amplitudes.

As depicted in Fig. 7.4b, the ceramic glue fixation has the highest peak value at the resonance frequency of 1503 Hz, while the resonance peaks for super glue, hot glue, and screw fixation drop slightly to the same level. The vibration with modal waxed sensor is less dampened but exhibits the largest eigenfrequency shifting, which deviates from our expectation.

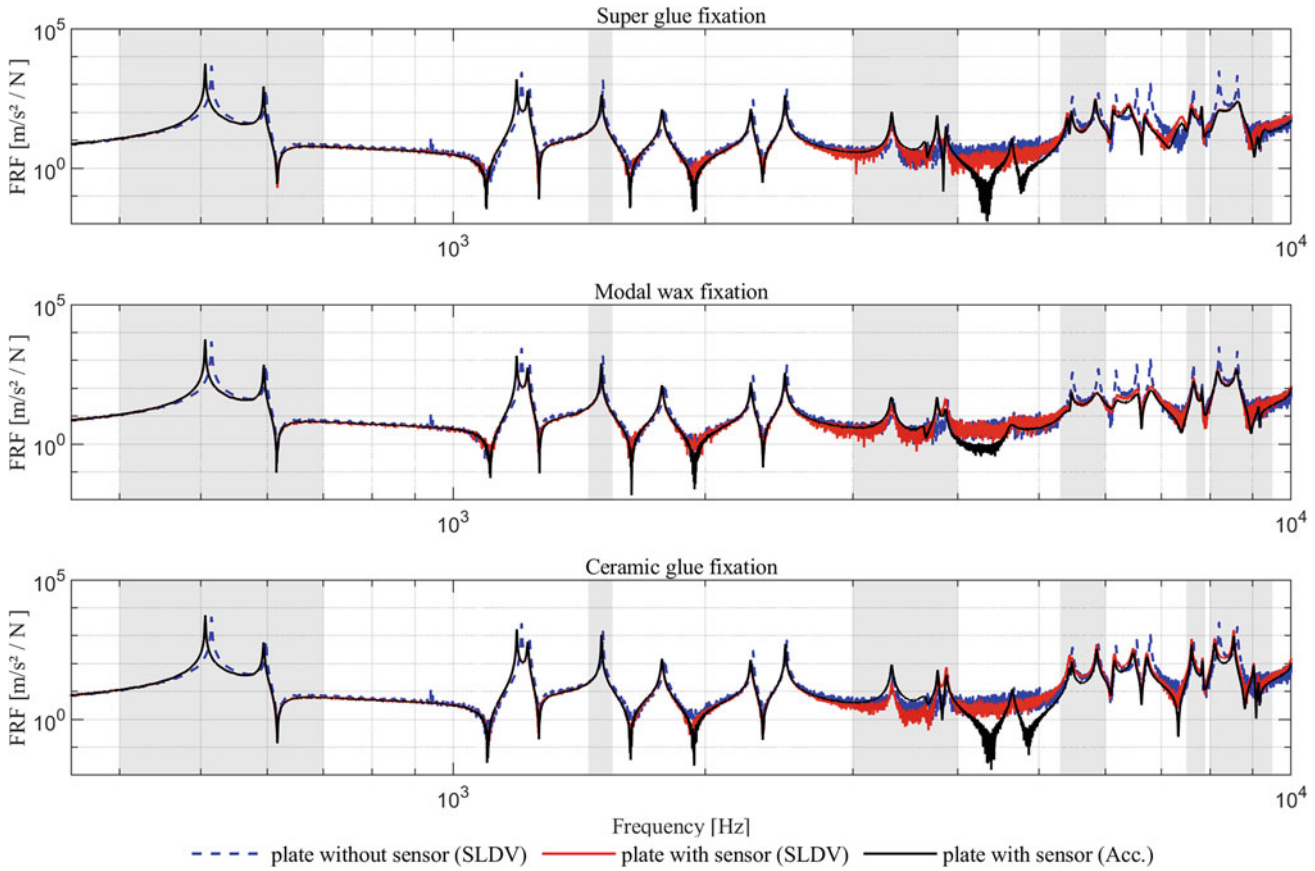

Fig. 7.3 FRFs at the sensor position using LDV and accelerometer measurements; sensor adhered with superglue (top), modal wax (middle), and ceramic glue (bottom)

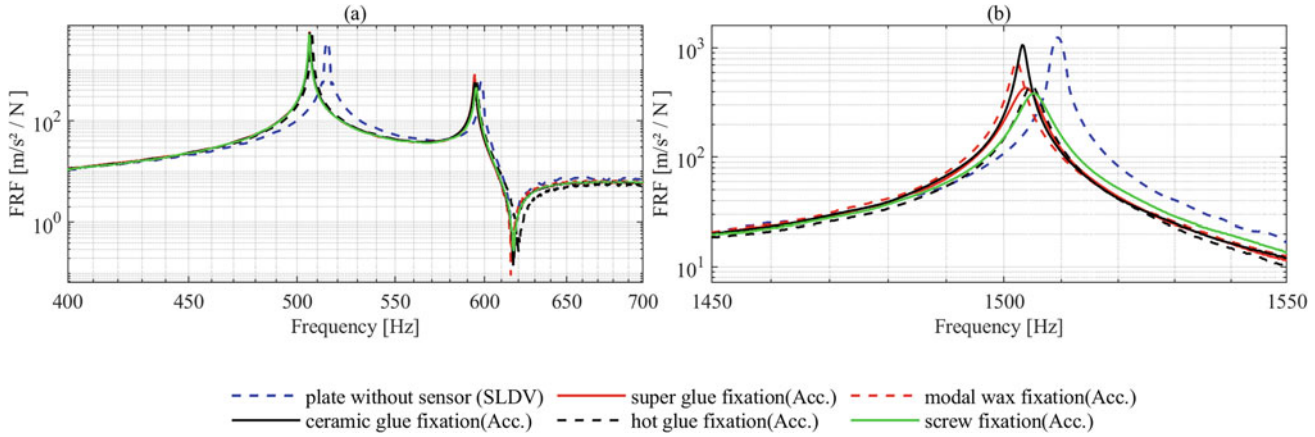

Fig. 7.4 FRFs at the sensor position; left: 400–700 Hz, right: 1450–1550 Hz

Furthermore, the similarity of the LDV and accelerometer FRFs implies a detuning of the dynamic behavior of the specimen caused by the sensor coupling in the whole examined frequency range. The sensor signal is still accurate, but the measured specimen interacts with the sensor and changes its modal parameters.

Figure 7.5a illustrates the FRFs between 3000 and 4000 Hz, where the superglue and ceramic glue exhibit many similarities. The screw fixation reduces the mass-induced natural frequency shifting compared to the other fixations. Using a screw-mounted accelerometer makes it easier to identify the eigenmode at 3600 Hz while leaving a significantly smaller peak amplitude at 3880 Hz. As shown in Fig. 7.5b, modal wax and hot glue behavior are comparable between 5300 and 5600 Hz with the lowest peak amplitude. In contrast, eigenmodes separate into two modes for super glue, ceramic glue, and

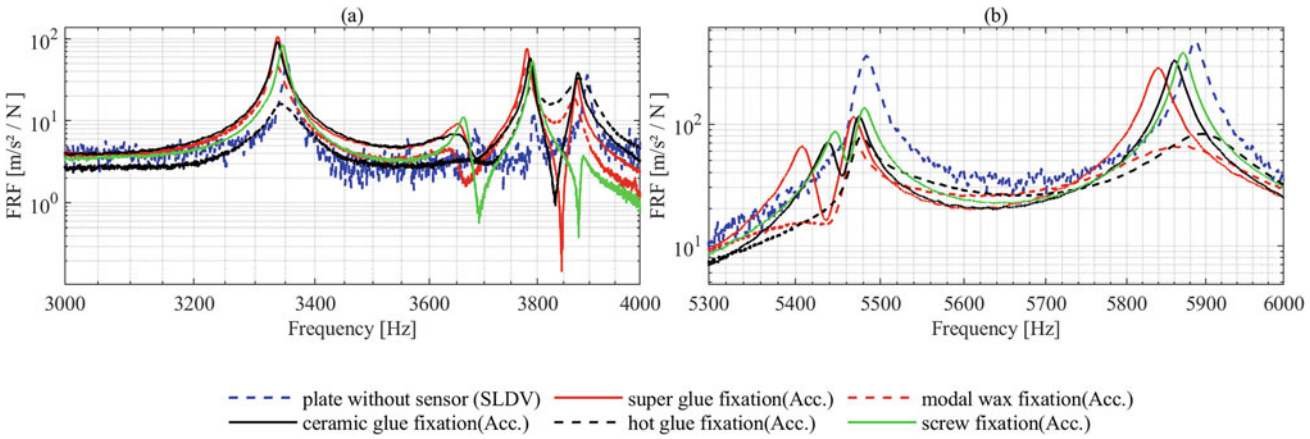

Fig. 7.5 FRFs at the sensor position; left: 3000–4000 Hz, right: 5300–6000 Hz

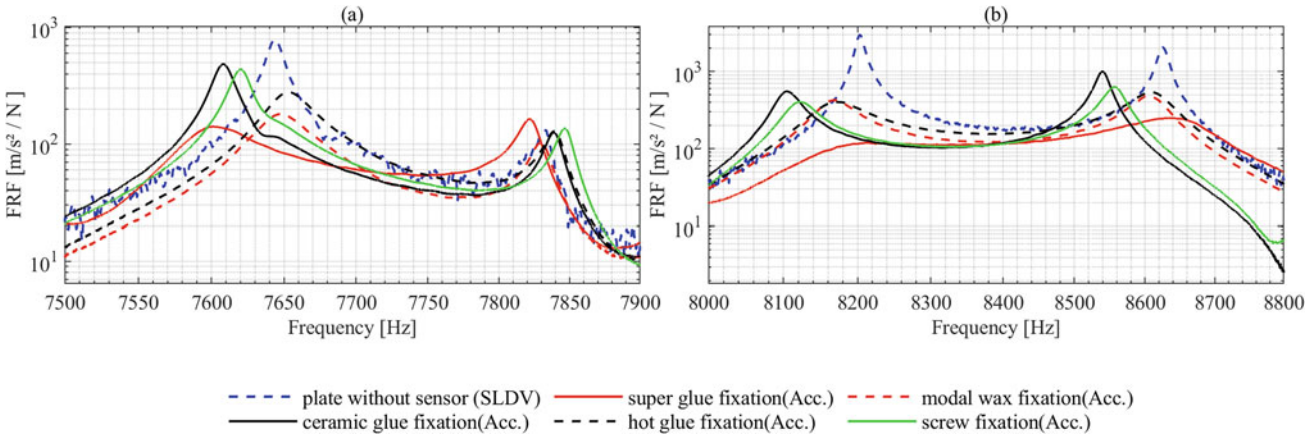

Fig. 7.6 FRFs at the sensor position; left: 7500–7900 Hz, right: 8000–8800 Hz

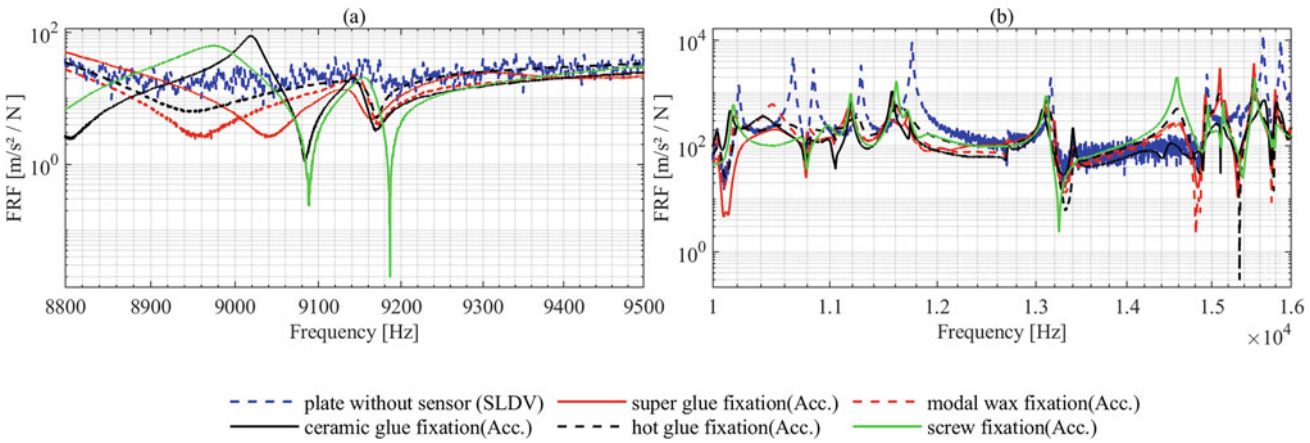

Fig. 7.7 FRFs at the sensor position; left: 8.8–9.5 kHz, right: 10–16 kHz

screw fixations. From 5800 to 6000 Hz, the less rigid adhesives (modal wax and hot glue) almost attenuated one eigenmode entirely. In addition, the eigenfrequency deviation from the reference FRF increases sequentially with the damping of screw mounting, ceramic glue, and super glue. The same performance is observed up to 6200 Hz. Moreover, if we examine the frequency range between 3000 and 6000 Hz, we can conclude that the two "less rigid" connections have greater damping than the others and that the natural frequency shifting with screw fixation is always less.

Over 7500 Hz, superglue degrades to the same level as modal wax, and the damping ratio is significantly higher, as shown in Fig. 7.6a. However, natural frequencies rise when the sensor is mounted using modal wax and hot glue. At approximately 7600 Hz, the damping of the superglue increases significantly.

As shown in Fig. 7.6b, between 8000 and 8800 Hz, superglue fixation ultimately dampens modes; peaks for ceramic glue and screw fixation are significantly lower; modal wax and hot glue provide higher damping than ceramic glue and screw, while the eigenfrequency shifting is less. In addition, the less rigid adhesives continue to exhibit similar behavior.

Figure 7.7a displays the frequency band from 8.8 to 9.5 kHz. The attached sensor detects an eigenmode at 9145 Hz that is absent from the reference FRF (blue curve) measured by LDV. As shown in Fig. 7.7b, from 10 kHz, ceramic glue fixation results in significantly higher damping and lower resonance peak than screw mounting. Specific peaks cannot be detected even with a screw-mounted accelerometer. It is remarkable that there is a significant amplitude increase in the resonance peaks for superglue compared to all other fixation types between 15 and 16 kHz. Above 16 kHz, the curves can no longer be aligned.

7.4 Conclusion and Outlook

This study examined how different sensor fixation techniques affected the FRF readings of a lightweight structure. Accelerometer and LDV measurements are utilized for comparison.

Because of mass addition, frequency shifting occurs for all eigenmodes. There is no outlier among the FRFs at low frequencies (up to 1 kHz). Compared to the two “less rigid” fixation methods that are assumed to exhibit similar behavior, modal wax causes lower damping at frequencies below 3800 Hz. This effect is resulted from metallic contact as the wax settles in the furrows and hot glue is hardening on the top of the asperities. The damping could result from the sensor and plate’s relative motion, and it can be assumed that fixation-induced damping increases as acceleration increases. From 5 kHz, mode separations are observed for “rigid” bonding (super glue, ceramic glue, and screw mounting), indicating that the mass is dominating at certain frequencies; due to the high damping, modal wax and hot glue become less sensitive to eigenmodes. Although superglue is effective up to 7 kHz, the error frequencies of the eigenmodes are higher compared to those of ceramic glue and screw mounting. The highest modal damping effects can be observed at frequencies between 8 and 15 kHz; above 15 kHz, the damping effect reduces. Ceramic glue and screw fixation have superior performance up to 10 kHz. Although screw fixation improves the accuracy of natural frequencies, the influence of varying pre-stress and screw mass remains problematic. Over 15 kHz, the resonance of the sensor mass becomes more dominating.

While the accelerometer is suitable for capturing local vibrations, the LDV is more suitable for obtaining mode shapes. As mentioned, vibration amplitudes decrease between 3.3 and 6 kHz. By analyzing the mode shapes, we found out that the sensor is located near a nodal point for these modes. The additional eigenmode at 8.8 kHz (see Fig. 7.7a) is identified to be an in-plane mode for the sensor-free plate, implying that the sensor attachment includes a z-component to the in-plane modes.

To summarize, the high sensitivity of acceleration sensors in measuring resonances and anti-resonances mainly benefits from the good SNR. However, the accelerometer’s installation and the adhesive’s application modify the local and global vibroacoustic behavior of the specimen. Up to 5 kHz, all of the investigated sensor fixation techniques detect eigenmodes with sufficient accuracy. At higher frequencies, the modes become more locally dominant, and due to the added mass and the fixation, the shifting of natural frequencies becomes more significant. Adhesives with high material damping like modal wax and hot glue result in significant increase in modal damping even for low frequencies. Due to ease of disassembly, modal wax can be recommended for a frequency range of interest below 1 kHz. Ceramic glue is recommended as a nondestructive alternative for screw fixation in vibration testing up to 10 kHz. In the case of exceptionally high frequencies, superglue is an alternative. For specific experimental tests aiming to identify modal damping, ceramic glue the most appropriate adhesive.

Another important outcome of the research is that besides the pure mass effect of the acceleration sensor, the fixation methods and the contact area (surface roughness) itself can detune the observed modal properties of the test specimen. This outcome is as well valid for attachment of a shaker.

In future research, influences of the mounting methods on in-plane accelerations and the effect of changing the thickness of the adhesive layer can be investigated, and the sensitivity of mass loading can be taken into account. Once the interactions of the connected sensor and the structure to be measured are fully understood, algorithms to compensate the fixation-induced effects might be developed.

Acknowledgements This study was partially supported by the Innovation and Career Center Integrated Engineering (IKC-IE), a cooperation project of the Brandenburg University of Technology Cottbus-Senftenberg (BTU-CS), the Eberswalde University for Sustainable Development (HNEE), and the Technical University of Applied Sciences Wildau (TH Wildau).

References

1. Cakar, O., Sanliturk, K.Y.: Elimination of transducer mass loading effects from frequency response functions. Mech. Syst. Signal Process. **19**(1), 87–104 (2005)
2. Karle, A.D., Bhoite, S.K., Amale, A.B.: An analysis of transducer mass loading effect Inshaker testing. J. Eng. Res. Appl. **4**(6), 207–212 (2014)
3. Marscher, W.D., Onari, M.M.: Optimal attachment methods for accelerometers. Presented at the MFPT 2019, Philadelphia PA, 2018
4. Shokrollahi, S., Adel, F., Ahmadian, H.: An investigation into the accelerometer mounting effects on signal transmissibility in modal measurements. Sci. Iran. **24**(5), 2436–2444 (2017)
5. Maierhofer, J., Gille, M., Rixen, D.J.: Thoughts on automatic impulse hammer parameters and sensor fixation methods. In: Sensors and Instrumentation, Aircraft/Aerospace and Dynamic Environments Testing, vol. 7, pp. 93–101. Springer (2023)
6. Colombo, S., Giannopoulos, A., Forde, M.C., Hasson, R., Mulholland, J.: Frequency response of different couplant materials for mounting transducers. NDT E Int. **38**(3), 187–193 (2005)
7. Blaschke, P., Schneider, S., Kamenzky, R., Alarcón, D.J.: Non-linearity identification of composite materials by scalable impact modal testing. In: Sensors and Instrumentation, vol. 5, pp. 7–14. Springer (2017)
8. Hoffmann, K.: Practical Hints for the Installation of Strain Gages, vol. 56. Hottinger Baldwin Messtech. GmbH (1996)

Chapter 8
Iterative Learning Control Based on Force Measurements for Automatic Impulse Hammers

Johannes Maierhofer and Daniel J. Rixen

Abstract Automatic impulse hammers have proven their advantages in experimental testing. Up to now, adjusting the resulting peak force is a cumbersome hand-tuning of the parameters of the hammer electronic. As the hammer is equipped with a high-quality force sensor anyway, the idea is close to utilize that force sensor signal to control the hammer. Usually these sensors are ICP-Sensors that are directly connected to the data acquisition system that is used to perform the desired measurements. This contribution shows a way to interpose the controller of the hammer and so allow the usage of the measured force. This is used in combination with an iterative learning control scheme to find the best parameters to achieve the desired impact force on the structure in a repeatable and convenient way.

Keywords Testing equipment · Automatic modal hammer · AMimpact · Non-linear testing · Experimental dynamic

8.1 Introduction

As topics like non-linear joint identification come into the focus of research, new methods need to be found to measure non-linear structures with reasonable effort in the lab. This contribution shows how the automatic modal hammer can be a useful system in the toolbox of experimental vibration measurement techniques.

Automatic modal hammers are coming more and more in structural dynamic labs. They have proven their advantages in experimental testing [7–9]. A major fraction of the lab time arises from the cumbersome hand adjustment of the parameters to achieve the desired peak force by still maintaining a single stroke impact. As the hammer is equipped with a high-quality force sensor anyway, this contribution shows a way to branch off the hammer's force signal and utilize it for the automatic setting of the parameters.

For demonstration purposes, the automatic hammer with an implemented force controller, cf. Fig. 8.1a, is investigated in combination with a non-linear system, a clamped-clamped beam with prestress, cf. Fig. 8.1b.

8.2 Automatic Hammer System Description

The automatic modal hammer *AMimpact* relies on the principle of a linear magnetic actuator to excite mechanical structures. The used actuator is built from an axis symmetric coil, the movable bolt, and a ferromagnetic housing. The magnetic force arises from the so-called reluctance forces which aim to minimize the magnetic energy stored in the system under actuation. This is achieved by designing an air-gap between the high permeability ferromagnetic material of the bolt and the housing such that minimizing the air-gap results in a forward driving force. The actuator is controlled by a microcontroller and corresponding power electronics.

J. Maierhofer (✉) · D. J. Rixen
Chair of Applied Mechanics, TUM School of Engineering and Design, Technical University of Munich, Garching, Germany
e-mail: j.maierhofer@tum.de; rixen@tum.de

M. Allen et al. (eds.), *Special Topics in Structural Dynamics & Experimental Techniques, Volume 5*,
Conference Proceedings of the Society for Experimental Mechanics Series, https://doi.org/10.1007/978-3-031-37007-6_8

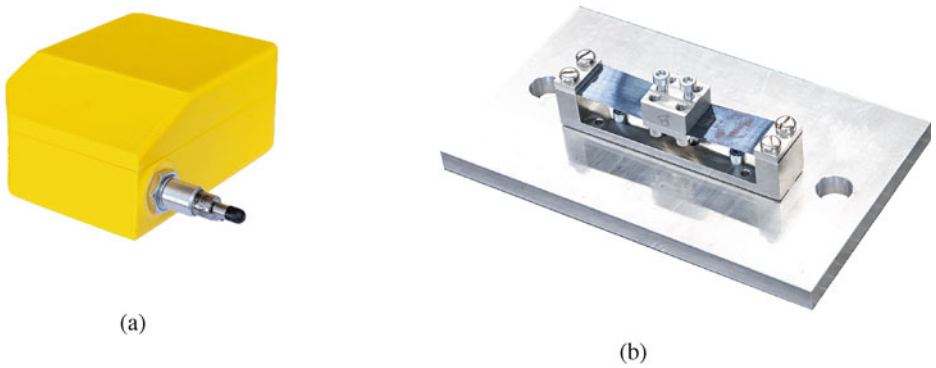

Fig. 8.1 *AMimpact* and the investigated non-linear beam structure. (**a**) Automatic impulse hammer *AMimpact* with attached PCB force sensor. (**b**) Clamped-clamped beam as non-linear structure

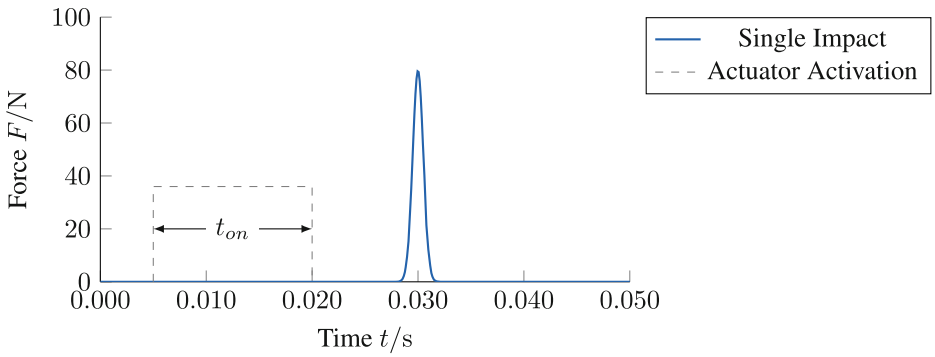

Fig. 8.2 Schematic operating principle: the impact happens after the acceleration phase, which is controlled with the voltage and the on-time

8.2.1 Operating Principle

The principle of operation is as follows: a supply voltage of 24 V or 36 V is generated to drive the coil, modulated by a transistor. During the *on-time* t_{on}, the bolt accelerates forward towards the structure. A short distance before the contact of the bolt with the structure, the current is shut off. Now, the bolt impacts the structure and is then retracted using a spring. The symbolic plot in Fig. 8.2 shows the relevant quantities and relations.

Using an automated modal hammer is often considered to avoid so-called double impacts. Double impacts are an unwanted phenomenon for many applications, but with classical hand hammering they are often only hard to avoid. For the automated modal hammer, there are two constellations which are responsible for double impacts or even worse, a series of fast repeating impacts. The most important risk for multiple impacts comes from the control parameters. A double impact will happen for the case that the forward force is still active although the impact already occurred. Due to the mainly elastic coefficient of restitution, the bolt has a velocity from the structure away, but the driving force will accelerate the bolt towards the structure again, and a second impact is imminent, cf. Fig. 8.3. Due to the relatively small mass of the hammer, the cycle time is very short, and a series of decreasing impacts can be the consequence.

A second constellation can arise from the dynamics of the structure in relation to the dynamics of the hammer itself. Further information on this effect and the general influence of double impacts can be found in [9].

8.2.2 Force Measurement

An important extension to the described automated system is the implementation of a fast force measurement into the hammer controller. With this the information about the impact is directly available in the controller software and can be used for the quality assessment of the previous impact as well for the parameter adapter of the upcoming impact. The force sensor used is the dismounted head of the *PCB, model 086E80*.

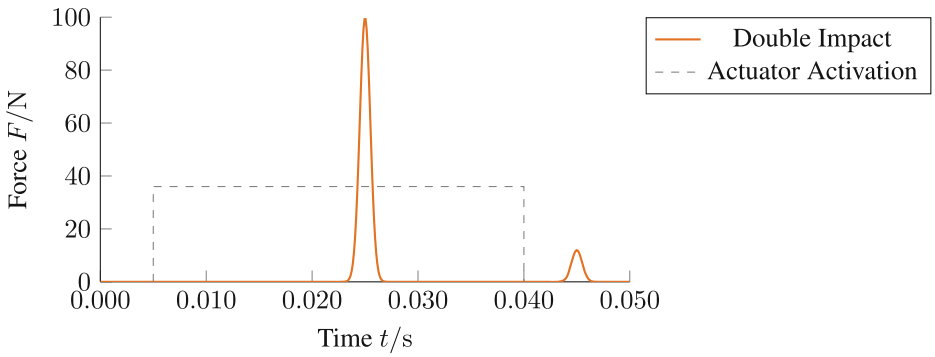

Fig. 8.3 Double impacts or a series of impacts occur for the on-time being too long

(a) (b)

Fig. 8.4 Prototype hardware with the dominant capacitor where the energy for the impulse is stored. (**a**) Top. (**b**) Bottom

Hardware To capture the force signal of the ICP-Piezo-Sensor without disturbing the signal, an operational amplifier is used as voltage follower. A voltage divider followed by a second voltage follower conditions the signal to the range 0 V to 3.3 V of common microcontrollers. For this contribution, a Raspberry RP2040 and its built-in 12 bit Analog-Digital-Converter (ADC) is used (Fig. 8.4).

Software The microcontroller software is implemented in MicroPython [10]. The advantage of using MicroPython is the good readability and easy but powerful syntax of Python. A fast sampling rate of the ADC is achieved by using the RP2040s Direct Memory Access (DMA) capabilities which means that the ADC writes the acquired samples directly into the memory of the controller. From there, the user program can read the values without time critical requirements. This decouples the fast real-time process of data capturing from the high-level logic of the software. This leads to a maximum sampling rate of 500 kHz for 2000 samples.

Measurement Data Two raw measurement data sets are captured with the adjustable test setup as seen in Fig. 8.5a. The results are shown in Fig. 8.5b. The first data set stems from a desired single impact, and the second from a double impact. The shown data are neither filtered nor cut. The blue force curve shows the maximum force that is achievable in the given setup without double impact. The activation of the actuator stops just right before the impact. The orange curve was produced by the permanently activation of the actuator. The impact happens a short time earlier and has a slightly higher value as the bolt is accelerated the complete travel distance. But, a second impact happens after the bounce back and again forward acceleration cycle.

To find the appropriate parameters for the desired impact force profile, more mechanical parameters have to be considered. It is the material pairing between the force-sensor-tip and the target, the mass of the hammer, and the retracting spring. More information on these parameters and their influence can be found in [7].

8.2.3 Repeatability Study

To check the repeatability of the system setup, an experimental test rig was built where the actuator can be positioned with a determined distance to the impact target. In this test-rig three series of force level with two different supply-voltages are

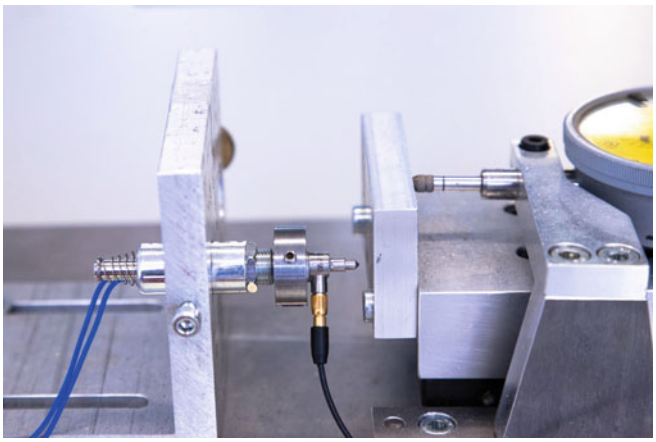

(a)

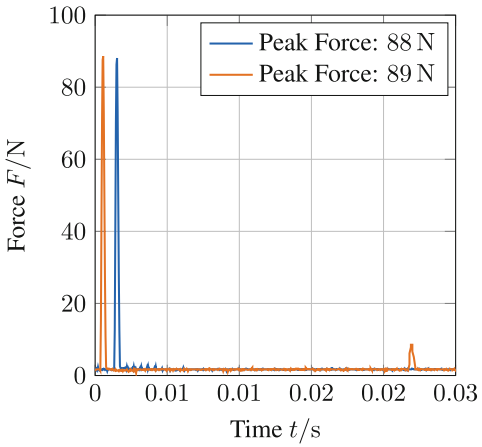

(b)

Fig. 8.5 Test setup to investigate impacts and the force measurement in a controlled manner. (**a**) Test rig to perform force measurements under stable conditions. (**b**) Force measurement with single and double impact. Material pairing: steel tip against aluminum plate. Sampling rate 25 kHz

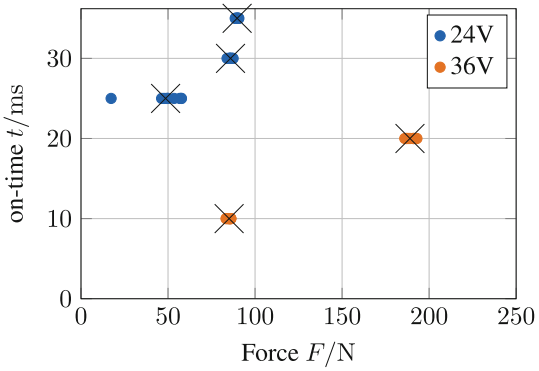

(a)

voltage	t_{on}	μ	σ
24V			
	20ms	48N	11N
	25ms	85N	1N
	30ms	90N	1N
36V			
	10ms	85N	1N
	15ms	192N	1N

(b)

Fig. 8.6 Repeatability result summary. (**a**) Peak forces for different sets of parameters. (**b**) Mean μ and standard deviation σ forces for tested settings

tested with 10 iterations. The results are shown in Fig. 8.6. Besides one outlier in the low force test series, the repeatability is very high and consistent.

The biggest unknown leading to the main part of the deviation is the stick-slip effect between the bolt and its housing. The later the bolt gets into motion, the less is the kinetic energy which results in a lower force. For the higher voltage, this effect becomes less relevant as the force is higher right in the beginning. Also for higher on-times, the effect becomes more irrelevant in terms of relation to the whole kinetic energy.

8.3 Dynamic Model Description

To simulate the dynamics of the impulse hammer, a very simple minimal model is constructed. The moving part of the actuator is assumed to be a 1-dof rigid mass with three applied forces: a very soft retaining spring, a constant friction force, and the driving force from the magnetic field. The driving force is modeled as linear proportional to the current in the coil. The electric circuit consists of an inductivity and a resistor in series. The voltage is controllable from the electronics, so it can be seen as the given input. The target structure is also implemented as single dof system. The contact point is approximated using the Hertzian theory (Fig. 8.7).

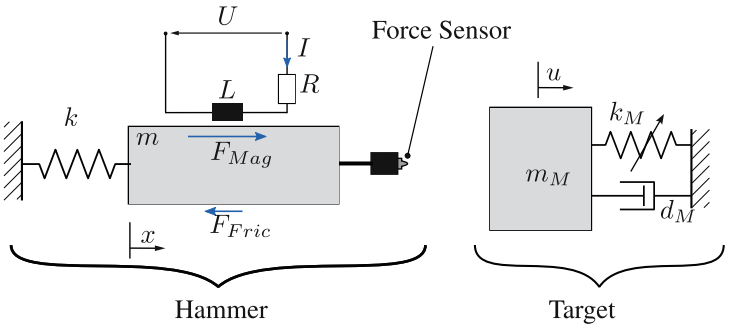

Fig. 8.7 Minimal model of the hammer as rigid body and a 1-dof non-linear target structure

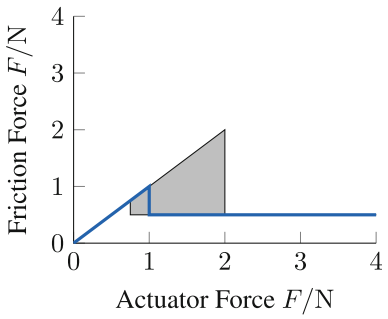

Fig. 8.8 Schematic friction model with variation in the static friction force

The simulation of the presented model is performed using Python in combination with NumPy, SciPy and was parametrized by hand to fit the experimental data qualitatively.

Friction The friction force is assumed to follow the Coulomb friction law. As there is no meaningful normal force, two forces are assumed for the static and kinetic friction. By previous experiments, the randomly changing static friction force was determined as the most unknown in the setup. This range is represented as gray area in Fig. 8.8.

Hertzian Contact The implemented Hertzian formula to compute the contact stiffness $k_{Contact}$ and damping $c_{Contact}$ is calculated with an assumed fixed force F. For the following simulations, standard material parameters for the steel tip and aluminum target are chosen. The radius r of the force sensor tip is assumed as 0.5 mm. The mixed Young's modulus calculates as

$$E = \frac{1}{\frac{1-\nu_{hammer}^2}{E_{hammer}} + \frac{1-\nu_{target}^2}{E_{target}}} \tag{8.1}$$

The penetration depth is computed from

$$t = \left(\frac{3F}{4E\sqrt{r}}\right)^{\frac{2}{3}}. \tag{8.2}$$

From the penetration depth, the stiffness and a damping can be derived. The damping represents the loss during the impact phase due to plasticity.

$$k_{Contact} = \frac{4}{3}E\sqrt{rt} \tag{8.3}$$

$$c_{Contact} = 0.005\sqrt{k_{Contact}} \tag{8.4}$$

This approach is very simple and gives a good estimation of the expected force, although the contact mechanic part is the one with the most potential to build a more sophisticated model to gain a deeper insight of the impact.

8.4 Iterative Learning Control

In literature, the iterative learning controller (ILC) is considered a special case of a closed-loop control unit. The ILC combines the techniques of a feedforward and a signal feedback. While the improvement process of the ILC signal from one run to the next is enabled by feedback, the signal of a single run is implemented by feedforward.

8.4.1 Theory

When using an ILC, it is assumed that observations from previous experimental runs contain results that can be used to improve the performance of future runs [1, 2]. Figure 8.9 shows the evolution of signals over time over several runs. The controlled system generates an output signal y_k, depending on the incoming system input variable u_k. As usual, the output variable y_k of the controlled system should follow a desired reference variable w. The control error ε_k is calculated as the difference of these two quantities. The input signal to the ILC is not only the current control error, but also the deviations $\varepsilon_0 \dots \varepsilon_{k-1}$ of all previous runs, together with the current system input u_k. Using this information, the ILC calculates a new variable u_{k+1} that is intended to minimize the control deviation. In reality, both the controlled system and the signals that occur are subject to measurement noise, which is not shown in Fig. 8.9 for the sake of clarity. Of central importance for the correct control of the system is the convergence of the ILC loop after a finite number of learning loops. The convergence of the ILC is also referred to as the stability of the learning control [2]. The design of iterative learning controls is particularly simplified for pass-invariant systems, which can also be described as time-invariant systems in the pass domain. For these types of systems, mutable behavior is possible during a single run as long as this behavior is invariant over all runs [2]. In Fig. 8.9, the reference variable w is run-invariant, as indicated by the missing index k. Thus, the reference variable is described as a constant in the pass-through domain.

Force Controller The force cannot be controlled prior to contact with the test structure, unlike energy, which depends solely on the mass and velocity of the impact hammer. To calculate an impact force, detailed knowledge of impact parameters such as the coefficient of restitution e and the contact duration of the impact partners is required. Therefore, an ILC was implemented to automatically introduce a desired force into the test structure. The excitation force determined by the ICP-

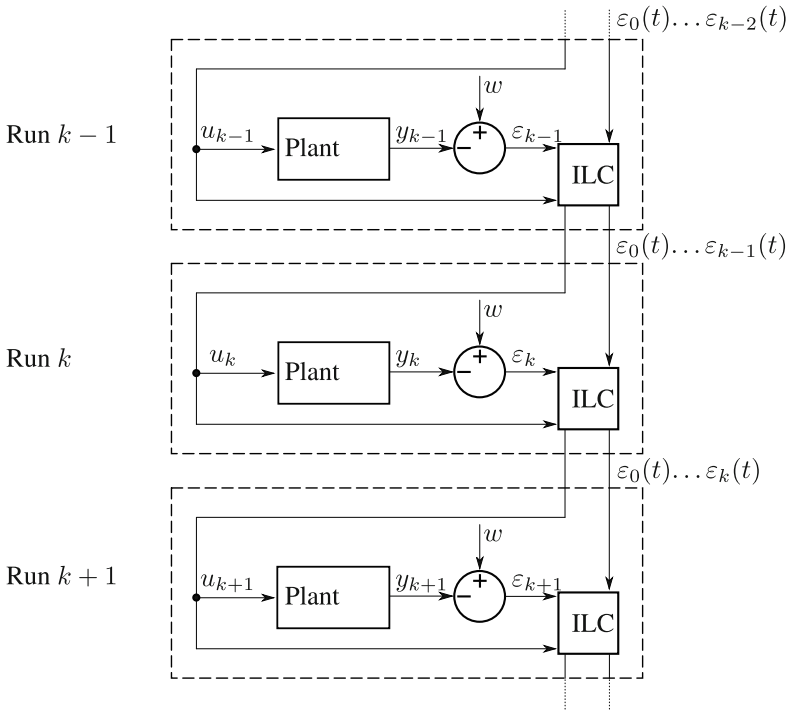

Fig. 8.9 Signals of an iterative learning control according to [2]

sensor is compared with the required force. The control deviation is used to calculate a new signal, similar to the PID controller, considering proportional, integral, and derivative components. In this case, the system input u represents the on-time t_{on} of the actuator at a given voltage.

$$u_{k+1} = u_k + K_p \varepsilon_k(t) + K_i \int_0^t \varepsilon_k(\tau)\, \mathrm{d}\tau + K_d \frac{\mathrm{d}\varepsilon_k(t)}{\mathrm{d}t}. \tag{8.5}$$

The peculiarity of calculating the system input for the following run is that the system input of the current run serves as the basis of the calculation (cf. Eq. 8.5). As already stated, the input signal ensures that the force deviation is reduced in the following pass of the ILC. After adjusting the input variable, the next ILC loop begins from the hammer's initial position at the rear end of the housing. It is important to ensure that each loop starts from the same point to fulfill the assumption of run in-dependency.

By iteratively adjusting the feed forward signal, the system converges to the reference force. For this purpose, a tolerance interval is also defined. If the applied force is within defined limits away from the required force, the excitation stroke was successful, and the program exits the iterative learning loop.

8.4.2 Simulation of the ILC

A simulation was used to illustrate the operation of an iterative learning control system. The impulse hammer simulation computes the maximum force during an impact using the previously sketched approach. The excitation force depends on several variables: the current trajectory of the electromagnetic actuator as well as the material properties of the test structure. The learning control influences the force input over the length of the period in which the electromagnet is supplied with current. Figure 8.10 illustrates the processes within the simulated actuator. At the beginning of the excitation stroke, the given voltage is applied. The current approaches the maximum current exponentially due to the inductivity of the coil. After the time t_{on}, which is set by the ILC-Algorithm, the voltage is turned off. The bolt moves ballistically towards the test structure due to its inertia. Also marked in the figure is the period during which the hammer is in contact with the test structure. During this short interval, at about 24 ms, the calculation of the excitation force is valid, and the maximum peak force is fed back into the ILC algorithm.

Figure 8.11 illustrates that the force input of the impulse hammer converges toward the desired force magnitude even with different operating voltages that are not ideally chosen. The required force of the excitation stroke was set to 200 N as an example, with an additional tolerance interval of ±2 N defined, within which a performed impact is also considered successful. The on-time of the electromagnet at the beginning of each ILC simulation was 10 ms, which explains the different force amplitudes at the first iteration.

The picture in Fig. 8.12 becomes more complicated for a fixed voltage, but a randomly changing static friction coefficient. This breaks the assumption of the ILC that each pass is invariant except the control variable. The static friction force is varied randomly from 0.5 N to 1.5 N for each impact simulation.

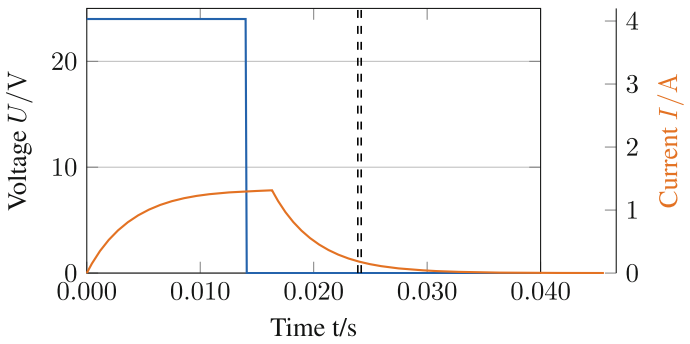

Fig. 8.10 Curve of voltage and current during a single run of an exemplary ILC loop. The vertical lines indicate the moment the force tip is in contact with the structure

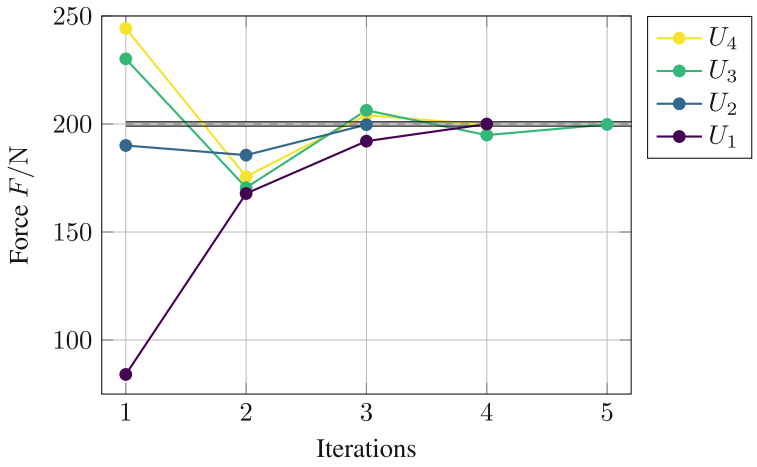

Fig. 8.11 Convergence behavior of the simulated peak force during an ILC cycle for different input voltages $U_1 < U_2 < U_3 < U_4$

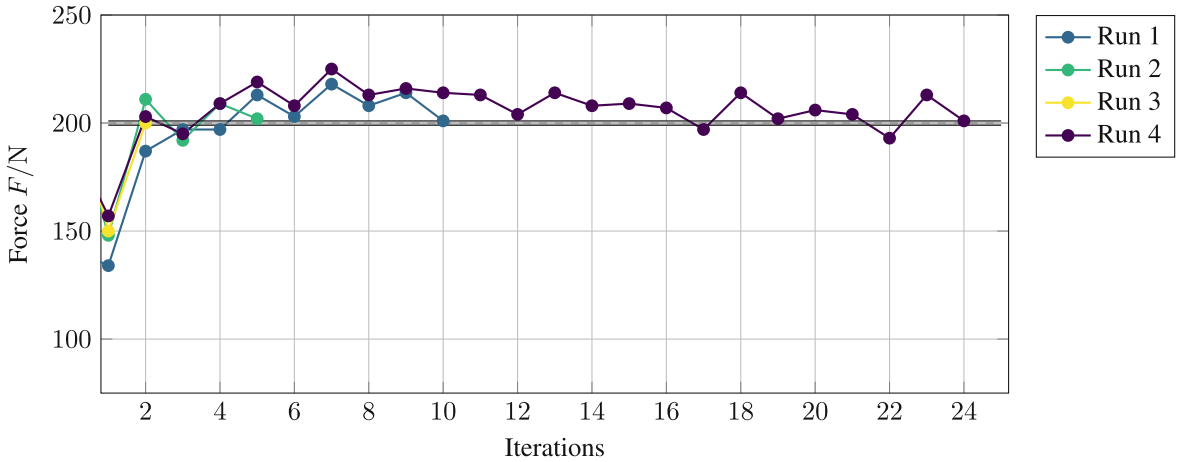

Fig. 8.12 Convergence behavior for randomly changing friction coefficients for each impact

8.4.3 Experimental Results

The experimental results are conducted in the same manner than the simulated ones. The voltage and all parameters are kept constant, and a series of ILC-runs are performed. Figure 8.13 shows a convergence that is in the range, expected from the simulations. The major uncertainty, as already showed in the simulation, is the stick-slip effect in the magnetic actuator. But it is even less pronounced than in the simulation assumed.

8.4.4 Discussion

The shown simple control mechanism can already provide a significant improvement in the handling of an automatic modal hammer. Exploiting the fact that the systems properties do not change between each impact, more advanced algorithms in combination with physical informed neuronal networks seem promising. With that method it should be possible to identify the unknown but deterministic properties, like the coefficient of restitution and the distance between hammer and structure. This could lead to new virtual measurements, for example, the transmitted energy during one impact. From this, a new reference value for the ILC-Controller could raise. Especially for non-linear joint identification, this could bring new moments in the experimental lab. These joints behave different for different levels of activation. It is not yet clear which kind of activation measure is helpful.

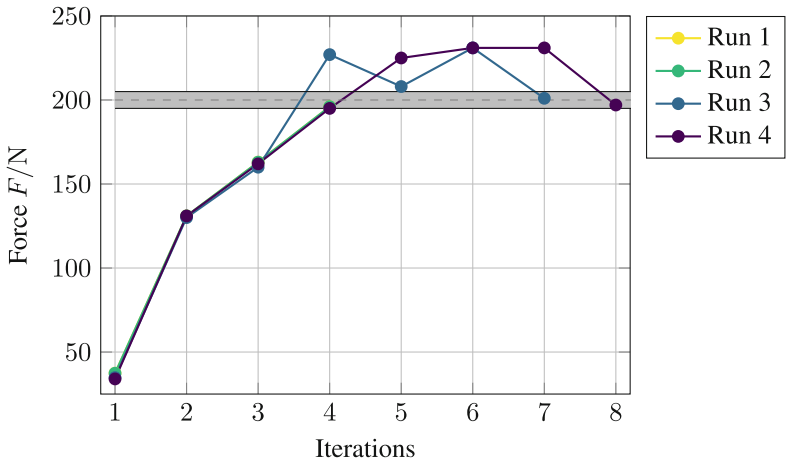

Fig. 8.13 Convergence plot for experimental data with constant 36 V supply voltage. The runs are sorted by their length of iteration. Further runs kept in the range of the exemplary showed runs

(a) (b)

Fig. 8.14 Experimental setup of non-linear clamped-clamped beam with pre-stress. (**a**) Clamped-clamped beam with a central mass mounted in a steel c-shaped frame. (**b**) Test Rig with impulse hammer positioned to the central point of the mass

8.5 Experimental Showcase: Nonlinear Structure

A rather exotic example of non-linear structural systems are music instruments, here mallet percussions, where the desired tones are produced by impacting vibration plates with mallets. The strength of the impact forms the sound due the non-linear nature of the system [3]. For quality testing, a repeatable and controllable force impact could be useful.

To demonstrate one use case where the impact force amplitude is important to know, an academic benchmark system with a clamped-clamped beam is set up. The beam is excited with impacts of increasing force amplitude, and the acceleration is measured.

8.5.1 System Description

A steel clamped-clamped beam is mounted with pre-stress (due to a thermal mounting procedure) to a C-shaped steel carrier. In the middle of the beam, a solid steel block is attached. The carrier is attached to an aluminum ground plate, cf. Fig. 8.14. The system was built by [5] to investigate non-linear joint dynamics in the coupling and decoupling analysis. The design is such that the system shows strong non-linear behavior in the low frequency range. [5] reports frequencies of around 28 Hz, 54 Hz, and 76 Hz for the first three resonances.

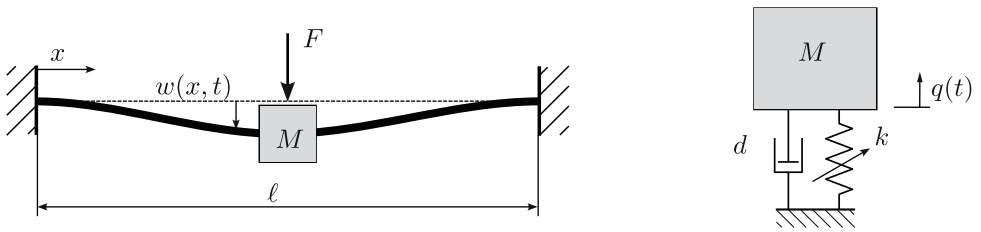

Fig. 8.15 Clamped-clamped beam with mass, modeled as single dof Duffing oscillator

8.5.2 *Duffing Oscillator Minimal Model*

The investigated system of a clamped-clamped beam with pre-stress and an additional mass in the middle can be described in approximation by the so-called *Duffing Oscillator* model with one degree of freedom, as visualized in Fig. 8.15. The Duffing equation (famous through Georg Duffing, a German engineer) describes a non-linear oscillator with a cubic stiffness term. Detailed information on the Duffing oscillator and the different solution approaches can be found in [4].

Deriving the partial differential equation of motion for a beam with pre-stress T_S for $w(x,t)$ leads with the commonly known quantities to:

$$\rho A \frac{\partial^2 w}{\partial t^2} + EI \frac{\partial^4 w}{\partial x^4} - \left(T_S + \frac{EA}{2\ell} \int_0^\ell \left(\frac{\partial w}{\partial x} \right)^2 \mathrm{d}x \right) \frac{\partial^2 w}{\partial w^2} = f(x,t) \tag{8.6}$$

Equation 8.6 is written without the added mass M. The mass is added as a point mass in the approximation. To find a single dof approximation, a Rayleigh-Ritz approach is chosen with an ansatz of:

$$\phi(x) = \sin(\frac{\pi x}{\ell}) \tag{8.7}$$

Separation of space and time, and integration over the beam length to minimize the approximation error, the following equation of motion is found:

$$(M+m)\ddot{q} + k_1 q + k_3 q^3 = F(t) \qquad \text{with:} \quad m = \frac{\rho A \ell}{2}, \quad k_1 = \frac{EI\pi^4}{2\ell^3}\left(1 + \frac{T_S \ell^2}{EI\pi^2}\right), \quad k_3 = \frac{EA\pi^4}{8l^3} \tag{8.8}$$

Note that the pre-stress only affects the linear stiffness. The positive cubic stiffness leads to a hardening of the systems for large deflections.

The general Duffing equation for the free-vibrating system without damping writes as:

$$\ddot{q} + \alpha q + \gamma q^3 = 0 \qquad \text{with:} \quad \alpha = \frac{k_1}{M+m}, \quad \gamma = \frac{k_3}{M+m} \tag{8.9}$$

where it unveils a hardening character for $\alpha > 0$ and $\gamma > 0$. After some advanced algebraic derivations, considering only the first term of the expansion of the exact analytical solution, the resonance frequency simplifies to [4]:

$$\Omega(Y) = \sqrt{\alpha + \frac{3}{4}\gamma Y^2} \qquad \text{with:} \quad Y := \text{peak amplitude} \tag{8.10}$$

This equation describes the resonance frequency shift due to the non-linear cubic stiffness for higher amplitudes.

Analytical Results For the given system, the added mass is $M = 137\,\mathrm{g}$ in contrast to 7 g of the full sheet metal. The linear beam stiffness (without tension) is $k_0 \approx 100\,\mathrm{N\,m^{-1}}$, so the linear stiffness is very much determined by the pre-stress tension. It also becomes clear that the beam without pre-stress would snap-through as of the low linear stiffness. A temperature difference of $\Delta T = 50\,\mathrm{K}$ during the mounting process leads to a resulting linear (i.e., $Y = 0$) resonance frequency of $f_0 = 75\,\mathrm{Hz}$. This result holds only under the assumption that the c-shape is rigid which is not true for high pre-stress values. Because of that, the c-shape was separately modeled as a beam and the static stiffness for the closing-shape determined to

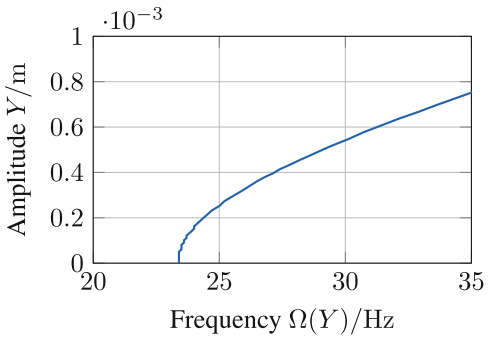

Fig. 8.16 Frequency shift for the Duffing oscillator with given, theoretical values

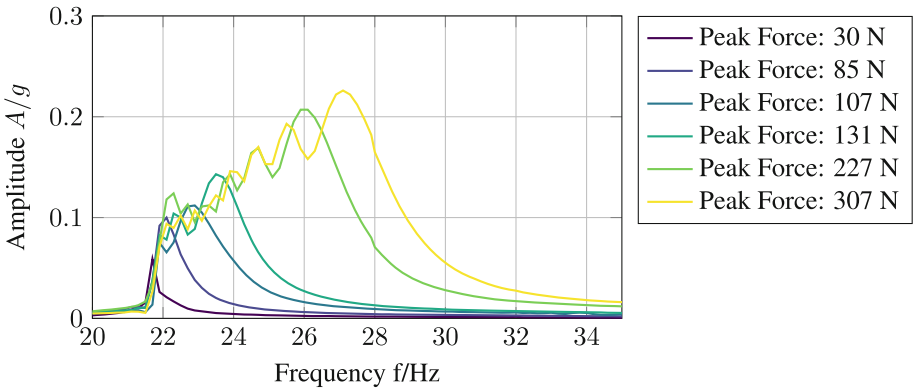

Fig. 8.17 Excerpt of the FFT of full response time signal ($T = 5\,\mathrm{s}$)

$k_{C-shape} \approx 1 \times 10^6\,\mathrm{N\,m^{-1}}$. This leads to a realistic, remaining pre-stress of $T_S = 70\,\mathrm{N}$. From there on, the linear resonance frequency is $f_0 = 24\,\mathrm{Hz}$. The computed frequency-amplitude relation from Eq. (8.10) is plotted in Fig. 8.16.

8.5.3 Experimental Results

For the experimental analysis, the beam structure is mounted in a vertical position to eliminate gravity effects on the mass as well as on the impulse hammer. An acceleration sensor is glued on the backside of the block mass. The frontside is excited in a central position with the impulse hammer, cf. Fig. 8.14b.

The time signals for the impulse and the response are recorded at 20 kHz for 5 s. As seen from the previous considerations, a frequency increase for higher amplitudes is expected. Although not meaningful in a quantitative sense, the fft of the time signal is taken for the increasing levels of excitation and visualized in Fig. 8.17. Increasing amplitudes lead to higher resonant frequency, but at the same time the peak becomes more blurry as the decay of the signal is more pronounced which lets the frequency fall again with the decay of amplitude over time. The result is considered to be very close to the analytical model Fig. 8.16.

The transient decay response of the systems contains all information about the frequency change of the dynamical system. To assess the non-linear behavior, so-called backbone curves are computed. The backbone curve indicates the relation of resonant frequency and amplitude for the free vibrating system. There are different methods available to calculate backbone curves from decay responses [6]. For this work, a qualitative look at the spectrogram in Fig. 8.18 is given. For that, the system is excited with the strongest impulse (peak force 307 N) possible, and the signal is recorded for 5 s. The system shows the typical stiffening effect that is expected from a clamped-clamped beam. The values from the spectrogram even fit better to the values calculated for Fig. 8.16.

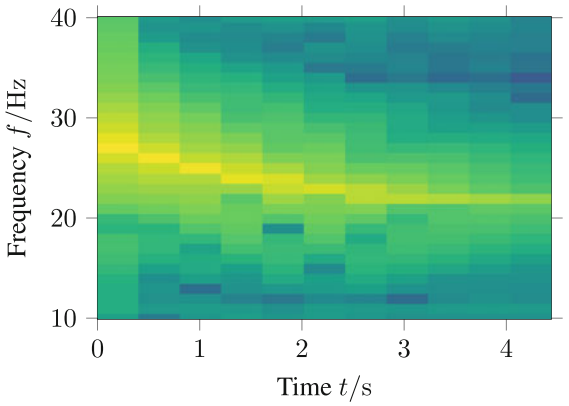

Fig. 8.18 Spectrogram for the first resonance frequency

8.5.4 Discussion

The Duffing oscillator has the property of overlaying backbone curves for different levels of force. This means every decay response will lead to the same backbone curve no matter from which force amplitude the system was excited. This pleasant behavior is not representative for joints, like bolted connections. For those systems it is crucial to excite them at the same level of force to generate signals that can be averaged or to compare different systems.

8.6 Summary

This contribution shows the implementation of a force data acquisition into the controller of the automated modal impact hammer. This allows us to evaluate the previous impact and draw conclusions for the parameters of the next impact. With the hereby closed feedback loop, iterative controllers are possible. The first implemented PID-strategy shows promising results, but there are many extensions possible. Also, the possibility of iterative learning controllers and the integration of neural networks is discussed but not implemented. With the newly created possibility to automatically perform a series of impacts with increasing forces, structures can be tested to see if a linear assumption is valid.

In the second part, an academic non-linear clamped-clamped beam structure is simplified to a single-dof Duffing oscillator. From that, the amplitude-dependent frequency is computed and compared with experimental data. With the automatic controlled impulse hammer, a series of measurements could be generated in the laboratory with very little effort.

Finally, two main points can be found as the main advantages of the recent AMimpact implementation: First, a consistent level of force is crucial to get meaningful linearization when FFT-based techniques are used on slightly non-linear systems. Second, a consistent level of force is necessary to activate nonlinearities in a similar manner from system to system for comparison purposes.

References

1. Bristow, D.A., Tharayil, M., Alleyne, A.G.: A survey of iterative learning control. IEEE Control Syst. Mag. **26**(3), 96–114 (2006). https://doi.org/10.1109/MCS.2006.1636313
2. Dijkstra, B.G.: Iterative Learning Control, with Applications to a Wafer-Stage. Ph.D. thesis, Delft University of Technology, The Netherlands (2004)
3. Jossic, M., Roze, D., Hélie, T., Chomette, B., Mamou-Mani, A.: Energy shaping of a softening Duffing oscillator using the formalism of Port-Hamiltonian Systems. In: 20th International Conference on Digital Audio Effects (DAFx-17). Edinburgh, UK (2017). https://hal.archives-ouvertes.fr/hal-01569873
4. Kovacic, I., Brennan, M.J. (eds.): The Duffing Equation. Wiley, New York (2011). https://doi.org/10.1002/9780470977859
5. Latini, F., Brunetti, J., D'Ambrogio, W., Fregolent, A.: Identification of normal modes of a set of strongly nonlinear springs. In: Material Research Forum Proceedings, Thomas Wohlbier (to be published) (2022)

6. Londoño, J.M., Neild, S.A., Cooper, J.E.: Identification of backbone curves of nonlinear systems from resonance decay responses. J. Sound Vib. **348**, 224–238 (2015). issn:0022-460X. https://doi.org/10.1016/j.jsv.2015.03.015. https://www.sciencedirect.com/science/article/pii/S0022460X15002333
7. Maierhofer, J., Gille, M., Rixen, D.J.: Thoughts on automatic impulse hammer parameters and sensor fixation methods. In: Sensors and Instrumentation, Aircraft/Aerospace and Dynamic Environments Testing, vol. 7, pp. 93–101. Springer International Publishing (2022). https://doi.org/10.1007/978-3-031-05415-0_9
8. Maierhofer, J., Mahmoudi, A.E., Rixen, D.J.: Development of a low cost automatic modal hammer for applications in substructuring. In: Conference Proceedings of the Society for Experimental Mechanics Series, pp. 77–86. Springer International Publishing (2019). https://doi.org/10.1007/978-3-030-12184-6_9
9. Maierhofer, J., Rixen, D.J.: Development of an Electrodynamic Actuator for an Automatic Modal Impulse Hammer, pp. 189–199. Springer International Publishing (2020). https://doi.org/10.1007/978-3-030-47630-4_18
10. Micropython ulab v5.1: (2022). https://github.com/v923z/micropython-ulab

Chapter 9
Experimental Slug Flow-Induced Fluid–Structure Interaction of a Pressurized Flexible Pipe

Graeme Hunt, David Pickles, Andrea Cammarano, and Gioia Falcone

Abstract An experimental study into the fluid–structure interaction of gas–liquid flows as they pass through a pipeline riser, like those utilized in the oil and gas industry, was carried out. In this study, a 10-m-long pipe with inner diameter of 50 mm at 10 bar (gauge) pressure was used with operating fluids of water and nitrogen. A two-phase flow regime diagram is used to determine liquid and gas volume flow rates that fall within the slug flow regime, and this was further refined using PETEX GAP and finally CFD software, STAR-CCM+, to determine the experimental test matrix. Axial strain gauges were positioned close to the flanges at the ends of the riser to measure strain at the cardinal points of the pipe at both the top and bottom of the riser. At approximately 2 m and 3 m horizontal distance from the entrance to the riser, accelerometers were attached to monitor the motion of the pipe at these positions. The motion of the pipe was observed to be almost exclusively in-plane, with only small out-of-plane motion registered on the accelerometers. Strain gauge measurements demonstrated that the increase in mass flow rate of the liquid phase/decrease in mass flow rate of the gas phase served increases the mean values of stain at both the entrance and exit of the riser. A monotonic increase in the magnitude of the rms of the fluctuations of the strain was observed for an increase in the flow rate of either the liquid or the gas phase. The highest flow rates tested introduce an irregular cyclic whipping motion in the flexible pipe in addition to the smooth oscillation motion.

Keywords Multiphase flow · Flow-induced vibration · Slug flow · Fluid · Structure interaction · Experiment

9.1 Introduction

Two-phase, gas–liquid flows are frequently observed in a variety of industrial processes, including sewage systems, power and processing plants, and pipelines conveying oil and gas prior to separation. Depending on the operating conditions of the system, the flow may fall into one of several flow regimes, some of which can lead to mechanical failure. A number of accidents have been reported as a result of vibration from flow-induced vibration (FIV) [1]. While several multiphase flow regimes exist, not limited to two phases, the focus of the study presented herein is that of two-phase gas–liquid slug flow. Liquid slugs are initiated and developed due to three main slugging mechanisms, and these are hydrodynamic slugging, terrain slugging, and severe slugging [2]. Due to safety concerns, the severe slugging regime is not included in this study. While a significant number of studies, both experimental and numerical, have been conducted upon multiphase flow in horizontal and vertical pipes, studies on inclined pipes and curved pipes are less frequent. However, in real-world industrial applications, many pipes are influenced by the terrain [3, 4] or industrial necessity such as risers from subsea to floating rigs [1]. In pipe structures, especially those involving curvature, such as U-bends, risers, and 90° bends, for example, the forces acting on the structure tend to fluctuate. This is due to the large difference in material properties, whereby the sudden change in the fluid density in the slug unit changes the momentum. The fluctuating force produced by this induces the structural vibration imposed on the structure by the fluid, which produces the flow-induced vibration observed in such pipes. Given this information, it is unsurprising that slug flow is known to produce significant vibration when compared to other multiphase flow regimes [5]. Conditions such as this are experienced in a variety of engineering applications such as oil pipelines, chemical systems, and the nuclear industry [6–8]. In addition to vibrations induced by the flow, slug flow can also be responsible for corrosion due to high slug frequency causing failure of protective coatings in pipelines [9].

G. Hunt (✉) · D. Pickles · A. Cammarano · G. Falcone
James Watt School of Engineering, College of Science and Engineering, University of Glasgow, Glasgow, UK
e-mail: graeme.hunt@glasgow.ac.uk

M. Allen et al. (eds.), *Special Topics in Structural Dynamics & Experimental Techniques, Volume 5*,
Conference Proceedings of the Society for Experimental Mechanics Series, https://doi.org/10.1007/978-3-031-37007-6_9

There have been several studies on FIV in rigid pipes, with researchers studying different configurations such as 90° bends, T-junctions, and U-bends [10–13]. The work on both 90° bends and U-bends indicated the importance of void fraction on the excitation forces exerted by the flow on the structure [11–13] of churn/slug flow. Both the amplitude and the frequency measured for the force fluctuations were observed to increase with increased flow velocity for the volumetric flow rates studied [12]. Each of these studies confirmed that the effect was down to the flow regime rather than the specific value of the void fraction indicating that it is imperative that the two-phase flow regime is correctly identified for any such analysis of FIV [5].

A small-scale (4 mm inner diameter, 95 cm length) experiment was conducted upon a free-hanging flexible pipe using an air–water test loop [14]. Vibration displacement was monitored revealing that in-plane motion was generated by the slug flow within the pipe. It was found that the second-order mode provided the dominant response in the pipe structure and that the slug flow features such as slug length, ratio of gas to liquid phase, and superficial velocity influenced the amplitude of the observed vibration.

In the current study, a much larger scale was chosen with a greater inner diameter (ID) and a correspondingly increased length to maintain a large aspect ratio. This increased scale permitted the addition of accelerometers to determine the acceleration that a particular point undergoes during oscillations, such that the mass of these instruments was insignificant compared to that of the pipe and so was considered non-intrusive. Additionally, the larger circumference of the pipe permitted the addition of strain gauges to determine the strain that the pipe undergoes close to the flanges attaching it to the rigid sections. Such information is key to understanding the positions and directions of the strain in pipes undergoing FIV to limit the risk of a structural failure. Also as mentioned above, it was considered of key importance that the correct flow regime is identified in advance of the experimental setup such that the analysis may be carried out with confidence. This formed the motivation for the development of the test matrix using multiple techniques.

9.2 Experimental Procedure

9.2.1 Test Matrix Design

To ensure that slug flow characteristics were obtained, a comprehensive matrix of test points in and close to the slug regime was scoped. Limiting factors placed on the choice of test points in addition to the slug flow requirement were that the gas flow rate was greater than 5 m^3/hr as this was the lower limit to which gas flow was calibrated at the NEL facility and a flow rate of 2–5 ms^{-1} so that the flow did not pass through the 10 m riser too quickly. Based on these stipulations, suitable windows for gas and liquid flow rate were ascertained through the spreadsheet digitized from Shell DEP 31.22.05.11 [15], which are defined in terms of the respective superficial velocities. To reduce the number of candidate test points, the one-dimensional multiphase flow software package, Petroleum Experts (PETEX) General Allocation Package (GAP), was used. The J-riser was modeled by discretizing a quarter ellipse with major and minor axes of length 7.7 m and 5 m, respectively, to approximate the riser profile, which was not known in advance. A straight, horizontal region was added to permit flow development prior to entering the riser section. For the GAP simulations, the system was assumed to be rigid, so that suitable test points could be identified solely based on their predicted flow regime behavior. Those that did not meet the criterion of slug flow at the entrance to the riser were discarded.

Increased confidence in the achievement of slug flow entering the riser was required before undertaking the experiment given the scale of the experiment. This was provided by using the commercial computational fluid dynamics (CFD) package Star-CCM+ (version 15.04.010) to predict the flow type and additionally provide an indication of the slug length, velocity, and frequency. Again, the riser was modeled as a rigid structure and the same quarter ellipse geometry was applied for the purposes of flow regime prediction as shown in Fig. 9.1. Given that in the experiment, the 2″ straight development section would be preceded by a length of 6″ piping, and it was concluded that a flat-stratified inlet condition would not be a realistic representation. As such, it was deemed that a sinusoidal wave function be applied at the inlet to introduce an unsteady surface. This was achieved by the introduction at the inlet of a sinusoidal function to define the free surface level of the liquid phase as a function of time [16–18].

In this multiphase CFD analysis, a fluid and a gas phase are modeled using the volume of fluid method (VOF) [19]. This method can be used to model the flow of two immiscible fluids, one continuous and the other dispersed. Due to the sharp change from 1 to 0 experienced for the volume fraction at the interface between the two fluids, a specific treatment is required to resolve this issue because simple higher-order schemes would fail. This is accomplished in Star-CCM+ (15.04.010) using the high-resolution interface capturing (HRIC) scheme [20], which is based on a normalized variable diagram (NVD). The kω SST (Menter) [21] model was used model turbulence in the system. Since the two-phase slug flow is time-dependent, an

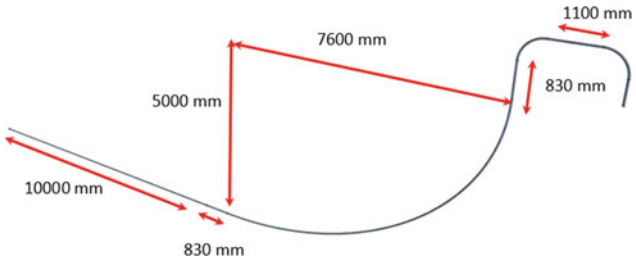

Fig. 9.1 CFD geometry of the riser and development region for flow prediction

Table 9.1 Flow rate and superficial velocities of test points

Test point number	Gas flow rate (Q_g) m^3/hr	Liquid flow rate (Q_l) m^3/hr	Gas superficial velocity (U_{sg}) ms^{-1}	Liquid superficial velocity (U_{sl}) ms^{-1}
SP1	18.3	0	2.5	0
SP2	9.6	0	1.3	0
SP3	7.3	0	1.0	0
SP4	5.5	0	0.75	0
MP1	7.3	10.9	1.0	1.5
MP2	5.5	14.5	0.75	2.0
MP3	18.3	14.5	2.5	2.0
MP4	5.5	10.9	0.75	1.5
MP5	7.3	14.5	1.0	2.0
MP6	9.6	14.5	1.3	2.0
MP7	18.3	5.5	2.5	0.75
MP8	18.3	4	2.5	0.6
MP9	18.3	3	2.5	0.4
MP10	15	3	2.0	0.4

implicit unsteady solver was used with a time step, $\Delta t = 0.0005$s. A total physical time of 30 s was employed to allow the slug flow to develop and stabilize. This timestep in conjunction with the cell size permitted the Courant number to be kept below 0.5 to minimize numerical diffusion.

Simulations were conducted on the test point matrix that GAP modeling indicated would produce slug flow at the inlet of the riser. An additional number of test points were rejected based on the CFD simulation results. Those failing to produce a satisfactory slug flow were excluded. Thus, finally a test matrix of ten multiphase test points (MP1–10) was produced with confidence that they would yield a slug flow in the experiment. Additionally, a series of single-phase (nitrogen) test points (SP1–4) were produced as a baseline with corresponding gas flow rates to those of the multiphase test points. A summary of various gas flow rates and liquid flow rates investigated is shown in Table 9.1. The locations of the test points on the flow regime map are shown in Fig. 9.2.

9.2.2 Experimental Setup

To assess the effect nitrogen/water slug flow has on the structure of a flexible "J"-Riser, a 10 m long Merlett Vacupress Cristal hose was installed in the TUV SUD National Engineering Laboratory's Advanced Multiphase Facility (AMF). The PVC hose has a galvanized steel spiral embedded within it and is reinforced with a polyester yarn. The pipe had a nominal internal diameter, ID = 2″, a burst pressure of 30 bar, a minimum bending radius of 170 mm, and weighed 1.6 kg/m. Stainless steel ASA150 flanges attached to both ends of the pipe allowed it to be hung freely between the rigid sections of the AMF test loop. The riser had a vertical drop of 5 m and a horizontal travel of 7.7 m. Upon pressurization, the pipe extended in length; therefore, to prevent sagging of the pipe, the first 2.3 m of the pipe was secured to a horizontal support. This ensured that this section of the pipe did not move and that the vertical drop and horizontal distance of the hose were not affected. A schematic diagram of the test rig installed in the AMF is shown in Fig. 9.3b.

The AMF can generate three-phase wet gas flows and multiphase flow in pressures between 10 and 140 bar. With a maximum gas flow rate of 3000 m^3/hr and a maximum liquid flow rate of 550 m^3/hr. For the purposes of this investigation, a

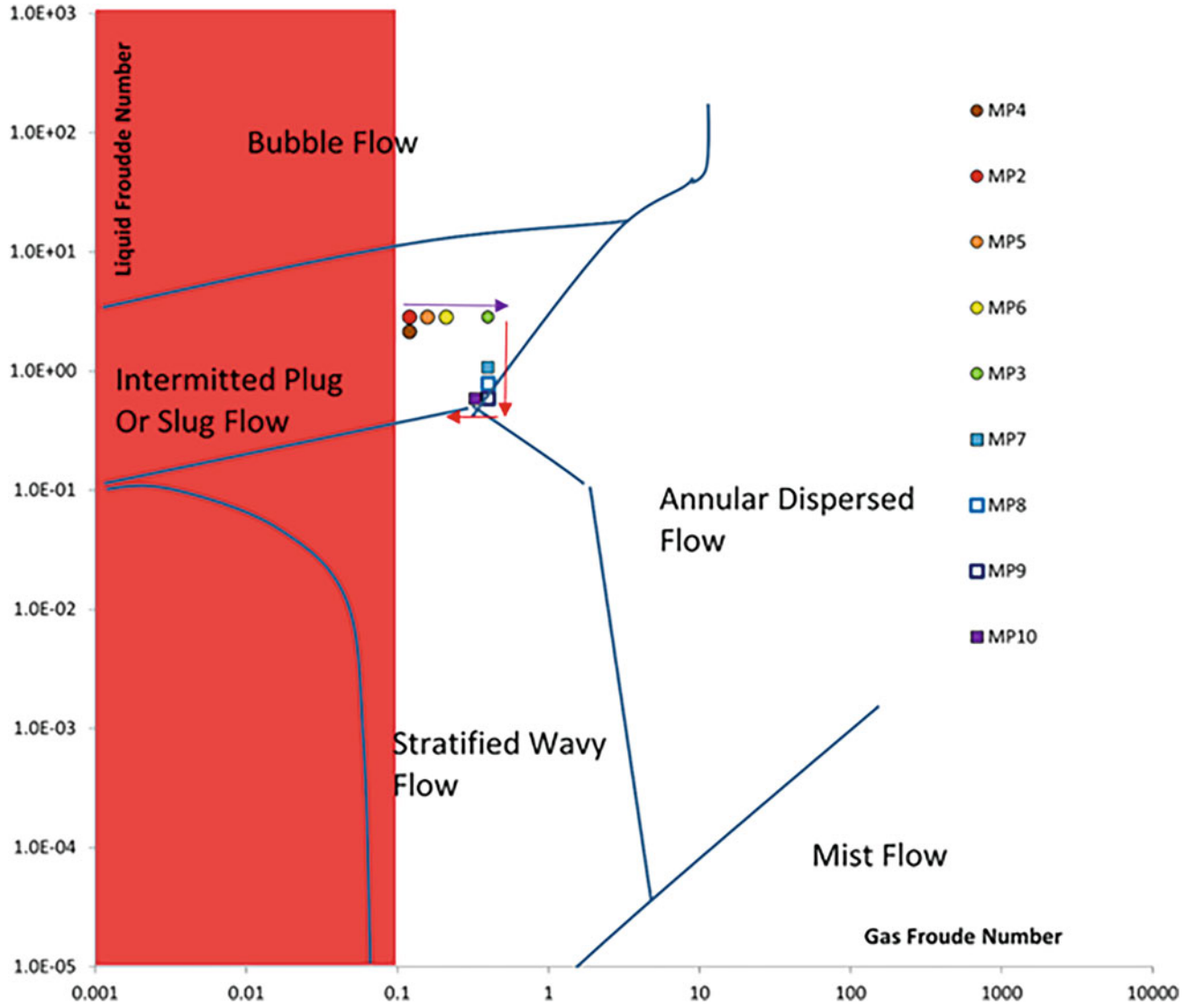

Fig. 9.2 Flow regime map showing uncalibrated region in red overlay and predicted flow regime of test points MP2-M10

mixture of nitrogen and water was used to generate the slug flow. A summary of the physical properties of the fluids used in this investigation is presented in Table 9.2. The gas flow rate Q_g was varied from 5.5 to 18.25 m^3/hr, and the liquid flow rate Q_l was varied from 0 to 14.5 m^3/hr. A list of various gas flow rates and liquid flow rates investigated is shown in Table 9.1.

To facilitate visualization of the flow inside of the pipe, custom PVC sections were connected to both the inlet and outlet of the flexible riser section, as shown in Fig. 9.3. Upstream of the flexible riser a Photron FASTCAM SA1.1 high-speed, 1-megapixel camera with a 1024 × 1024-pixel CMOS sensors fitted with a Nikon AF NIKKOR 24–85 mm focal length lens set to f/2.8 was used to record the structure of the flow entering the riser. This camera was positioned to record a 0.116 m section of the horizontal clear PVC pipe. Immediately after exiting the riser, in the vertical section of the test loop, was a Photron FASTCAM Mini Ax digital high-speed, 1-megapixel camera with a 1024 × 1024-pixel CMOS sensor fitted with a Nikon AF NIKKOR 50 mm focal length lens set to f/1.8. This was mounted on the bespoke observation platform custom-built for this purpose and used to acquire images of the flow as it exited the riser. This camera was positioned to record a 0.123 m section of the vertical clear PVC pipe 4.6 ID from the end of the flexible riser ($y = 5.25$ m). Light diffuser boards and spotlights ensured that images recorded from both cameras were back-lit and had uniform background light intensities. The cameras were both configured to record 10 sequences of 1000 images at 1000 fps, 120 seconds apart simultaneously for each test point investigated. The strain gauge data, accelerometer data, and camera data were all triggered to start acquiring data within 12.5 ns using a custom data acquisition system.

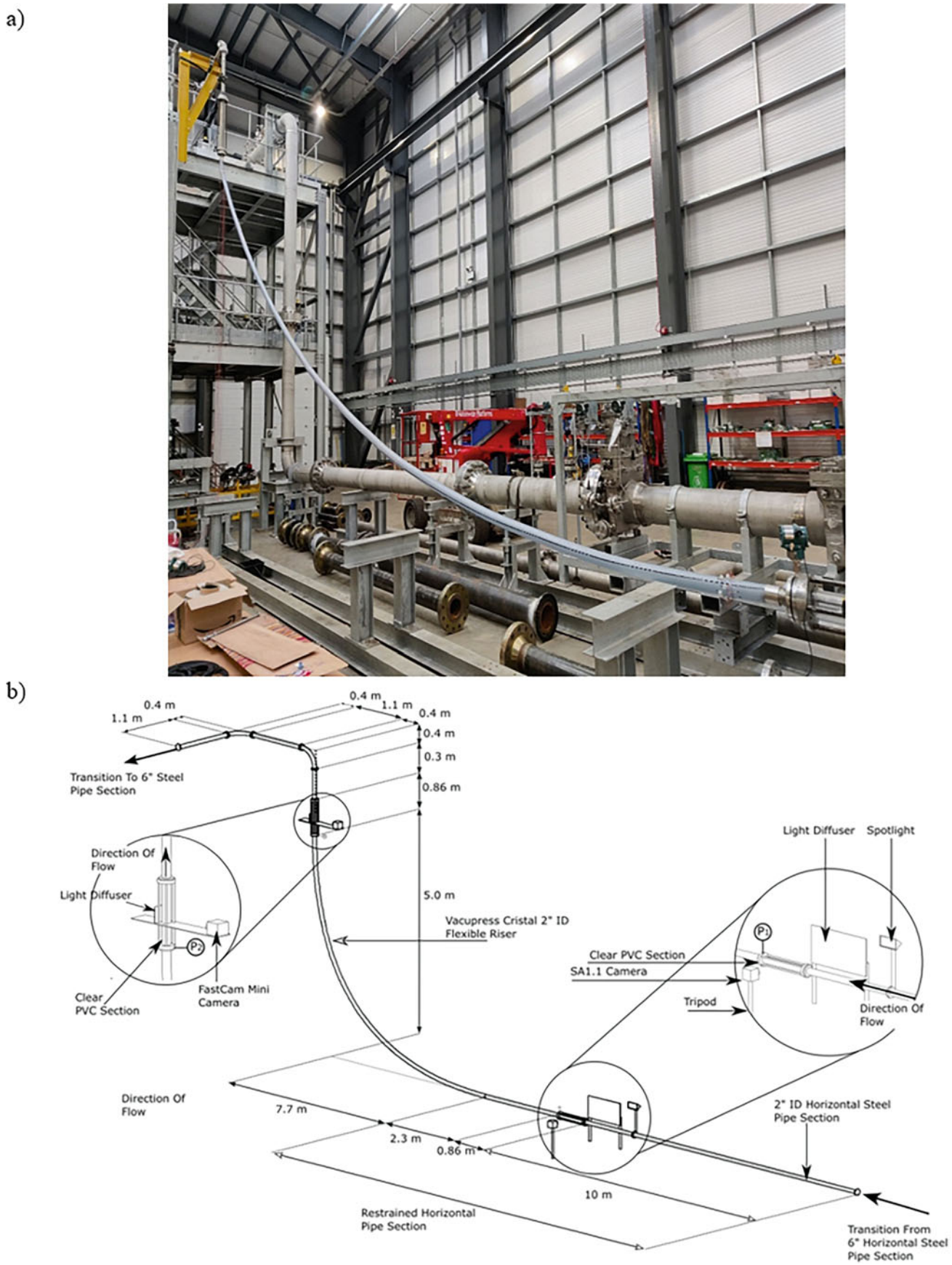

Fig. 9.3 Experimental setup depicted as (**a**) photographic representation and (**b**) schematic representation detailing associated lengths

Table 9.2 Material properties of working fluids

Fluid	Density (ρ) kgm^{-3}	Dynamic viscosity (μ) Pa.s	Surface tension (σ) Nm^{-1}
Water	1041 ± 0.3	1.18 ± 0.025	0.072
Nitrogen	13.67 ± 0.285	0.018 ± 0.000045	–

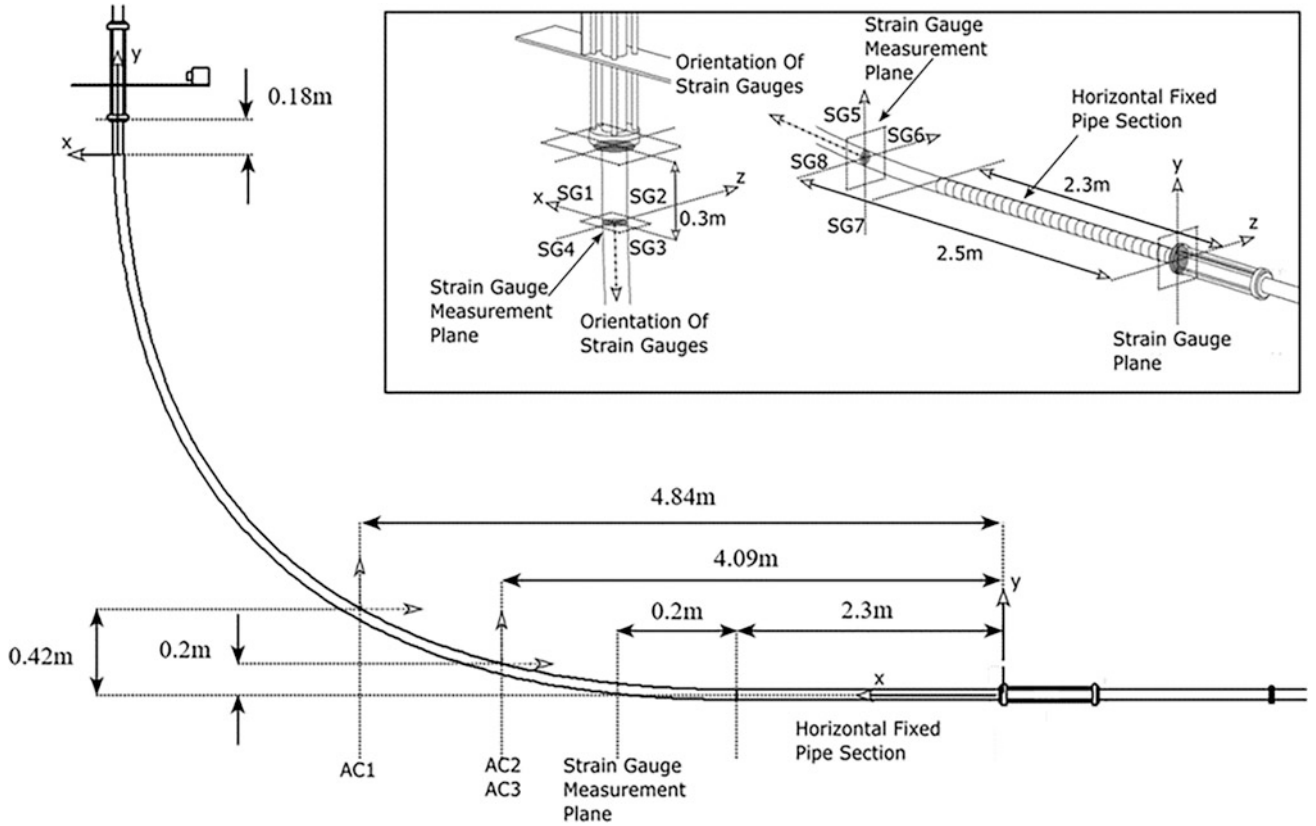

Fig. 9.4 Schematic of positioning of strain gauges and accelerometers with respect to the fixed flange positions with position and orientation of strain gauge planes and positions (inset)

A Cartesian (x, y, z) coordinate system, with its origin at the geometric center of the hose at the flange outlet plane at the bottom of the hose, is defined so that y-axis is vertically upwards, and the x-axis is orientated with the direction of the flow at this location.

To measure the movement of the pipe, three single-axis PCB:352C22 ICP accelerometers were attached to the pipe at specific locations as shown in Fig. 9.4. Two accelerometers, AC1 and AC2, were mounted on top of the pipe, $x/\text{ID} = 35.3$ and $x/\text{ID} = 50$, from the flange outlet plane at the bottom of the hose, respectively. A third accelerometer (AC3) was positioned on the side of the pipe to measure the out-of-plane movement in the positive z-axis, $x/\text{ID} = 35.3$, from the flange outlet at the bottom of the hose. The data from all three accelerometers were acquired, simultaneously, over a period of 20 mins with a data acquisition rate of 1600 Hz.

A set of four axially aligned, Youmile BF120-3AA, 120 Ohm strain gauges were mounted onto the surface of the pipe 2.5 m from the flange outlet plane at the bottom of the riser. The four strain gauges were equidistantly distributed around the perimeter of the pipe (SG5, SG6, SG7, SG8). A second set of strain gauges were also mounted, axially, to the surface of the pipe 3.5 ID before the end of the flexible hose (SG1, SG2, SG3, SG4) as shown in Fig. 9.4. The data from all eight accelerometers were acquired simultaneously, over a period of 20 minutes with a data acquisition rate of 1562 Hz. It should be noted that the strain gauges were installed after the pipe had been pressurized in order to prevent them from being damaged when the pipe deformed during pressurization. At the beginning of each day of testing, the null offset was applied to each of the strain gauges. This was performed when the pressurized pipe was hanging freely with zero gas flow rate and zero liquid inside of the pipe.

9.3 Results

9.3.1 Flow Entering Riser

Visualization of the flow in the pipe prior to entering the flexible riser section was performed using high-speed cameras to facilitate the characterization of the flow features. Post-processing of the videos was conducted by defining slug parameters such as gas slug length S_g, liquid slug length S_l, and averaged gas slug frequency S_f as shown in Fig. 9.5. These features were extracted from the videos, processed, and measured in MATLAB. Figure 9.5 shows an example of the structure of the flow entering the riser for the multiphase test point, MP4. Inversion of the raw images allowed slugs to be identified more efficiently. This technique assumes that the velocity of flow inside of the pipe, for each test point, is constant and that the slugs do not affect this.

Analysis of Table 9.3 shows that the flow entering the pipe matched the flow regime predicted by both the CFD and the PETEX GAP investigations described earlier. Unfortunately, for a gas flow rate of 15.0 m^3/hr and a liquid flow rate of 3.0 m^3/hr (MP10) the size of the gas slugs was very large, meaning the lengths of the slugs could not be extracted from the videos recorded. Additionally, for some of the test points the gas entrainment in the liquid slugs was excessive and coupled with the circular cross section of the pipe precluded accurate measurement of some slug parameters. While some correlation was obtained between slug parameters produced in the experiment, there was significant disagreement between them, and the values were obtained from either CFD or PETEX GAP. The influence of the movement of the flexible riser section on the slug parameters at the entrance to said section is believed to be primarily responsible for this. The complex interaction between the fluid and the pipe (whereby the motion and shape of the pipe affect the flow features, and the flow affects the motion and shape of the pipe) limits the accuracy of rigid structure analysis. Conversely, the rigid structure modeling was able to predict the flow regime successfully, if not the exact flow statistics.

9.3.2 Pipe Motion

Figure 9.6 shows the mean and the variation in the acceleration experienced by the pipe when a constant gas flow rate, $Q_g = 18.25$ m^3/hr, was applied and the liquid flow rate, Q_l, was increased in steps from 0 to 14.5 m^3/hr. In this instance, a liquid flow rate of zero indicated a single-phase gas-only test point. As can be seen in Fig. 9.6a, the average acceleration the riser section experiences is not significantly greater than zero. Figure 9.6b demonstrates that increasing the liquid flow rate, while maintaining a constant gas flow rate, yields an increase in the magnitude of the fluctuations experienced by the flexible riser section. Further, it is clear that for single-phase flow of pure gas both the mean and the vibrations of the pipe were close to zero, indicating that there was little or no movement of the pipe under gas-only conditions. It is interesting to note that

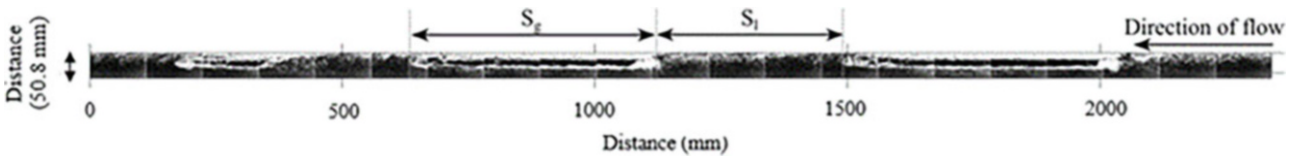

Fig. 9.5 Reconstruction of the structure of the flow entering the horizontal clear viewing section

Table 9.3 Table of statistic of slugs entering the riser

Test point	Averaged gas slug length S_g (m)	Standard deviation of gas slug length	Averaged gas slug frequency (Hz)	Averaged liquid slug length S_l (m)	Standard deviation of liquid slug length
MP1	–	–	2.5	–	–
MP2	0.478	0.233	3.17	0.622	0.346
MP3	0.164	0.827	–	0.710	0.642
MP4	0.521	0.256	2.85	0.449	0.281
MP5	0.657	0.321	2.44	0.703	0.374
MP6	0.880	0.450	2.16	0.766	0.459
MP10	>3.861	–	0.375	0.363	0.155

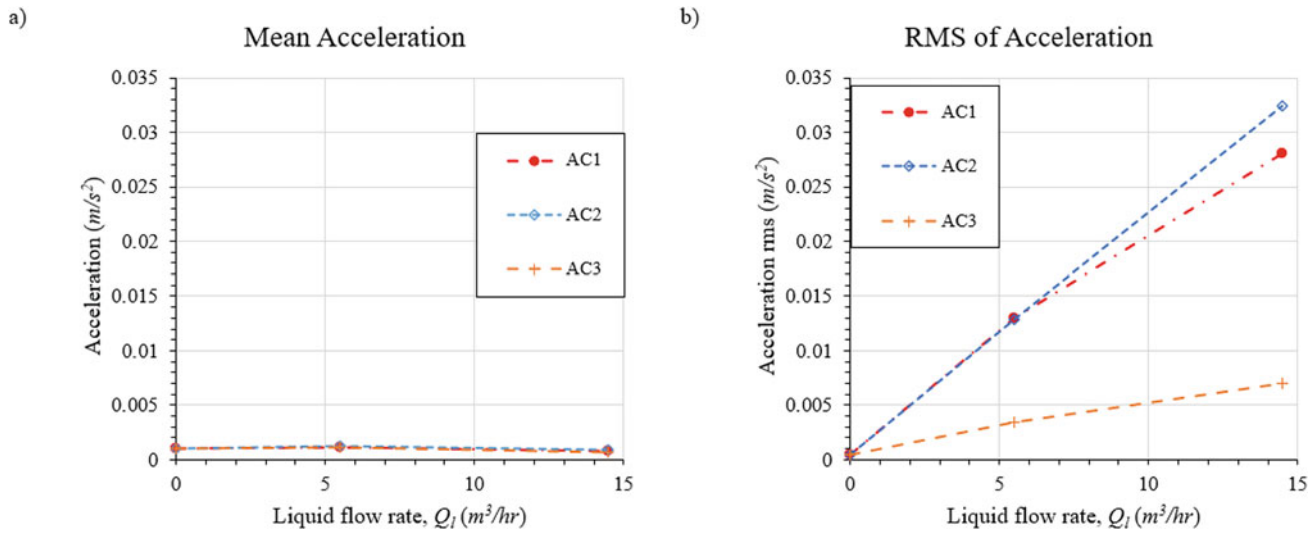

Fig. 9.6 Showing (**a**) the mean acceleration and (**b**) the RMS of the fluctuations of the accelerations experienced by the flexible riser when the gas flow rate was kept constant, and the liquid flow rate varied

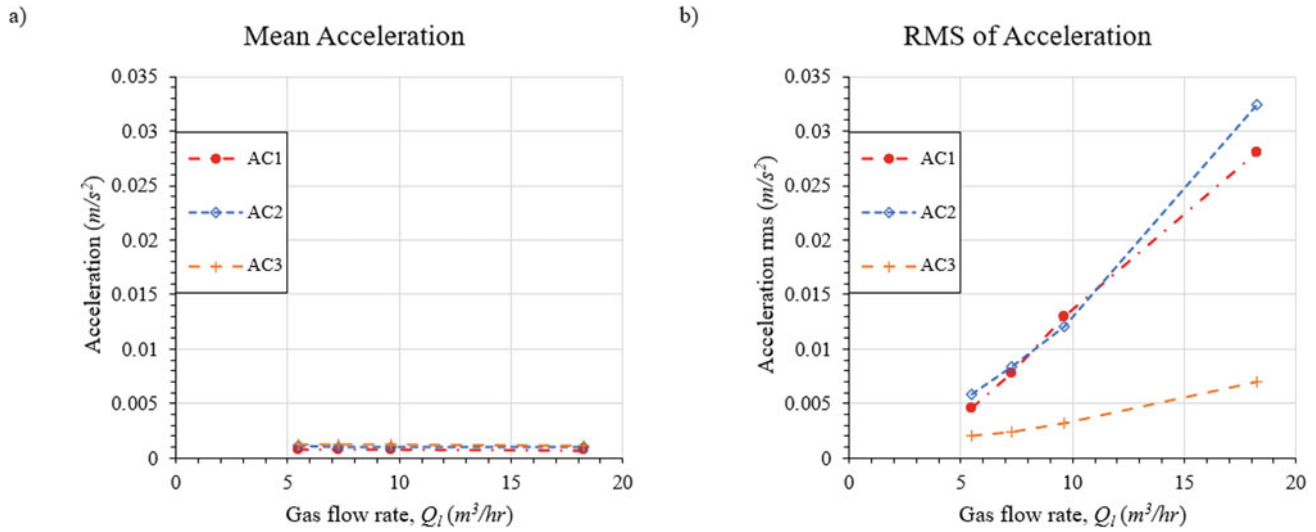

Fig. 9.7 Showing (**a**) the mean acceleration and (**b**) the RMS of the fluctuations of the accelerations experienced by the flexible riser when the liquid flow rate was kept constant, and the gas flow rate varied

magnitude of acceleration measured by the accelerometers mounted on top of the pipe (AC1 and AC2) was considerably larger than on the side of the pipe (AC3). This implied that the pipe motion was predominantly in the plane of the riser and that out-of-plane motion was of much lower significance.

The converse of this procedure whereby liquid flow rate was kept constant at $Q_l = 14.5$ m^3/hr and the gas flow rate was varied from $Q_g = 5.5$–18.25 m^3/hr is shown in Fig. 9.7, detailing the mean and fluctuation of the acceleration. Again, the average accelerations experienced by the pipe were approximately zero, as shown in Fig. 9.7a. Analysis of Fig. 9.7b shows that, for a liquid flow rate of $Q_l = 14.5$ m^3/hr, increasing the gas flow rate significantly increased the magnitude of the unsteadiness experienced by all three accelerometers. The dominance of in-plane motion was confirmed by the unsteadiness of the acceleration experienced by AC1 and AC2, which were significantly higher than those of AC3. Indicating that the pipe out-of-plane movement was significantly smaller than that in-plane movement. At lower gas flow rates, $5.5 \leq Q_g < 10.25$ m^3/hr, the fluctuations in accelerations experienced by AC1 and AC2 were similar in value; however, at a gas flow rate of $Q_l = 14.5$ m^3/hr that experienced by AC2 was noticeably larger than AC1. The same can be observed in Fig. 9.6.

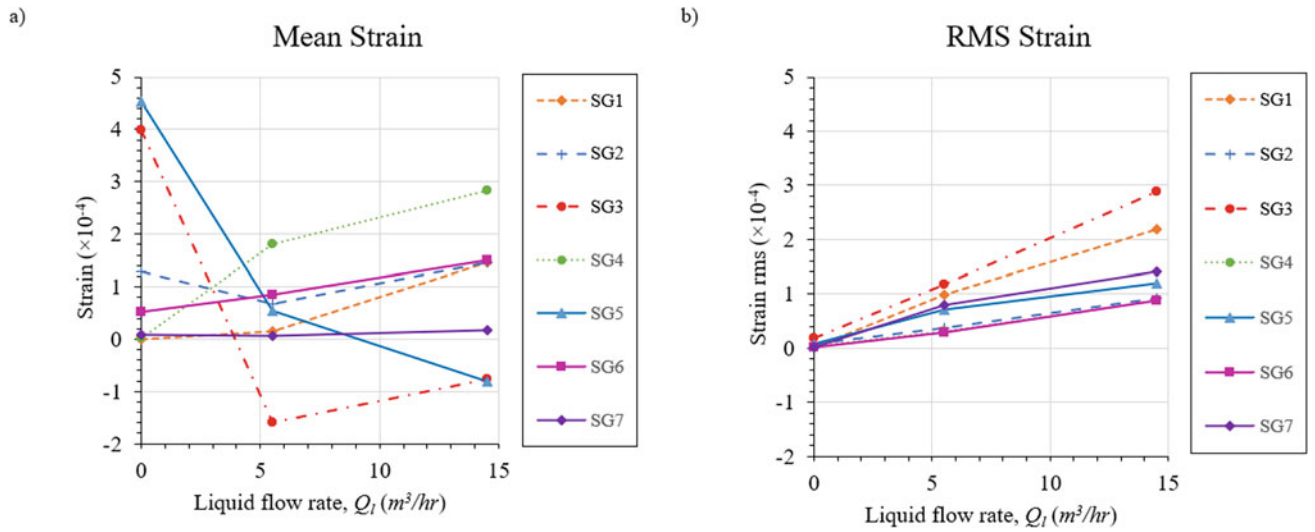

Fig. 9.8 Showing (**a**) the mean strain and (**b**) the RMS of the fluctuations of the strain gauge data about the mean are presented when the gas flow rate is kept constant, and the liquid flow rate varied

For both data sets presented, this corresponds with an observable change in the motion of the pipe when $Q_g = 14.5$ m^3/hr (MP3) and $Q_g = 18.25$ m^3/hr (MP3). This presents an interesting development whereby at higher flow rates for either liquid or gas the movement of the pipe became greater toward the central region of the pipe. For all other test points, the lower section of the pipe moved in a consistent fashion, in-plane, and oscillating up and down smoothly as a result of the slug flow inside of the pipe. For MP3, the motion could occasionally become jerky and whip-like with increased amplitude observed toward the central region of the riser section. For a period of time, at the bottom of the riser, the slug flow generates large vertical motions; however, after an unknown number of slugs the flow appears to generate a much larger pipe displacement. The larger vertical displacement generates some slack in the higher-up section on the riser, which therefore sags backward. Upon the generation of this slack, the lower section of the riser returns to its original location generating a violent tugging motion on the riser. This motion is notionally similar to that of a whip. After the in-plane whipping motion occurs, the pipe starts to move out of plane. It is believed that the rigid fixed ends of the flexible riser prevented the whiplash from propagating further; therefore, in order to dissipate the energy within the pipe, the pipe moved out of plane. The out-of-plane movement generally dissipated by the time the pipe experienced its next whipping motion. Increased flow rates beyond those of MP3 were predicted to show slug flow, but these tests were abandoned due to safety concerns as the amplitude of the waves and whipping effect increased to such an extent that the first such test point had to be stopped during testing.

The movement of the pipe described previously generated strains in the flexible riser at the fixed connections with the flanges. Figure 9.8 shows the mean strain and the RMS of the fluctuations of the strain experienced by the flexible riser when the gas flow rate was maintained at $Q_g = 18.25$ m^3/hr and the liquid flow rate, Q_l, was increased in steps from 0 to 14.5 m^3/hr. The mean strains experienced by most of the strain gauges on the riser increased as the liquid flow rate increased from 5.5 to 14.5 m^3/hr. It is believed that the variation in the mean strains experienced by the riser occurs because of the increased amount of water in the pipe, which therefore affects its weight. This in turn determined a different minimum energy profile for the pipe as the mass contained within it changed and thus applied additional strain to the pipe.

Analysis of Fig. 9.8b shows that increasing the liquid flow rate increased the unsteadiness of the strains experienced by the flexible riser at both the bottom and top of the riser. As a result of the pipe movement, which was predominantly in-plane, the strain experienced by the strain gauges mounted in-plane (SG1, SG3, SG5, and SG7) was larger than those measuring the out-of-plane strain. The peak strain experienced by the pipe occurred on the underside of the pipe at the top of the riser, for test point MP3. This corresponds with the large pipe displacements described earlier and the whip-like motion of the pipe. The very small variation in the unsteadiness of the coupled, out-of-plane, strain gauges (SG2-SG4) indicates that at the bottom of the riser the pipe did not deform out of plane. Unfortunately, due to the failure of SG8 it is not possible to determine if there is a significant amount of deformation of the riser at the top. The unsteadiness of the coupled, in-plane, strain gauges (SG1-SG3 and SG5-SG7) indicates that the pipe deforms in-plane due to its motion. This observation confirms the results from the analysis of the accelerometers.

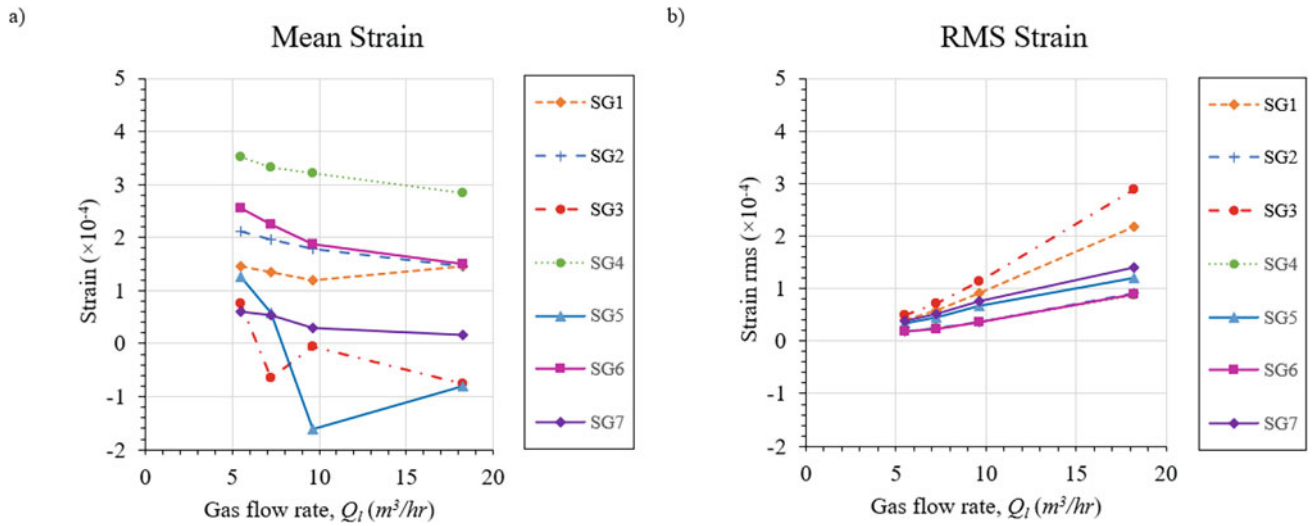

Fig. 9.9 Showing (**a**) the mean strain and (**b**) the RMS of the fluctuations of the strain gauge data about the mean are presented when the liquid flow rate is kept constant, and the gas flow rate varied

The mean strain and the RMS of the fluctuations of the strain experienced by the flexible riser when the liquid flow rate was kept constant at $Q_l = 14.5$ m^3/hr and the gas flow rate was varied from $Q_g = 5.5$ –18.25 m^3/hr are shown in Fig. 9.9. In agreement with Fig. 9.8a, maintaining the liquid flow rate while increasing the gas flow rate appeared to slightly reduce the mean strain experienced by each strain gauge (as can be seen in Fig. 9.9a). This reinforces the proposal that the decrease in the mean strains experienced by the riser occurs because of the proportionally lower mass of liquid in the pipe, producing the inverse of the result described previously.

9.4 Conclusion

An investigation into the effect nitrogen/water slug flow has on the structure of a flexible riser has been performed using surface-mounted strain gauges, accelerometers, and high-speed cameras. The results show that under single-phase flow conditions (100% gas), the flexible riser does not move significantly. However, when multiphase slug flow traveled through the flexible riser, significant pipe movements were observed. The experimental data show that the flexible riser moved, predominantly in the plane of the pipe. By comparison, little out-of-plane motion is observed.

With increased liquid flow rate (for constant gas flow rate), the mean of the strain was observed to increase. Likewise, the increase in flow rate of gas (for constant liquid flow rate) served to decrease the mean value of the strain. This is likely caused by the flexible pipe adopting a different minimum energy configuration due to increased mass in the pipe corresponding to a greater proportion of liquid present. As the flow rates of either liquid or gas was increased (under a constant flow rate condition for the other phase), the acceleration and strain caused by the movement of the pipe were seen to increase. This is reflected in the rms values of the fluctuations for both strain and acceleration in all cases.

At the highest flow rates tested, the movement of the pipe became greater toward the central region of the pipe. For lower flow rates, the movement was more evenly distributed between the lower to the central region. This motion was typified by an in-plane continuous smooth oscillation of the pipe as the slug flow passed through it. At the increased flow rate (e.g., MP3), the smooth motion would be sporadically interrupted by jerky and whip-like movement with higher amplitude, which dominated toward the central region of the riser section.

Acknowledgements The authors are grateful for the funding support from the Engineering and Physical Sciences Research Council (EPSRC) of UK Research and Innovation through the "MUltiphase Flow-induced Fluid-flexible structure InteractioN in Subsea applications (MUFFINS)" project grant EP/P033148/1. The authors would like to thank the assistance provided by the EPSRC RELIANT, Risk EvaLuatIon fAst iNtelligent Tool for COVID-19 (No. EP/V036777/1).

References

1. Wang, L., Yang, Y., Li, Y., Wang, Y.: Dynamic behaviours of horizontal gas-liquid pipes subjected to hydrodynamic slug flow: Modelling and experiments. (2018). https://doi.org/10.1016/j.ijpvp.2018.02.005
2. Al-Safran, E.: Investigation and prediction of slug frequency in gas/liquid horizontal pipe flow. J. Pet. Sci. Eng. **69**, 143–155 (2009). https://doi.org/10.1016/j.petrol.2009.08.009
3. Yang, Y., Li, J., Wang, S., Wen, C.: Gas-liquid two-phase flow behavior in terrain-inclined pipelines for gathering transport system of wet natural gas. Int. J. Press. Vessel. Pip. **162**, 52–58 (2018). https://doi.org/10.1016/J.IJPVP.2018.03.005
4. Gourma, M., Verdin, P.G.: Two-phase slug flows in helical pipes: Slug frequency alterations and helicity fluctuations. Int. J. Multiph. Flow. **86**, 10–20 (2016). https://doi.org/10.1016/j.ijmultiphaseflow.2016.07.013
5. Miwa, S., Mori, M., Hibiki, T.: Two-phase flow induced vibration in piping systems. Prog. Nucl. Energy. **78**, 270–284 (2015). https://doi.org/10.1016/J.PNUCENE.2014.10.003
6. Gourma, M., Verdin, P.G.: Nature and magnitude of operating forces in a horizontal bend conveying gas-liquid slug flows. J. Pet. Sci. Eng. **190**, 107062 (2020). https://doi.org/10.1016/J.PETROL.2020.107062
7. Abdulkadir, M., Mbalisigwe, U.P., Zhao, D., Hernandez-Perez, V., Azzopardi, B.J., Tahir, S.: Characteristics of churn and annular flows in a large diameter vertical riser. Int. J. Multiph. Flow. **113**, 250–263 (2019). https://doi.org/10.1016/J.IJMULTIPHASEFLOW.2019.01.013
8. Mohmmed, A.O., Al-Kayiem, H.H., Osman, A.B., Sabir, O.: One-way coupled fluid–structure interaction of gas–liquid slug flow in a horizontal pipe: Experiments and simulations. J. Fluids Struct. **97**, 103083 (2020). https://doi.org/10.1016/J.JFLUIDSTRUCTS.2020.103083
9. Thaker, J., Banerjee, J.: Characterization of two-phase slug flow sub-regimes using flow visualization. J. Pet. Sci. Eng. **135**, 561–576 (2015). https://doi.org/10.1016/J.PETROL.2015.10.018
10. Belfroid, S.P.C., Cargnelutti, M.F., Schiferli, W., Van Osch, M.: Forces on bends and T-joints due to multiphase flow. Am. Soc. Mech. Eng. Fluids Eng. Div. FEDSM. **3**, 613–619 (2011). https://doi.org/10.1115/FEDSM-ICNMM2010-30756
11. Riverin, J.L., de Langre, E., Pettigrew, M.J.: Fluctuating forces caused by internal two-phase flow on bends and tees. J. Sound Vib. **298**, 1088–1098 (2006). https://doi.org/10.1016/j.jsv.2006.06.039
12. Riverin, J.L., Pettigrew, M.J.: Vibration excitation forces due to two-phase flow in piping elements. undefined. **129**, 7–13 (2007). https://doi.org/10.1115/1.2388994
13. Liu, Y., Miwa, S., Hibiki, T., Ishii, M., Morita, H., Kondoh, Y., Tanimoto, K.: Experimental study of internal two-phase flow induced fluctuating force on a 90° elbow. Chem. Eng. Sci. **76**, 173–187 (2012). https://doi.org/10.1016/J.CES.2012.04.021
14. Zhu, H., Gao, Y., Zhao, H.: Experimental investigation on the flow-induced vibration of a free-hanging flexible riser by internal unstable hydrodynamic slug flow. Ocean Eng. **164**, 488–507 (2018). https://doi.org/10.1016/J.OCEANENG.2018.06.071
15. Flow Regime Map for Two-Phase Flow | Excel Calculations, http://excelcalculations.blogspot.com/2012/02/flow-regime-map.html
16. Frank, T.: The 11 th International Topical Meeting on Nuclear Reactor Thermal-Hydraulics (NURETH-11) Numerical Simulation of Slug Flow Regime for an Air-Water Two-Phase Flow in Horizontal Pipes
17. Al-Hashimy, Z.I., Al-Kayiem, H.H., Kadhim, Z.K., Mohmmed, A.O.: Numerical simulation and pressure drop prediction of slug flow in oil/gas pipelines Computational Methods in Multiphase Flow VIII 57. WIT Trans. Eng. Sci. **89** (2015). https://doi.org/10.2495/MPF150051
18. Al-Hashimy, Z.I., Al-Kayiem, H.H., Time, R.W., Kadhim, Z.K.: Numerical characterisation of slug flow in horizontal air/water pipe flow. Int. J. Comput. Methods Exp. Meas. **4**, 114–130 (2016). https://doi.org/10.2495/CMEM-V4-N2-114-130
19. Hirt, C.W., Nichols, B.D.: Volume of fluid (VOF) method for the dynamics of free boundaries. J. Comput. Phys. **39**, 201–225 (1981). https://doi.org/10.1016/0021-9991(81)90145-5
20. Mahrenholtz, O., Markiewicz, M.: Nonlinear water wave interaction. WIT Press, Southampton (1999)
21. Menter, F.R.: Two-equation eddy-viscosity turbulence models for engineering applications. AIAA J. **32**, 1598–1605 (1994). https://doi.org/10.2514/3.12149

Chapter 10
Deep Learning-Based Pixel-Level Colonoscopy Analysis

John Lewis and Young-Jin Cha

Abstract Colorectal cancer (CRC) is a common form of cancer that affects the large intestine. CRC is one of the most severe and aggressive forms of cancer, and thus, early treatment and detection are essential. Early detection of CRC is primarily available through the detection of polyps through endoscopic imaging procedures. This method is labor-intensive and subject to human error. To circumvent these issues associated with human error and improve upon limitations associated with human detection, deep learning-based procedures have been developed and convolutional neural networks (CNNs) have been introduced for the automated detection and segmentation of polyps. Current problems associated with polyp segmentation with CNNs are overfitting, boundary pixel definitions, an inability to account for the different range of textures, sizes, and shapes with polyps, among other issues. With the ultimate goal of addressing these issues, we developed a multiscale segmentation network (MSSNet) designed specifically for polyps (Lewis and Cha, Sci Rep, 2023). In this paper, we conducted some additional case studies to investigate the performance of MSSNet. This dual model network surpasses state-of-the-art results (SOTA) and is evaluated using the CVC-ClinicDB dataset. The mean intersection-over-union (mIoU) and dice (mDice) score were 0.889 and 0.935, respectively.

Keywords Segmentation · Polyp · Colonoscopy · Endoscopy · Deep learning · Convolutional neural networks · Transformers · Medical images

10.1 Introduction

Colorectal cancer (CRC) is a severe form of cancer that impacts the digestive tract, predominantly impacting the colon and rectum. As conferred by [2, 3], CRC is the third most common form of cancer across both sexes, with an estimated 5-year survival rate between 48.6 and 59.4% [4]. Screening procedures in the form of endoscopic imaging processes are recommended to begin at age 50 and consist of moving a camera through the digestive tract and screening for polyps, which is an early sign of CRC [5]. While effective at improving patient outcomes in terms of prognosis as shown by [6], endoscopic imaging procedures are costly and time-consuming and must be conducted by trained medical professionals. One method of approaching this issue is in the form of automated polyp detection on a pixel-based level (segmentation) with deep learning-based and convolutional neural network-based (CNN) methodologies, as seen in [7–13].

Of the deep learning-based methodologies that have been produced in recent years [14–20], the vast majority of them employ a convolutional approach. Moreover, these models often comprise an encoder–decoder structure as seen in [11, 21, 22]. These approaches to polyp segmentation operate by downsampling an image through progressive convolutions or pooling operations, followed by an upsampling sequence which increases the output feature map to the input image dimension size, while further extracting semantic information. These approaches are inherently limited in that they are limited to a local receptive field by nature of the convolution operation. This local receptive field restriction results in a loss

J. Lewis (✉)
Department of Civil Engineering, University of Manitoba, Winnipeg, MB, Canada

University of Manitoba, Winnipeg, MB, Canada
e-mail: lewisj34@myumanitoba.ca

Y.-J. Cha
Department of Civil Engineering, University of Manitoba, Winnipeg, MB, Canada

M. Allen et al. (eds.), *Special Topics in Structural Dynamics & Experimental Techniques, Volume 5*,
Conference Proceedings of the Society for Experimental Mechanics Series, https://doi.org/10.1007/978-3-031-37007-6_10

of global context or long-range feature relationships. Ways of ameliorating this are through the usage of skip connections [23], which connect more coarse representations with their decoded counterparts at later points in the network.

Other issues impacting deep learning-based approaches to polyp segmentation are the collection of boundary pixel information. Boundary regions are often poorly defined with respect to images of polyps and constitute a problem with respect to model accuracy. Models such as [8, 24] have attempted to compensate for this issue. Both of these models utilized reverse attention (RA) mechanisms and parallel partial decoders (PPDs) which better integrate higher-level features and recover boundary pixel information. Some models have opted for an ensemble approach, as seen in [9, 10, 25], which can be defined as those approaches which use a combinatory approach to generating a model, in which multiple different models are used. For example in [10], two Mask R-CNNs were utilized to achieve state-of-the-art (SOTA) performance. However, issues associated with ensemble methods are that while they generate increased performance, they also incorporate a larger number of parameters and often perform slower relative to other models.

10.2 Methodology

Our method proposed for polyp segmentation, MSSNet [1], is a dual encoder–decoder structure that consists of an original arrangement of novel and generic modules. The encoder branch is a dual encoder, consisting of two main streams, the novel local feature encoder, a convolutional-based module, with a simultaneously run generic transformer encoder, plainly referred to as the transformer encoder. Both paths in the encoder branch of MSSNet collectively work as a feature extraction module, with the local feature encoder focusing on local phenomena and the transformer encoder extracting global dependencies. Following the encoder branch is the decoder branch, which consists of a set of fuse modules, as well as the local feature decoder, receiving input from both the transformer encoder and the local feature encoder directly and through skip connections. The design objective of the encoder branch is to intelligently focus on global dependencies and local-level phenomena independently of one another, which is done simultaneously. The design objective of the decoder branch, as a whole, is to generate output segmentation maps and classify tissue as healthy or as containing a polyp, while also maintaining the global or local-level features obtained in the encoder. The fuse modules amalgamate information from both the transformer component and the CNN-based component and, through deep supervision, generate candidate output segmentation maps. An overall schematic detailing the model is shown in Fig. 10.1.

The encoder branch receives an input RGB image, $x \in \mathrm{R}^{H \times W \times 3}$, and processes it through both the local feature encoder and the transformer encoder. The local feature encoder consists of a series of newly designed convolutional modules and pooling operations in which the majority were uniquely designed for the purpose of polyp segmentation in MSSNet. Both the local feature encoder and the transformer encoder return an output feature map 1/16th the size of the input image they each receive. The ultimate goal of dividing the encoder branch into two distinct paths is to have each path focus on global and local-level feature information, respectively. Thus, the local feature encoder focuses on local feature information. The receptive fields within the local feature encoder path are small, with dimensionality reductions conducted through pooling

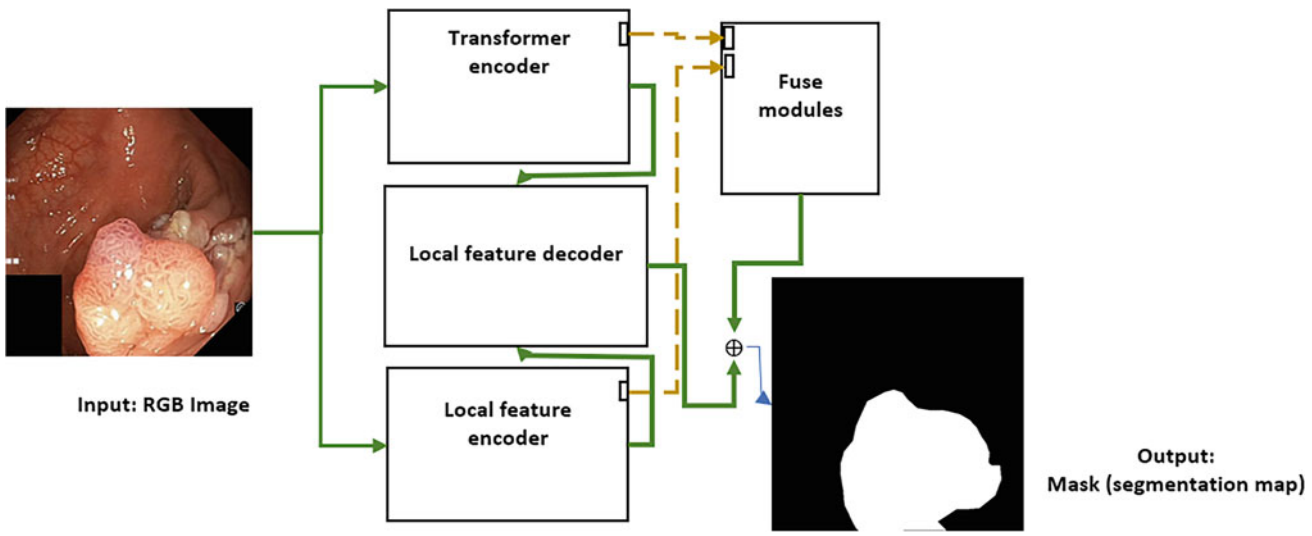

Fig. 10.1 Schematic of MSSNet [1]

and a maximum kernel size set to 3×3. Skip connections are present throughout the module to assist in the model's attention mechanism.

The transformer encoder is pretrained and developed by [26]. The transformer encoder receives an input RGB image, which is received simultaneously by the local feature encoder. In this path, the transformer encoder first operates by modifying the input image to a flattened sequence of patches, which is then followed by a linear projection on to a sequence of patch embeddings and then the addition of learnable parameters which produces a sequence of tokens, z_0. This process is then followed by the attention mechanism which consists of two sequential modules, the multiscale self-attention (MSA) module and the multilayer perceptron (MLP). Most importantly, the transformer encoder focuses on global dependencies by its attention mechanism. To assist in model convergence and speed up training time, each component of the attention mechanism is followed by layer normalization (LN).

The decoder branch consists of two key components, the fuse modules and the local feature decoder, each of which generates candidate output segmentation maps. The local feature decoder works to effectively recover local features by decoding the output from the local feature encoder and the transformer encoder. The output from the local feature encoder is processed through a sequence of operations which consist of a novel arrangement of various generic and novel modules. Separable convolutions are used throughout to reduce model complexity and increase model runtime, while maintaining SOTA accuracy. In all convolutional operations present, both dilated and standard separable, the receptive field of the module is kept small, similar to the local feature encoder, given that local contingencies are easier to learn and contribute more to a model's capacity to learn input–output relationships. The output from the transformer encoder is similarly put through a sequence of small-receptive field convolutions in the local feature decoder to extract more spatial relationships while retaining global dependencies learning in the transformer encoder. Each fuse module in the network is essentially small encoder–decoder modules, in which the input to the module is the concatenated output from coarse feature maps from the transformer encoder and the local feature encoder. As each fuse module produces an output segmentation map, these elements comprise the primary deep supervision mechanism in the network, which increases the model convergence time. The increased number of parameters also further enhances the model's capacity to generate distinctions between healthy tissue and polyp and improve upon the model's accuracy.

10.3 Analysis

The performance of MSSNet is evaluated with respect to the CVC-ClinicDB [27] dataset. The original dataset contained 612 images gathered from 31 colonoscopy videos. The size of the training, testing, and validation sets for the CVC-ClinicDB dataset was 551, 61, and 61, respectively. The original image resolution size for this dataset was 384×288. The ground truths were identified manually by a series of clinical professionals identified in the original research paper presenting the dataset. In terms of the pixel makeup of each of the ground truth images, 1 indicates polyp and 0 indicates healthy tissue in the context of the dataset. The model was trained using the Adam optimizer, and the deep learning primitive framework used was PyTorch.

The two evaluation metrics used for model performance determination were the mean Dice score (mDice) and the mean intersection-over-union (mIoU) score. The formulas for each of these equations are presented in Eq. (10.1) and Eq. (10.2). The model was trained using the PyTorch framework and used a warm-up polynomial learning rate scheduler with the Adam optimizer. The initial learning rate was 2.1052×10^{-5}, and the loss function used in model training was also IoU. The images were a variable range of image sizes in the original datasets and were reshaped and normalized to an image size of 512×512. For normalization, the mean, μ, was 0.5 and the standard deviation, σ, was 0.5.

$$L_{\text{IoU}} = \frac{|\sigma\ (x_{\text{n}}) \cap y_{\text{n}}|}{|\sigma\ (\text{x}_{\text{n}}) \cup y_{\text{n}}|} \tag{10.1}$$

$$L_{\text{dice}} = \frac{2 \times |\sigma\ (x_{\text{n}}) \cap y_{\text{n}}|}{|\sigma\ (x_{\text{n}}) + y_{\text{n}}|} \tag{10.2}$$

where x_{n} is output from MSSNet, σ is the sigmoid function and $\sigma(x_{\text{n}})$ is the output segmentation map detailing the pixelwise probabilities of each pixel corresponding to healthy tissue or polyp, which is generated by the sigmoid activation of the output from MSSNet, and y_{n} is the ground truth corresponding to the input image.

We evaluate MSSNet by training it on the CVC-ClinicDB dataset solely and the model produces exemplary results. The model achieved a combined mean dice score (mDice) and mean intersection-over-union (mIoU) across all test sets

Table 10.1 Numerical results on CVC-ClinicDB dataset

Metric	mDice	mIoU
Value	0.935	0.889

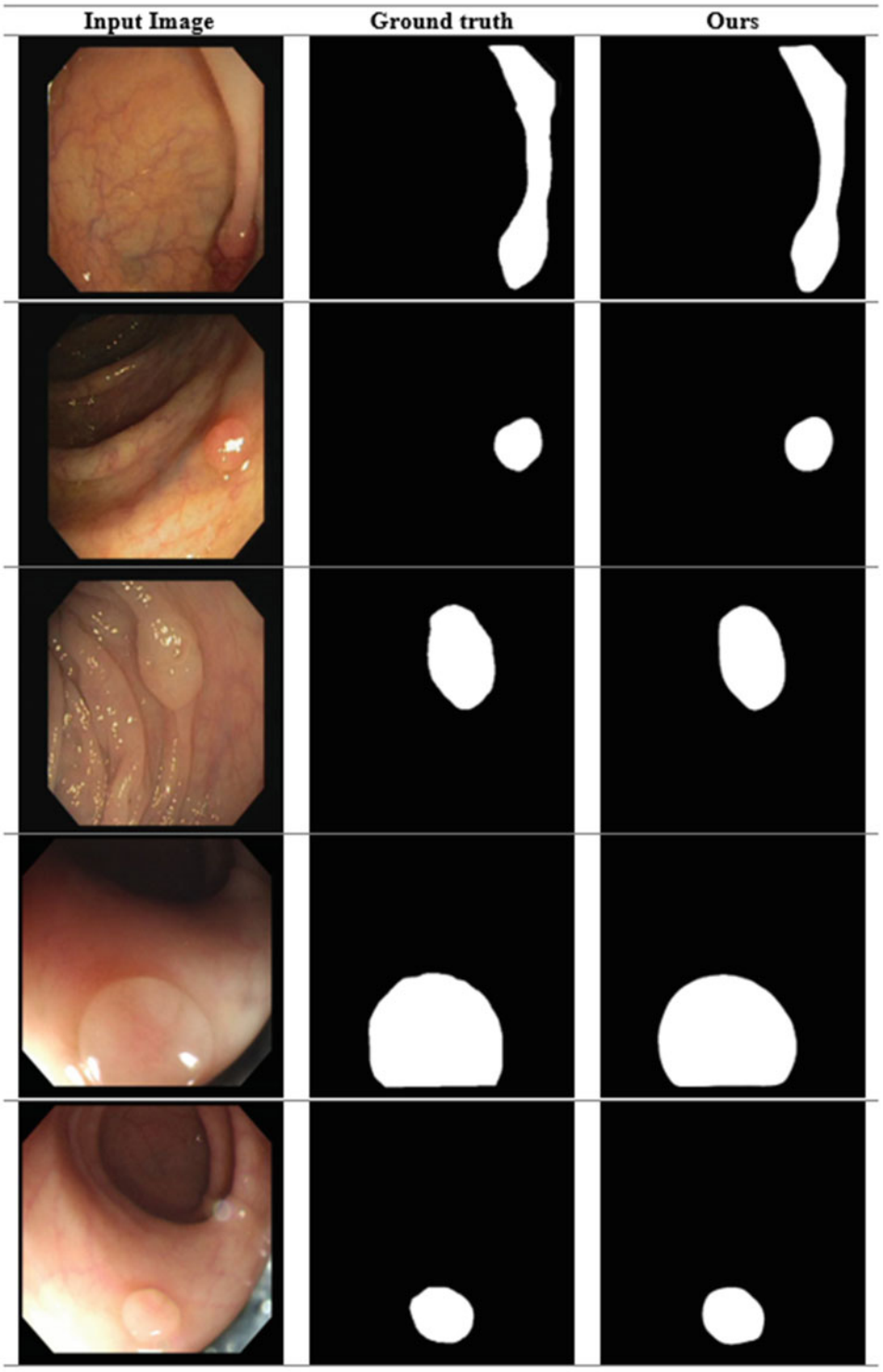

Fig. 10.2 Experimental results on the CVC-ClinicDB dataset [1]

of 0.937 and 0.887, respectively, as shown in Table 10.1. Thus, MSSNet is capable of automated pixelwise detection of polyps at SOTA performance. A sample of the predicted output of input images of polyps is presented in Fig. 10.2, and the corresponding results evaluated against existing methods are shown in Table 10.1. MSSNet's exemplary performance is attributed to the fact that MSSNet is capable of focusing on global and local features independently of one another through each segment of the encoder and decoder branches.

10.4 Conclusion

The polyp segmentation network, MSSNet [1], was presented to demonstrate its effectiveness at learning global and local features, along with its ability to capture boundary pixel information. MSSNet is capable of identifying, on a pixel-based level, the location of polyps given an input image of the digestive tract. A number of novel components were generated for this research study, such as the local feature encoder, local feature decoder, and the fuse module, along with many of their respective components, therein. The model is a dual encoder–decoder framework which is capable of focusing more intelligently on local and global phenomena independently. Through deep supervision, the local feature branch, the transformer branch, and the fuse modules all produce candidate output segmentation maps, which both increase the model performance through additional parameters present and increase model convergence time with deep supervisory approaches.

Acknowledgements This research was partially supported by a Research Manitoba Innovation Proof-of-Concept Grant (4914), and a CFI JELF grant (37394).

References

1. Lewis, J., Cha, Y. J., & Kim, J.: Dual encoder-decoder-based deep polyp segmentation network for colonoscopy images. Scientific Reports **13**(1), 1183 (2023)
2. Vannelli, A.: Colorectal Cancer. IntechOpen, London (2013)
3. Swinson, D., Seymour, M., Adairm, R.A.: Colorectal cancer. Oxford University Press, Oxford (2012)
4. Morris, M., Iacopetta, B., Platell, C.: Comparing survival outcomes for patients with colorectal cancer treated in public and private hospitals. Med. J. Aust. **186**(6), 296–300 (2007)
5. Engin, O.: Colon Polyps and the Prevention of Colorectal Cancer. Springer, Cham (2015)
6. Zauber, A.G., Winawer, S.J., O'Brien, M.J., Lansdorp-Vogelaar, I., van Ballegooijen, M., Hankey, B.F., Shi, W., Bond, J.H., Schapiro, M., Panish, J.F., Stewart, E.T., Waye, J.D.: Colonoscopic polypectomy and long-term prevention of colorectal-cancer deaths. N. Engl. J. Med. **366**(8), 687–696 (2012)
7. Cheng, M., Kong, Z., Song, G., Tian, Y., Liang, Y., Chen, J.: Learnable oriented-derivative network for polyp segmentation. In: Medical Image Computing and Computer Assisted Intervention – MICCAI 2021, pp. 720–730 (2021)
8. Fan, D.-P., Ji, G.-P., Zhou, T., Chen, G., Fu, H., Shen, J., Shao, L.: PraNet: parallel reverse attention network for polyp segmentation. In: Medical Image Computing and Computer Assisted Intervention – MICCAI 2020, Lima (2020)
9. Guo, X., Zhang, N., Guo, J., Zhang, H., Hao, Y., Hang, J.: Automated polyp segmentation for colonoscopy images: a method based on convolutional neural networks and ensemble learning. Med. Phys. **46**(12), 5666–5676 (2019)
10. Kang, J., Gwak, J.: Ensemble of instance segmentation models for polyp segmentation in colonoscopy images. IEEE. **7**, 26440–26447 (2019)
11. Mahmud, T., Paul, B., Fattah, S.A.: PolypSegNet: a modified encoder-decoder architecture for automated polyp segmentation from colonoscopy images. Comput. Biol. Med. **128**, 104119–104119 (2021)
12. Ngoc Lan, P., An, N.S., Hang, D.V., Long, D.V., Trung, T.Q., Thuy, N.T., Sang, D.V.: NeoUNet : towards accurate colon polyp segmentation and neoplasm detection. In: Advances in Visual Computing, ISVC 2021, pp. 15–28 (2022)
13. Sánchez-González, A., García-Zapirain, B., Sierra-Sosa, D., Elmaghraby, A.: Automatized colon polyp segmentation via contour region analysis. Comput. Biol. Med. **100**, 152–164 (2018)
14. Cha, Y.J., Choi, W., Büyüköztürk, O.: Deep learning-based crack damage detection using convolutional neural networks. Comput. Aided Civ. Inf. Eng. **32**(5), 361–378 (2017)
15. Cha, Y., Choi, W., Suh, G., Mahmoudkhani, S., Büyüköztürk, O.: Autonomous structural visual inspection using region-based deep learning for detecting multiple damage types. Comput. Aided Civ. Inf. Eng. **33**(9), 731–747 (2018)
16. Kang, D., Cha, Y.J.: Autonomous UAVs for structural health monitoring using deep learning and an ultrasonic beacon system with geo-tagging. Comput. Aided Civ. Inf. Eng. **33**(10), 885–902 (2018)
17. Beckman, G.H., Polyzois, D., Cha, Y.-J.: Deep learning-based automatic volumetric damage quantification using depth camera. Autom. Constr. **99**, 114–124 (2019)
18. Wang, Z., Cha, Y.-J.: Unsupervised deep learning approach using a deep auto-encoder with a one-class support vector machine to detect damage. Struct. Health Monit. **20**(1), 406–425 (2021)

19. Ali, R., Cha, Y.J.: Attention-based generative adversarial network with internal damage segmentation using thermography. Autom. Constr. **141**, 104412 (2022)
20. Kang, D., Cha, Y.J.: Efficient attention-based deep encoder and decoder for automatic crack segmentation. Struct. Health Monit. **21**, 2190 (2021)
21. Jha, D., Ali, S., Tomar, N.K., Johansen, H.D., Johansen, D., Rittscher, J., Riegler, M.A., Halvorsen, P.: Real-time polyp detection, localization and segmentation in colonoscopy using deep learning. IEEE Access. **9**, 40496–40510 (2021)
22. Pozdeev, A.A., Obukhova, N.A., Motyko, A.A.: Automatic analysis of endoscopic images for polyps detection and segmentation. In: 2019 IEEE Conference of Russian Young Researchers in Electrical and Electronic Engineering (EIConRus), Saint Petersburg and Moscow (2019)
23. Ronneberger, O., Fischer, P., Brox, T.: U-net: convolutional networks for biomedical image segmentation. In: Medical Image Computing and Computer-Assisted Intervention – MICCAI 2015 (2015)
24. Song, P., Li, J., Fan, H.: Attention based multi-scale parallel network for polyp segmentation. Comput. Biol. Med. **146**, 105476–105476 (2022)
25. Zhang, Y., Liu, H., Hu, Q.: TransFuse: fusing transformers and CNNs for medical image segmentation. In: Medical Image Computing and Computer Assisted Intervention – MICCAI, pp. 14–24 (2021)
26. Dosovitskiy, A., Beyer, L., Kolesnikov, A., Weissenborn, D., Zhai, X., Unterthiner, T., Dehghani, M., Minderer, M., Heigold, G., Gelly, S., Uszkoreit, J., Houlsby, N.: An image is worth 16x16 words: transformers for image recognition at scale. arXiv:2010.11929, 2020
27. Bernal, J., Sánchez, F.J., Fernández-Esparrach, G., Gil, D., Rodríguez, C., Vilariño, F.: WM-DOVA maps for accurate polyp highlighting in colonoscopy: validation vs. saliency maps from physicians. Comput. Med. Imaging Graph. **43**, 99–111 (2015)

Chapter 11
Design and Integration of a Hydroelastic Solver in the Dynamic Model of a Scaled Marine Hydrokinetic Kite

Carson M. McGuire and Matthew Bryant

Abstract This study presents the framework and initial characterization of a hydroelastic solver for the dynamic model of an underwater marine hydrokinetic (MHK) kite. MHK kites are systems designed to optimally harvest current and tidal energy from bodies of water by executing cross-current flight patterns to augment velocity and therefore power generation. Due to the significant fluid-dynamic loading experienced by MHK kites, robust structural analysis of the kites is integral to successful system design. Hydroelastic analysis allows the coupled hydrodynamic loading and structural deformation of a MHK kite wing to be predicted. The hydroelastic solver outlined here uses a finite-element method to discretize a given wing geometry into a user-selected number of nodes. At each node, hydrodynamic and structural parameters are defined. The hydroelastic solver contains two sub-solvers: (i) a hydrodynamic solver and (ii) an elastic solver. The hydrodynamic solver uses airfoil coefficient lookup tables and Prandtl lifting line theory to estimate lift, drag, and pitching moment at each node across the wing. The elastic solver receives the point loads and moments from the hydrodynamic solver and deforms a defined structural representation of the wing. This hydroelastic solver process is iterated until wing deformation has converged. The integrated model is used to predict the cyclic variation in wing deflection and twist during closed-loop-controlled cross-current flight. Such predictions could prove useful for evaluating hydroelastic effects on optimal kite flight controller tuning, or appropriate design of the kite wing for structural fatigue life considerations.

Keywords Hydroelastic · Hydrokinetic · FEA · Kite · Energy

11.1 Introduction

Marine hydrokinetic (MHK) systems are a growing research field and offer environmentally and economically sustainable methods of harvesting hydroelectric energy from ocean currents and tides. Tidal and current energy represents a significant potential for harvesting, with an estimated 334 TWh per year of available tidal energy [1] and 163 TWh per year of ocean current energy [2] in US coastal waters alone. MHK systems are leveraged to harvest this available energy to power utility-scale power to remote coastal communities [3] as well as support the so-called blue economy, which consists of off-grid, offshore devices such as autonomous vehicles, marine buoys, and navigational aids [4].

A primary challenge of MHK systems is that regions of highest energy availability typically do not allow economical deployment of said systems. Often, high velocity water currents are located above seabeds that are over 1000 m deep, such as the case of the Gulf Stream [5], or are significantly distanced from customers. Since seabed-mounted towers are impractical to build tall enough to access high velocity flows, a solution to use tethered energy-harvesting kites was found. This problem was experienced similarly in the airborne wind-energy (AWE) field, and likewise airborne kite solutions have been explored. Commercial solutions are under active development, such as Windlift [6] (AWE), Kitepower [7] (AWE), and Minesto [8] (MHK). All kites regardless of flight medium execute figure-eight or elliptical motions, which allows the vehicle to move at speeds 5–10 times the prevailing flow speed, increasing power generation and allowing operation in low-flow environments.

Power is generated by kites through two typical methods: the spinning of onboard turbines (termed *fly-gen*) or the cyclic spooling of a ground-fixed winch-generator system (termed *ground-gen*). This research focuses on the ground-gen method of energy harvesting, where the kite is spooled out under high tension while executing cross-current motions, then spooled in

C. M. McGuire (✉) · M. Bryant
Department of Aerospace Engineering, North Carolina State University, Raleigh, NC, USA
e-mail: cmmcguir@ncsu.edu

M. Allen et al. (eds.), *Special Topics in Structural Dynamics & Experimental Techniques, Volume 5*,
Conference Proceedings of the Society for Experimental Mechanics Series, https://doi.org/10.1007/978-3-031-37007-6_11

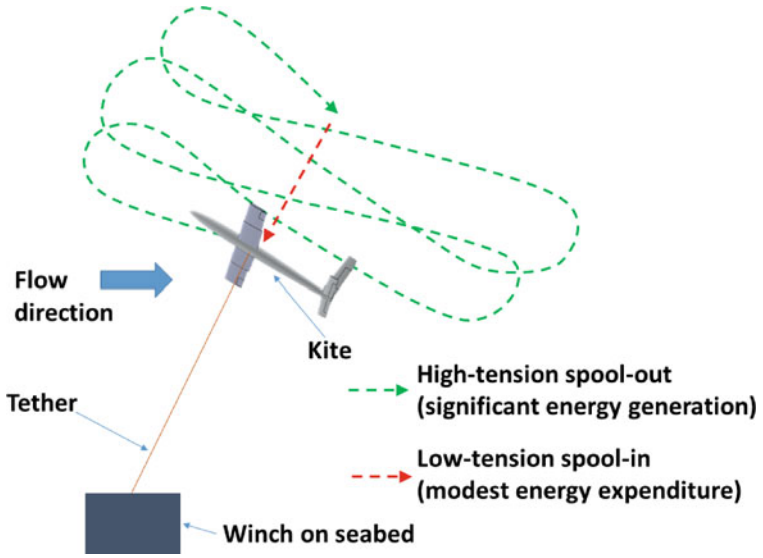

Fig. 11.1 Concept of operations for a MHK kite executing cyclic figure-eight flight maneuvers and spool-in/spool-out winching during *ground-gen* power generation

under low tension in non-cross-current flight, as illustrated in Fig. 11.1, generating a net power output from the system across each flight cycle. Structural deformation has been considered in AWE systems, such as in [9], which evaluates a carbon-fiber composite wing, and [10], which evaluates a soft, inflatable wing. Very recently, MHK kite structural optimization was evaluated by adding structural elements of a constant material to both the kite wing and fuselage [11]; however, this work considered only rectangular-planform wing vertical deflection and neglected variance in hydrodynamic loading due to wing deformation. Most research on MHK kites, however, assume the kite wing to be completely rigid. Elastic deformation of the wing will result in variation to the lift and drag experienced when compared to a rigid wing, as wing deformation couples with aerodynamic loading on the wing.

Beyond MHK and AWE systems, the importance of coupling between fluid-elastic dynamics and vehicle flight dynamics has been well established in the aircraft literature by [12, 13], and others. While effects due to flexibility have been explored on kite tether models [14], the implications on kite flight of the fluid-elastic deformation of kite wings has not been fully investigated to date. Using an experimentally validated multi-degree-of-freedom dynamic simulation of a MHK kite, we provide the framework of a hydroelastic solver predicting wing deflection and twist and its initial characterization for an approximated wing structure of a 6061-T6 aluminum rectangular tube.

11.2 Methods

In this section, we introduce the dynamic and hydroelastic models for the MHK kite under consideration. The dynamic model simulates the motion of the MHK kite during ground-gen flight and considers hydrodynamic loading from the kite lifting surfaces. The hydroelastic model approximates the hydrodynamic loading from the wing and estimates wing deformation during flight.

11.2.1 Kite Dynamic Model

The dynamic model is of a tethered ground-gen MHK kite executing crosswind figure-eight flight and cyclic spool-in/spool-out tether motion, subject to forces and moments due to lift, drag, buoyancy, and gravity. The kite is spatially constrained to move on the surface of a sphere, following an assumption of a taught tether at all time during flight. The translational and rotational movement of the kite is dictated by the hydrodynamic forces generated by the lifting and control surfaces. The simulated tether is terminated at a ground-fixed winch, which spools-in and spools-out the tether cyclically to generate

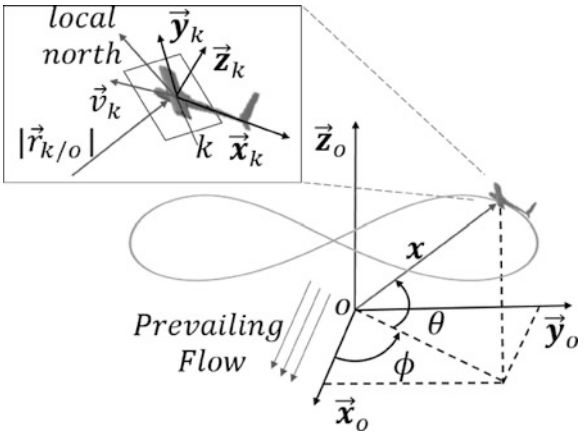

Fig. 11.2 Definition of ground and kite body frames used in the dynamic model. The k and o frame orthonormal coordinate systems, elevation angle θ, azimuth angle ϕ, kite velocity $\vec{v}_k$, as well as the distance from the o frame to the k frame $|r_{k/o}|$ are shown

power. Figure 11.2 defines the ground and kite frame axes and shows an example figure-eight flight path. The dynamic model is built in MATLAB/Simulink. Readers are referred to [15] for a more detailed discussion of the state variables defining the kite motion and controller design.

11.2.2 Hydroelastic Model

The hydroelastic model is an iterative finite-element model and features an elastic and a hydrodynamic solver to predict the deformation and loading of the kite main wing. The wing is analyzed in two halves, a port half and a starboard half, to match the existing dynamic model framework. The wing is symmetric with geometry as outlined in Table 11.1 and has a uniform NACA-2412 airfoil profile. For elastic analysis, the half-wing is first split into m nodes along the span, resulting in $m-1$ finite elements of equal length. For this analysis, the wing is approximated structurally as a cantilevered rectangular tube to match a typical box-beam spar configuration and, for modeling simplicity, is assumed to experience only bending deflections in $\vec{z}$, as defined in Fig. 11.3, and twist about $\vec{y}$.

For each node $n = 0$ to $n = m$, the parameters outlined in Table 11.2 are tracked. Positions y and z and angle ϕ_T are solved for by the elastic solver, detailed below. Local chord length c is linearly interpolated from c_{root} to c_{tip} along the semi-span. Velocity v is provided from the kite dynamic model. Forces L and D and moment M are calculated by the hydrodynamic solver, detailed below. α_{0l} is found for the wing airfoil profile at the local Reynolds number using XFOIL. Force components $L_{\vec{y}_k}$ and $L_{\vec{z}_k}$ are solved using the element deflection angle, θ_n, from node $n-1$ to n.

The elastic model considers L, D, and M at each node and correspondingly deforms the tube. The tube properties outlined in Table 11.3 are considered by the elastic solver for each node. A hybrid analytical-numerical approach is used so that non-

Table 11.1 Wing geometry parameters

Parameter	Description	Value	Units
c_{root}	Root chord length	1	m
c_{tip}	Tip chord length	0.8	m
b	Wingspan	10	m
S	Reference area	9	m^2
AR	Aspect ratio	11.111	–

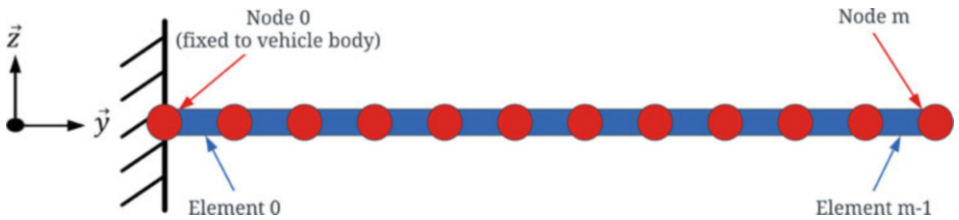

Fig. 11.3 Example of cantilevered tube (blue) split at m nodes (red) and definition of the wing frame. Since each wing is solved for individually, $\vec{y}$ is not necessarily aligned with $\vec{y}_k$

Table 11.2 Values tracked for each node

Variable	Description	Units
y_n	Coordinate along $\vec{y}$	m
z_n	Coordinate along $\vec{z}$	m
c_n	Airfoil chord length	m
v_n	Local flow velocity in the $\vec{x}_k$ direction	m/s
L_n	Lift force	N
D_n	Drag force	N
M_P, n	Pitching moment	N-m
$\alpha_{0l,n}$	Airfoil angle of attack corresponding to zero-lift	deg.
$L_{\vec{y},n}$	Component of lift force in the $\vec{y}$ direction	N
$L_{\vec{z},n}$	Component of lift force in the $\vec{z}$ direction	N
$\phi_{T,n}$	Tube twist	rad.

Table 11.3 Tube structural properties at each node

Parameter	Description	Units
E_n	Elastic modulus	GPa
G_n	Shear modulus	GPa
I_n	Area moment of inertia	m^4

Table 11.4 Elastic solver variables

Variable	Description	Units
P_n	Shear force	N
$M_{B,n}$	Bending moment	N-m
$\theta_{elem,n}$	Element deflection angle	deg.
$\Delta_{elem,n}$	Element length	m
$M_{T,n}$	Twisting moment	N-m
$x_{c/4,n}$	Longitudinal distance between airfoil quarter-chord location and leading edge	m
$x_{E,n}$	Longitudinal distance between tube elastic axis and leading edge	m
b_{CS}	Rectangular tube base length	m
h_{CS}	Rectangular tube height length	m
t_w	Tube wall thickness	m

uniform structural properties along the semi-span can be considered. Each wing element is evaluated as a cantilevered tube fixed at node n and having boundary conditions corresponding to the deflection and twist at node n, enforcing continuity between adjacent elements. The tube nodes are then evaluated sequentially from 1 to m using analytical tube deformation Eqs. (11.1), (11.3), (11.5), (11.6), (11.7), and (11.8) from [16]. Definitions for the terms in these equations are found in Table 11.4. θ_0, y_0, $M_{T,0}$, and ϕ_0 all equal zero. Δ_{elem} is the length of each finite element.

First, the shear force at each node is found as:

$$P_n = P_{n-1} - L_n \tag{11.1}$$

where the shear force at node 0, or root shear force, is:

$$P_0 = \sum_{i=1}^{m} L_i \tag{11.2}$$

Next, bending moment for each node is found as:

$$M_{B,n} = M_{B,n-1} - P_n \Delta_{elem} \tag{11.3}$$

where the bending moment at node 0, or root bending moment, is:

$$M_{B,0} = \sum_{i=1}^{m} L_i \Delta_{elem} \tag{11.4}$$

The deflection angle for the element ending at node n is:

$$\theta_{elem,n} = \theta_{elem,n-1} + \frac{M_n \Delta_{elem}}{E_n I_n} \tag{11.5}$$

The deflection for each node is then solved by:

$$y_n = y_{n-1} + \sin(\theta_{elem,n}) \Delta_{elem} \tag{11.6}$$

To analyze the twist of the beam, first twisting moment at each node is found as:

$$M_{T,n} = M_{T,n-1} + M_{P,n} - L_n (x_{c/4,n} - x_{E,n}) \tag{11.7}$$

And finally, for the case of a cantilevered rectangular tube, the twist at each node is solved by:

$$\phi_{T,n} = \phi_{T,n-1} + \frac{M_{T,n} \Delta_{elem}}{2 A_m^2 G_n t_w} (b_{CS} + h_{CS} - 2t_w) \tag{11.8}$$

where,

$$A_m = (h_{CS} - t_w)(b_{CS} - t_w) \tag{11.9}$$

The hydrodynamic model is split into two subsections, (i) lift and induced drag analysis and (ii) parasitic drag and pitching moment analysis. The lift and induced drag analysis uses classical lifting-line theory (LLT), also known as Prandtl lifting-line theory. The parasitic drag and pitching moment analysis leverages XFOIL to evaluate airfoil coefficients in viscous flow of variable Reynolds number. Induced and parasitic drag are combined to find the total drag on the kite.

Classical LLT was selected for its rapid execution speed so that simulation times of the dynamic model could be minimized. The details of classical LLT can be found in any aerodynamics textbook, such as [17]. LLT approximates the flow around a finite wing with a system of parallel trailing vortex distributions shed from the local flow circulation along the wing. When evaluated, these vortex distributions allow for the solution of lift distribution as well as induced drag along the wing. For the LLT analysis, the wing is split into a different number of nodes, q, which are equally spaced rotationally, as shown in Fig. 11.4. These nodes also do not include either end of the wing. This spacing leads to higher node density towards the wing tips, allowing for wing tip effects to be captured in greater detail. The circulation along the wing is approximated using a Fourier series with q terms as:

$$\Gamma(\theta_L) = 2bV_\infty \sum_{N=1}^{q} A_N \sin(N\theta_L) \tag{11.10}$$

Where A_N are Fourier coefficients, which depend on the geometry of the wing and the wing angle of attack. The lift per unit span, L', can be found at any point along the wing as:

$$L'(y_L) = L'(\theta_L) = \rho V_\infty \Gamma(\theta_L) \cos(\alpha_{ind}(\theta_L)) \tag{11.11}$$

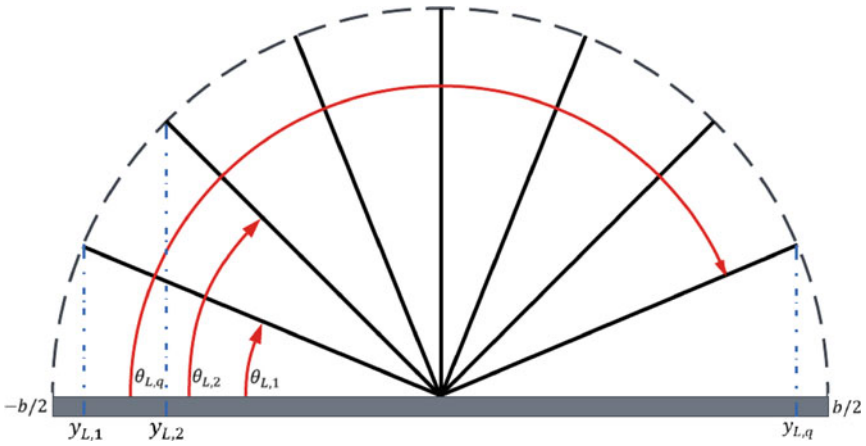

Fig. 11.4 Definition of $\theta_{L,q}$, $y_{L,q}$ for use in LLT. A linear spacing in θ_L allows for a more accurate solution since wing tip effects are captured in greater detail

where $\alpha_{ind}(\theta_L)$ is the induced flow downwash angle at θ_L, ρ is the density of the fluid medium, and V_∞ is the free-stream fluid velocity.

$$\alpha_{ind}(\theta_L) = \sum_{N=1}^{q} \frac{N A_N \sin(N\theta_L)}{\sin(\theta_L)} \tag{11.12}$$

The induced drag, or drag due to lift, D_i, per unit span can also be found and is added to the parasitic drag found during the later XFOIL analysis:

$$D'_{ind}(\theta_L) = \rho V_\infty \Gamma(\theta_L) \sin(\alpha_{ind}(\theta_L)) \tag{11.13}$$

The lift and induced drag per unit span values are linearly interpolated to find their values at each node position, L'_n and $D'_{ind,n}$, then lift and induced drag forces at each node are found by:

$$L_n = L'_n \Delta_{elem} \tag{11.14}$$

$$D_{ind,n} = D'_{ind,n} \Delta_{elem} \tag{11.15}$$

XFOIL [18, 19] is a program used to analyze airfoil profiles at subsonic flow speeds and can solve for both viscid and inviscid flows. XFOIL usage is common in aerospace literature, for example, to evaluate morphing wing UAVs [20, 21], and has been integrated into more comprehensive tools such as XFLR5 [22]. XFOIL version 6.99 was used for this analysis. Airfoil drag and pitching moment coefficients, C_d and C_m, respectively, were pre-generated for a sweep of Reynolds numbers and airfoil angles of attack. Reynolds numbers up to 5e6 and angles of attack of -30 to 30° in steps of 0.1° were evaluated. These sweeps were chosen to match expected flow conditions during simulated flight. Once generated, the C_d and C_m coefficients were tabulated into lookup tables. Knowing the flow conditions across the wing and the vehicle body angle of attack, α_k, from the dynamic model, a Reynolds number (Re) and angle of attack can be found for each node as:

$$Re_n = \frac{v_n c_n}{\nu} \tag{11.16}$$

$$\alpha_n = \alpha_k + \phi_{t,n} \tag{11.17}$$

where ν is the kinematic viscosity of water. The C_d and C_m coefficients at each node are then found using the pre-generated lookup tables, using linear interpolation for Re and angle of attack values not equal to the table breakpoints. Finally, the drag

force and pitching moment are found as:

$$D_n = \frac{1}{2}\rho v_n^2 c_n C_{d,n} \Delta_{elem} + D_{i,n} \tag{11.18}$$

$$M_{P,n} = \frac{1}{2}\rho v_n^2 c_n^2 C_{m,n} \Delta_{elem} \tag{11.19}$$

Once the hydrodynamic forces L_n, D_n, and $M_{P,n}$ are evaluated for all nodes using the hydrodynamic solver, the tube deformation is evaluated using the elastic solver. Of course, since the wing has twisted, α_n has changed at each node and since the wing has deflected, a portion of lift now acts along the $\vec{y}$ axis. The resulting lift components can be found as:

$$L_{\vec{y}} = L_n \sin\theta_{elem,n} \tag{11.20}$$

$$L_{\vec{z}} = L_n \cos\theta_{elem,n} \tag{11.21}$$

The hydrodynamic solver is next re-run as part of an iteration loop to close the hydroelastic solver. The percent difference in deflection, W_{defl}, between two iterations r and $r-1$ is found for each node as:

$$W_{defl,n} = 100\frac{|y_{n,r} - y_{n,r-1}|}{(y_{n,r} + y_{n,r-1})/2} \tag{11.22}$$

and the average percent difference over the wing is found as:

$$W_{defl,avg} = \frac{\sum_{q=0}^{m} W_{defl,q}}{m} \tag{11.23}$$

A similar process is repeated to find the percent difference in twist, W_{twist}, for each node,

$$W_{twist,n} = 100\frac{|\phi_{t,n,r} - \phi_{t,n,r-1}|}{(\phi_{t,n,r} + \phi_{t,n,r-1})/2} \tag{11.24}$$

and averaged over the wing as:

$$W_{twist,avg} = \frac{\sum_{q=0}^{m} W_{twist,q}}{m} \tag{11.25}$$

$W_{defl,avg}$ and $W_{twist,avg}$ are compared against user-set convergence targets, and once met, the iterative process stops and a final deformed wing is reported. Due to the definitions of $W_{defl,avg}$ and $W_{twist,avg}$, at least two iterations must be performed before the convergence criteria can be met. Typically, the solver converges in five or fewer iterations for a 1 percent average percent difference target with a structure containing 30 nodes. If the solver does not converge in a large number of iterations, increasing the number of nodes often corrects this issue. A flowchart overview of the framework for this hydroelastic model can be found in Fig. 11.5.

11.2.3 Hydroelastic Model Integration into the Kite Dynamic Model

The hydroelastic solver was designed in MATLAB/Simulink to fit the existing kite dynamic model framework. The hydroelastic solver is implemented as part of the plant. From the kite dynamic model, the hydroelastic solver is provided with details of the flow, including the flow vectors at the root and tip of the wing and the angle of attack of the vehicle. Combining this with the wing geometry parameters from Table 11.1 and tube parameters from Table 11.3, the hydroelastic solver estimates lift and drag forces on the kite. These forces are returned to the kite dynamic model and considered when simulating the kite motion during closed-loop-controlled spool-in/spool-out figure-eight flight.

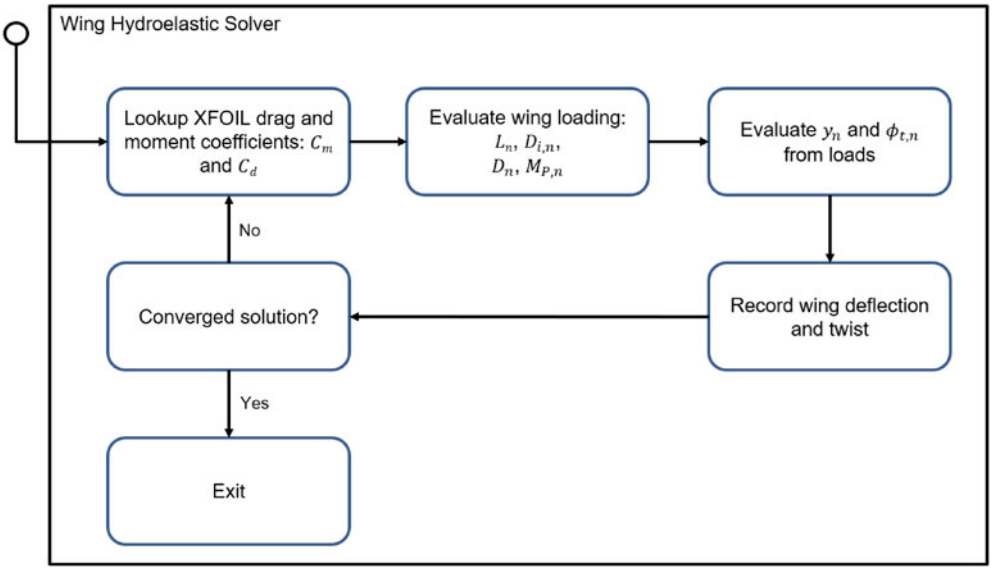

Fig. 11.5 Flowchart of the general framework for the presented iterative hydroelastic solver. This process is run for each wing (port and starboard) on each time step of the dynamic model simulation

11.3 Analysis and Discussion

For this analysis, the wing structure was approximated as a constant cross-section rectangular tube spar with parameters listed in Table 11.5 and having 30 nodes. The wing aerodynamic geometry followed the parameters listed in Table 11.1 and had zero starting twist or sweep. E and G where chosen to match 6061-T6 aluminum, and b_{CS} and h_{CS} were chosen to approximate a box-beam spar that could fit within the airfoil profile; these values are listed in Table 11.5. t_w was swept for a range of values to evaluate the calculation of wing tip deflection and twist for differing wing structure. I was calculated for each t_w using Eq. (11.26) for the case of a rectangular tube. Contributions from the wing skin were ignored in the structural model for simplicity and conservativeness.

$$I = \frac{1}{12} b_{CS} h_{CS}^3 - \frac{1}{12}(b_{CS} - 2t_w)(h_{CS} - 2t_w)^3 \tag{11.26}$$

Figure 11.6 shows expected behavior of periodic deflection and twisting of the wing tip. Also, decreasing wall thickness shows the expected trend of increasing magnitude in wing tip deflection and twist. We see mostly significant positive and some negative deflection of the wing tip, in addition to slight wing tip twist throughout the flight. Figure 11.6 is periodic due to the figure-eight flight of the simulated kite. The deflection is mostly positive due to the velocity augmentation at positive angles of attack across both wings during cross-wind flight; however, when leaving the cross-current pattern, a negative angle of attack can sometimes be experienced leading to negative wing deflection. 6061-T6 is a conventional material for aerospace applications due to its high strength-to-weight ratio. Compared to AWE systems, MHK kites can accommodate larger tube thicknesses, and therefore, higher system weight, due to the medium of operation causing large fluid-dynamic loading. However, total system weight must still be balanced to maintain a typical slight positive buoyancy criteria for MHK kites.

11.4 Conclusions

This work presented a methodology for studying the performance impact on MHK kite power generation when considering fluid-elastic deformation of the kite wings. A hydroelastic solver was developed and integrated into a MHK kite dynamic model configured as a *ground-gen* system. The hydroelastic solver estimates wing tip deflection and twist throughout the spool-in/spool-out figure-eight flight of the simulated MHK kite with a cantilevered rectangular tube approximated structural model. For a 6061-T6 aluminum rectangular tube, large wing tip deflections of up to 24% the wing span and absolute wing tip

Table 11.5 Wing geometry parameters

Parameter	Description	Value	Units
b_{CS}	Rectangular beam base length	0.40	m
h_{CS}	Rectangular beam height length	0.10	m
t_w	Tube wall thickness	Varies	m
E	Modulus of elasticity	69	GPa
G	Shear modulus	26	GPa
I	Area moment of inertia	Varies	m^4

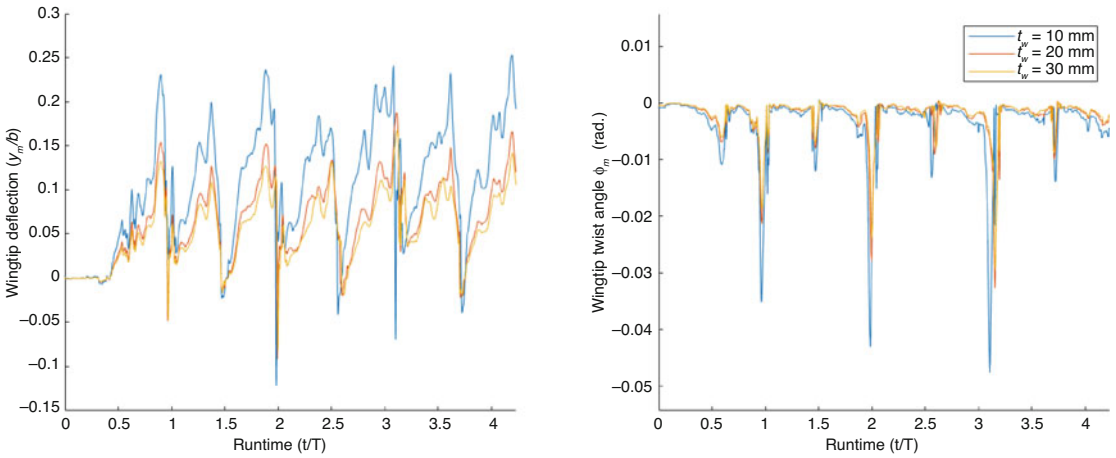

Fig. 11.6 Port wing tip deflection (left) and twist angle (right) for three t_w values. The wing tip deflection is reported as a nondimensionalized value against the wing span b. The time axis is nondimensionalized against the period T of the figure-eight laps ($T = 40$ s). Figure-eight flight starts at $t/T \approx 0.5$. For uniformity, twist values for both wings are reported about the $\vec{y}_k$ axis

twist of up to 2.6° were predicted. This study did not include the wing skin in the hydroelastic analysis, which has potential to carry a large amount of bending and twisting load. Future evolution of the hydroelastic solver should include estimates of material stress and fatigue to further support structural design decisions. The analysis methodology presented here could be used to further understand the impact of wing flexibility on MHK kite controller design and optimization. As well, it has the potential to support accurate and rapid structural design and analysis of a MHK kite wing, reducing material usage and further economically incentivizing the use of energy harvesting kites.

Acknowledgments This research was supported by the North Carolina Coastal Studies Institute, award number DGE-1746939.

References

1. Haas, K.A., Fritz, H.M., French, S.P., Smith, B.T., Neary, V.: Assessment of Energy Production Potential from Tidal Streams in the United States (2011). Georgia Tech Research Corporation, Atlanta
2. Haas, K.A., Fritz, H.M., French, S.P., Neary, V.: Assessment of Energy Production Potential from Ocean Currents Along the United States coastline (2013). Georgia Tech Research Corporation, Atlanta
3. ARPA-E: Arpa-e sharks website
4. LiVecchi, A., Copping, A., Jenne, D., Gorton, A., Preus, R., Gill, G., Robichaud, R., Green, R., Geerlofs, S., Gore, S., Hume, D., McShane, W., Schmaus, C., Spence, H.: Powering the blue economy: exploring opportunities for marine renewable energy in maritime markets. U.S. Department of Energy (2019)
5. Zeng, X., He, R.: Gulf Stream variability and a triggering mechanism of its meander in the South Atlantic Bight. J. Geophys. Res. Oceans **121**, (2016). https://doi.org/10.1002/2016JC012077
6. Windlift: Windlift website (2019)
7. Kitepower: Kitepower website (2022)
8. Minesto: Minesto website (2019)
9. Candade, A.A., Ranneberg, M., Schmehl, R.: Structural analysis and optimization of a tethered swept wing for airborne wind energy generation. Wind Energy **23**(4), 1006–1025 (2020)
10. Bosch, A., Schmehl, R., Tiso, P., Rixen, D.: Dynamic nonlinear aeroelastic model of a kite for power generation. J. Guid. Control Dyn. **37**(5), 1426–1436 (2014)

11. Naik, K., Beknalkar, S.S., Reed, J., Mazzoleni, A., Fathy, H., Vermillion, C.: Pareto optimal and dual-objective geometric and structural design of an underwater kite for closed-loop flight performance. J. Dyn. Syst. Meas. Control **145**(1), 011005 (2022)
12. Shearer, C.M., Cesnik, C.E.S.: Nonlinear flight dynamics of very flexible aircraft. J. Aircraft **44**(5), 1528–1545 (2007)
13. Chang, C.-S., Hodges, D.H., Patil, M.J.: Flight dynamics of highly flexible aircraft. J. Aircraft **45**(2), 538–545 (2008)
14. Ghasemi, A., Olinger, D.J., Tryggvason, G.: Simulation of tethered underwater kites moving in three dimensions for power generation. In: Energy Sustainability, vol. 57595, pp. V001T07A003. American Society of Mechanical Engineers (2017)
15. Cobb, M., Reed, J., Daniels, J., Siddiqui, A., Wu, M., Fathy, H., Barton, K., Vermillion, C.: Iterative learning-based path optimization with application to marine hydrokinetic energy systems. IEEE Trans. Control Syst. Technol. **30**, 639–653 (2021)
16. Beer, F.P., Russel Johnston, E. Jr., DeWolf, J.T., Mazurek, D.F.: Mechanics of Materials. McGraw-Hill, New York (2014)
17. Anderson, J.D.: Fundamentals of Aerodynamics. McGraw-Hill, New York (2011)
18. Drela, M.: Xfoil website (2019)
19. Drela, M.: Xfoil: An analysis and design system for low reynolds number airfoils. In: Mueller, T.J., (ed.), Low Reynolds Number Aerodynamics, pp. 1–12. Springer, Berlin, Heidelberg (1989)
20. Lafountain, C., Cohen, K., Abdallah, S.: Use of xfoil in design of camber-controlled morphing uavs. Comput. Appl. Eng. Educ. **20**(4), 673–680 (2012)
21. Gabor, O.S., Koreanschi, A., Botez, R.M.: Optimization of an unmanned aerial system'wing using a flexible skin morphing wing. SAE Int. J. Aerospace **6**(1), 115–121 (2013)
22. Xflr5 website: (2022)

Chapter 12
A Simplified Finite Element Joint Model Updated with Experimental Modal Features

Jonathan K. Black, Skylar J. Callis, Aaron Feizy, Christopher Lin Johnson, Nicholas A. J. Lieven, and Manuel A. Vega

Abstract Finite element modeling (FEM) and analysis (FEA) are commonly employed for structural design evaluation and iteration. With current technology, full-fidelity modeling of larger assemblies is often computationally prohibitive, requiring simplification of the model's complex features. One such feature that is frequently simplified is the bolted joint, which is ubiquitous in engineering structures. However, approximate methods for modeling joints introduce inaccuracies. To understand this model-induced error, this paper explores a novel, computationally efficient method for the modeling of bolted connections. This method introduces several parameters local to the joints that can be adjusted to improve the accuracy of the model; these parameters define the size of a tied contact area and the properties of a virtual material region. To maintain computational efficiency on complex structures, this method is compatible with a linear, eigenvalue modal analysis. To test this novel method, it was applied to the finite element modeling of bolted connections in a four-story structure. Experimental modal analysis was conducted to validate the FE model. Additionally, Bayesian model calibration was used to quantify the model parameter uncertainties and update geometric and material properties. Overall, this paper presents a viable, experimentally validated method to efficiently model bolted connections in multi-connection structures.

Keywords Model updating · Finite element · Modal analysis · Bolted joints · Bayesian calibration

12.1 Introduction

While bolted connections are ubiquitous across engineering assemblies, there is no standard method to model a bolted connection in FEM. The size of the assembly, the kinds of analysis to be performed, and the behaviors of interest determine the appropriate simplifying assumptions. Often, bolted connections are simplified—or all together eliminated—from the finite element (FE) models of complex assemblies to ensure computational feasibility. However, these simplifications can lead to inaccuracies in the FEM results.

Previous studies of modeling bolted connections have examined methods with a wide array of both fidelity and computational cost [1–4]. One complicating factor in modeling bolted connections is friction. Friction leads to energy dissipation, stick-slip behavior, and nonlinear hysteretic behavior—all of which has historically been difficult to model. Bograd et al. presented a review of joint models which account for these frictional effects [1]. Additionally, Pirdayr et al. applied a thin elasto-plastic interface layer to model a lap joint [2]. Unfortunately, methods that account for energy dissipation or nonlinear stiffness cannot be adopted with a real-valued, linear eigenvalue solver in the frequency domain.

J. K. Black
Department of Mechanical Engineering, Brigham Young University, Provo, UT, USA

S. J. Callis
Department of Mathematical Sciences and Department of Civil, Environmental, and Geospatial Engineering, Michigan Technological University, Houghton, MI, USA

A. Feizy
Department of Aerospace Engineering, Texas A & M, College Station, TX, Texas

C. L. Johnson (✉) · M. A. Vega
W-13 Advanced Engineering Analysis Group, Los Alamos National Laboratory, Los Alamos, NM, USA
e-mail: clj@lanl.gov

N. A. J. Lieven
Department of Aerospace Engineering, University of Bristol, Bristol, UK

M. Allen et al. (eds.), *Special Topics in Structural Dynamics & Experimental Techniques, Volume 5*,
Conference Proceedings of the Society for Experimental Mechanics Series, https://doi.org/10.1007/978-3-031-37007-6_12

Some models of bolted connections attempt to capture model sensitivity to bolt preload. The effective stiffness of a bolted connection is related to the tension in the bolt due to preload; larger preloads generally increase the stiffness of the connection. Kim et al. present four bolt models which account for the effect of bolt preload and the pressure applied to the contact surfaces [3]. These methods include one which models the bolt as a separate body composed of brick elements subjected to an initial strain, two methods for approximating the bolt with beam elements, and another method that applies preload as a distributed force with no bolt. However, none of these methods are applicable to linear eigenvalue analysis, which ignores applied loads and initial stresses. A solution to this issue was proposed by Roberts and Cornwell, who model a bolted connection with bonded contact regions between bolts and members. By varying the size of the circular contact area, they account for the variable bolt preload [4]. Unlike the Kim et al. methods, the Roberts and Cornwell method can be used in linear, eigenvalue-based frequency analysis.

Once a methodology for modeling bolts in a FEM is selected, model updating can be used to improve the agreement between the FEM and experimental results. Model updating endeavors to correct discrepancies between simulation and reality that are due to the uncertainties in the material and geometric properties of a given assembly.

The Bayesian framework has been previously used to update FE models to impose correlation with experimental results. While Marwala applies the Bayesian framework to updating the mass and stiffness matrices directly [5], other authors such as Jensen and Papadimitriou use the Bayesian framework for updating the material properties of a FE model [6]. The Bayesian framework allows for probability distributions of each unknown parameter to be constructed, which can provide insight on the value of updating certain parameters [5].

This paper will examine a novel method of modeling a bolted connection that does not require modeling of the bolts or bolt holes. Inspired by Roberts and Cornwell, the joint is modeled with a tied contact region around the bolt [4]. Additionally, the contact area is extruded through the members to establish a volume of "virtual material" (VM) with properties distinct from the rest of the structure. This technique was designed to be compatible with linear, eigenvalue-based modal analysis to maintain computational efficiency.

To test this novel method, it was applied to the finite element modeling of bolted connections in a four-story structure. Experimental modal analysis was conducted to validate the FE model. Furthermore, Bayesian model updating was used to reduce the uncertainty in the material and geometric properties so that the FE model can correlate better with the experimental results.

12.2 Experimental Modal Tests

The goal of the experimental tests was to determine the natural frequencies and mode shapes of the four-story structure. This experimental data was then used to update and validate the FE model. The experimental setup of the four-story structure was constructed in order to capture all modes of interest, including bending in the axis of excitation, bending perpendicular to the axis of excitation, and torsion. Figure 12.1 shows the labeled components of the test setup in its entirety.

12.2.1 Experimental Setup

The four-story structure, constructed of aluminum, was mounted to a pair of rails with four annular bearings bolted to the bottom floor. The structure was mounted to a large aluminum plate, and the entire assembly was placed on a bed of polystyrene foam in order to isolate it from external noise. Experimentation was conducted in two main ways: with a modal shaker attached at the center of the bottom floor with a stinger parallel to the rails, and with a modal hammer. The shaker stinger was attached to a force transducer which measured the input acceleration. The axis through which the modal shaker excited the structure is referred to as the x-axis. The z-axis is defined to be the axis perpendicular to the x-axis in the plane of the structure's floors. Along the height of the test structure, accelerometers were placed at the center of each floor such that they were oriented with the x-axis; similarly, additional accelerometers were placed oriented with the z-axis. Furthermore, accelerometers facing the z-axis were placed on one of the corners of each floor in order to capture the torsional modes of the structure. This configuration, with its accelerometers in multiple directions, allowed for the measurement of bending modes in the x-axis, z-axis, and in torsion. Furthermore, these accelerometers provided positional data in order to determine the mode shapes and calculate the Modal Assurance Criterion (MAC) number with respect to the FE model. Accelerometer positions can be seen in Fig. 12.2.

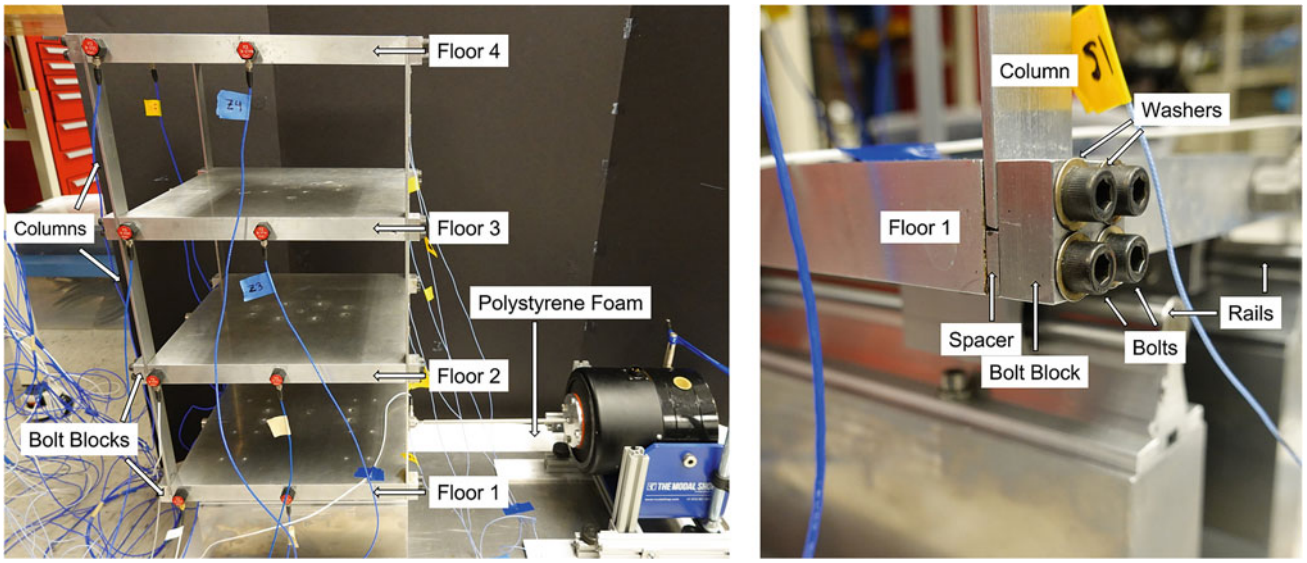

Fig. 12.1 Labeled experimental setup with close-up view of a joint

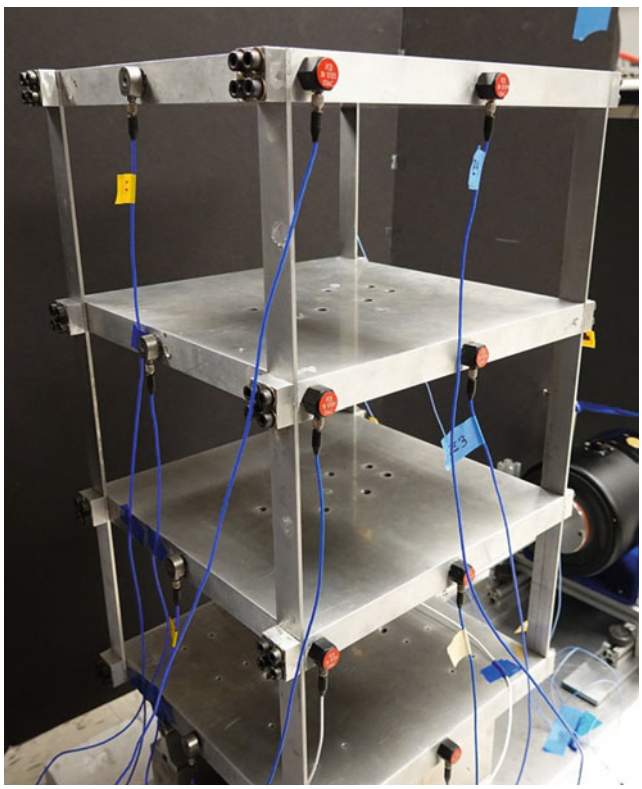

Fig. 12.2 Accelerometer placement on the test structure

12.2.2 Experimental Procedures

In each experimental setup, the quantity of interest was the frequency response function (FRF) from each floor. For the first setup, a white noise input was used to drive the shaker with a frequency limit at 250 Hz. Because the shaker input was white noise, a Hanning window was applied to the input signal in order to process data properly in the frequency domain. The natural frequencies were gathered from the frequency response function of the structure and, along with their phase angles, determined the mode shapes.

The first test configuration captured the first three modes, all of which are bending in the x-axis. To capture modes which are predominantly along the axis perpendicular to the rails (the z-axis), the test structure was disconnected from the modal shaker entirely, and a modal hammer was used to excite the dynamic response of the structure. For this experimental setup, the data acquisition system required a force-exponential window to determine the FRFs of the structure. The structure was struck with the modal hammer on the top floor directly opposite the position of the accelerometer. This input allowed for the largest possible dynamic response from the structure under these conditions. Torsional modes were extracted in a similar manner, where the modal hammer and force-exponential windowing were used to extract the natural frequencies. To extract the torsional modes, the structure was struck on the corner farthest away from the position of the accelerometers in order to more easily cause the structure to rotate while on the rails. Figure 12.2 shows two accelerometers on the top floor on the Z face; the spots on the face directly opposite to these accelerometers are where the structure was hit with the modal hammer for both Z and torsional modes.

These experimental procedures only revealed the first three modes in each direction. Preliminary FEA results demonstrate that these nine modes are the only modes which include the movement of each floor. The remaining modes are those which are column dominant—only columns enter bending modes—or vertically dominant, only the centers of the columns and floors deflect, making a "jellyfish" shape. In the case of the column dominant modes, adding accelerometers to the center of the columns added too much mass and could not be used to reliably determine the response of the structure. The scope of this project, as limited by the dynamics of the test body, restrict analysis to the nine relatively lower modes. These nine modes still describe the dynamics of the system bounded by realistic reactions to realistic excitation. Being a model of a building, high frequency excitation above 400 Hertz (the lower bound of the higher frequency modes) is not realistic at the kind of amplitudes necessary to properly excite the structure. Movement of the whole structure on a floor-by-floor basis is more relevant to the analysis of the simplified bolt model as they describe the relevant structural dynamics of the system with respect to a range of excitation which is likely to occur.

12.2.3 Experimental Results

The natural frequencies and mode shapes of the structure were both obtained by processing magnitude and phase data for each floor. In Fig. 12.3, the magnitude and phase angle of the response is plotted with the natural frequencies marked with a dashed line. Natural frequencies for the first three modes in each direction are shown in Table 12.1.

In the frequency response plots shown in Fig. 12.3, there are several clear peaks which indicate natural frequencies. The X-bending modes are distinct and are bounded very neatly below 50 Hz. The Z-bending and torsional modes have a wider spread and occur in a similar frequency range to each other. The torsional modes were distinguished from the Z-modes by their presence in the FRFs for the corner sensors (Fig. 12.3c) and their absence in the FRFs for the sensors in the center of the faces (Fig. 12.3b). An accelerometer on the corner of a Z-face is expected to measure Z-bending modes as well as torsional modes, while an accelerometer in the center of the Z-face should only measure Z-bending modes. It is important to note the presence of a Z-bending mode at an even lower frequency than any of those in the X direction. This presence of a mode in

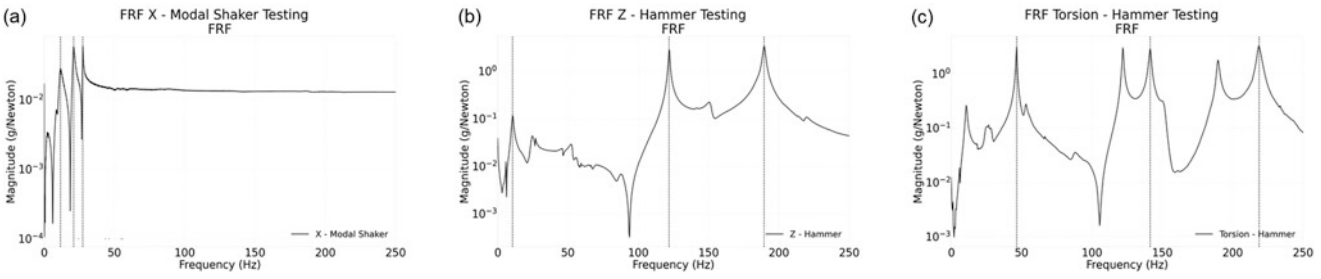

Fig. 12.3 Frequency response functions for (**a**) X-bending modes, (**b**) Z-bending-modes, (**c**) torsional modes

Table 12.1 Natural frequencies for the nine (9) measured modes

	Mode 1	Mode 2	Mode 3
X-Bending	12.12 Hz	20.95 Hz	27.46 Hz
Z-Bending	10.42 Hz	121.9 Hz	189.2 Hz
Torsion	46.36 Hz	141.0 Hz	218.4 Hz

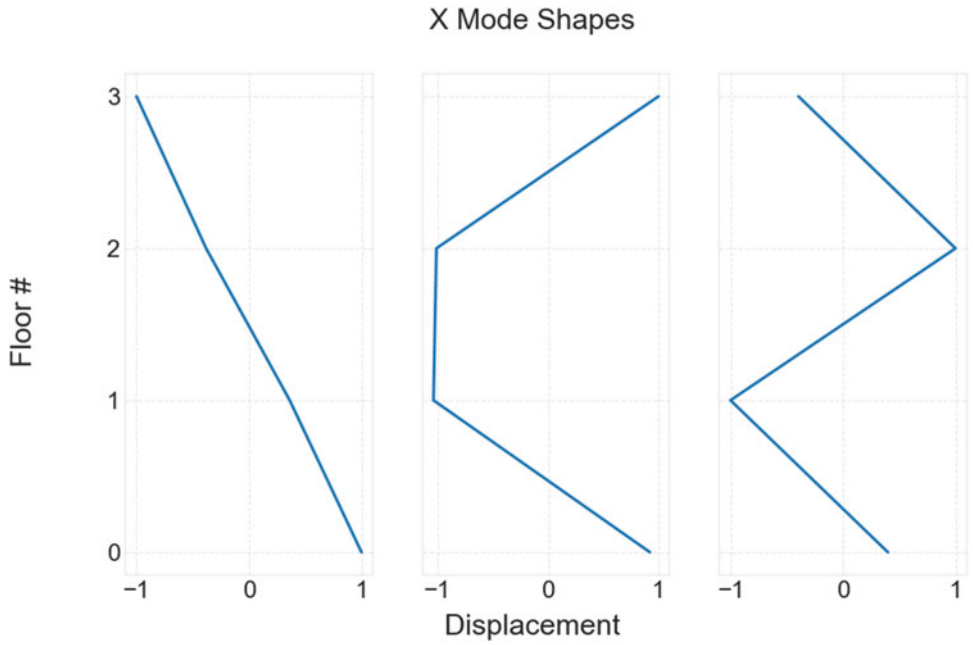

Fig. 12.4 Mode shapes recovered for X-bending modes

the Z-direction at such a low frequency defies intuition, as the columns are much thicker in the Z-axis than in the X-axis. This mode is likely to be the consequence of low frequency "rocking" of the whole structure about the compliant foam base.

Figure 12.4 shows the normalized mode shapes for the X-axis bending modes. The X-axis modes determined from the modal shaker tests are also representative of the mode shapes and order for the other directions. For this reason, only these modes are shown, as both the Z-axis and torsional the mode shapes are similar and follow the same order of appearance. The "straight" bending mode appears first, followed by the "c" shaped mode, and ending with the alternating "zig-zag" pattern.

12.3 Finite Element Modeling

To evaluate the novel joint modeling methodology, two variants of the FE model were created in ABAQUS: a baseline model and a novel model. This section describes the finite element models, their assumptions, and the mesh convergence study. Figure 12.5 shows the geometry of the full assembly side-by-side with the actual structure; this geometry was consistent across both model variants.

12.3.1 Baseline Model

To assess the value of the novel model, a baseline model was developed that follows common practice for low-fidelity modeling of large assemblies with bolted connections.

As discussed in the introduction, the assumptions made when modeling bolted connections depend largely on the scale and purpose of the model. The focus of this paper is on methods for modeling bolted connections which are applicable to large assemblies with potentially thousands of fasteners. Those circumstances call for a defeatured bolt model. Large assemblies often ignore the effects of fasteners entirely, considering the entire interface to be fused, via a tied constraint, so that no relative motion is possible at the interface. Following that standard, the baseline model ties the entire interface wherever there is contact between parts.

The physical structure was mounted on rails with bearings on the base floor, and the rails are mounted to a base plate that is supported by a foam pad, as seen in Fig. 12.1. The largest source of compliance in this boundary condition was the foam pad under the base, and the aspect ratio of the rectangular base plate made it easier to tip in the z-direction than in the x-direction. In order to replicate this unequal angular stiffness at the base, the surfaces on the base plate that corresponded

Fig. 12.5 The actual 4-story structure next to the geometry used in the ABAQUS models

to the area of the bearings were coupled to a central reference point, and that point was attached to ground through five stiff springs—one for every degree of freedom except translation in X, the direction of the rails. A stiffer spring was attached to the rotation about the Z-axis than rotation about the X-axis to account for how the rails constrained the structure's rotation. This setup can be seen in Fig. 12.6.

The spring stiffness of the spring controlling rotation about the X-axis was included as a model updating parameter (see Sect. 12.4) so that the frequency of the first Z mode could be tuned to match the experiment.

The following simplifying assumptions are often made when performing a frequency analysis in FEM and were judged to be of negligible significance:

- Accelerometers and associated wiring were omitted from the model.
- The effects of the structure's own weight were neglected.
- Linear, isotropic material stiffness models were used (i.e., constant Young's modulus).

The natural frequencies predicted by the baseline model are tabulated in Table 12.2. Compared to the experimentally measured frequencies, the root mean squared percent error (RMSPE) of this model is 7.93%.

12.3.2 Parameterized Joint Model

The joint model explored in this paper aimed to achieve higher fidelity than the baseline model without greatly increasing complexity. The basic simplifications and assumptions used in the baseline model were maintained, but several additional features local to the joints were defined in order to capture the contributions of the bolted connections to the dynamics.

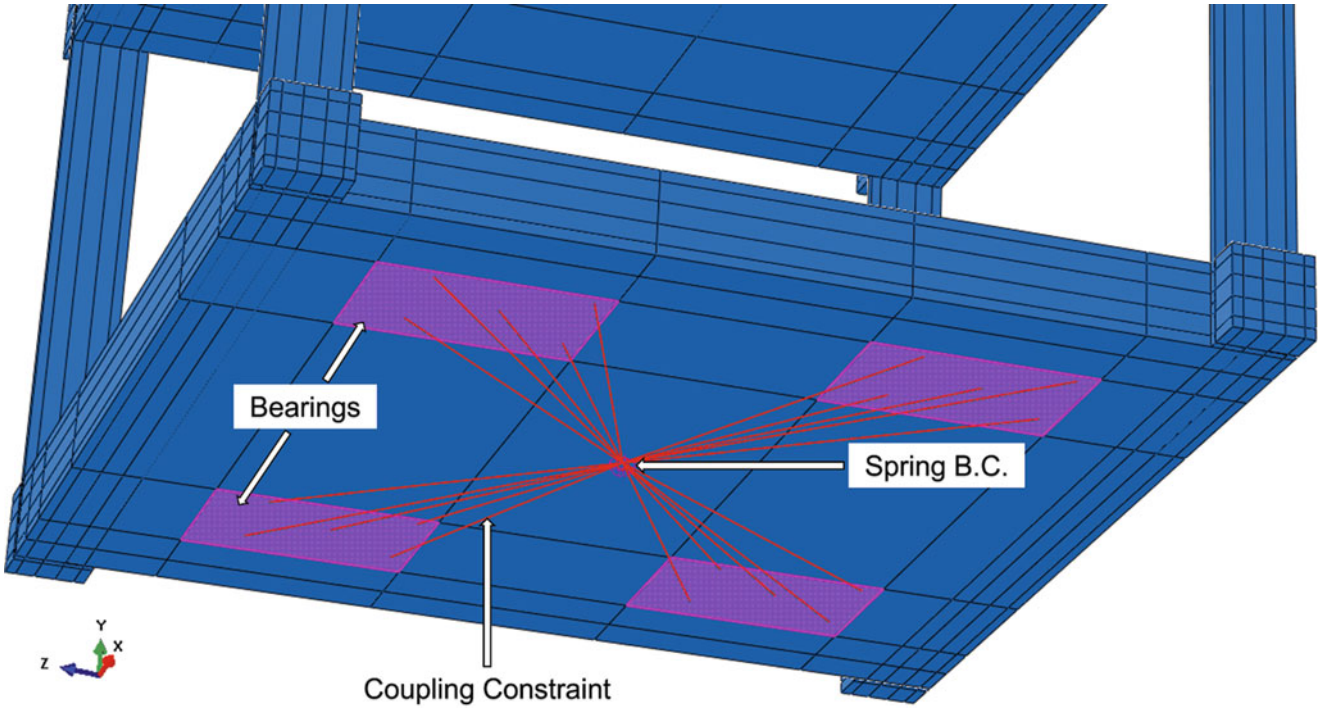

Fig. 12.6 Distributed coupling constraint and spring used to create a non-rigid boundary condition on the base of the structure

Table 12.2 Natural frequencies for the nine modes, according to the baseline model

	Mode 1	Mode 2	Mode 3
X-Bending	11.36 Hz	21.63 Hz	28.27 Hz
Z-Bending	12.26 Hz	119.9 Hz	195.3 Hz
Torsion	50.62 Hz	151.5 Hz	232.7 Hz

Holes, bolts, and threads were not modeled explicitly; instead, bolted connections were modeled as a tied region of variable size. This tied region is referred to henceforth as the contact area. Although the contact area was defined as a square to facilitate meshing with brick elements, the side length of that square, which was chosen as an updating parameter, was called the contact area "diameter", or d.

As discussed by Roberts and Cornwell, varying the area of a tied constraint can model varying bolt pretension [4]. Increasing the contact area increases the joint stiffness comparably to the effects of increasing pretension, as higher pretension causes a larger region of the interface to behave as if it were fused.

The other novel feature of the joint model was a "virtual material" that was assigned to a volume near the contact area. Figure 12.7 shows the regions to which the virtual material is assigned. The partitions created for the contact area were used to define the virtual material volume in all parts through which the bolt passes in the physical structure (bolt blocks, columns, spacers, and floors). The volume extended into the floors approximately the same depth as the tapped holes in the structure. Varying the properties of this virtual material reflects the fact that this volume of the model is occupied in reality by a mixture of aluminum, steel, and air as well as the fact that the effective stiffness of the region will be affected by the characteristics of the bolted connection.

For ease of modeling and to reduce the number of updating parameters, every joint in the structure was assumed to behave identically. This assumption was justified by the fact that every bolt in the physical structure was tightened to the same preload torque.

This model was designed to be compatible with linear, eigenvalue modal analysis, implemented with the Lanczos solver in ABAQUS CAE. Because of the assumptions inherent in the statement of the eigenvalue problem, the model does not account for friction or hysteretic nonlinear stiffness.

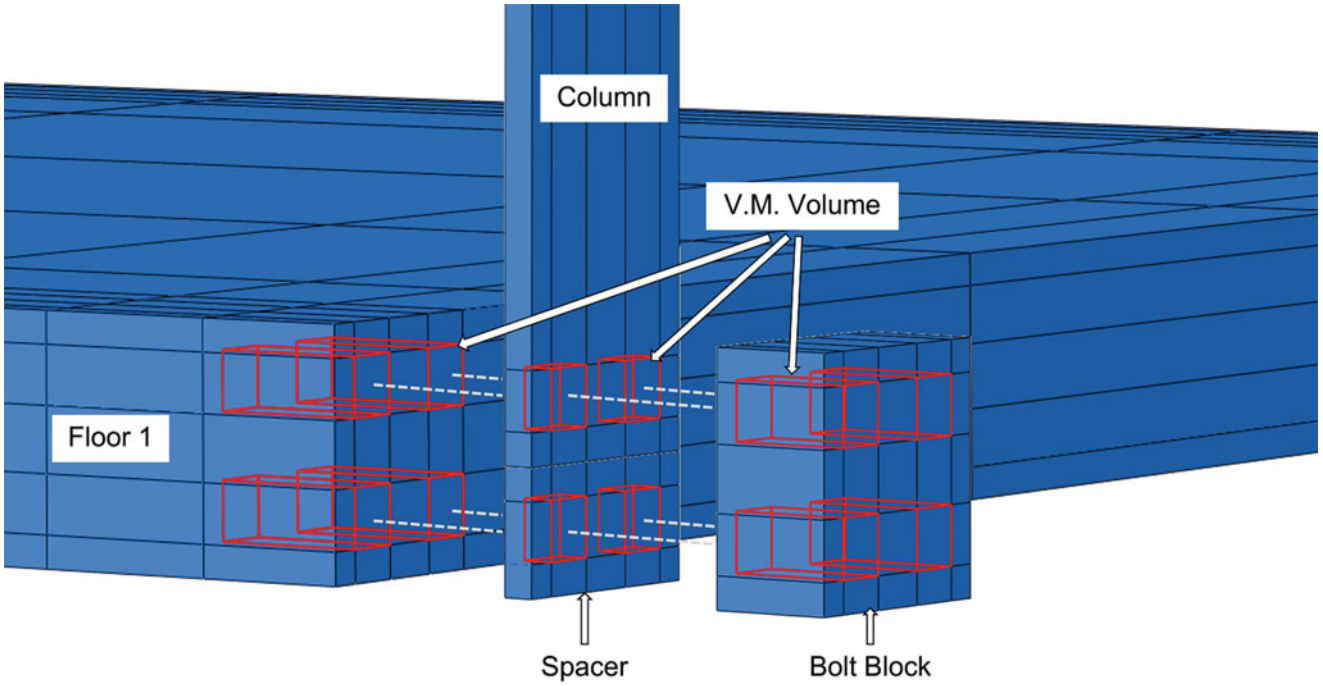

Fig. 12.7 An exploded view of one of the corners of the model, showing the volume to which the virtual material is assigned (Regions outlined in red and labeled "V.M. Volume")

12.3.3 Mesh Convergence Study

Before model updating, a mesh refinement study was performed to investigate the numerical uncertainty introduced by discretization. Hemez and Stull recommend that truncation error be quantified through mesh refinement before attempting model calibration [7]. If the discretization error is large compared to the experimental variability, then any model updating would likely be compensating for that systematic discretization error instead of learning the actual uncertain parameters [7].

The FE model was constructed with C3D8R reduced-integration hexahedral ("brick") elements in ABAQUS CAE. A nonuniform mesh sizing allowed for the possibility of leaving the mesh coarse in low-strain regions, like the floors, while refining it at more critical locations, like the columns and contact areas. For the mesh convergence study, however, uniform refinement ratios in every direction were enforced. Starting with a relatively coarse mesh, the mesh sizing was halved in every direction to produce the medium refinement mesh, which was then halved in every direction again.

The discretization error was assumed to follow a power law relationship such that the frequencies would converge monotonically according to:

$$f \approx f_0 + a\Delta x^p, \tag{12.1}$$

where f_0 is the theoretical continuum solution, a is a constant, Δx is the grid spacing, and p is the rate of convergence. Figure 12.8 shows the error, relative to the extrapolated solution, for the frequencies of each of the nine modes for each mesh. The assumption of monotonic convergence appears to have been violated in the case of Mode z_1, but otherwise held true. The three different types of modes followed noticeable patterns: the X-bending modes all had the same relatively high rate of convergence, the Z-bending modes had lower rates of convergence, and the rate of convergence of the torsional modes seemed to decrease with increasing mode number. It was to be expected that different modes would converge at different rates, as the kinds of loading present vary between modes. Aside from Mode z_1, however, each mode appeared to converge superlinearly.

For the purposes of the updating process, a mesh was identified that could be solved in less than a minute of total CPU time (Intel®Xeon®Gold 5118 CPU @ 2.30GHz [8]) while keeping the discretization error small relative to the experimental uncertainty. The selected mesh had 65,600 elements and had 0.872% RMSPE relative to the extrapolated results from Fig. 12.8. The most erroneous mode, mode x_3, had a 1.51% error. This mesh refinement error (RMSPE = 0.872%) is significantly lower than the modeling error (RMSPE = 7.93%, see Sect. 12.3.1), so model updating could proceed without concerns of the updating process compensating primarily for systematic discretization error.

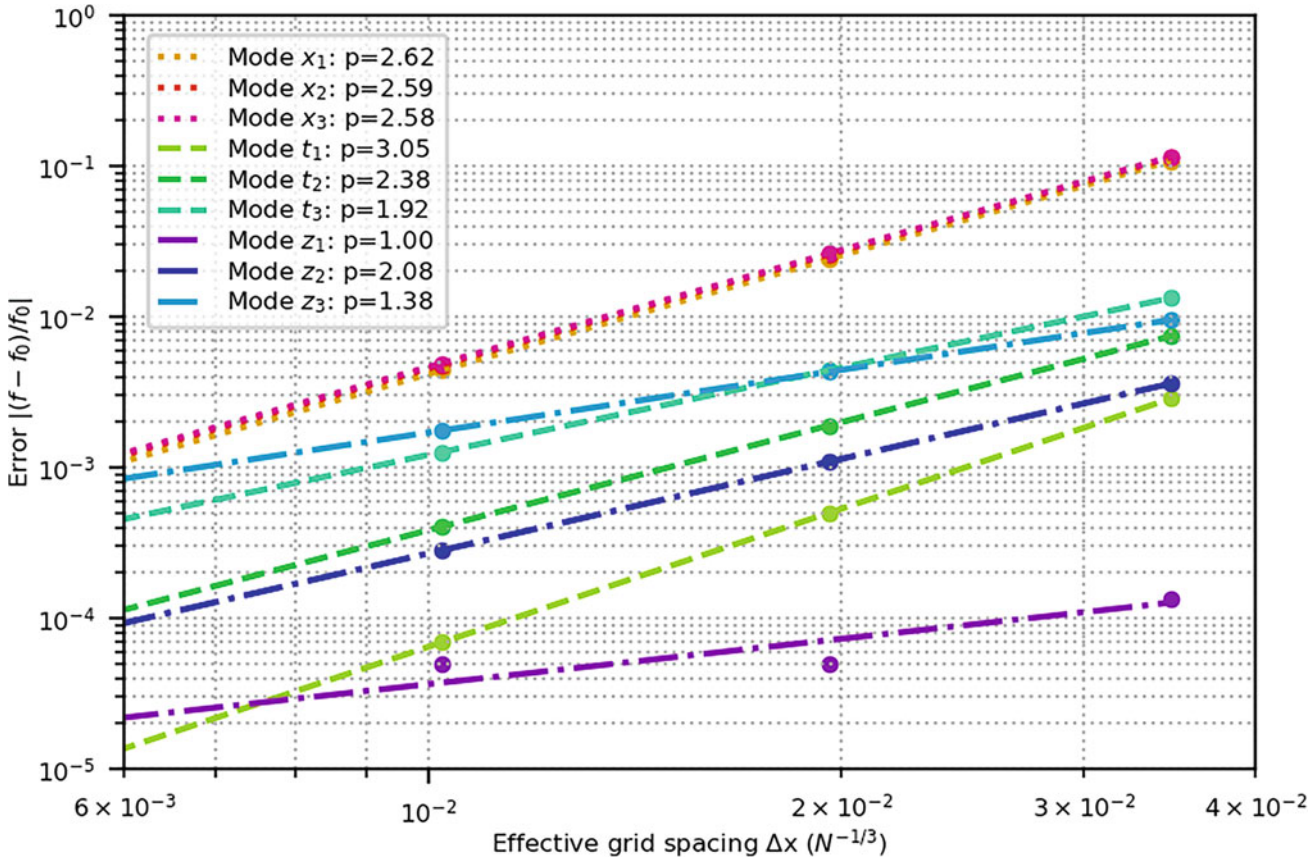

Fig. 12.8 Results of the mesh convergence study. The error is calculated relative to the extrapolated continuum solution. p is the rate of convergence for each mode. The effective grid spacing was calculated as the cubed root of the total number of elements in the model because the actual grid spacing was nonuniform

12.4 Model Updating

To improve the accuracy of the novel model, Bayesian model calibration was used to refine the material and geometric properties of the model. In this process, an analysis of variance (ANOVA) was performed to determine if all of the identified parameters contributed to the model output. Once it was determined that all the parameters were significant, a space-filling algorithm was used to select points in the parameter space. These points were used to fit a linear regression model, which served as a surrogate for the computationally expensive FEM analyses. Using the linear regression surrogate model, Bayesian parameter updating was completed on the six dimensional parameter space. This follows Jensen and Papadimitriou, who used the Bayesian framework for updating the geometric and material properties of a model [6].

12.4.1 Updating Parameters

There were three categories of parameters identified in the novel FEM. Across these categories, six parameters were chosen to update the model. These parameters are:

- Properties of the aluminum
  - Young's Modulus of aluminum (E_{Al})
  - Density of aluminum (ρ_{Al})

Table 12.3 Ranges of updating parameters

	Lower bound	Upper bound	Units
E_{Al}	35	105	GPa
ρ_{Al}	1.35	4.05	$\frac{g}{cm^3}$
d	1.0	11.0	mm
E_{VM}	35	306	GPa
ρ_{VM}	1.35	11.67	$\frac{g}{cm^3}$
k_{BC}	5	50	$10^3 \frac{N*m}{rad}$

- Properties of the novel joint model
  - Contact area "diameter" (d)
  - Young's Modulus of the Virtual Material (E_{VM})
  - Density of the virtual material (ρ_{VM})
- Properties of the boundary condition
  - Spring constant of the boundary condition spring (k_{BC})

The range of values for all of the updating parameters can be seen in Table 12.3.

The first category of updating parameters, the properties of aluminum, are not specific to the novel joint modeling methodology. In all mechanical assemblies, there is some inherent uncertainty in the material properties due to manufacturing variability and other variables. Furthermore, since the four-story structure has been inherited, the exact type of aluminum it is made of is unknown. This causes additional uncertainty beyond typical material variability. The range of aluminum properties explored for this model are based on the average properties of aluminum alloys logged in MatWeb [9]. The lower bound for these properties was taken as 0.5 times the average property, and the upper bound was taken as 1.5 times the average property.

The next category of updating parameters directly impacts the finite element connection representation. These parameters can be further split into two categories: the contact area diameter and the virtual material properties. The range for the contact area diameter was determined by the geometric constraints of the model. It was determined that the smallest geometric resolution in the model would be 1mm. Therefore, the smallest contact area diameter would be 1mm. The largest contact area diameter was selected so that the space between the edge of the contact area and the edge of a part would not be smaller than 1mm.

Since the virtual material does not have a direct physical analog, the property range of the virtual material was selected to be wider than that of aluminum. Physically, the volume that the virtual material occupies contains the threaded hole and the bolt itself. Therefore, some of its volume is aluminum and some of it is steel. However, the virtual material will not have the exact same properties as the bolt steel, since it should also account for the stiffness imparted by the thread contacts and the unmodeled bolt head. The bounds on the material properties of the virtual material were taken to be 0.5 times the properties of aluminum and 1.5 times the properties of steel. As before, the properties of aluminum were taken to be the average aluminum alloy properties [9]. The properties of steel were taken to be the average properties of cold work steel logged in MatWeb [10].

The final updating parameter of the FEM is the spring constant for the boundary condition spring (k_{BC}). The mode that is most affected by this parameter is the first bending mode perpendicular to the rails (mode z_1). It was known that this mode should occur near 10.42 Hz (see Sect. 12.2.3); therefore, the lower and upper bounds for the spring constant were chosen, through trial and error, to place mode z_1 between approximately 5 Hz and 15 Hz.

12.4.2 Space-Filling for FE Model Simulations

In order to explore the space of the FEM updating parameters, points were selected using the space-filling Sobol sequence. The first advantage of using Sobol points is that they are inherently ordered. If a higher number of sampling points are desired, later points can be added to a pre-existing data set. This is not true of pseudo-random algorithms, where the total number of points impacts their locations. Additionally, Sobol sequence sampling yields points that are more evenly distributed in a high dimensional space than a pseudo-random selection of points. Sobol sampling also fills the parameter space using fewer points than a parameter grid sampling.

To retain the balanced properties of Sobol sampling, the number of points should be chosen to be 2^n for an integer n. To examine the parameter space of the novel FEM, $2^{10} = 1024$ samples were used.

For each of the 1024 points in the parameter space, ABAQUS was used to return the FEA mode shapes and frequencies. Before this data could be used in a regression model, the modes had to be ordered to match the experimental modes. Each ABAQUS model returned up to 20 modes between 1 Hz and 600 Hz. From all of these modes, the nine that best matched the experimental data were extracted. To find the ABAQUS modes that best matched experimental data, a modified modal assurance criterion (MAC) was developed.

First, the modes were compared with a traditional MAC matrix. The MAC is defined as:

$$MAC_{ij} = \frac{|\{\Psi_{exp-i}\}^T\{\Psi^*_{fem-j}\}|^2}{\{\Psi_{exp-i}\}^T\{\Psi^*_{exp-i}\}\{\Psi_{fem-j}\}^T\{\Psi^*_{fem-j}\}} \tag{12.2}$$

where MAC_{ij} is the MAC value comparing experimental mode i and FEM mode j, Ψ_{exp-i} is the ith mode shape vector of length m derived from the experimental modal analysis, and Ψ_{fem-j} is the jth mode shape vector of length m derived from the FEM [11]. It is required that both the experimental and FEM mode shape vectors have the same number of degrees of freedom. Since there are more ABAQUS modes than experimental modes, the matrix of MAC values is a rectangle. The top matrix in Fig. 12.9 shows the unmodified MAC matrix for a randomly selected point in the parameter space.

However, because each mode shape vector is of length $m = 12$, there are concerns of spatial aliasing when using the unmodified MAC matrix. To address this concern, a penalty matrix was developed based on the differences between the experimental and FEM frequencies. The penalty matrix is defined as:

$$P_{ij} = \frac{|\omega_{exp-i} - \omega_{fem-j}|}{f_{lim}} \tag{12.3}$$

where P_{ij} is the penalty value comparing experimental mode i and FEM mode j, ω_{exp-i} is the ith frequency derived from the experimental modal analysis, ω_{fem-j} is the jth frequency derived from FEA, and f_{lim} is a frequency limit imposed on the penalty. The frequency limit was chosen to be 200 Hz, which is roughly half of the largest natural frequency identified in FEA. The middle matrix in Fig. 12.9 shows the penalty matrix.

This penalty matrix is subtracted from the MAC matrix to yield the modified MAC. Due to the construction of the penalty matrix, any pair of frequencies with a difference greater than the limit of 200 Hz will be negative. These values are taken to be zero in the modified MAC. The bottom matrix in Fig. 12.9 shows the modified MAC matrix.

From the modified MAC matrix, the maximum value in each row is taken to be the best correlated FEA mode to a given experimental mode. The frequencies of these "best-match" modes are extracted and ordered to correspond to the experimental frequency order. These data points with ordered frequencies can then be used to train the surrogate model.

12.4.3 FE Surrogate Model

A linear regression model was developed as a surrogate for computationally expensive FE model evaluations. This model takes as input the six updating parameters, and outputs nine natural frequencies in the corresponding order to the experimental frequencies. While one ABAQUS FEM analysis runs in approximately one minute, the surrogate model can run 14,414 times in one minute. This makes it ideal for methods such as Bayesian updating, which require thousands of data points.

To capture the nonlinear relationships between the updating parameters and the natural frequencies, the feature space was augmented before linear regression. First, physics-informed relationships were considered. In general, stiffness and mass are related to natural frequency according to the following relationship:

$$\omega_0 = \sqrt{\frac{k}{m}}\,, \tag{12.4}$$

where ω_0 is the natural frequency of a simple harmonic oscillator with stiffness k and mass m. Because the Young's Moduli and the spring stiffness at the boundary condition (k_{BC}) correspond to stiffness, and the densities correspond to mass, the natural frequencies should be proportional to $\sqrt{E_{Al}}$, $\sqrt{E_{VM}}$, $\sqrt{k_{BC}}$, $\frac{1}{\sqrt{\rho_{Al}}}$, and $\frac{1}{\sqrt{\rho_{VM}}}$. Including these physics-informed terms in the feature vector greatly increased the model accuracy. The purely linear model had an r^2 value of 49.818%, while the physics-informed model had an r^2 value of 98.326%. However, investigating the parity plot seen in Fig. 12.10

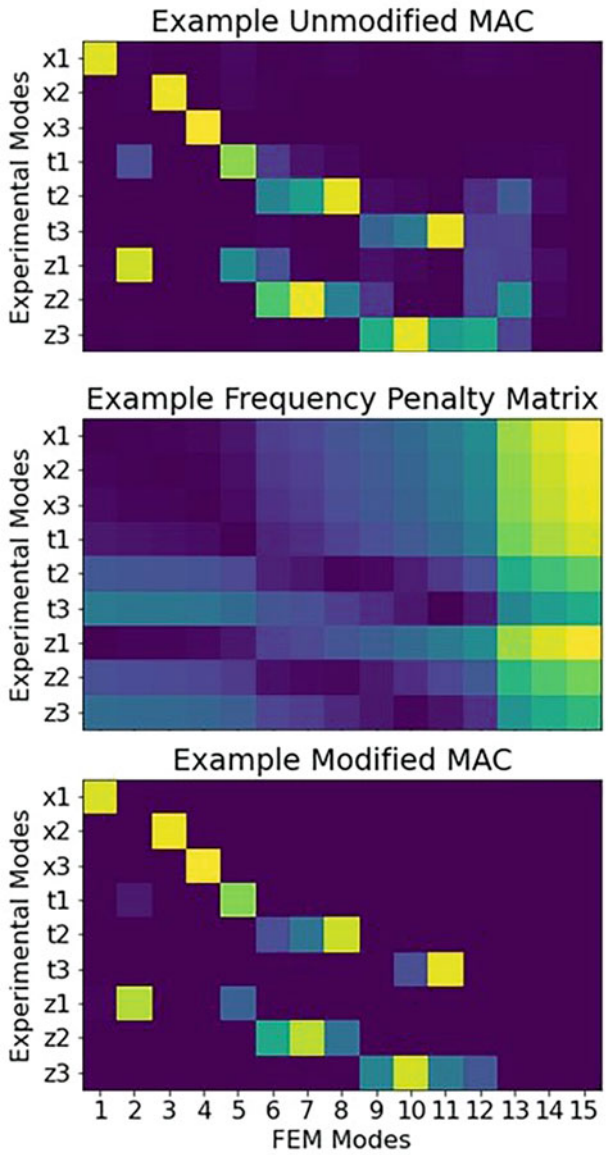

Fig. 12.9 Example MAC, penalty, and modified MAC matrices

revealed systematic curvature in the residuals of this physics-based model. This suggests that it did not fully capture the relationship between the updating parameters and the natural frequencies. It was known that interactions existed between the updating parameters—for example, changing the contact area changed the volume of virtual material and therefore the optimal VM density. Hence, the 15 (6 choose 2) interaction terms between the features were added to the feature vector. This final adjustment eliminated the curvature from the parity plot and increased the r^2 value to 99.683%. All reported r^2 values are average fivefold cross-validation scores on the testing data sets.

12.4.4 Parameter Sensitivity Analysis

In order to confirm that the updating parameters chosen significantly affect the natural frequencies identified, an analysis of variance (ANOVA) was performed. Table 12.4 shows the results of the ANOVA on the six updating parameters. Tables 12.5 and 12.6 show the results for the 15 interaction terms. It can be seen from Tables 12.4 through 12.6 that each of the six

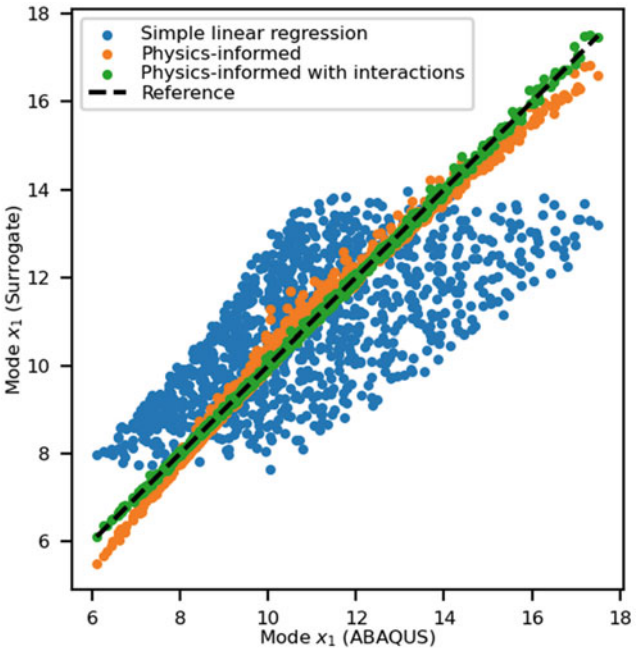

Fig. 12.10 Parity plot for the three iterations of the linear regression model. This plot is for the x_1 mode frequency. The other eight parity plots follow similar trends

Table 12.4 P-values from ANOVA for the 6 main model features. Bolded entries denote statistical significance ($p < 0.05$)

Mode	d	$\sqrt{k_{BC}}$	$\sqrt{E_{Al}}$	$\sqrt{E_{VM}}$	$\frac{1}{\sqrt{\rho_{Al}}}$	$\frac{1}{\sqrt{\rho_{VM}}}$
x_1	**5.6e—6**	9.9e–1	**6.4e–130**	4.1e–1	**3.3e–169**	4.2e–1
x_2	**1.5e–6**	9.9e–1	**3.1e–138**	4.1e–1	**2.8e–158**	4.3e–1
x_3	**9.7e–7**	9.9e–1	**7.0e–138**	4.3e–1	**3.1e–158**	4.3e–1
t_1	**2.0e–15**	9.7e–1	**4.2e–124**	**1.9e–2**	**1.1e–149**	**4.0e–2**
t_2	**1.7e–12**	9.7e–1	**4.9e–128**	**3.3e–2**	**9.0e–152**	**4.0e–2**
t_3	**3.4e–7**	9.7e–1	**5.2e–137**	8.7e–2	**1.8e–153**	**4.0e–2**
z_1	7.4e–1	**8.6e–257**	**1.9e–2**	8.1e–1	**3.9e–78**	5.3e–1
z_2	**1.2e–15**	7.0e–1	**5.4e–118**	**4.1e–2**	**4.4e–161**	3.6e–1
z_3	**2.0e–10**	7.0e–1	**4.0e–127**	8.7e–2	**1.0e–161**	3.6e–1

Table 12.5 P-values from ANOVA for the interaction terms (1–8 of 15) Bolded entries denote statistical significance ($p < 0.05$)

Mode	$d:\sqrt{k_{BC}}$	$d:\sqrt{E_{Al}}$	$d:\sqrt{E_{VM}}$	$d:\frac{1}{\sqrt{\rho_{Al}}}$	$d:\frac{1}{\sqrt{\rho_{VM}}}$	$\sqrt{k_{BC}}:\sqrt{E_{Al}}$	$\sqrt{k_{BC}}:\sqrt{E_{VM}}$	$\sqrt{k_{BC}}:\frac{1}{\sqrt{\rho_{Al}}}$
x_1	**1.0e–4**	**2.0e–27**	**1.5e–5**	**1.9e–32**	**1.7e–5**	**1.5e–26**	6.0e–1	**4.5e–35**
x_2	**3.8e–5**	**1.1e–29**	**5.0e–6**	**5.1e–33**	**6.6e–6**	**8.3e–28**	6.0e–1	**1.8e–33**
x_3	**2.8e–5**	**4.6e–30**	**3.9e–6**	**1.8e–33**	**4.8e–6**	**9.3e–28**	6.2e–1	**1.8e–33**
t_1	**1.2e–11**	**2.5e–46**	**8.2e–16**	**4.8e–51**	**1.5e–15**	**9.8e–26**	1.1e–1	**2.5e–32**
t_2	**1.6e–9**	**3.9e–41**	**5.9e–13**	**2.9e–45**	**3.8e–13**	**2.4e–26**	1.5e–1	**1.2e–32**
t_3	**1.2e–5**	**7.8e–31**	**9.4e–8**	**1.5e–33**	**1.5e–8**	**1.1e–27**	2.5e–1	**6.8e–33**
z_1	**4.2e–40**	3.4e–1	6.9e–1	**1.8e–8**	4.4e–1	**2.7e–188**	**1.3e–97**	**0.0e+0**
z_2	**2.2e–12**	**3.1e–46**	**1.3e–15**	**1.1e–53**	**7.8e–13**	**2.4e–26**	1.0e–1	**8.1e–36**
z_3	**2.2e–8**	**7.5e–37**	**1.3e–10**	**1.9e–42**	**5.0e–9**	**1.3e–27**	1.6e–1	**7.2e–36**

updating parameters and their 15 interactions is statistically significant ($p < 0.05$) for at least one of the nine modes. It is also evident that different parameters are most significant for different modes. For example, the density of the virtual material (ρ_{VM}) is most significant in the torsional modes. Additionally, the boundary condition spring, k_{BC}, is only significant in mode z_1, the quasi-rigid-body rotation about the base due to the foam support.

Table 12.6 P-values from ANOVA for the interaction terms (9–15 of 15) Bolded entries denote statistical significance ($p < 0.05$)

Mode	$\sqrt{k_{BC}} : \frac{1}{\sqrt{\rho_{VM}}}$	$\sqrt{E_{Al}} : \sqrt{E_{VM}}$	$\sqrt{E_{Al}} : \frac{1}{\sqrt{\rho_{Al}}}$	$\sqrt{E_{Al}} : \frac{1}{\sqrt{\rho_{VM}}}$	$\sqrt{E_{VM}} : \frac{1}{\sqrt{\rho_{Al}}}$	$\sqrt{E_{VM}} : \frac{1}{\sqrt{\rho_{VM}}}$	$\frac{1}{\sqrt{\rho_{Al}}} : \frac{1}{\sqrt{\rho_{VM}}}$
x_1	5.2e–1	**6.1e–32**	**0.0e+0**	**4.9e–24**	**1.6e–41**	2.6e–1	**3.1e–31**
x_2	5.2e–1	**2.2e–33**	**0.0e+0**	**5.3e–25**	**1.1e–39**	2.7e–1	**8.0e–30**
x_3	5.2e–1	**3.6e–33**	**0.0e+0**	**5.8e–25**	**1.6e–39**	2.7e–1	**8.0e–30**
t_1	1.1e–1	**5.4e–39**	**0.0e+0**	**5.1e–29**	**3.8e–47**	**2.4e–3**	**1.8e–35**
t_2	1.1e–1	**1.4e–38**	**0.0e+0**	**1.3e–29**	**3.2e–46**	**3.7e–3**	**8.6e–36**
t_3	1.1e–1	**5.4e–38**	**0.0e+0**	**7.5e–31**	**5.1e–44**	**8.4e–3**	**4.8e–36**
z_1	**9.8e–79**	1.8e–1	**5.8e–50**	1.1e–1	**3.0e–21**	5.2e–1	**1.8e–17**
z_2	3.4e–1	**4.2e–36**	**0.0e+0**	**6.4e–23**	**1.9e–47**	5.0e–2	**7.8e–31**
z_3	3.3e–1	**4.0e–36**	**0.0e+0**	**3.8e–24**	**1.4e–45**	**7.7e–2**	**7.1e–31**

12.4.5 Bayesian Parameter Updating

Since all six of the updating parameters were deemed significant by the ANOVA, they were all considered as model updating parameters. The Bayesian updating framework was used to refine the distributions of the unknown parameters. The priors for these parameters were uniform distributions truncated at the bounds defined in Table 12.3. Additionally, the error between the experimental and FEM results, σ, was also taken as an updating parameter. The prior of σ was taken to be the exponential log-likelihood function:

$$f(x|\lambda) = \lambda e^{-\lambda x} \tag{12.5}$$

where $\lambda = 1$. The Bayesian process uses the linear regression model discussed in Sect. 12.4.3 as a surrogate for ABAQUS results. It updates the parameters based on all nine experimentally identified natural frequencies. The Python packages Theano and Pymc3 were used to step through the Bayesian updating process [12, 13]. Sample sizes were set at 15,000 for the prior draws, 5000 for the posterior draws, and 5000 for the posterior tune.

To evaluate the success of the Bayesian updating process, the prior predictive and posterior predictive distributions were examined. The prior predictive distributions are defined by the frequency output of points sampled from the prior distributions. The posterior predictive distributions are defined by the frequency output of points sampled from the normal posterior distributions calculated through Bayesian updating. If the Bayesian updating process was successful, the mean of the posterior predictive distribution should be closer to the experimental natural frequency and the standard deviation of the posterior predictive distribution should be smaller. This represents more certainty in the values of the updating parameters and therefore more certainty in the correct natural frequency output.

When Bayesian updating was applied to the surrogate model updating on all six parameters, the prior predictive and posterior predictive distributions looked very similar. The prior predictive and posterior predictive for each of the nine natural frequencies are shown in Fig. 12.11. These distributions indicate that very little information was "learned" through the Bayesian updating process, as the margins for uncertainty remained the same. This may be due to the non-uniqueness of the solution in six dimensional space. The Bayesian updating process assumes that the correct values for the unknown parameters are unimodal. However, since updating was occurring on all of the mass and stiffness terms, there are many solutions yielding the same frequency output. As seen in Eq. 12.4, if both the stiffness and mass term are doubled, the natural frequency remains the same.

In order to address this issue, the density of aluminum (ρ_{Al}) was experimentally measured and found to be $2.688 \frac{\text{g}}{\text{cm}^3}$. The Bayesian updating process was applied again to the five-dimensional parameter space, holding ρ_{Al} constant. This removed the non-uniqueness problem for the value of E_{Al}, and possibly for the other parameters as well. The posterior predictive distributions in this case did show improvement of the prior predictive distributions, as seen in Fig. 12.12. The standard deviations are smaller for all nine frequencies, and the means are either closer to the experimental frequency or showed no change.

The posterior distributions calculated after performing Bayesian updating on five parameters are described in Table 12.7. The density of aluminum was held constant at $\rho_{Al} = 2.688 \frac{\text{g}}{\text{cm}^3}$ based on experimental measurements.

The natural frequencies for each of the nine modes are tabulated in Table 12.8, comparing the experimental frequencies to the baseline FEA model and the updated novel FEA model. For the updated model, the updating parameters were set to the mean of the posterior distribution defined in Table 12.7. The RMSPE was calculated relative to the experimental frequencies.

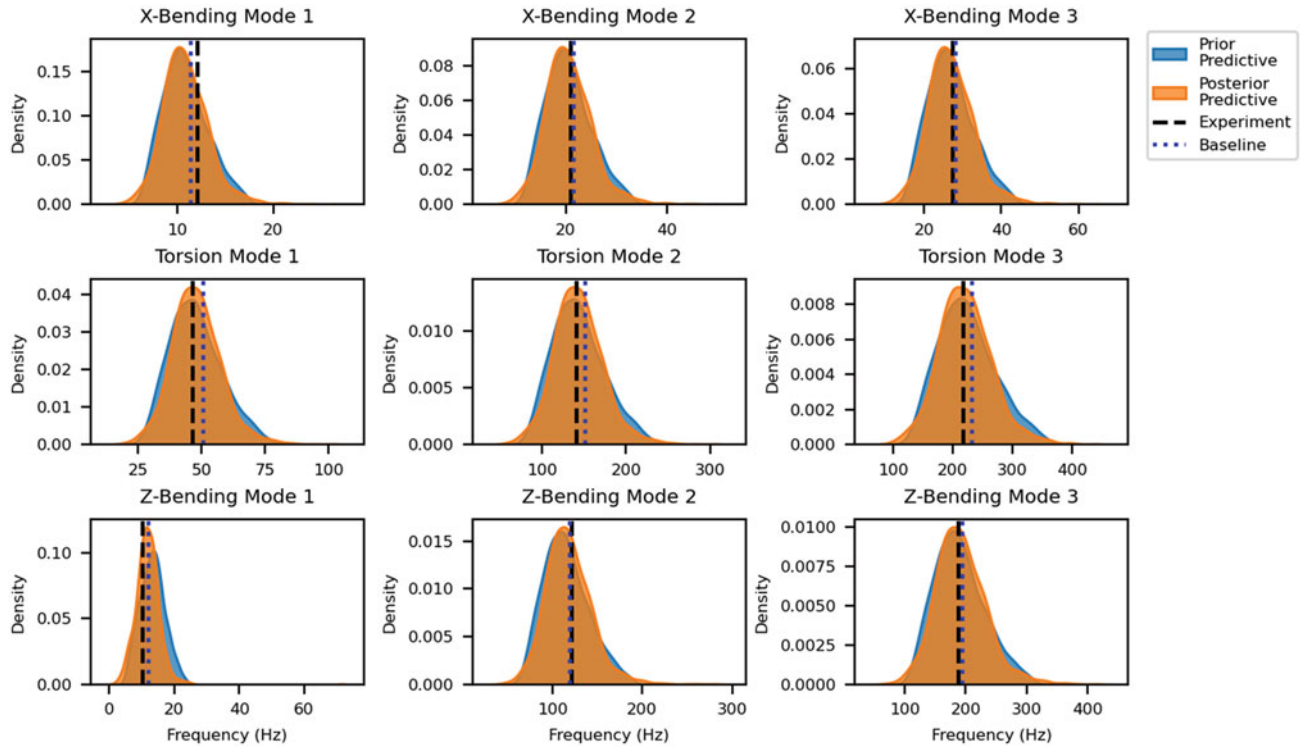

Fig. 12.11 Prior and posterior predictive distributions, updating on all six parameters

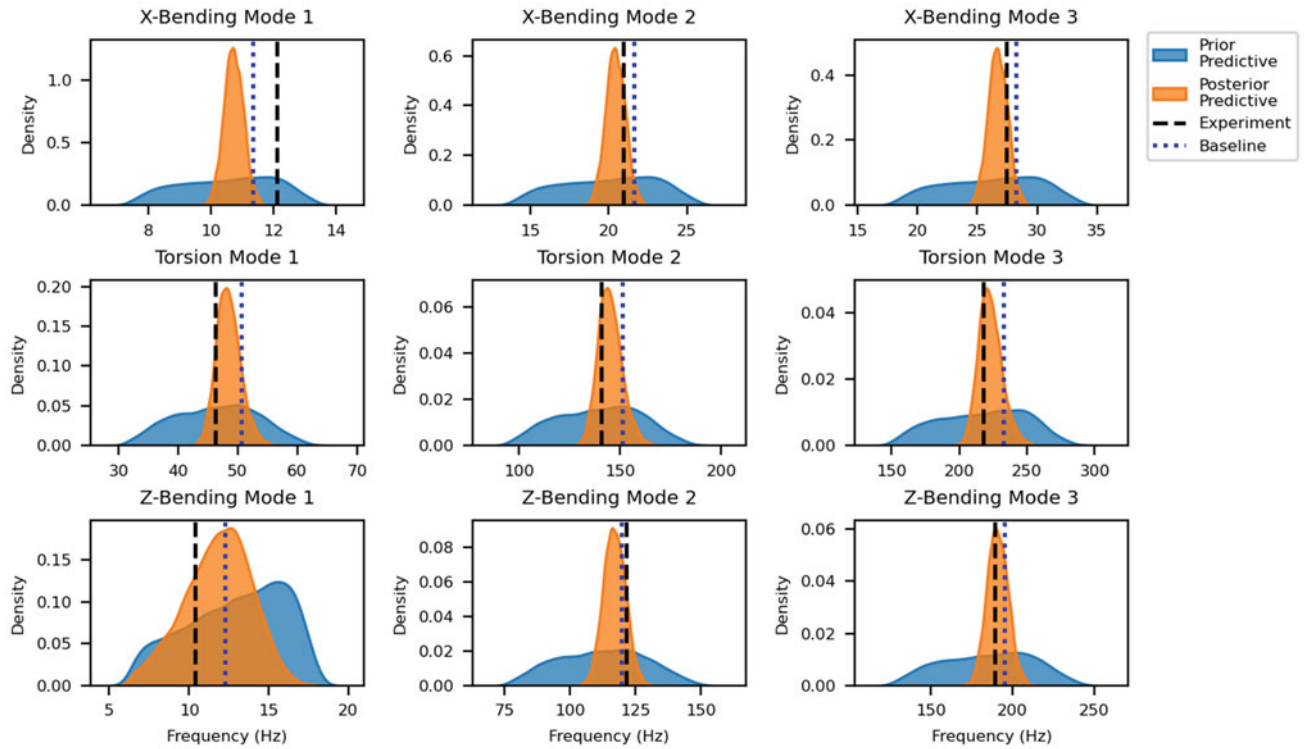

Fig. 12.12 Prior and posterior predictive distributions, updating on five (5) parameters, holding ρ_{Al} fixed

Table 12.7 Posterior and prior distributions for the five (5) updating parameters

	Mean μ	Standard deviation σ	Prior distribution	Units
E_{Al}	67.08	3.482	35–105	GPa
d	9.401	1.405	1.0–11.0	mm
E_{VM}	171.0	76.62	35–306	GPa
ρ_{VM}	8.989	1.993	1.35–11.67	$\frac{g}{cm^3}$
k_{BC}	21.35	8.684	5–50	$10^3 \frac{N*m}{rad}$

Table 12.8 Natural frequencies as measured, according to the baseline model, and according to the updated novel model. Percent error was calculated relative to the experimentally measured frequencies

	Mode	Experiment	Baseline model (% Error)	Updated model (% Error)
X modes	x_1 (Hz)	12.12	11.36 (−6.29%)	10.72 (−11.59%)
	x_2 (Hz)	20.95	21.63 (3.26%)	20.37 (−2.77%)
	x_3 (Hz)	27.46	28.27 (2.95%)	26.63 (−3.04%)
Torsion modes	t_1 (Hz)	46.36	50.62 (9.20%)	47.84 (3.19%)
	t_2 (Hz)	141.0	151.5 (7.47%)	143.3 (1.65%)
	t_3 (Hz)	218.4	232.7 (6.56%)	220.3 (0.88%)
Z modes	z_1 (Hz)	10.42	12.26 (17.61%)	11.91 (14.31%)
	z_2 (Hz)	121.9	119.9 (−1.61%)	117.1 (−3.96%)
	z_3 (Hz)	189.2	195.3 (3.24%)	190.7 (0.81%)
RMSPE			7.93%	6.55%

While Bayesian updating shows promise once the non-uniqueness has been addressed, a more thorough investigation is needed. When Bayesian updating on six (6) parameters was examined, the prior predictive distribution was defined through the Sobol space-filling points. Additionally, both the prior predictive and posterior predictive distributions used ABAQUS evaluations to determine the frequencies. Due to time constraints, the Bayesian updating process on five (5) parameters was less rigorous. In this case, the prior predictive was defined by randomly sampling from the uniform prior distributions. Both the prior predictive and posterior predictive distributions used the linear regression surrogate model instead of ABAQUS evaluations. These shortcomings lead to less certainty in the results of the Bayesian updating performed on five (5) updating parameters.

12.5 Conclusions

This paper outlines the implementation and parameter updating of a novel methodology for modeling bolted connections in FEA. The proposed combination of tied contact areas and virtual material region shows promise as a computationally efficient method for modeling bolted connections in complex assemblies. For the four-story assembly examined here, implementing this novel joint model reduced the error by 1.38% from a baseline model with tied constraints at all contact regions.

To identify the unknown parameters that define the contact area and virtual material, Bayesian parameter updating was utilized. However, Bayesian updating becomes infeasible if the solution space for the unknown parameters is multimodal. It is recommended to fix at least one parameter related to the mass or stiffness of the structure to avoid this issue. The density of the bulk material is suggested to be fixed, as this value can usually be easily determined experimentally.

12.6 Future Work

To further develop this bolt modeling methodology, there are multiple improvements suggested. One such simple improvement would be to define the virtual material stiffness properties as anisotropic. Since the virtual material represents the bolts, it reasonably would not have uniform and isotropic properties. By adding another virtual material stiffness property to update on, this model may better account for the behavior at the joints.

It is also suggested to test how much experimental data is required for the successful updating of the model. This paper uses all nine experimentally determined modes during the Bayesian parameter updating process. It is possible that only a

subset of modes are necessary to update the unknown parameters with similar accuracy to what was achieved in this paper. To identify which experimental modes should be selected, it is suggested to examine the modes with high strain energy near the bolted connections.

Alternatively, if a high-dimensional space is desired either as an updating parameter space or as an output space, it is recommended that principal component analysis (PCA) be used to reduce the dimensionality. A high dimensional output space would be desirable if the model were to be validated on the mode shapes as well as the natural frequencies. Following the procedures of Chen et al., PCA could be used to make updating in these high dimensional spaces more feasible [14].

Further work is also suggested to develop an empirical formula for the novel joint model updating parameters. Such a formula would relate bolt size, preload, and material to FEM contact area, virtual material Young's modulus, and virtual material density. If such a formula were validated, it could accelerate or bypass the model updating and Bayesian updating on the joint model parameters. Additionally, this may help with the non-uniqueness problem posed to the Bayesian updating. By greatly reducing the size of the priors for the joint model parameters, there may be more success in updating the remaining model parameters.

Acknowledgments This research was funded by Los Alamos National Laboratory (LANL) through the Engineering Institute's Los Alamos Dynamics Summer School. The Engineering Institute is a research and education collaboration between LANL and the University of California San Diego's Jacobs School of Engineering. This collaboration seeks to promote multidisciplinary engineering research that develops and integrates advanced predictive modeling, novel sensing systems, and new developments in information technology to address LANL mission relevant problems.

The authors would like to thank the Los Alamos Dynamic Summer School (LADSS) program for giving them the opportunity to complete this research. Special thanks are given to Adam Wachtor, Skylar Richmond Friesen, and Chuck Farrar for facilitating the program.

Additional thanks are given to François Hemez for his time lecturing to LADSS and his time consulting on the mesh refinement study.

References

1. Bograd, S., Reuss, P., Schmidt, A., Gaul, L., Mayer, M.: Modeling the dynamics of mechanical joints. Mech. Syst. Signal Process. **25**(8), 2801–2826 (2011)
2. Pirdayr, A., Mohammadi, M., Kazemzadeh-Parsi, M.J., Rajabi, M.: Self-loosening effects on vibration characteristics of plates with bolted joints: an experimental and finite element analysis. Measurement **185**, 109922 (2021)
3. Kim, J., Yoon, J.-C., Kang, B.-S.: Finite element analysis and modeling of structure with bolted joints. Appl. Math. Model. **31**, 895–911 (2007)
4. Roberts, T., Cornwell, P.J.: An investigation of vibrational characteristics of lap joints using experimental and analytical methods. In: Conference Proceedings of the Society for Experimental Mechanics Series. Springer, Cham (2021)
5. Marwala, T.: Finite-Element-Model Updating Using a Bayesian Approach, pp. 183–201. Springer London, London (2010)
6. Jensen, H., Papadimitriou, C.: Bayesian Finite Element Model Updating, pp. 179–227. Springer International Publishing, Cham (2019)
7. Hemez, F.M., Stull, C.J.: On the legitimacy of model calibration in structural dynamics. In: Conference Proceedings of the Society for Experimental Mechanics Series. Springer New York (2012)
8. Intel®Xeon®Gold 5118 Processor: https://ark.intel.com/content/www/us/en/ark/products/120473/intel-xeon-gold-5118-processor-16-5m-cache-2-30-ghz.html
9. MatWeb: Aluminum Alloys, General. https://www.matweb.com/search/DataSheet.aspx?MatGUID=e3ec70f03a754733bad2f2a471ab9b61&ckck=1
10. MatWeb: Overview of materials for cold work steel. https://www.matweb.com/search/DataSheet.aspx?MatGUID=35ad17f3e1cc4ad598184f227669a24c
11. Allemang, R.J.: The modal assurance criterion - twenty years of use and abuse. Sound Vib. **37**, 14–23 (2003)
12. "Theano". https://theano-pymc.readthedocs.io/en/latest/.
13. PyMC. https://www.pymc.io/welcome.html
14. Chen, X., Shen, Z., Liu, X.: A PCA-based approach for structural dynamics model updating with interval uncertainty. Acta Mech. Solida Sin. **32**(1), 105–119 (2019)

Chapter 13
Efficient Methods for Flexibility-Based Meso-scale Dynamic Modeling

Raj Pradip Khawale, Suparno Bhattacharyya, Dustin Bielecki, Rahul Rai, and Gary Dargush

Abstract With the advent of additive manufacturing comes the opportunity to design novel components and systems, especially when one considers hierarchical structures. Our recent work Bielecki et al. (Struct Multidiscip Optim 64(6):3473–3487, 2021); Bielecki et al. (Multiscale compliant topology optimization for twistable wing design. In: AIAA AVIATION 2021 FORUM (2021), pp. 2429) has demonstrated a highly effective framework of multi-scale topology optimization for designing such structures. In this work, we focus on enhancing the efficiency of the analysis at the meso-scale by introducing a new complementary energy formulation. This enables the computationally attractive formulation of parametrically defined filament-based meso-structures of arbitrary path within each unit cell. We have implemented this framework for dynamical problems, specifically, for modal analysis. We considered mass lumping and static condensation within the unit meso-scale cells. Computational experiments are provided to test the robustness, accuracy, and computational efficiency of the approach.

Keywords Modal analysis · FEM · Structural dynamics · Computational mechanics · Energy-based method

13.1 Introduction

Development in additive manufacturing allows designing of complex hierarchical structures, such as Voronoi forms, lattice structures, and triply periodic minimal surfaces. Interesting applications involve compliant, auxetic, band-gap structures, contemporary architectures, and bone regeneration, to name a few. For such applications, we need a process to design the best possible structures that follow given conditions and constraints. Topology optimization (TO) is a technique that minimizes an objective function by following the constraints such as volume fraction and allowable stress. The optimization process involves performing forward analysis, finding the sensitivity of the objective function to the design variables, and updating parameters in every iteration during inverse analysis [1].

This extended abstract discusses a new method for the forward analysis of the static and dynamic TO problems without solving computationally expensive high-dimensional multi-scale finite element models. The method is based on the idea of complementary energy (CE). Our recent works [2, 3] demonstrated an effective framework for multi-scale TO under statically applied loads by combining the concepts of engineering mechanics and deep learning. In the present work, we extend the CE-based framework to consider dynamical problems, specifically, modal analysis, and show the accuracy of the framework by comparing the analysis results with that of the commercial finite element code Abaqus.

13.2 Analysis Framework

A typical approach for predicting optimal topology of a mechanical element is to construct a composite using periodic repetition of unit cells to determine the effective material properties of the composite, using homogenization theory [4]. Here

R. P. Khawale (✉) · S. Bhattacharyya · D. Bielecki · R. Rai
Department of Automotive Engineering, Clemson University, Greenville, SC, USA
e-mail: rkhawal@g.clemson.edu; suparno.bhattacharyya@gmail.com; dbielec@g.clemson.edu; rrai@clemson.edu

G. Dargush
Department of Mechanical Engineering, University at Buffalo, Buffalo, NY, USA
e-mail: gdargush@buffalo.edu

M. Allen et al. (eds.), *Special Topics in Structural Dynamics & Experimental Techniques, Volume 5*,
Conference Proceedings of the Society for Experimental Mechanics Series, https://doi.org/10.1007/978-3-031-37007-6_13

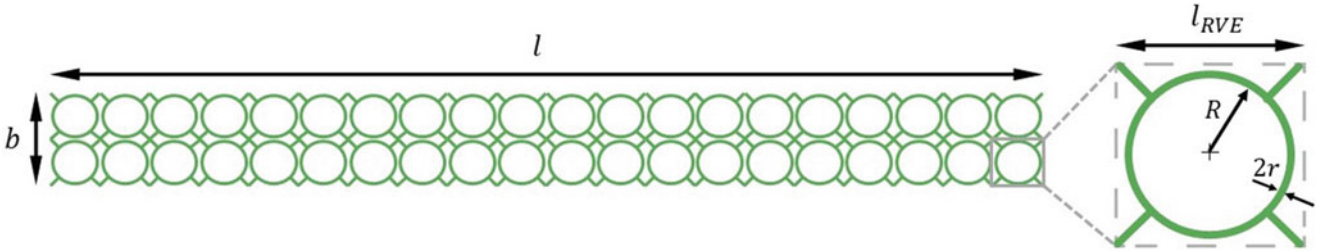

Fig. 13.1 Modeling of a beam of non-dimensional length $l = 1$, width $b = 0.1$, and thickness $t = 0.0001$ using an assembly of 20×2 repeating unit cells. Each unit cell contains a circular loop of radius R having a tube radius of r along with four equi-spaced straight anchors of equal length. The distance between the outer end-points of the anchors is given by l_{RVE}. For this case $R = 0.0225$, $r = 0.006$

we choose unit cells as parametrically defined filament curves. Knowing the parametric form of unit cells allows for the use of complementary energy approaches for estimating their mechanical response analytically. This, in turn, obviates the need to analyze structures containing a large number of finite elements required by using a solid model approach, leading to a reduction in the computational effort in the overall TO process.

The principle of complementary energy is a generalization of Castigliano's 2nd theorem [5], which states that among all the statically possible states of stress in a structure, the correct one minimizes the associated total complementary energy written as a function of the kinetic variables. This idea is leveraged to estimate deformation of unit cells under applied loading conditions, which is calculated by taking the partial derivatives of the complementary energy of the structure with respect to the applied forces and moments. While the method extends to all elastic structures, in the present work, the focus is on linear elastic response under generalized Hooke's law.

In Fig. 13.1, we show a composite of a thin rectangular beam undergoing in-plane deformation using unit cells. Each unit cell is made of a filament or tube, consisting of a central loop and four anchors. Our goal here is to understand the dynamical behavior of the composite by studying its natural frequencies for different levels of discretization with unit cells. This composite is refined at seven different levels starting from 2×20, as shown in Fig. 13.1, to 8×80 unit cells along the width and length, respectively. At different levels, the loop radius, tube radius, and anchor lengths of the unit cells were designed such that the total mass of the composite remained unchanged. Unit cell design is also constrained by the Euler-Bernoulli beam condition, which requires the tube diameter to be less than or equal to one-tenth of the length of the anchors. The details of the modal analysis at different levels of discretization is discussed in the next section.

We use Castiglianos's theorem to *analytically* determine the flexibility matrix of the individual unit cells. The internal complementary energy U^* associated with the bending and axial response of an unit cell is given by the line integral

$$U^*(\xi) = \int_0^{\xi} \left\{ \frac{\mathbf{P}(\mathbf{s}(\zeta)) \cdot \mathbf{P}(\mathbf{s}(\zeta))}{2EA} + \frac{\mathbf{M}(\mathbf{s}(\zeta)) \cdot \mathbf{M}(\mathbf{s}(\zeta))}{2EI} \right\} \left|\left| \frac{d\mathbf{s}}{d\zeta} \right|\right| d\zeta \tag{13.1}$$

where $\mathbf{P}$ is the axial force vector and $\mathbf{M}$ is the bending moment vector along the filament of the unit cell, which is parameterized by the position vector $\mathbf{s}$, as a function of the intrinsic variable ξ (or dummy variable ζ). Meanwhile, $\cdot$ represents the inner (dot) product, E is Young's modulus of the material, A is the cross-sectional area of the tube, I is the area moment of inertia of the tube-cross section, and $||d\mathbf{s}/d\zeta||$ is the Jacobian of the transformation. Subsequently, the stiffness matrices of individual unit cells are developed from the inverse of the corresponding flexibility matrices and then assembled to determine the stiffness of the overall composite. Static condensation is used to eliminate the angular degrees of freedom, and modal eigenfrequency analysis is performed using a lumped mass matrix.

13.3 Results and Discussion

This section discusses the findings on the convergence and accuracy of the CE-based framework for modal analysis. It is observed that after increasing the refinement of the rectangular beam with unit cells, the natural frequency values saturate, as may be expected. The convergence plots for the first and second natural frequencies are depicted in Fig. 13.2, and the corresponding mode shapes for the 2×20 mesh are shown in Fig. 13.3.

To compare the accuracy of the CE-based framework, an analogous finite element analysis is performed within the Abaqus simulation software. We use beam element (B23) as the element type for the simulation of multi-scale structures. We observe

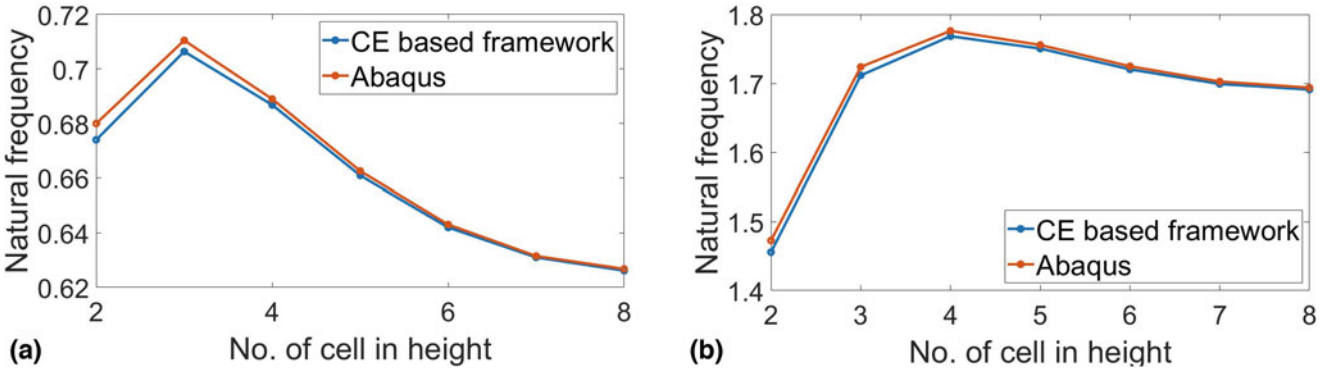

Fig. 13.2 Estimation of natural frequencies at different levels of discretizations and comparison with Abaqus. The convergence for the first and second natural frequencies are shown in (**a**) and (**b**), respectively. There is less than 1% difference between Abaqus and CE-based framework results

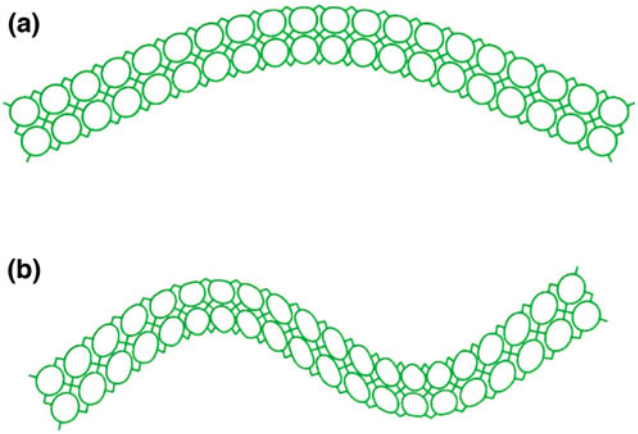

Fig. 13.3 Mode shapes for the in-plane vibration of the 2×20 grid of unit cells. In (**a**) and (**b**), the mode shapes corresponding to the first two natural frequencies are shown, where the non-dimensional cyclic frequencies are 0.677 and 1.464, respectively

less than 1% difference between Abaqus and CE-based framework results, which is evident in Fig. 13.2. This framework mimics the Abaqus results for less refined structures such as 2×20 unit cells and highly refined structures such as 8×80 unit cells as well. Finally, we have observed the CE-based framework is computationally quite fast compared to the existing structural analysis software and algorithms. The algorithms based on finite element methods generally need a finer mesh for better accuracy. On the other hand, the CE-based framework directly uses the analytical formulation; thus, it does not need a finer mesh for better accuracy. The extension to three-dimensional unit cells for both static and dynamic problems with analytical CE representations of the filament paths also appears to be quite attractive for use within multi-scale TO.

References

1. Bendsoe, M.P., Sigmund, O.: Topology Optimization: Theory, Methods, and Applications. Springer Science & Business Media, New York (2003)
2. Bielecki, D., Patel, D., Rai, R., Dargush, G.F.: Multi-stage deep neural network accelerated topology optimization. Struct. Multidiscip. Optim. **64**(6), 3473–3487 (2021)
3. Bielecki, D.D., Patel, D., Alegria, L., Rai, R., Dargush, G., Menasco, W.: Multiscale compliant topology optimization for twistable wing design. In: AIAA AVIATION 2021 FORUM (2021), pp. 2429
4. Bendsøe, M.P., Kikuchi, N.: Generating optimal topologies in structural design using a homogenization method. Comput. Methods Appl. Mech. Eng. **71**(2), 197–224 (1988)
5. Castigliano, A.: Théorie de l'équilibre des systèmes élastiques et ses applications, vol. 1. AF Negro, Chicago (1879)

Chapter 14
Micromechanics of Internal Frictions in Thermoplastic Composites Exposed to High-Frequency Vibrations

Thijs Masmeijer, Ed Habtour, and Dario di Maio

Abstract Recently introduced class of fiber-reinforced thermoplastic polymer composites (FTPC) in aerospace structures offer a high stiffness-to-weight ratio, cost-saving, and recyclability advantages compared to their thermoset composites. However, their structural performance under high-frequency vibratory loads during their service life is not well understood. Such loads instigate internal material friction inside the microcracks. In this paper, we propose a combined dynamic characterization and fracture mechanics modeling for evaluating the evolution of damage precursors (microcracks) in FTPC due to the presence of internal frictional forces. In order to run simulations to calculate self-heating caused by vibration, one must run transient analysis, because of the contact elements which calculate the amount of friction generated. This work proposes for the first time to apply the structure's Operating Deflection Shape as a dynamic load to include that friction. An innovation of the proposed method is the inclusion of microscopic self-heating in the microcracks as a consequence of high-frequency frictional forces. The Finite Element Method (FEM) is utilized to perform the dynamic analysis for a thermoplastic composite beam with a microcrack exposed to high-frequency vibration fatigue.

Keywords Thermoplastic composites · Vibration · Microcracks · Dynamics · Fracture mechanics · Self-heating

14.1 Introduction

Recent advances in sustainable thermoplastic manufacturing have accelerated the development of fiber-reinforced thermoplastic polymer composites (FTPC) structures for aerospace application components. Just like fiber-reinforced thermoset composites, FTPC structures hold promise for aerospace platforms due to their stiffness-to-weight ratio. However, investigations of the damage accumulation in FTPC during operational conditions, such as vibrations, remain underexplored. Studying fatigue in FRPs is essential for understanding the structural integrity of the laminates over their complete service life to ensure the safety of aircraft [1].

Most of the current research related to the structural performance of FTPC is focused on low-loading rate mechanical testing. Mechanical tests mainly consist of tension, or 3- or 4-point bending tests. Fatigue tests span low-cycle fatigue (LCF) to high-cycle fatigue (HCF) and are tested on various stress ratios. It is well known that low mechanical loading rates for fatigue testing can be a labor- and time-intensive process, and often is not reflective of the real-world operational conditions [2]. This makes the alternative to mechanical testing, vibration fatigue testing, a valuable research direction: It has the capability for higher loading rates and often has more representative loading conditions. A challenge of vibration fatigue testing is its susceptibility to self-heating. The increase in the vibration cycles will lead to an increase in the localized self-heating in the adjacent continuum around the microcracks. Subsequently, the thermoplastic polymer matrix will lead to localized material compliance, i.e., localized time-temperature dependence. The effects of higher frequency and temperature require additional tests and the calculation of shift factor(s), as described in [3].

The self-heating effect was observed small quantities of heat generated during the early loading cycles due to visco-elastic conditions and the dissipation of heat in high cycle fatigue [4, 5]. Both these investigations were on quasi-static conditions.

T. Masmeijer (✉) · E. Habtour
The William E. Boeing Department of Aeronautics and Astronautics, University of Washington, Seattle, WA, USA
e-mail: thijsmas@uw.edu; habtour@uw.edu

D. di Maio
Department of Mechanical Engineering, University of Twente, Enschede, Netherlands
e-mail: d.dimaio@utwente.nl

M. Allen et al. (eds.), *Special Topics in Structural Dynamics & Experimental Techniques, Volume 5*,
Conference Proceedings of the Society for Experimental Mechanics Series, https://doi.org/10.1007/978-3-031-37007-6_14

The level of self-heating reported in these studies is much lower than reported in studies on visco-elastic materials [5–12]. The studies all involve mechanical testing at a high enough loading rate to induce self-heating, and all report the detrimental effect of self-heating on the remaining life of composites. One of the major causes for the self-heating is friction at the crack-tip interface during loading [13–15], as shown in Fig. 14.1. One of the limited modeling efforts to estimate the effect of friction in crack growth was performed by Keoschkerjan et al. [16]. This work shows how the self-heating of the material changes the system dynamics. The self-heating effect in composites under vibration has been extensively studied by Katunin et al. [17–31]. These works lead to evaluating fatigue on the self-heating properties; some of those properties were exploited for Structural Health Monitoring. Research is proposed by Shou et al. in [32] about self-heating in a composite particulate under vibration.

The foundation on how to conduct the vibration fatigue test is given by Di Maio et al. [3, 33, 34], Magi et al. [35, 36], and Voudouris et al. [37]. In [36] a modeling approach based on the Virtual Crack Closure Technique (VCCT) is applied to a Finite Element (FE) model undergoing vibration fatigue. The model determines the strain energy release rate at the crack tip as a crack propagates. The strain energy release rate is used as a measure to describe how fast cracks will grow during vibration fatigue tests. In the modeling approach, an automated VCCT routine was written using MatLab, which interacted with FEM solver software ABAQUS. We observe that the routine linking ABAQUS and Matlab is impractical, and obstructs the practical implementation of the approach. In this paper, for the first time, a modeling approach is proposed where building the model and conducting the VCCT analysis was performed within ABAQUS. The VCCT approach was based on calculating the Strain Energy Release Rate at a propagating crack tip. Based on the observation that the self-heating effect is caused by friction at the crack-tip interface [13–15], this work investigates the effect of friction on the VCCT analysis. The all-ABAQUS modeling approach is depicted in Fig. 14.2.

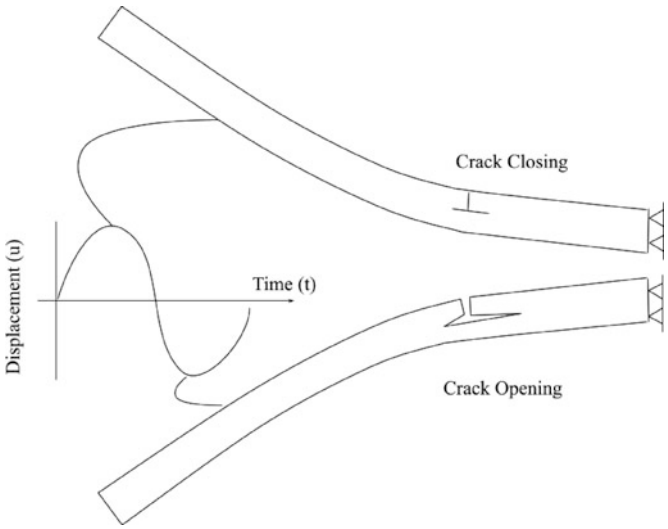

Fig. 14.1 During one oscillation the crack will open and close, causing two different loading conditions

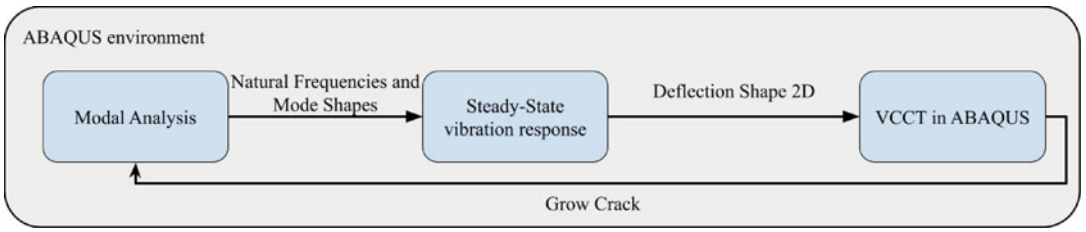

Fig. 14.2 Flowchart diagram of analysis carried out by the FE solvers and outputs similar to [37]. The complete model is run within the ABAQUS environment

14.2 Background

To have predictable and reproducible results, it is common to introduce an artificial transverse crack in the specimen during vibration fatigue tests. The typical failure in composites is due to delimitation, where transverse cracks initiate and grow between the composite laminates. The evolution of the crack is inherently driven by Mixed Mode Conditions, which consist of Mode I: Opening, and Mode II: In-plane Shearing. The vibration load cycle can be described with the closing and opening of a crack, as depicted in Fig. 14.1. During the opening of the crack, Mode I is expected to be dominant, and during the closing of the crack, Mode II is expected to be dominant.

Using VCCT, the energy can be calculated for each mode separately, as expressed by Eq. (14.1) for mode I. The components of Eq. (14.1) are labeled in Fig. 14.3, except for width b of the continuum element and the Strain Energy Release Rate for mode I, G_I. G_{II} is found similarly, but the force and displacement in u-direction are used.

$$G_I = \frac{1}{2}\left(\frac{v_{1,6}F_{v,2,5}}{bd}\right) \tag{14.1}$$

$$G_{II} = \frac{1}{2}\left(\frac{u_{1,6}F_{u,2,5}}{bd}\right) \tag{14.2}$$

Usually an equivalent strain energy release rate (G_{equiv}), and an equivalent critical strain energy release rate ($G_{\text{equiv,C}}$) are calculated for Mixed Mode loading conditions, where $G_{\text{equiv}} = G_I + G_{II}$. $G_{\text{equiv,C}}$ can be found using, for example, the BK-law as described in Benzeggagh [39]. However, we show that this step is not required in this study. The VCCT is developed for quasi-static loading conditions. In quasi-static models, the load (or displacement) is increased incrementally, and cracks are propagated when threshold f is met:

$$f = \frac{G_{\text{equiv}}}{G_{\text{equiv,C}}} \geq 1.0 \tag{14.3}$$

This is not true for fatigue. Under fatigue conditions cracks propagate, despite a low G_{equiv}. In fatigue the crack growth behavior is described using the Paris–Erdogan law:

$$\frac{da}{dN} = C(\Delta K)^m \tag{14.4}$$

where ΔK is the range of the stress intensity factor during a cycle. The crack length is a. The fatigue crack growth for a load cycle N is $\frac{da}{dN}$. C and m are material property constants. Magi [40] proposed that an equivalent law can be set up with ΔK replaced by G_{equiv}, where C and m are updated material constants. The modified Paris-Erodagan law is depicted in Fig. 14.4. The region where the law is representative is marked between the dashed lines.

$$\frac{da}{dN} = C(G_{\text{equiv}})^m \tag{14.5}$$

It is important to point out that since cracks will propagate despite threshold f not being met, the modified modeling approach does not require any values for $G_{\text{equiv,C}}$. This allows us to modify the classic VCCT model, in this paper.

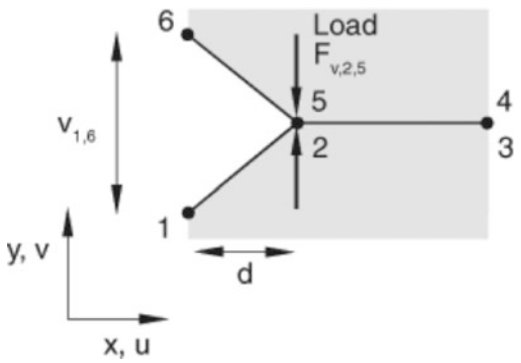

Fig. 14.3 Mode I loading with each component labeled [38]

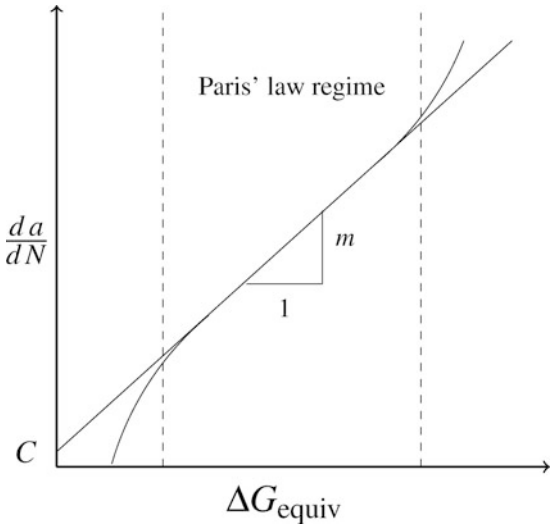

Fig. 14.4 The modified Paris Law by Magi et al. [40] on a log-log scale. The figure is reproduced from [40]

14.3 Analysis

Investigating the change in the Strain Energy Release Rate during the opening of the crack was performed computationally using FEM models in a complete ABAQUS environment. The geometries of each FEM model were replicated from the comparative fracture analyses published by Rarani et al. [41]. In their analysis, they estimated the strain energy release rate for mode I using VCCT, cohesive zone, and XFEM methods and compared them to the experimental results. Their model was utilized to verify a quasi-static VCCT model. Next, the model was modified to represent vibration fatigue tests.

Our proposed model is modified from the quasi-static model to describe vibration fatigue, as depicted in Fig. 14.5. The approach is schematically depicted in Fig. 14.2. Note that every step in this approach is within the ABAQUS environment. The base model was constrained by a single pin at the neutral line on the right side. A 35 mm pre-crack (solid line) was followed by the crack region along the neutral line, shown in the dotted line. The top-left and bottom-left tips of the specimen were assigned a 10 mm displacement upward and downward, respectively.

After verification, the model was modified to investigate the vibration fatigue behavior in thermoplastic composites. The 35 mm pre-crack was removed from the model. The right-side boundary condition was replaced with pins at the top and bottom. This corresponds to a knife edge fixture commonly seen in vibration fatigue tests [33, 35]. A 0.01 mm wide slot was created 15 mm from the right boundary to promote delamination between the plies. The slot depth was the distance from the center line to the beam surface. The slot width was chosen to achieve two objectives: (i) to avoid zero-pivot convergence errors and (ii) to prevent the buckling of the delamination. A crack front will start from the transverse crack towards the pinned boundary. Note, that the slot will promote a crack front that could grow the delamination into or away from the pinned boundary. Tests of similar specimens and materials have shown that delaminations typically grow towards the pinned boundary [42]. The displacement boundary conditions of the top-left and bottom-left tips were removed. During one oscillation in vibration fatigue, the specimen reaches two maximum displacements, as was depicted in Fig. 14.1. A positive displacement corresponded to crack closing and a negative displacement to crack opening. These two absolute orientations were investigated parallel to each other. Each investigation consisted of applying the first vibration mode shape (flexural mode) of the specimen as displacements in, first, the crack opening and, second, the crack closing. The used Operating Deflection Shapes were scaled to always have a fixed displacement at the free tip of 4 mm. To obtain these shapes first eigenvalue extraction was conducted in ABAQUS to obtain the natural frequencies and mode shapes. The step was run with a structural damping coefficient of 0.1%, which was an average of previous run tests on similar materials and was meant to be an indicative value. With the natural frequencies and mode shapes, a mode-based steady-state dynamic analysis step was conducted to obtain the Operating Deflection Shapes. In this step, a -1 N load was applied at the free tip of the specimen. The deflection shapes were acquired separately for each crack length of interest. Finally, the modified VCCT analysis was conducted. Since the critical Strain Energy threshold, f, will never be met, the VCCT step was conducted for each crack length separately. This allowed for matching the deflection shapes to the current crack length.

The used material properties of both models are set out in Table 14.1. The input material properties for the FEM analysis were the longitudinal and transverse elastic moduli (E_1 and E_2, respectively), the shear modulus, G_{12}, and Poisson ratio, ν_{12} [3, 43].

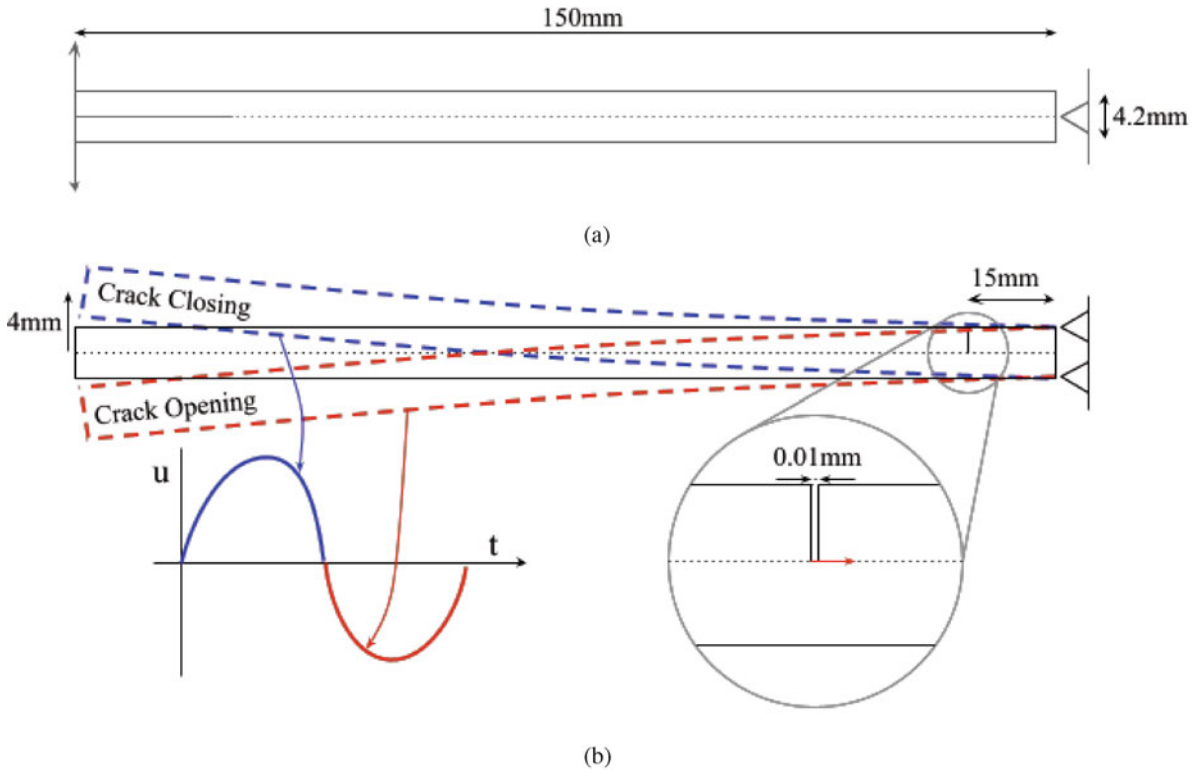

Fig. 14.5 (**a**) Reference model by Rarani et al. [41] used for model verification. (**b**) The modified model for vibration fatigue. (**a**) Base model for verification with Rarani et al. [41]. (**b**) Model for vibration fatigue

Table 14.1 Material properties of the E-glass/epoxy laminate from Rarani et al. [43] used in the reference model. The material properties of PEEK Carbon Fiber were used in previously conducted vibration fatigue tests [3]. The fracture properties for PEEK Carbon Fiber are not necessary since no critical strain energy is required

	E_1 (GPa)	E_2 (GPa)	G_{12} (GPa)	ν_{12}
E-glass/epoxy laminate	33.5	10.23	4.26	0.27
PEEK Carbon Fiber	135	10	5.2	0.28

The FE model included multiple interactions. Two hard contacts were included in the model near the cracked area. The first hard contact was between the two vertical sides of the 0.01 mm wide slot, and the second was between the delamination and the base structure. Tangential behavior was included between the propagating cracks with a fixed friction coefficient (μ) of 0.75, which came from tests conducted by Voudouris et al. [37].

The same mesh and elements (CPE4) were utilized as the 2D VCCT model in Rarani et al. [41]. The thickness of the specimen is divided into 20 elements. The element size was 0.2 mm, which resulted in a total of 15,000 elements. The quasi-static VCCT models were successfully verified with the model from Rarani [41]. The verification results are provided in the appendix.

14.4 Results

Opening the crack causes the Frequency Response Functions (FRFs) to shift, as depicted in Fig. 14.6. An FRF describes the magnitude and phase of the output response as a function of an input frequency. The shift of the FRFs is attributed to a loss of stiffness. Figure 14.7 sets out how the natural frequency drops as the delamination propagates. The drop in natural frequency seems linear with the crack length and the slope is negative. The slope is negative as expected, as the opening of a crack would make the specimen less stiff, i.e., the natural frequency will drop. Remember that a 0.01 mm slot was included between the delamination tips to negate buckling of the delaminations and zero-pivot errors in the Hard contact, as described

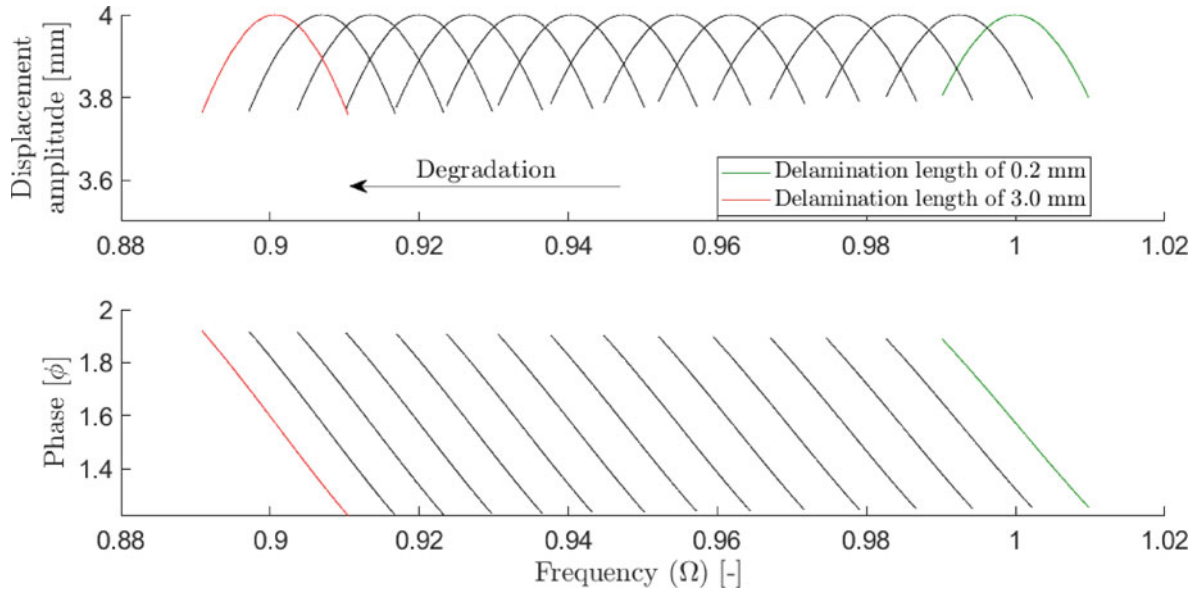

Fig. 14.6 Development of the Frequency Response Function (FRF) due to the growing crack. Note that the FRFs are scaled such that the displacement amplitude at the resonance corresponds to the 4 mm chosen by us. The frequency is normalized according to $\Omega = f/f_{n,1}$, where $f_{n,1}$ is the first natural frequency at the delamination length of 0.2 mm of 204.0 Hz

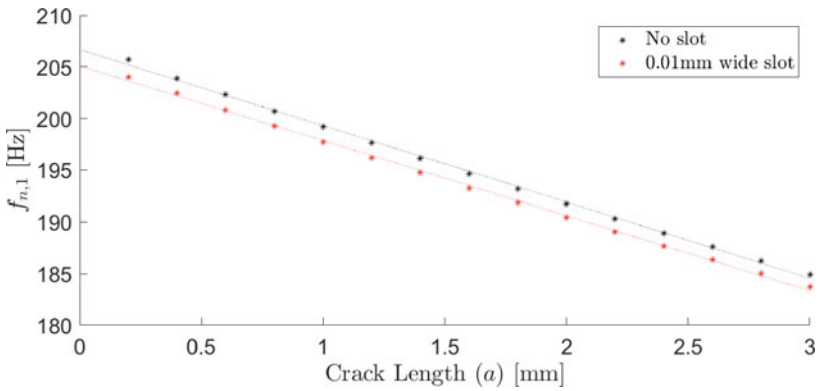

Fig. 14.7 Shift of the natural frequencies due to the propagation of the crack. The intercept and slope of the no-slot model are 206.7 Hz and −7.4 Hz/mm, respectively. The intercept and slope of the model with slot are 205.1 Hz and −7.2 Hz/mm, respectively

in section ANALYSIS. The effect of this slot was a reduction of the natural frequency with −1.6 Hz and had little effect on the slope of the natural frequencies. The reduced natural frequency is as expected because the slot reduces the stiffness of the specimen.

The development of the strain energy release rates for each crack length, ranging from 0.2 mm to 3 mm with steps of 0.2 mm, was set out in Fig. 14.8. Here G_{11} and G_{12} describe mode I (Opening) and mode II (In-plane Shearing), respectively. The results with and without friction are included to compare the effect of friction on the model. The first observation is that the strain energy release rate is significantly higher in the orientation where the crack opens. The difference in G_{ij} between the fiction and no friction case is found to be small compared to the overall G_{ij}. For the crack opening case when the crack is small, we observe that G_{11} is significantly higher than G_{12}. As the crack opens G_{11} first drops quickly and starts to drop linearly at approximately 1 mm. G_{12} first increases and then drops linearly at approximately 1 mm. In the crack closing case when the crack is small G_{11} we observe that Mode II is dominant. As the crack propagates Mode II converges to zero, while Mode I keeps increasing. This is unexpected since when the crack closes, the delamination slides over each other, which is behavior better described by Mode II.

In order to properly compare the effects of friction on crack growth, the differences in G_{ij} were set out in Fig. 14.9. For the crack opening loading condition, the difference in strain energy release rate is zero. This makes sense since the interaction between the delamination and the base structure is inactive when the crack opens. For the crack closing case the difference in G_{12} seems to plateau at 0 as the crack grows. The difference in G_{11} seems to grow as the delamination length increases. We

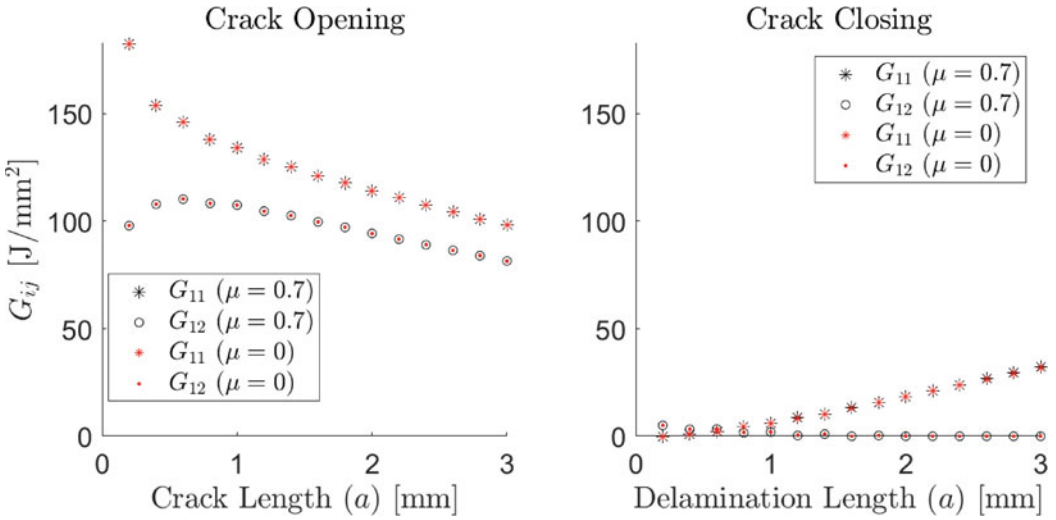

Fig. 14.8 Development of the Strain Energy Release Rate near the fixture (right) with friction ($\mu = 0.7$) and without friction

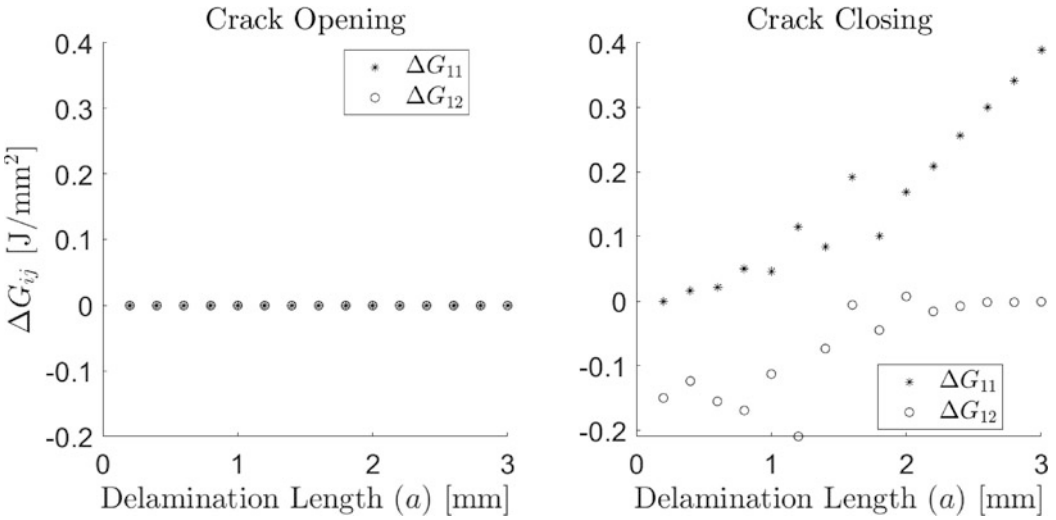

Fig. 14.9 Development of the difference between the Strain Energy Release Rate with friction ($\mu = 0.7$) and without friction. The difference is calculated as the frictionless case minus the case with friction

observe that for the crack closing loading condition some data points have large deviations from the trend. We expect that this behavior comes from the small observed differences caused by the friction component and by instability in the model.

14.5 Conclusion

The modeling approach was able to produce an accurate relationship between the strain energy release rate and the crack length. A previous modeling approach required a link between ABAQUS and Matlab [3]. The novel approach in this work was fully in an ABAQUS environment, removing this major roadblock. The inclusion of friction between the delamination and the base structure had little effect on the absolute results of the strain energy release rate. Nonetheless, the small change in the energy release rate could still be an invaluable indicator for precursors to damage at the micro-scale in fiber-reinforced thermoplastic polymer composites (FTCP). We ask the reader to consider the effects of small deviations in strain energy release rates. In vibration fatigue, where strain energy is released over millions of cycles, the cumulative difference can still have a significant impact on the self-heating behavior of FTPCs. The novel modeling approach allows for further exploration of the behavior of self-heating in fiber-reinforced thermoplastic polymer composites.

Appendix: Verification of the VCCT Model

(Figures 14.10 and 14.11)

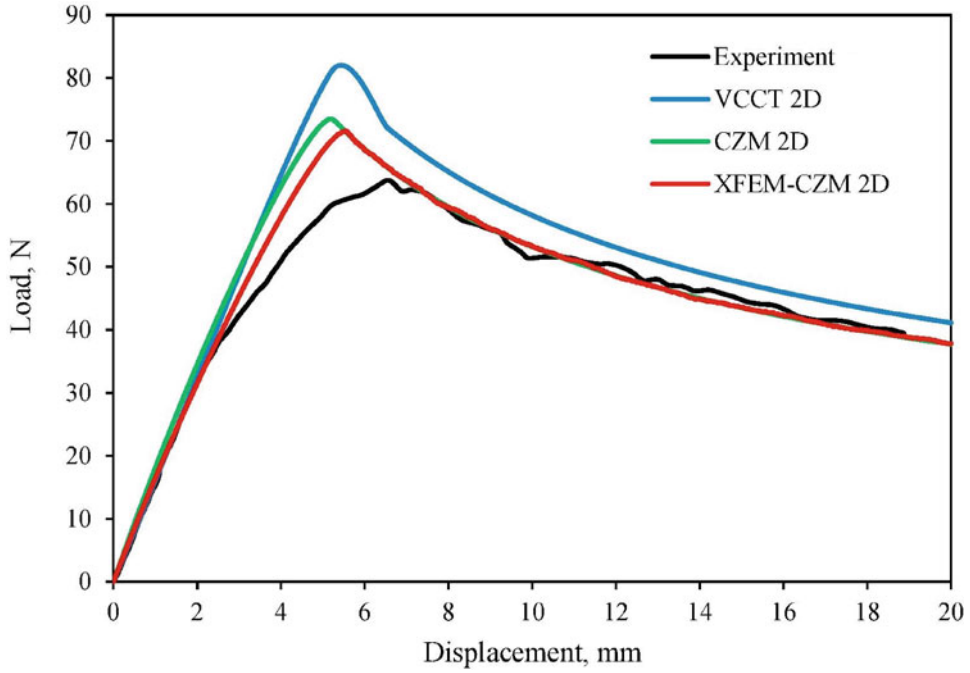

Fig. 14.10 Modelling and experimental results from Rarani et al. [41] and [43]. Figure modified from [41]

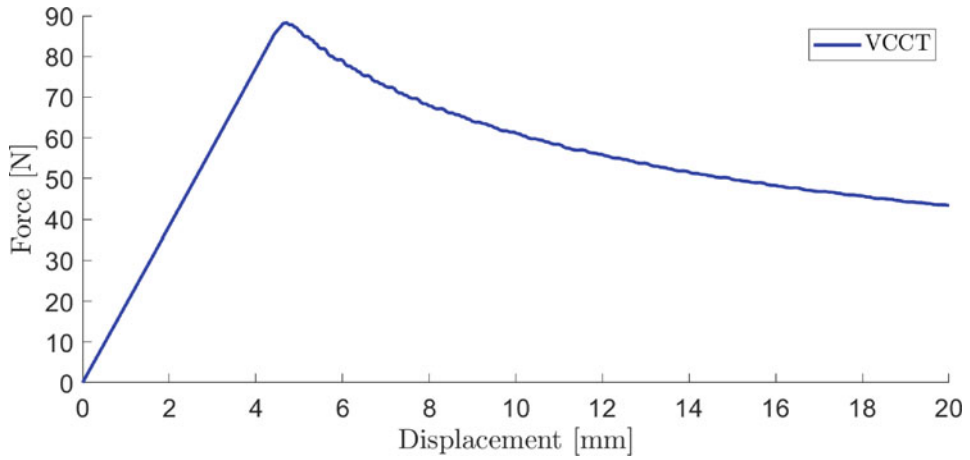

Fig. 14.11 Results from the matched VCCT model

Acknowledgments The authors would like to express their gratitude to the University of Twente and the University of Washington for providing the authors the opportunity to investigate the topics of this paper.

References

1. Alam, P., Mamalis, D., Robert, C., Floreani, C., Ó Brádaigh, C.M.: The fatigue of carbon fibre reinforced plastics—a review. Compos. Part B Eng. **166**, 555–579 (2019)
2. Habtour, E., Di Maio, D., Masmeijer, T., Gonzalez, L.C., Tinga, T.: Highly sensitive nonlinear identification to track early fatigue signs in flexible structures. Journal of Nondestructive Evaluation, Diagnostics and Prognostics of Engineering Systems **5**(2), 021005 (2022)
3. Di Maio, D., Voudouris, G., Sever, I.A.: Investigation of fatigue damage growth and self-heating behaviour of cross-ply laminates using simulation-driven dynamic test. Int. J. Fatigue **155**, 106617 (2022)
4. Maquin, F., Pierron, F.: Heat dissipation measurements in low stress cyclic loading of metallic materials: From internal friction to micro-plasticity. Mech. Mater. **41**, 928–942 (2009)
5. Guo, Q., Zaïri, F., Yang, W.: Evaluation of intrinsic dissipation based on self-heating effect in high-cycle metal fatigue. Int. J. Fatigue **139**, 105653 (2020)
6. Peyrac, C., Jollivet, T., Leray, N., Lefebvre, F., Westphal, O., Gornet, L.: Self-heating method for fatigue limit determination on thermoplastic composites. Procedia Eng. **133**, 129–135 (2015)
7. Shojaei, A.K., Volgers, P.: Fatigue damage assessment of unfilled polymers including self-heating effects. Int. J. Fatigue **100**, 367–376 (2017)
8. Mahmoudi, A., Mohammadi, B.: Theoretical-experimental investigation of temperature evolution in laminated composites due to fatigue loading. Compos. Struct. **225**, 110972 (2019)
9. Pitarresi, G., Scalici, T., Catalanotti, G.: Infrared thermography assisted evaluation of static and fatigue mode II fracture toughness in FRP composites. Compos. Struct. **226**, 111220 (2019)
10. Shen, F., Kang, G., Lam, Y.C., Liu, Y., Zhou, K.: Thermo-elastic-viscoplastic-damage model for self-heating and mechanical behavior of thermoplastic polymers. Int. J. Plast. **121**, 227–243 (2019)
11. Hülsbusch, D., Kohl, A., Striemann, P., Niedermeier, M., Strauch, J., Walther, F.: Development of an energy-based approach for optimized frequency selection for fatigue testing on polymers—exemplified on polyamide 6. Polym. Test. **81**, 106260 (2020)
12. Huang, J., Garnier, C., Pastor, M.L., Gong, X.: Investigation of self-heating and life prediction in CFRP laminates under cyclic shear loading condition based on the infrared thermographic data. Eng. Fract. Mech. **229**, 106971 (2020)
13. Lang, R.W., Manson, J.A.: Crack tip heating in short-fibre composites under fatigue loading conditions. J. Mater. Sci. **22**, 3576–3580 (1987)
14. Huang, J., Li, C., Liu, W.: Investigation of internal friction and fracture fatigue entropy of CFRP laminates with various stacking sequences subjected to fatigue loading. Thin-Walled Struct. **155**, 106978 (2020)
15. Mortazavian, S., Fatemi, A., Mellott, S.R., Khosrovaneh, A.: Effect of cycling frequency and self-heating on fatigue behavior of reinforced and unreinforced thermoplastic polymers. Polym. Eng. Sci. **55**, 2355–2367 (2015)
16. Keoschkerjan, R., Harutyunyan, M., Wurmus, H.: Analysis of self-heating phenomenon of piezoelectric microcomponents actuated harmonically. Microsyst. Technol. **9**, 75–80 (2002)
17. Katunin, A.: Analytical model of the self-heating effect in polymeric laminated rectangular plates during bending harmonic loading. Eksploatacja i Niezawodnosc—Maintenance and Reliability **48**, 91–101 (2010)
18. Katunin, A., Kostka P, H.W., Holeczek, K.: Frequency dependence of the self-heating effect in polymer-based composites. J. Achiev. Mater. Manuf. Eng. **41**(1-2), 9–12 (2010)
19. Katunin, A., Fidali, M.: Experimental identification of non-stationary self-heating characteristics of laminated composite plates under resonant vibration. Kompozyty **11**, 214–219 (2011)
20. Katunin, A.: Critical self-heating temperature during fatigue of polymeric composites under cyclic loading. Compos. Theory Pract. **12**, 72–76 (2012)
21. Katunin, A.: Thermal fatigue of polymeric composites under repeated loading. J. Reinf. Plast. Compos. **31**, 1037–1044 (2012)
22. Katunin, A., Fidali, M.: Fatigue and thermal failure of polymeric composites subjected to cyclic loading. Adv. Compos. Lett. **21**, 096369351202100 (2012)
23. Katunin, A., Fidali, M.: Self-heating of polymeric laminated composite plates under the resonant vibrations: Theoretical and experimental study. Polym. Compos. **33**, 138–146 (2012)
24. Katunin, A.: Domination of self-heating effect during fatigue of polymeric composites. Procedia Struct. Integrity **5**, 93–98 (2017)
25. Katunin, A.: A concept of thermographic method for non-destructive testing of polymeric composite structures using self-heating effect. Sensors **18**, 74 (2017)
26. Katunin, A., Wronkowicz, A.: Characterization of failure mechanisms of composite structures subjected to fatigue dominated by the self-heating effect. Compos. Struct. **180**, 1–8 (2017)
27. Katunin, A., Wronkowicz, A., Bilewicz, M., Wachla, D.: Criticality of self-heating in degradation processes of polymeric composites subjected to cyclic loading: A multiphysical approach. Arch. Civ. Mech. Eng. **17**, 806–815 (2017)
28. Katunin, A.: Evaluation of criticality of self-heating of polymer composites by estimating the heat dissipation rate. Mech. Compos. Mater. **54**, 53–60 (2018)
29. Katunin, A.: Criticality of the self-heating effect in polymers and polymer matrix composites during fatigue, and their application in non-destructive testing. Polymers **11**, 19 (2018)
30. Katunin, A., Wachla, D.: Analysis of defect detectability in polymeric composites using self-heating based vibrothermography. Compos. Struct. **201**, 760–765 (2018)
31. Katunin, A., Wachla, D.: Minimizing self-heating based fatigue degradation in polymeric composites by air cooling. Procedia Struct. Integrity **18**, 20–27 (2019)

32. Shou, Z., Chen, F., Yin, H.: Self-heating of a polymeric particulate composite under mechanical excitations. Mech. Mater. **117**, 116–125 (2018)
33. Di Maio, D., Magi, F.: Development of testing methods for endurance trials of composites components. J. Compos. Mater. **49**, 2977–2991 (2015)
34. Di Maio, D., Magi, F., Sever, I.A.: Damage monitoring of composite components under vibration fatigue using scanning laser doppler vibrometer. Exp. Mech. **58**, 499–514 (2018)
35. Magi, F., Di Maio, D., Sever, I.: Damage initiation and structural degradation through resonance vibration: application to composite laminates in fatigue. Compos. Sci. Technol. **132**, 47–56 (2016)
36. Magi, F., Di Maio, D., Sever, I.: Validation of initial crack propagation under vibration fatigue by finite element analysis. Int. J. Fatigue **104**, 183–194 (2017)
37. Voudouris, G., Di Maio, D., Sever, I.A.: Experimental fatigue behaviour of CFRP composites under vibration and thermal loading. Int. J. Fatigue **140**, 105791 (2020)
38. Smith, M.: ABAQUS/Standard User's Manual, Version 6.9. Dassault Systèmes Simulia Corp, Johnston (2009)
39. Benzeggagh, M.L., Kenane, M.: Measurement of mixed-mode delamination fracture toughness of unidirectional glass/epoxy composites with mixed-mode bending apparatus. Compos. Sci. Technol. **56**, 439–449 (1996)
40. Magi, F.: Vibration Fatigue Testing for Identification of Damage Initiation in Composites (2016)
41. Heidari-Rarani, M., Sayedain, M.: Finite element modeling strategies for 2d and 3d delamination propagation in composite DCB specimens using VCCT, CZM and XFEM approaches. Theor. Appl. Fract. Mech. **103**, 102246 (2019)
42. Masmeijer, T.: Vibration Fatigue Testing and Modeling for Identification of Damage Initiation and Propagation in Fiber Reinforced Plastics—University of Twente Student Theses (2021)
43. Heidari-Rarani, M., Shokrieh, M.M., Camanho, P.P.: Finite element modeling of mode i delamination growth in laminated DCB specimens with r-curve effects. Composites Part B: Engineering **45**, 897–903 (2013)

Chapter 15
Investigating Compressing Particle Damper Pockets in Beams Manufactured by Laser Powder Bed Fusion Additive Manufacturing

Yanzhou Fu, Satme Joud, Austin R. J. Downey, Lang Yuan, Tianyu Zhang, and Daniel Kiracofe

Abstract Components manufactured by laser powder bed fusion (LPBF) additive manufacturing can have particle dampers designed into the part by leaving unfused powder inside a defined pocket of the part during manufacturing. These pockets of unfused material have inherent damping capabilities that suppress the vibrations and potentially reduce component wear. Particle dampers have been shown to be a simple and effective way to increase the damping of a structural component manufactured by LPBF; however, the compressing effects of the particle damper pocket inside the beam have not been studied. The amount of unfused powder inside the pocket is difficult to control (or even measure) during manufacturing; therefore, this study reports preliminary investigations on the effects of energy absorption provided by changing the volume of the pocket. In this study, beams are printed with 316L stainless steel powder with single particle dampers. Thereafter, the cover of the pocket is deformed, decreasing the volume of the pocket. The energy absorption characteristics of the particle damper are quantified. The unfused powder pocket's damping characteristics are assessed by observing the structure's response to various excitation methods. An input-output relationship can be deduced using a reference accelerometer and an accelerometer mounted passed the damper pocket with respect to the fixity. With this relationship established, the magnitude of damping and the phase attributed to it is determined. Studying the damping characteristics of various compressed pocket sizes and powder quantities will provide helpful information to enhance particle dampers' efficiency using LPBF techniques.

Keywords Laser powder bed fusion · Particle damper · Structural dynamics · Multifunctional materials · Additive manufacturing

15.1 Introduction

Laser powder bed fusion (LPBF), one of the additive manufacturing technologies, has unrivaled strengths due to its design and manufacturing freedom. With the improvement of the LPBF processes and materials, it has been widely applied to engineering, medicine, and aerospace, especially for aerospace, which is a field that needs products with lower weight but good structural integrity [1]. Particle dampers made using LPBF have been proven as an efficient way to increase structure damping, which is made by keeping some un-melted powder inside of the structure on purpose. It works through a combination of non-elastic impact and friction between powder particles and pocket walls. With the unique advantages of no additional mass and space needed, which can reduce unnecessary vibration to prevent high cycle fatigue simultaneously. Interest in particle dampers for aerospace applications has been growing.

Lots of research focusing on particle damper performance have been done. For example, Ehlers et al. investigated the particle damping performance on a beam manufactured by LPBF [2]. The damping performance is evaluated under various

Y. Fu · S. Joud · L. Yuan · T. Zhang
Department of Mechanical Engineering, University of South Carolina, Columbia, SC, USA
e-mail: yanzhouf@email.sc.edu; Jsatme@email.sc.edu; langyuan@cec.sc.edu; tz5@email.sc.edu

A. R. J. Downey (✉)
Department of Mechanical Engineering, University of South Carolina, Columbia, SC, USA

Department of Civil and Environmental Engineering, University of South Carolina, Columbia, SC, USA
e-mail: austindowney@sc.edu

D. Kiracofe
Department of Mechanical Engineering, University of Cincinnati, Cincinnati, OH, USA
e-mail: kiracodl@ucmail.uc.edu

M. Allen et al. (eds.), *Special Topics in Structural Dynamics & Experimental Techniques, Volume 5*,
Conference Proceedings of the Society for Experimental Mechanics Series, https://doi.org/10.1007/978-3-031-37007-6_15

beam parameter sets. The results show that a particle damper can dramatically reduce the vibration amplitudes for the first to seventh bending mode. Guo et al. explored the particle damper's damping performance with experiment and numerical approaches by attaching the damper to a cantilever beam [3]. Schmitz et al. studied the damping and mode shape modification on a thin wall made by LPBF [4]. The experimental result shows that the damping increases with bigger powder core width. In addition, the mode shape is deformed relative to the solid wall results as the core width is increased and wall thickness is decreased. Scott-Emuakpor et al. evaluated the damping performance sustainment from the endurance, repeatability, and recovery sides on cantilevered beams produced by LPBF [5]. Moreover, the authors investigated the damping performance of LPBF beams with unique internal structures [6]. The results show that with only 1–4% inner volume unfused powder, the four unique beams can provide up to ten times damping compared with the referenced solid beam.

From the literature review above, it can be concluded that the cantilever beam is an easy and effective way to measure the particle damper's damping performance, as demonstrated by prior results. However, the effects changing the volume of the pocket post manufacturing have not been investigated. As the amount of unfused powder inside of the pocket is hard to control during printing, therefore, this study reports preliminary investigations on the effects of energy absorption provided by indenting the volume of the pocket. In this study, a beam is printed by 316L stainless steel powder with a single pre-designed particle damper. Thereafter, the cover of the pocket is deformed. Decreasing the volume of the pocket and the damper's damping performance is quantified. The unfused powder pocket's damping characteristics are assessed by observing the structure's response to impulse excitation. An input-output relationship is established by analyzing the data from accelerometers.

15.2 Experiment Setup and Methodology

In this research, a 75 mm × 10 mm cantilever beam with a 2.5 mm thickness is fabricated with 316L stainless steel powder by an AcontyMIDI LPBF printer, as shown in Fig. 15.1. A 20 mm × 8 mm pocket with 1.5 mm thickness is located 5 mm from the top. The key printing parameters such as power, speed, laser spot, and hatch distance are 200 W, 800 mm/s, 100 μm, and 100 μm. A solid beam with the same dimension and printing parameters is used as a reference.

The excitation for the free vibration test is an impulse generated by the cantilever beams fixed to a structure in free fall hitting a seismic mass. Tests were carried out on a Lansmont P30 shock test system. Two beams are fixed on the testing platform through the pre-designed holes, as shown in Fig. 15.2. Two IEPE accelerometers are attached to the beam to measure the impulse response (Model 352A92, which is from PCB Piezotronics). The test platform is dropped from a height of 76 mm to generate the impulse force. The data is collected at 50,000 S/s using an IEPE signal conditioner (NI 9234 from NI). Each test is repeated ten times. The signal obtained during free vibration data is then used to deduce the damping properties of the particle damper.

As stated before, this work investigates the effects of pocket volume change. A particle damper beam with different levels of the indent is tested on the shock test system. The indentation process is implemented by an MTS Exceed E43

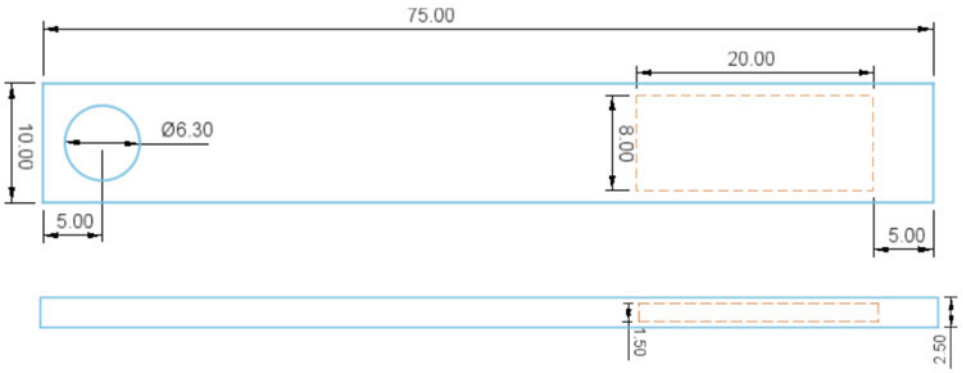

Fig. 15.1 The designed cantilever beam with unfused powder pocket

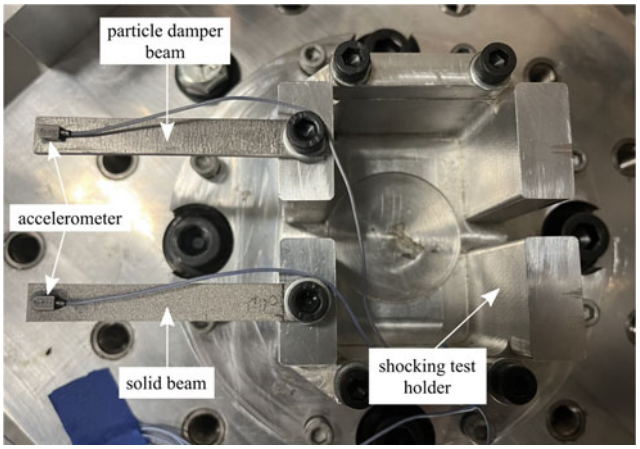

Fig. 15.2 The experiment setup on a shock test machine with a solid beam and particle damper beam

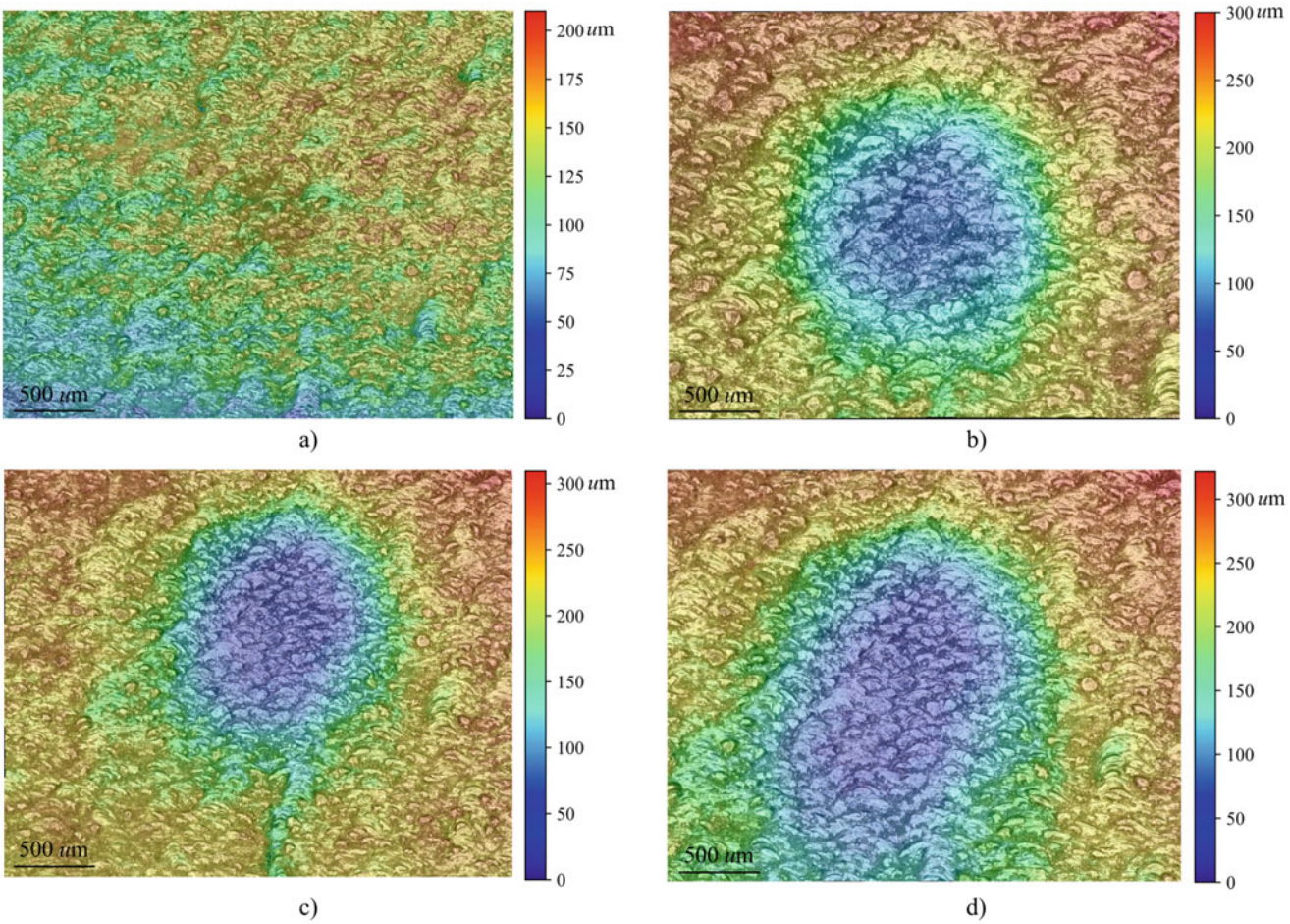

Fig. 15.3 Microscope topography images, showing the particle damper beam surface topography: (**a**) before indent; (**b**) with a 91 μm indentation; (**c**) with a 99 μm indentation; and (**d**) with a 111 μm indentation

electromechanical load frame on the particle damper beam: the first indent is applied with 2000 N force on the particle pocket's top surface while the second and third are loaded with 1000 N force. The microscope topography images of the beam before and after the indent are shown in Fig. 15.3. These surface topography measurements are captured by a Keyence VHX 700 digital microscope. The min-to-max surface heights obtained from the surface topography measurements are reported in Table 15.1.

Table 15.1 Surface height change of the particle damper beam

Particle damper beam	min-height (μm)	max-height (μm)	Surface height change (μm)
Before indent	37.44	210.70	0
After first indent	0	301.77	91.07
After second indent	0	310.56	99.86
After third indent	3.93	322.08	111.38

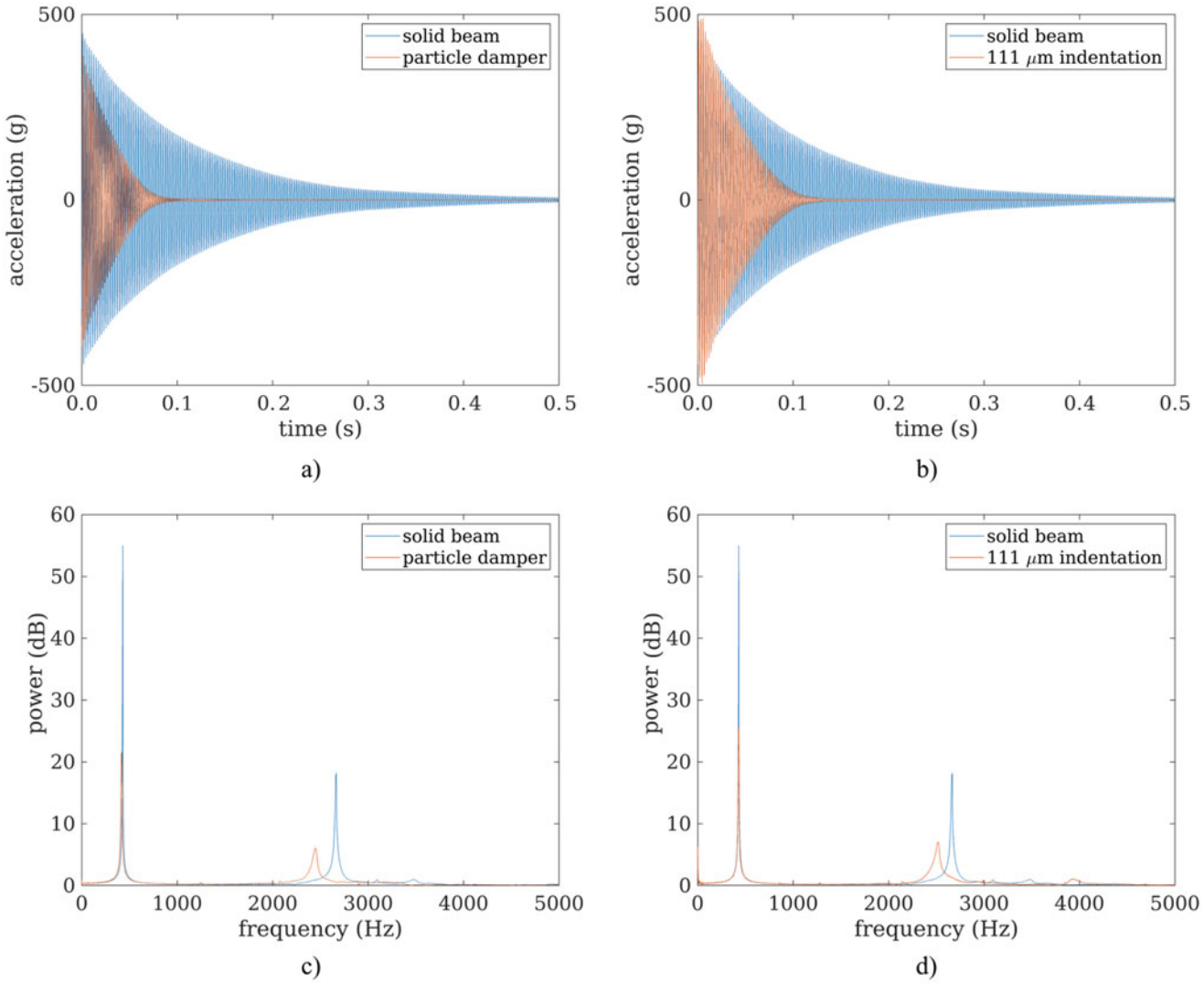

Fig. 15.4 The vibration curves and fast Fourier transform (FFT) analysis: (**a**) the vibration for the solid beam and particle damper beam before indent; (**b**) the vibration for the solid beam and particle damper beam with a 111 μm indentation; (**c**) FFT analysis for the solid beam and particle damper beam before the indent; and (**d**) FFT analysis for the solid beam and particle damper beam with a 111 μm indentation

15.3 Results and Discussion

The beams' time domain and frequency response after processing is shown in Fig. 15.4. Figure 15.4a and b display the vibration of the solid beam and particle damper beam before the indent and with a 111 μm indentation after the third indent. From the figure, it can be concluded that the vibration of the solid beam lasts much longer than the beam with a particle damper. Compared with the particle damper beam without the indent, the damper beam with a 111 μm indentation after the third indent has a higher density, which reduces the damping and increases the beam vibration. In Fig. 15.4c and d, the

Table 15.2 Shock test result for the solid and particle damper beam

Test sample	max frequency (Hz)	Damping ratio	Q factor	Q factor standard deviation
Solid beam	428.7	0.00287	174.8	1.89
Particle beam	416.0	0.00430	116.7	4.88
91 μm indentation	425.7	0.00420	119.4	4.52
99 μm indentation	425.8	0.00408	122.8	4.48
111 μm indentation	428.7	0.00401	124.6	4.17

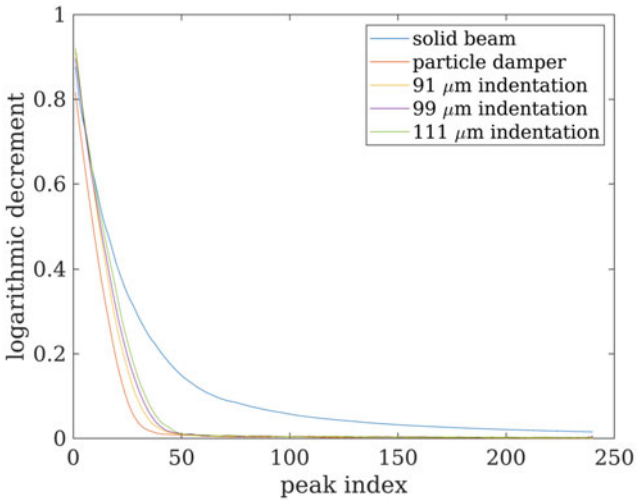

Fig. 15.5 Decay rates for the solid beam and particle damper beam

frequency response for different beams is presented. From Fig. 15.4c and d, it can be deduced that the particle damper beam before and after the indent has a lower magnitude, which indicates the beam with a particle damper has higher damping than the solid beam.

Due to particle dampers' nonlinear nature, a consistent metric to calculate the Q factor was put in place. A set window of free decay cycles was used for all test iterations, where the initial transient at the beginning and the low signal-to-noise ratio at the end of the data sets were disregarded. Table 15.2 shows the shock test result for the solid and particle damper beam. The results are an average of ten tests that make up the dataset. The particle damper before the indent has the largest damping. After the indent, the damping approaches the solid one. The Q factor is a dimensionless parameter that describes how underdamped an oscillator or resonator is. A high Q factor means low damping, which causes the system to vibrate longer. As shown in Table 15.2, the beam with a particle damper has a much lower Q factor compared with the solid beam, which means the particle damper has good damping qualities. The Q factor of the particle damper beam increases with a higher magnitude of the indent. It indicates that a high powder density cuts the beams damping performance down.

The beams' decay rate is displayed in Fig. 15.5. A quickly changing logarithmic decrement implies a highly non-linear damping behavior [2]. From the figure, we can see that the solid beam has the lowest decay rate that matches the free vibration curve. With the increasing indentation, the particle damper's decay rate increases. The gap between the solid beam and the beam with particle damper becomes smaller and smaller. However, even with a higher magnitude of the indent, the particle damper beam still has better damping performance than the solid one.

15.4 Conclusion

This paper presented an investigation into changing the volume of particle damper's post manufacturing. A cantilever beam with an unfused powder pocket manufactured by laser powder bed fusion is used. To measure the effect of a pocket volume change on energy absorption, the beam with particle damper is indented three times to study the effect of indenting (i.e., compressing) the damper pocket. The beam damping performances are tested before and after the indent with a solid beam as a reference. The experiment results show the particle damper inside of the beam can dramatically reduce the beam vibration. With compressing the pocket volume, the particle damper density increases, which cuts down the unconsolidated powders'

energy absorption capacity. However, the vibration of the beam with an indented particle damper still decays faster than the solid beam. Future work will focus on the quantification of precise powder density before and after the indent and then evaluate its effect on damping performance for a wider range of inputs and over multiple modes. With the relationship established between powder density and damping performance, particle dampers' efficiency in the laser powder bed fusion (LPBF) techniques can be enhanced.

Acknowledgments This material is partially supported by the South Carolina Space Grant Consortium under grant 521179-RP-SC007. The support of the South Carolina Space Grant Consortium is gratefully acknowledged. Any opinions, findings, and conclusions, or recommendations expressed in this material are those of the authors and do not necessarily reflect the views of the South Carolina Space Grant Consortium.

References

1. Fu, Y., Downey, A.R.J., Yuan, L., Zhang, T., Pratt, A., Balogun, Y.: Machine learning algorithms for defect detection in metal laser-based additive manufacturing: a review. J. Manuf. Process. **75**, 693–710 (2022)
2. Ehlers, T., Tatzko, S., Wallaschek, J., Lachmayer, R.: Design of particle dampers for additive manufacturing. Addit. Manuf. **38**, 101752 (2021)
3. Guo, H., Ichikawa, K., Sakai, H., Zhang, H., Zhang, X., Tsuruta, K., Makihara, K., Takezawa, A.: Numerical and experimental analysis of additively manufactured particle dampers at low frequencies. Powder Technol. **396**, 696–709 (2022)
4. Schmitz, T., Gomez, M., Ray, B., Heikkenen, E., Sisco, K., Haines, M., Osborne, J.S.: Damping and mode shape modification for additively manufactured walls with captured powder. Precis. Eng. **66**, 110–124 (2020)
5. Scott-Emuakpor, O.E., George, T., Beck, J., Runyon, B.D., O'Hara, R., Holycross, C., Sheridan, L.: Inherent damping sustainability study on additively manufactured nickel-based alloys for critical part. In: AIAA Scitech 2019 Forum (2019), pp. 0410
6. Scott-Emuakpor, O., George, T., Runyon, B., Holycross, C., Langley, B., Sheridan, L., O'Hara, R., Johnson, P., Beck, J.: Investigating damping performance of laser powder bed fused components with unique internal structures. In: Turbo Expo: Power for Land, Sea, and Air, vol. 51159. American Society of Mechanical Engineers, New York (2018), pp. V07CT35A020

Chapter 16
Additively Manufactured Component Characterization by Machine Learning from Resonance Inspection Techniques

Stephanie Gonzalez, Sierra D. Horangic, Joseph H. Lahmann, Timothy J. Ulrich, and Parisa Shokouhi

Abstract The lack of reliable, nondestructive part qualification for additively manufactured (AM) parts hinders their adoption in key industries of national interest such as aerospace and defense. Resonant ultrasound spectroscopy (RUS) is a relatively low-cost and nondestructive method for accurately determining material properties. In this work, we explored potential applications for using machine-learning techniques to computationally speed up RUS in deriving the material properties of AM parts, as well as identifying print quality of parts post-build. We performed mode identification on 226 cylinders manufactured via laser powder bed fusion (LPBF) from an A20X alloy. A lack of visual separation in the data lead to the use of statistical and dimensionality reduction techniques with the resonance peaks as well as examining the overlaid resonance spectra. We then performed classic RUS using a genetic algorithm to find the density, Young's modulus, and Poisson's ratio. By constraining these three parameters according to porosity relations relating all three material properties and training a random forest regression from finite element analysis simulations within a range of representative values, we could predict the material parameters with a lower mean RMS than compared to those values resulting from the less-constrained genetic algorithm.

Keywords Nondestructive Evaluation · RUS · Laser Doppler Vibrometry · Additive Manufacturing · Machine Learning

16.1 Introduction

Broader incorporation of additively manufactured (AM) parts in aerospace, automotive, and other industries could result in cost and lead time reductions, novel material development, unique designs, mass reduction through lightweight designs, and improved sustainment [1]. Despite its many benefits, AM is sensitive to a host of defects such as void or crack formation. Because there are various mechanisms within AM processes by which defects can be formed, nondestructive evaluation (NDE) methods are required to enact widespread use of AM parts in critical applications. X-ray radiography and computed tomography (CT) scans are currently used for high-resolution AM part inspection yet is often not fine enough to detect defects within individual layers [2]. Besides radiography and CT scans, methods such as magnetic particle testing, liquid penetrant testing, acoustic emission testing, eddy current testing, and visual testing have been employed as nondestructive testing techniques to varying degrees of success [3]. These methods have their own drawbacks including components needing to be cleaned before and after inspection, sensitivity being affected by the finish of a component, the ability to only inspect

S. Gonzalez
Department of Mechanical and Aerospace Engineering, University of Texas at El Paso, El Paso, TX, USA
e-mail: sgonzalez80@miners.utep.edu

S. D. Horangic
Department of Mechanical Engineering, Stanford University, Stanford, CA, USA

J. H. Lahmann
Department of Mechanical Engineering, Rose-Hulman Institute of Technology, Terre Haute, IN, USA

T. J. Ulrich (✉)
Los Alamos National Laboratory, Los Alamos, NM, USA
e-mail: tju@lanl.gov

P. Shokouhi
Pennsylvania State University, State College, PA, USA

M. Allen et al. (eds.), *Special Topics in Structural Dynamics & Experimental Techniques, Volume 5*,
Conference Proceedings of the Society for Experimental Mechanics Series, https://doi.org/10.1007/978-3-031-37007-6_16

non-porous surfaces, variability in magnetic permeability, and their effectiveness is restricted to conductive materials [3]. As such, there is a need for a reliable and more general nondestructive test for AM part inspection.

One promising technique is resonant ultrasound spectroscopy (RUS), which is a nondestructive evaluation technique that fits experimental modes to finite element (FE) calculated modes in order to obtain material properties like elements of the elastic moduli tensor. Elastic moduli influence the distribution of modes; the stiffer the sample is along one degree of freedom, the higher the frequency of the corresponding mode. The geometry of the sample influences the range of frequencies where the modes occur [4], and thus, the method can be used to infer changes in these properties from a standard reference point. RUS is of interest for AM part qualification due to these attributes. RUS has also been used to track the shifting of modes toward lower frequencies when a material undergoes phase transition. This is due to a relationship between RUS-derived elastic moduli and internal energy [5]. Previous attempts to determine material properties of complex geometries have consisted of mode matching and optimizing the fit between simulation and observed behavior. This process is referred to as inversion. The inversion process is a time-intensive, iterative minimization problem and largely relies heavily on accurate mode order matching for accuracy [6]. This project consisted of experimental modal testing on all samples, using various dimensionality reduction and statistical graphing techniques to look for visual separation in the data, and comparing the performance of classic RUS and a simulation-trained random forest regression model on calculating density, Poisson's ratio, and Young's modulus.

16.2 Background

Laser powder bed fusion (LPBF) selectively melts two-dimensional (2D) cross sections of the part to the previous layers of the part to successively create parts layer by layer. Laser processing parameters have a large effect on the densification and microstructure of materials used in LPBF technology. The high-energy density deposited into the metal powder by the laser leads to a full melting of the powder resulting in nearly or fully dense parts without the need for post-processing [7].

AM parts often have atypical geometry, which makes laser doppler vibrometry (LDV) an attractive option for modal testing since it is agnostic to shape. LDV covers broad frequencies and dynamic responses, which is not attainable by contact sensors. Results of a test previously conducted on rectangular parallelepiped specimens showed that LDV could detect modes that failed to be detected by contact approaches. In this case, non-contact detection exhibited superior sensitivity to detect frequencies as opposed to other approaches using contact sensors [8]. Implementing RUS using LDV has been recognized as an effective approach for material parameter estimation. However, RUS still suffers from the costly inversion process, which requires repeated simulations to be run while optimizing the model modes to the experimental. This makes using machine-learning (ML) models to learn this inversion an attractive idea.

ML techniques have an increasing popularity due to their ability to recognize subtle trends in complex datasets. Applying these methods to NDE methods has seen varied success across different materials and part inconsistencies. Chen et al. determined the elastic constants of a part made of piezoelectric material with high accuracy in as little as 150 ms. This was accomplished using 3 deep neural sub-networks which trained on a randomly created training set from FE analysis, only looking at a feature vector containing resonant frequencies [9]. From tests conducted by McGuigan et al., it was concluded that material property variance from the AM printing process played just as much of a role in defining the resonance spectra as their geometrical defects [3]. Oblaton et al. showed that resonant acoustic methods with purely experimental and labeled data, coupled with regularized linear discriminant analysis (RLDA), could result in 80% prediction accuracy of their test dataset [10]. Furthermore, calculating elastic constants can also be used to imply other information about the system. Ghosh et al. applied an ML algorithm to determine from raw spectral data the dimensionality of the order parameter for at lower temperatures [11].

16.3 Methodology

All testing was on a set of 226 cylinders of 10 mm diameter, Fig. 16.1, built with A20X across two build plates. Baseline parts were manufactured using laser settings of 200 W with a scan speed of 1000 mm/s and a hatch spacing of 0.1 mm. Altered parts were printed with one of these parameters varied up to ±25%. These parameters can be combined into a volumetric energy term according to Eq. 16.1, where P is laser power, d is hatch spacing, s is scanning speed, and t is layer thickness.

Fig. 16.1 A sample test part, printed out of A20x with machine parameters engraved during printing on the top face

$$\text{Energy density} = \frac{P}{s \cdot d \cdot t} \tag{16.1}$$

Before modal testing, an eigenfrequency analysis was performed using Abaqus. This determined which modes could reasonably achieve mesh convergence, as well as provide a prediction for the modal shapes present. The parameter labeling on the top of the parts was defeatured for simulation convergence, as it was found to result in negligible changes to the eigenfrequencies. To confirm mesh convergence, various modes were examined along decreasing mesh size. The most efficient mesh size was determined to be at 0.4 mm, where the first 30 modes were seen to be converging. Higher modes were excluded from consideration due to lack of convergence.

An experimental testing rig was designed and fabricated with the goal of minimally constraining the test part during testing, Fig. 16.2. Excitation was driven by a piezoelectric transducer and read with a point LDV at the crest of the part. The fixture created a point contact at 45° between the cylinder and the domed transducer and allowed for the excitation of as many modes as possible. A removable jig on the fixture allowed for a consistent placement of the cylinder and supportive foam served for minimal support to approximate a zero-boundary condition.

Frequency windows around modes of interest were identified, and the data collection excited the part across this spectrum, recording the response amplitude. Each window for each part resulted in a frequency response function (FRF) such as Fig. 16.3.

Mode matching (as well as further validation of the simulation) was done by matching 2D modal shapes. Test parts were excited at a mode, then scanned across the surface with a 2-D LDV for all the modes identified as detectable in our setup. This identification is represented in Table 16.1.

Simulations served a second purpose beyond determining experimental windows. It is also used in the creation of a synthetic dataset for training regression models. Prior work by Ramakrishnan provides the basis for calculating Young's modulus and Poisson's ratio from density, as established by Eqs. 16.2, 16.3, and 16.4 [12]. So, a synthetic dataset was created by varying only the density of the part.

$$P = 1 - \frac{\rho}{\rho_0} \tag{16.2}$$

Table 16.1 The correlation between the simulated mode shapes and experimentally observed mode shapes

Mode feature #	1	2	3	4	5	6	7	8	9	10
Mode #	1	2	4	9	10	13	14	15	22	23
Observed shape	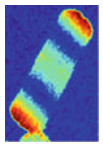	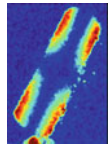	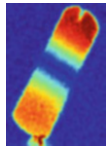	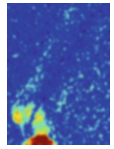	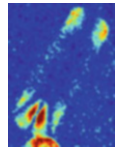	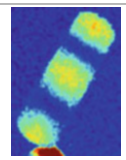	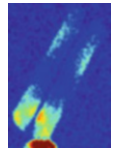	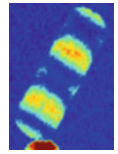	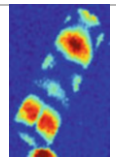	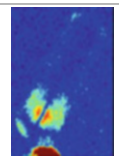
Simulation predicted shape		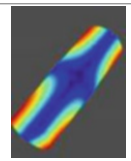	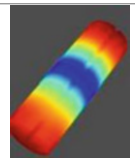	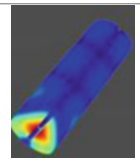	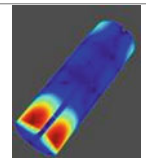	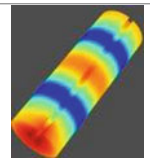	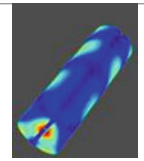	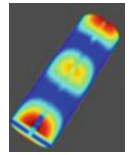	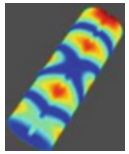	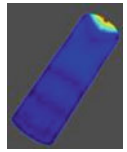

Note: mode 23 appears to be mismatched; this mode was found to be sensitive to small variations in material properties

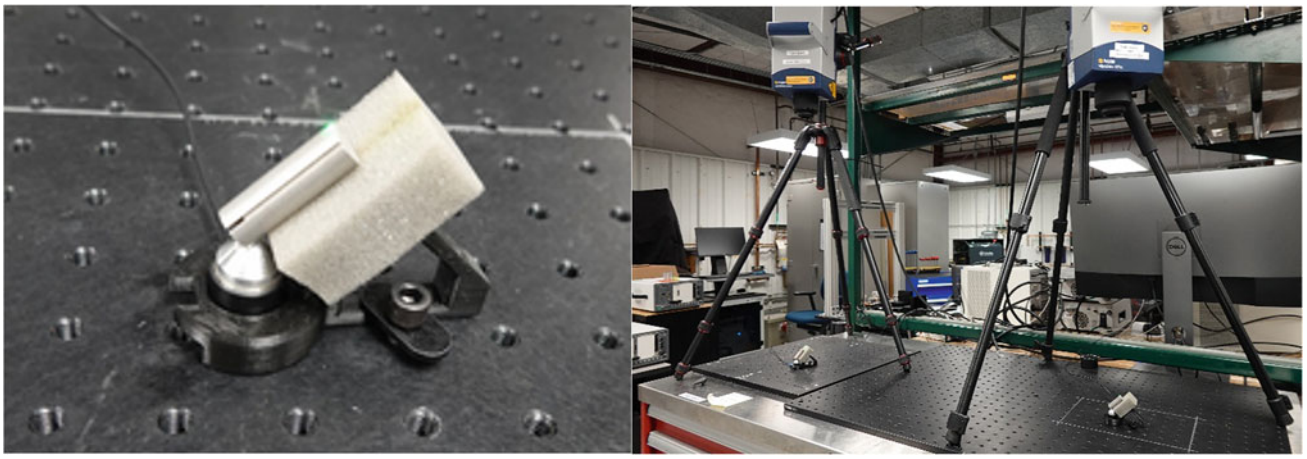

Fig. 16.2 Left: Excitation rig loaded with a part, showing orientation and direction of LDV. Right: two experimental testing rigs shown side by side

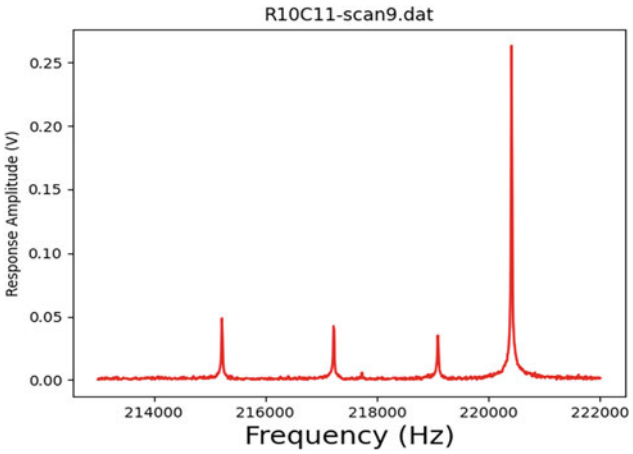

Fig. 16.3 A sample experimental FRF showing a dense nodal region

$$E = E_0 \frac{(1-P)^2}{1+(2-3v)\,P} \tag{16.3}$$

$$v = \frac{4v + 3P - 7v_0 P}{1 + 2P - 3v_0 P} \tag{16.4}$$

16.4 Analysis

Variability of the testing rig was evaluated by testing a single part repeatedly, removing and remounting from the test rig six times. Standard deviations for nearly all modes in this test were all under 10 Hz. One mode saw a standard deviation of nearly 50 Hz and was subsequently excluded from further analysis due to excessive noise. Drift was also evaluated by leaving the same part on the test rig overnight, during which 136 scans were run for each of the frequency ranges of interest. The calculated standard deviation of the modal frequencies is shown in Table 16.2. This is likely due to temperature variation, which could be confirmed in the future by tracking temperature.

To understand the differences between the baseline and altered parts, the scans for each window were overlaid as shown in Fig. 16.4. From this, we can see that the spectra for the altered parts lie solidly within the reasonable range of response for the baseline. Looking at the statistical distributions, there is no clear separation either in comparing the frequency distribution for each mode (Fig. 16.5) or the peak width distribution for each mode (Fig. 16.6).

Table 16.2 Standard deviation of the modal frequencies as measured across all modal scans

Mode	1	2	3	4	5	6	7	8	9	10
Modal frequency	43.1 kHz	43.4 kHz	88.8 kHz	136.5 kHz	143.8 kHz	172.2 kHz	178.1 kHz	184.4 kHz	220.7 kHz	229.1 kHz
Standard deviation	7.7 Hz	8.1 Hz	14.8 Hz	23.9 Hz	24.6 Hz	29.8 Hz	31.7 Hz	32.9 Hz	38.7 Hz	41.2 Hz

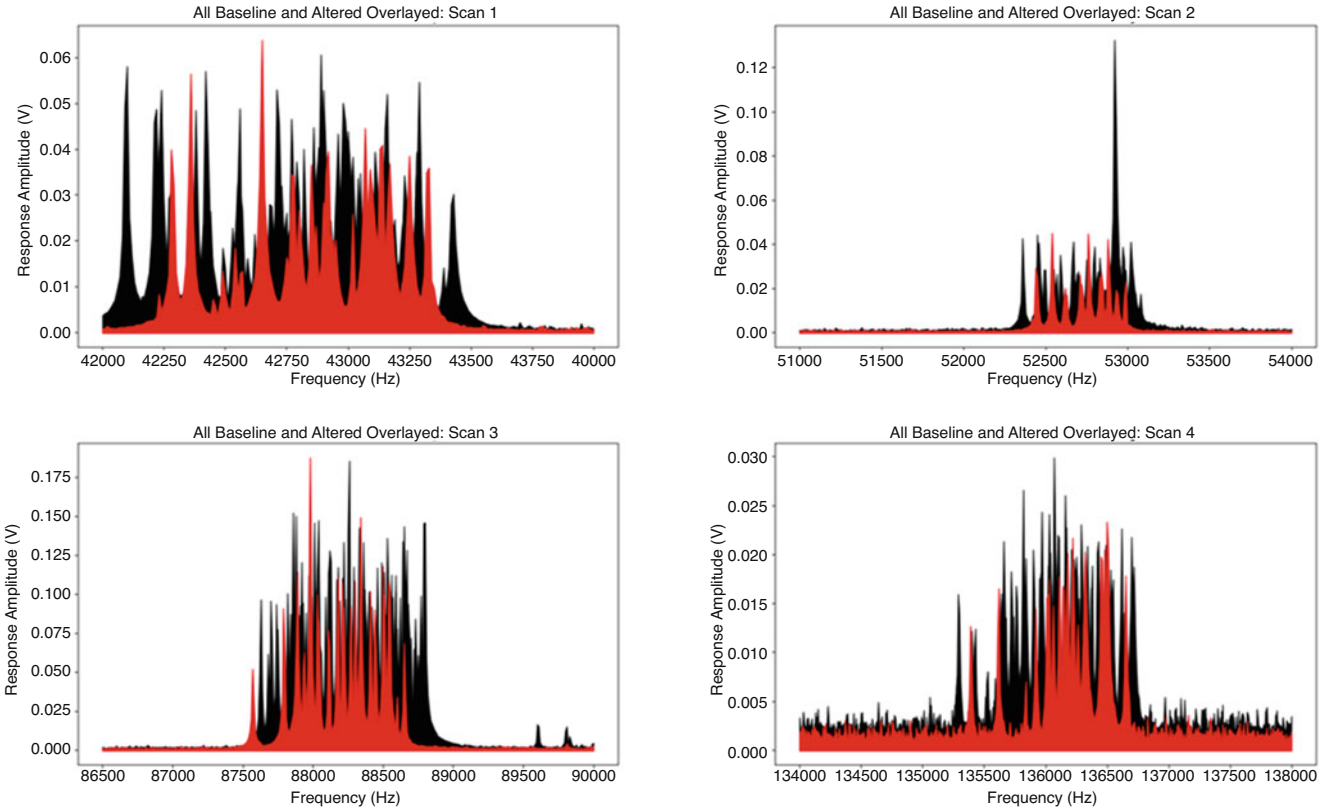

Fig. 16.4 Overlaid FRF scans of baseline (black) and altered (red) parts, displaying how the range of responses of the altered parts is firmly within the range of the baseline

Various dimensionality reduction techniques were also applied to the data to look for insight for separation, including linear principal component analysis (PCA), kernel PCA (cosine, radial basis function, and polynomial kernels), and manifold learning techniques (isomap, local linear embedding, and spectral embedding). These were all applied on various combinations of modal frequency, amplitude, and peak width. For all, the first three components (or two in the case of manifold learning) were plotted and examined visually, with the true labels of the build parameters (in the form of volumetric energy density) coloring data points. In all cases, there was no clear separation in the data between the baseline and altered parts.

Density-based spatial clustering of applications with noise (DBSCAN) clustering was used to delineate clusters when visualizing datasets [13]. Figure 16.7 shows clustering of the parts based on their damping fraction for all seven modes. One dense, distinct cluster, as well as another comprised of outliers can be seen. Visualizing these results along the first three damping components clearly showed a physical correlation between the yellow cluster and internal damping—the cluster appears near the corner with the lowest damping fractions, and the outliers have larger damping fractions for at least one of their modes. This could indicate that damping could be a valuable feature to track during any component characterization.

To look at the performance of a ML model learning the RUS inversion, a random forest regression was implemented by training on the synthetic dataset created according to Ramakrishnan's correlations. Table 16.3 shows the gap between the predicted values by RUS and the regression. The average root-mean-square RMS error from the frequency matching of all parts was found to be 0.92% for the random forest regression as compared to 1.51% for standard RUS. This performance boost with the random forest regression is likely due to the standard RUS inversion being under constrained and finding a local minimum.

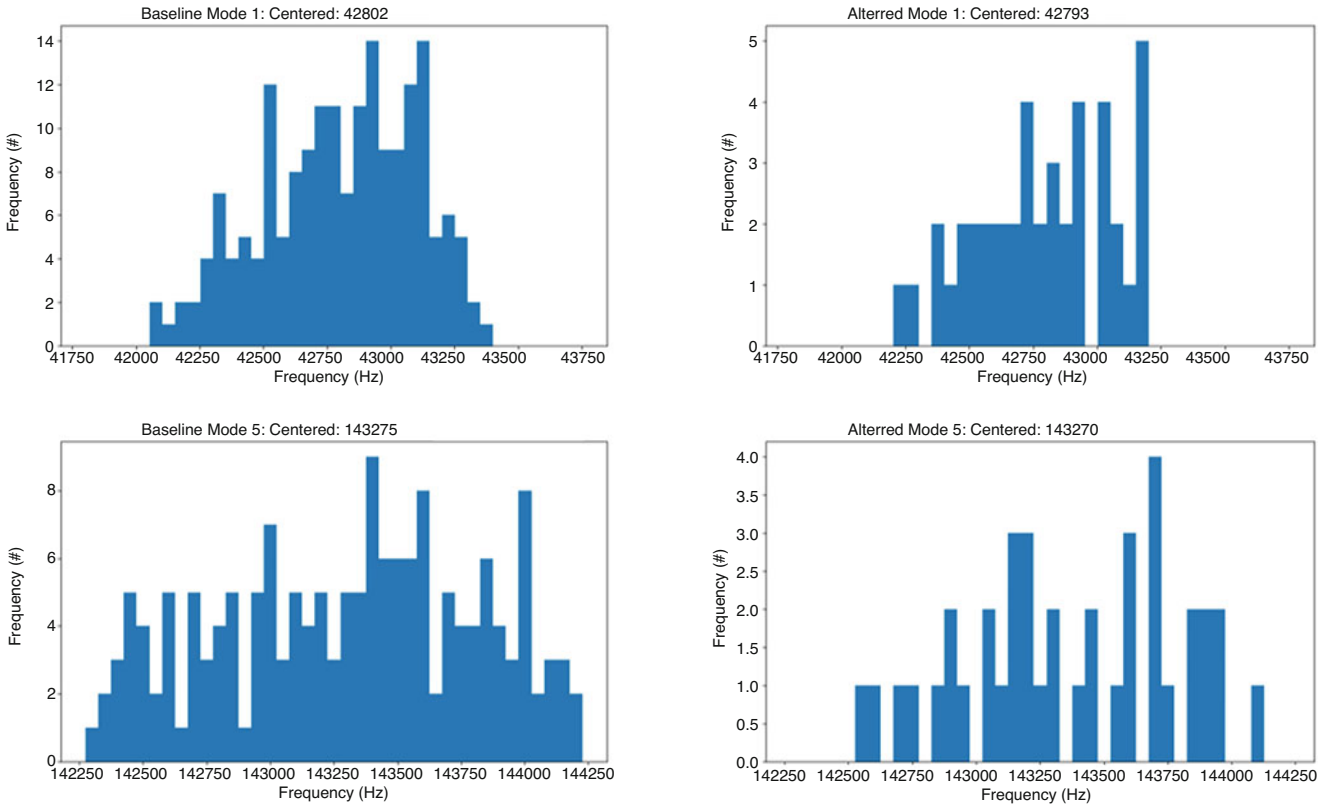

Fig. 16.5 Sample modal distributions indicate the similarity between baseline and altered results

Table 16.3 The sample comparison between RUS and random forest regression for one baseline part (R3 C10) in calculating the material properties

	Predicted density	Predicted elastic modulus (MPa)	Predicted Poisson's ratio
Regression	2.77 g/mm^3	77,800	0.339
RUS	2.78 g/mm^3	63,470	0.316

16.5 Conclusion

The experimental results indicate that it is likely the test parts used are all within the relative bounds of acceptable printing parameters. For the methods utilized, there was no detectable shift in the material properties correlated with the build parameters, although DBSCAN clustering indicates the possibility of a clumping of parts along their damping characteristics. Plotting after dimensionality reduction, statistical distributions, and overlaid raw data can give insight to the feature selection process when designing a model for NDE.

The experimental results further indicate this random forest regression outperforms our standard RUS inversion in prediction accuracy. This ML regression has a high initial computational cost, with subsequent calculations becoming negligible after the model is trained. Conventional RUS has a relatively constant need to perform many simulations for a single regression. Given a high volume of parts, this ML regression would easily outstrip conventional RUS. Ultimately, this work indicates the potential of training ML regressions using constrained training data.

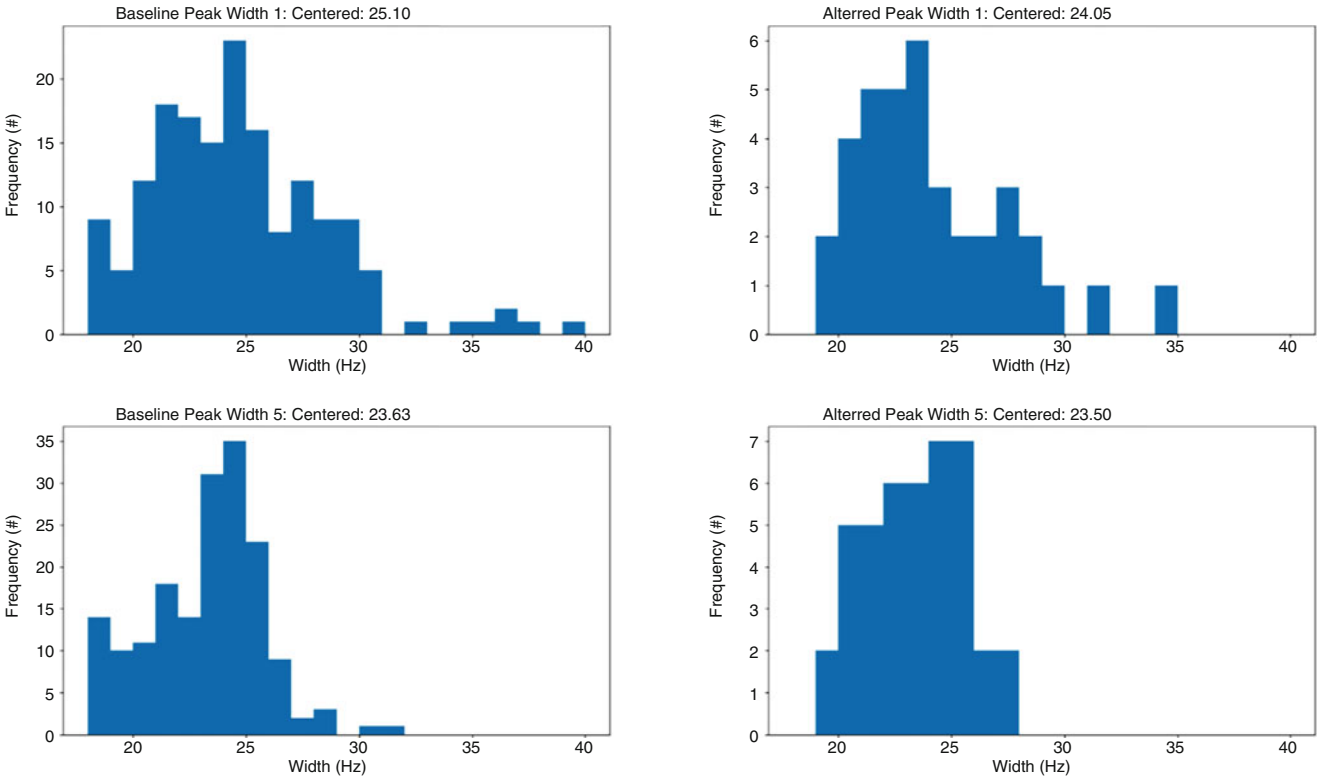

Fig. 16.6 Sample peak width distributions indicate the similarity between baseline and altered results

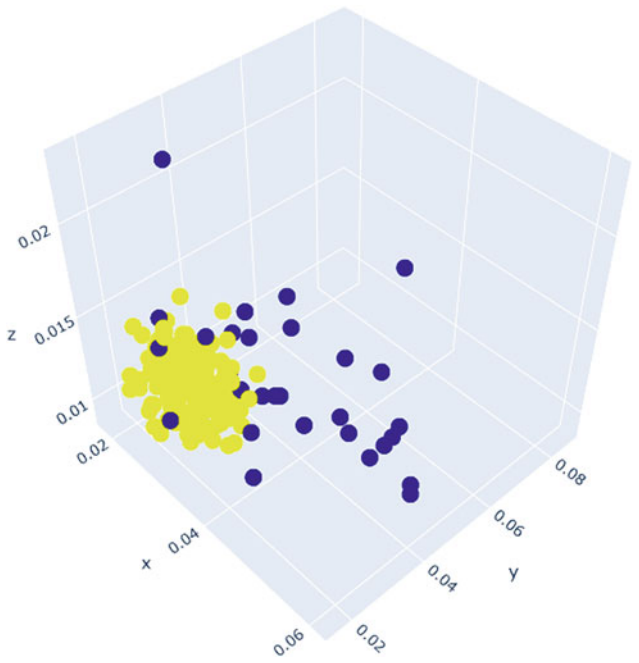

Fig. 16.7 DBSCAN labeling based on the damping for all modes

Acknowledgments This research was funded by Los Alamos National Laboratory (LANL) through the Engineering Institute's Los Alamos Dynamics Summer School. The Engineering Institute is a research and education collaboration between LANL and the University of California San Diego's Jacobs School of Engineering. This collaboration seeks to promote multidisciplinary engineering research that develops and integrates advanced predictive modeling, novel sensing systems, and new developments in information technology to address LANL mission relevant problems.

Furthermore, we would like to thank Mr. Luke Beardslee for authoring and supplying the RUS code used to calculate inversions on all test parts. We would also like to thank Dr. Adam J. Wachtor for his guidance, editing suggestions, and support during the entire course of research.

References

1. Milner, B., Gradl, P., et al.: Metal additive manufacturing in aerospace: a review. Mater. Des. **209**, 110008 (2021). https://doi.org/10.1016/j.matdes.2021.110008. ISSN 0264-1275
2. Edgar, S.: Non-destructive testing of additive manufactured parts. 2020. https://www.azom.com/article.aspx?ArticleID=19038
3. McGuigan, S., Arguelles, A.P., Obaton, A.-F., Donmez, A.M., Riviere, J., Shokouhi, P.: Resonant ultrasound spectroscopy for quality control of geometrically complex additively manufactured components. In: Additive Manufacturing, vol. 39, p. 101808. Elsevier BV (2021). https://doi.org/10.1016/j.addma.2020.101808
4. Zadler, B.J., Le Rousseau, J.H., Scales, J.A. and Smith, M.L.: Resonant ultrasound spectroscopy: theory and application. Geophysical Journal International, **156**(1), pp.154–169. (2004)
5. Balakirev, F.F., et al.: Resonant ultrasound spectroscopy: the essential toolbox. Rev. Sci. Instrum. **90**(12), 121401 (2019)
6. Beardslee, L., Remillieux, M., Ulrich, T.J.: Determining material properties of components with complex shapes using resonant ultrasound spectroscopy. Appl. Acoust. https://doi.org/10.1016/j.apacoust.2021.108014
7. Cobbinah, P., Nzeukou, R., Onawale, O., Matizamhuka, W.: Laser powder bed fusion of potential superalloys: a review. Metals. **11**, 58 (2020). https://doi.org/10.3390/met11010058
8. AIP Conf.Proc. **1949**, 170002 (2018); Published Online: 20 April 2018
9. Chen, Z., Miao, X., Li, S., Zheng, Y., Xiong, K., Qin, P., Han, T.: Data fusion method and probabilistic pairing approach in elastic constants measurement by resonance ultrasound spectroscopy. In: IEEE Transactions on Instrumentation and Measurement, vol. 69, Issue 6, pp. 2948–2958. Institute of Electrical and Electronics Engineers (IEEE) (2020). https://doi.org/10.1109/tim.2019.2925409
10. Obaton, A.-F., Wang, Y., Butsch, B., Huang, Q.: A non-destructive resonant acoustic testing and defect classification of additively manufactured lattice structures. In: Welding in the World, vol. 65, Issue 3, pp. 361–371. Springer Science and Business Media LLC (2021). https://doi.org/10.1007/s40194-020-01034-7
11. Ghosh, S., Matty, M., Baumbach, R., Bauer, E.D., Modic, K.A., Shekhter, A., Mydosh, J.A., Kim, E.-A., Ramshaw, B.J.: One-component order parameter in URu 2 Si 2 uncovered by resonant ultrasound spectroscopy and machine learning. In: Science Advances, vol. 6, Issue 10. American Association for the Advancement of Science (AAAS) (2020). https://doi.org/10.1126/sciadv.aaz4074
12. Choren, J.A., Heinrich, S.M., Silver-Thorn, M.B.: Young's modulus and volume porosity relationships for additive manufacturing applications. J. Mater. Sci. **48**(15), 5103–5112 (2013). https://doi.org/10.1007/s10853-013-7237-5
13. Ester, M., Kriegel, H.-P., Sander, J., Xu, X.: A density-based algorithm for discovering clusters in large spatial databases with noise. www.aaai.org (1996)

Chapter 17
Experimental Modal Analysis of an Additively Manufactured Model

Aditya Panigrahi, Brianna Blocher, Marc Eitner, and Jayant Sirohi

Abstract Additive manufacturing methods have advanced a lot in the past year. Methods like Fused Deposition Modeling (FDM) have gained popularity due to their versatility in material and minimal limitation on the geometry. Structural modeling of additively manufactured parts can, however, be complicated. This is primarily due to the dependence of material stiffness on print settings such as layer height, infill density, and infill pattern. In addition, the material can exhibit anisotropic characteristics due to parameters like the adhesiveness of layers, the orientation of the raft, and the layer deposition speed. This study conducts an experimental modal analysis on a 40% scaled model whose geometry is based on the aircraft Initial Concept 3.X (IC3X). The test article was manufactured using FDM, and ABS was chosen as the material. Fiber-optical strain sensors were attached to the test article and were used to record the response to structural excitation. Static tests were performed in addition to dynamic testing to further evaluate the test article's stiffness. The static test cases were used to update a finite element model of the test article and to obtain precise values of the Young's modulus, which is dependent on printer settings. The natural frequencies obtained from both the numerical model and dynamic testing showed good agreement.

Keywords FEA · Experimental modal analysis · Additive manufacturing · Fiber-optic · FDM

17.1 Introduction

Additive manufacturing (AM) is hailed as a significant revolution in manufacturing engineering due to its minimal geometry and materials limitations. Fused Deposition Modeling (FDM) has become an integral part of rapid prototyping among the various AM methods enabling engineers to produce complex parts. In FDM, a filament is pushed into a heated Liquidifier and is extruded through a nozzle. The nozzle is free to move along two orthogonal axes. The nozzle deposits the molten material onto a stage that can move up and down, which results in the material cooling down and solidifying. This process is carried out until all the layers are deposited on top of each other. For a hollow part, FDM considers the gap between the outer and inner geometry of the model and uses layers to fill that gap. The user can select parameters like the infill density, part orientation, and infill pattern based on the application. These parameters can heavily influence the mechanical properties of the printed part [1–3]. Raffic et al. [4] investigated the effect of these parameters on the tensile strength of ABS (acrylonitrile butadiene styrene). According to their research, infill density significantly increases the strength due to the increased strength provided by high infill density. Parts made with the FDM process exhibit anisotropic material behavior due to the orientation of the filament that is deposited at each layer of the part. Due to these parameters, a part fabricated using the FDM process can deviate substantially from the original design, typically more than a part made using conventional subtractive manufacturing processes (e.g., milling of metal).

It is essential that the effects of these printing parameters are evaluated. A common task for structural engineers is to match experimental data with a numerical model. This study investigates a large, 1.5 m-long 40% scale model of a hypersonic air vehicle manufactured using the FDM process. The model was instrumented with 23 fiber optical strain sensors, and static tests and modal analysis (impact testing) were performed. This study evaluates how well a large-scale FDM model matches static and dynamic numerical predictions (FEA).

A. Panigrahi (✉) · B. Blocher · M. Eitner · J. Sirohi
Department of Aerospace Engineering and Engineering Mechanics, The University of Texas at Austin, Austin, TX, USA
e-mail: aditya.panigrahi@austin.utexas.edu; brianna.blocher@austin.utexas.edu; marceitner@utexas.edu; sirohi@utexas.edu

M. Allen et al. (eds.), *Special Topics in Structural Dynamics & Experimental Techniques, Volume 5*,
Conference Proceedings of the Society for Experimental Mechanics Series, https://doi.org/10.1007/978-3-031-37007-6_17

17.2 Methodology

17.2.1 Initial Concept 3.X Vehicle (IC3X)

The Initial Concept 3.X Vehicle (IC3X) was designed by the Air Force Research Laboratories (AFRL) as part of an initial sizing study [5]. For this project, the IC3X was scaled down by 40% and used as a test article to conduct static and dynamic structural tests. The model was manufactured using a Stratasys Fortus 450MC^{TM}, which is a Fused Deposition Modeling machine capable of printing parts made out of materials like ABS (acrylonitrile butadiene styrene) and PLA (polylactic acid). ABS was chosen as the material for the IC3X test article.

The internal structure of the test article was explicitly designed to increase the sensitivity of internal strain sensors to bending moments. A thin wall section would lead to structural instability for a test article of this size, whereas a thick wall would increase the stiffness and provide a low signal-to-noise ratio. The solution to this problem was to implement localized reduction of wall thicknesses at intervals along the length of the model where the strain sensors were attached. This localized wall thickness reduction is referred to as a flexure region. Figure 17.1 shows the schematic of the test article, along with a magnified region that shows the flexure region. The test article was mounted on a metal sting, as shown in Fig. 17.2.

17.2.2 Experimental Setup

17.2.2.1 Fiber Optical Strain Sensors

As mentioned earlier, the flexure region is the ideal place to attach strain sensors. The system used for measuring the strain from the FBG fiber is called GTR FBG Interrogator (GTR1001-E) and have broad applications. For example, GTR 1001-E can be used on an airframe for shape sensing [6]. Each FBG measures strain at one location. Sensors embedded in the fiber operate at a 19.23 kHz sample rate and can record strain values as low as 1μ strain. Five channels or strings of FBG fibers are attached along the length of the IC3X model. Figure 17.3 shows a schematic of sensor locations.

17.2.2.2 Experimental Modal Setup

In this study, experimental modal analysis was conducted by using an impact hammer to excite the model, and the strain sensors were used to measure the response. The impact hammer (PCB 086B03) was connected to an NI DAQ system to record the impulse response. The red dot on Fig. 17.3 shows the impact location. Response from the impulse was recorded separately for each channel. A metal tip was attached to the hammer in order to improve the impact, and the response was measured at the sampling frequency of 19.23 kHz, same as the FBG system.

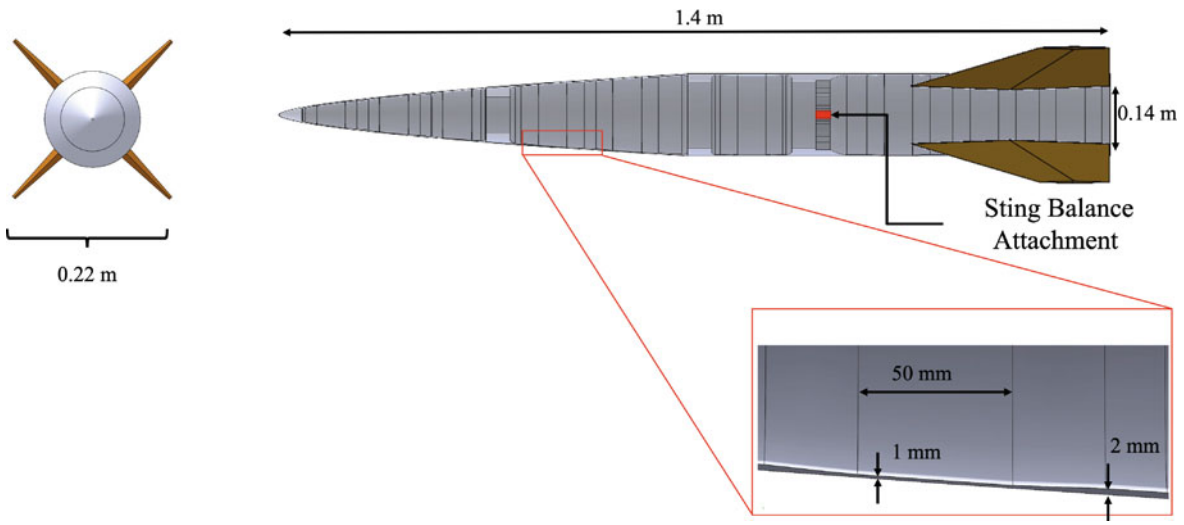

Fig. 17.1 IC3X 40% scale model test article

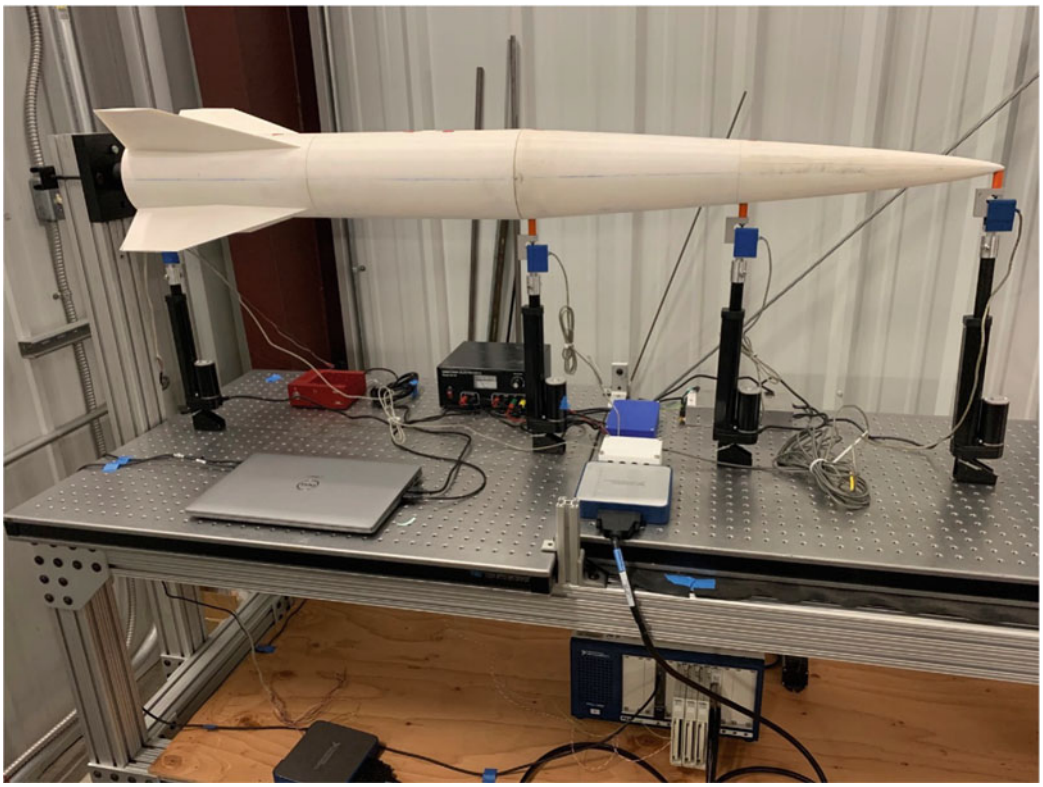

Fig. 17.2 Test article setup

17.2.3 Numerical Model

ANSYS mechanical module was used to develop a numerical model for the test article. A fixed boundary condition was applied to the faces interfacing with the sting. In ANSYS mechanical, the primary input is the static load applied on the test article, which ensures that the numerical model setup is as close as possible to the experimental setup.

17.3 Results and Discussion

17.3.1 Updating the Young's Modulus of ABS

The Young's modulus of an FDM material can vary based on the printer settings, as was discussed previously. While the ABS material used for the test article has a range for Young's modulus provided from its manufacturer (2.46 GPa-2.14 GPa), it was important for the numerical modeling to obtain a more accurate value.

For this study, a cylinder of length 0.34 m and a wall thickness of 2 mm was printed in the same printer with the same orientation and infill pattern as the IC3X test article. The cylinder was instrumented with conventional foil strain gages, and static loads were applied. Due to the simple geometry, it was possible to use the strain equation for a beam [7], as shown in Equation (17.1), from which Young's modulus was calculated. M is the bending moment, y is the radius between the neutral axis to the location of the strain gauge, I is the area moment of inertia, and $\epsilon_{measured}$ is the measured strain.

$$E_{Theo} = \frac{My}{\epsilon_{measured} I} \tag{17.1}$$

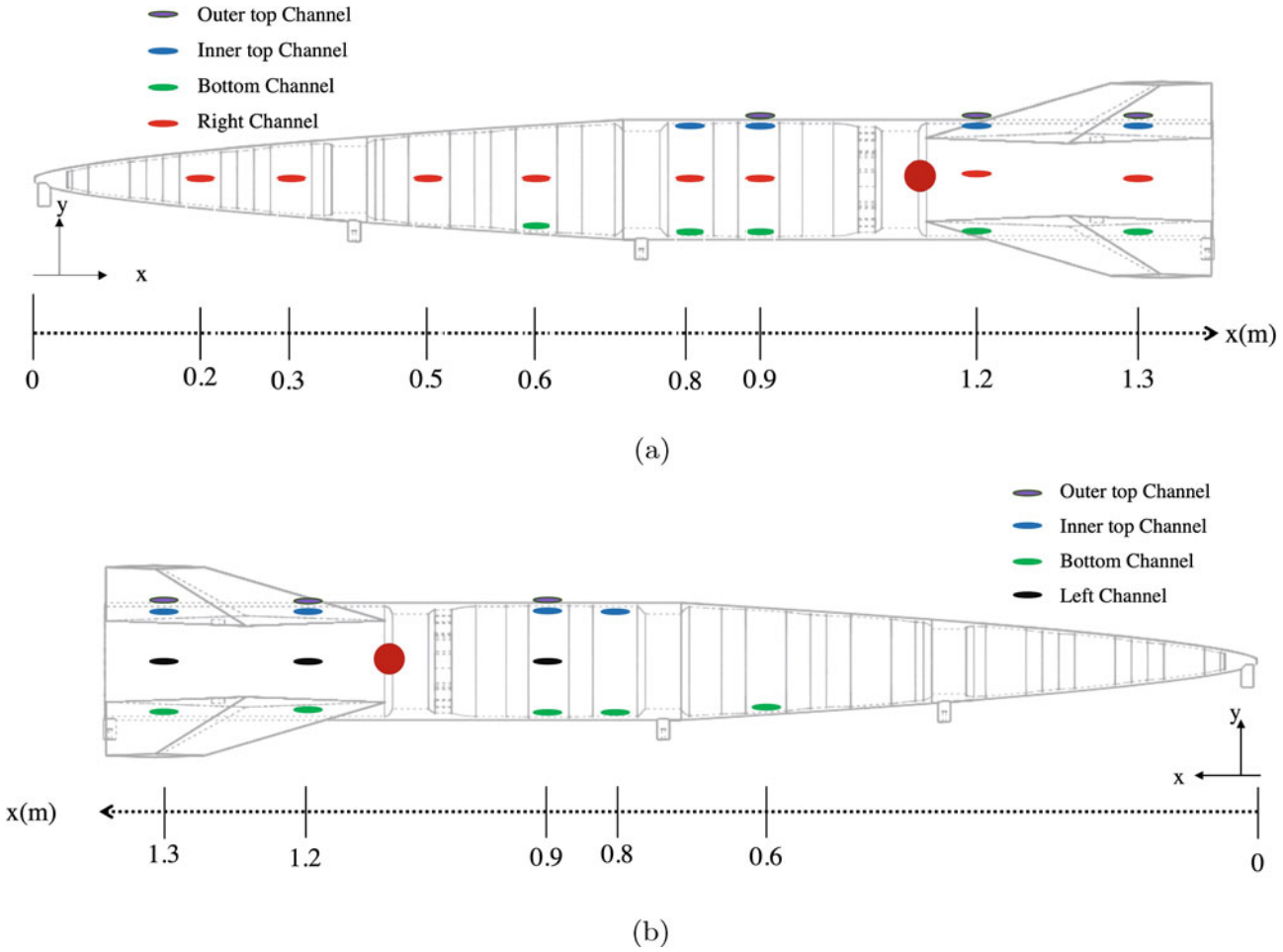

Fig. 17.3 Schematic of sensor placement on the IC3X. (**a**) Sensor placement (right side view). (**b**) Sensor placement (left side view)

A full bridge strain gage was applied 127 mm from the base. One end of the cylinder was clamped to enforce fixed boundary conditions, and weights were applied at the free end of the cylinder. The extracted Young's modulus from these strain measurements was 2.293 ± 0.0219 GPa, which was within the manufacturer-provided range. Thus, a Young's Modulus of 2.293 GPa was used in the FEA model.

17.3.1.1 Geometry Update

Due to the printer resolution, which results from the layer thickness of the FDM process, there are discrepancies in wall thickness between the CAD model and the final printed model. Since these discrepancies affect the area moment inertia, which affects the strain, the geometry used for the numerical solution must be updated to get a good agreement between the numerical model and experiments. In order to update the geometry, a linear actuator was used to apply a compressive force at the middle of the nose cone. Three strain sensors on the bottom channel were considered since they experienced bending moments. The thickness of the flexures was changed in the CAD software. Table 17.1 shows the changes in the wall thickness that were made to match the numerical solution to the experimental values. Figure 17.4 compares the strain calculated by the numerical model for the original and updated geometry for a single sensor. Small changes in wall thickness can have significant effects on the strain. This updated geometry and the new Young's Modulus were implemented on the numerical model.

Table 17.1 Geometry modifications after model updating

Location	Original (CAD) thickness [mm]	Updated (CAD) thickness [mm]
All thick parts	2.00	2.03
Most downstream flexure	1.5	1.51
All other flexures	1.0	0.91

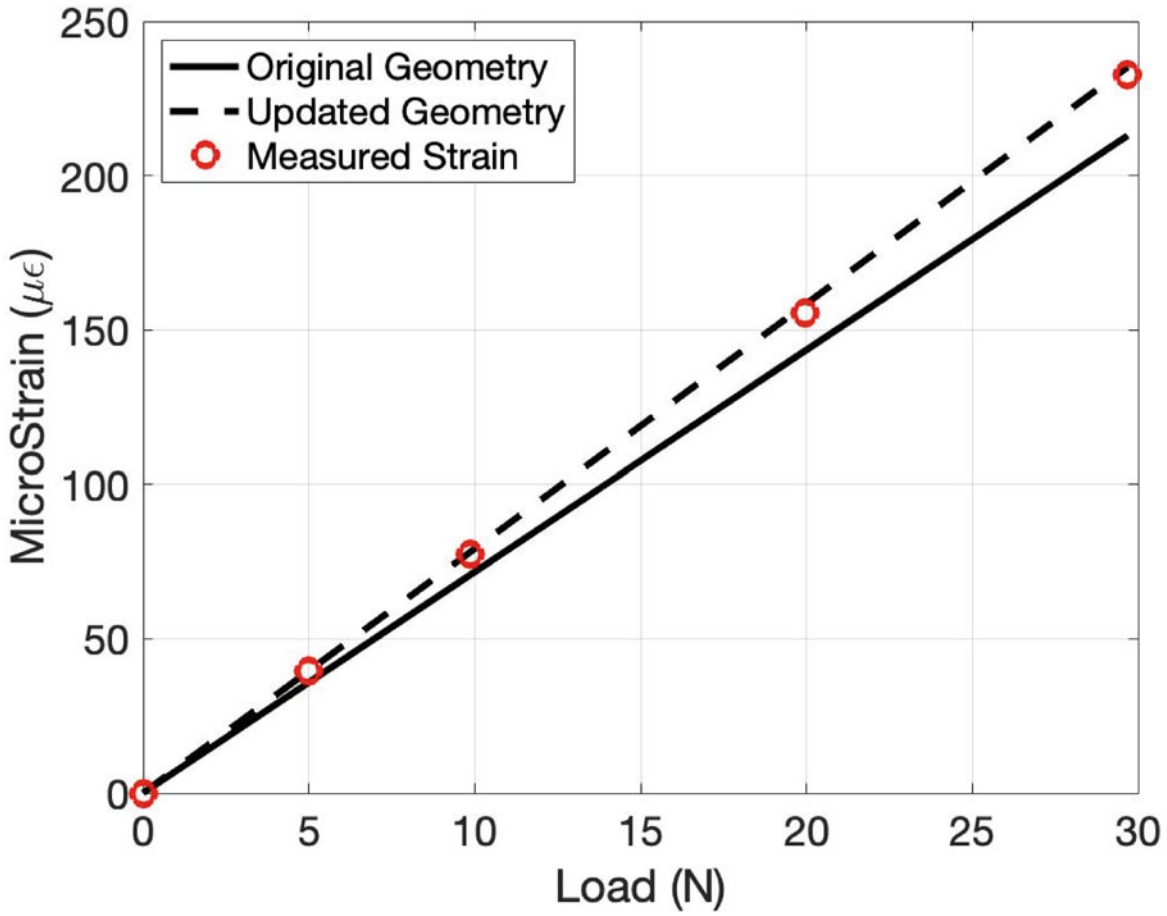

Fig. 17.4 Effect of changing flexure thickness on strain values from the numerical model

17.3.2 Frequency Response Functions

The modal parameters of the model were computed from the Frequency Response Functions (FRF), which were obtained from the measured strain and applied impulses. Figure 17.5 shows the power spectra of four impacts. They show minimal variation of magnitude for the considered frequency range of 0–300 Hz and were therefore selected to calculate the FRFs.

As mentioned earlier, four impacts were performed at the exact location for each channel shown in Fig. 17.3 and averaged to get an FRF for each sensor. Figure 17.6 shows the impulse and the resultant strain response for a single sensor. It can be seen that the impulse creates periodic strain response whose amplitude dies down as time goes on. This behavior was consistent in all of the sensors for all of the trials. A low-pass filter with a cut-off frequency of 700 Hz was applied to the signal to reduce the noise in the signal.

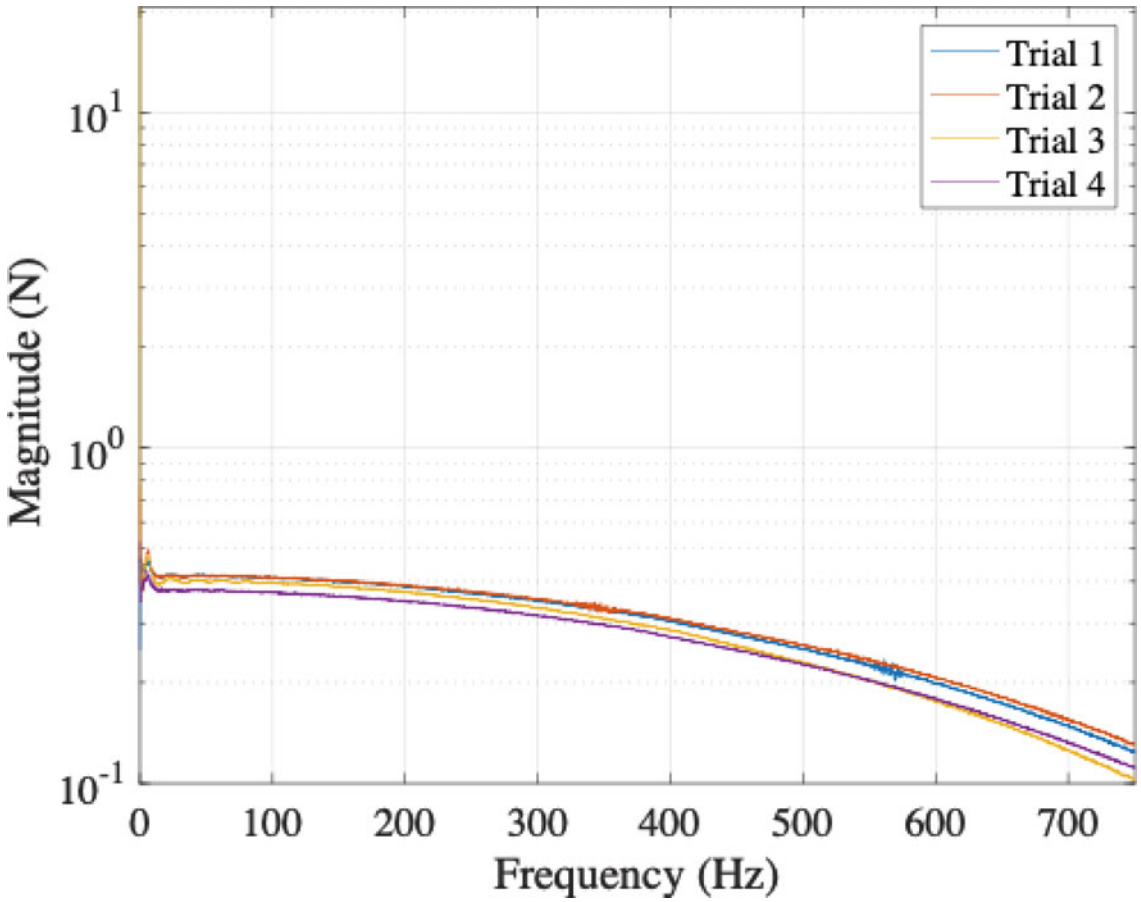

Fig. 17.5 Power spectra of impacts from impact hammer

Figure 17.7 shows the averaged FRF plotted over the FRFs of each trial for a single sensor. The averaged FRF appears clean and indicates a good signal-to-noise ratio of the measured data. The stabilization diagram for each FRF was computed using the MATLAB system identification toolbox. It was used to find the distinct stable peaks to identify the system's natural frequencies. Table 17.2 lists the natural frequencies determined from the stabilization diagrams of the FRFs of four sensors. These values are compared with the natural frequencies determined from the numerical FEA model.

17.4 Conclusion

Static tests resulted in geometry updates, significantly improving predictions model stiffness. Updating Young's Modulus and the flexure geometry helped generate more accurate strain values when compared to the static numerical model. For the dynamic testing part of this study, the modal analysis showed a good correlation in natural frequencies for both numerical and experiment values.

Structural dynamics of a large-scale part manufactured using additive manufacturing, like the test article of IC3X, is influenced by multiple parameters like infill density and pattern, which can affect the stiffness of the model, which in turn can affect the modes of the system. Therefore, a future study is planned in which the same rocket model is made from aluminum and will undergo the same model updating and modal analysis steps as in this study. A comparison of both results (ABS and aluminum model) will help identify issues related to the stiffness of large-scale FDM parts.

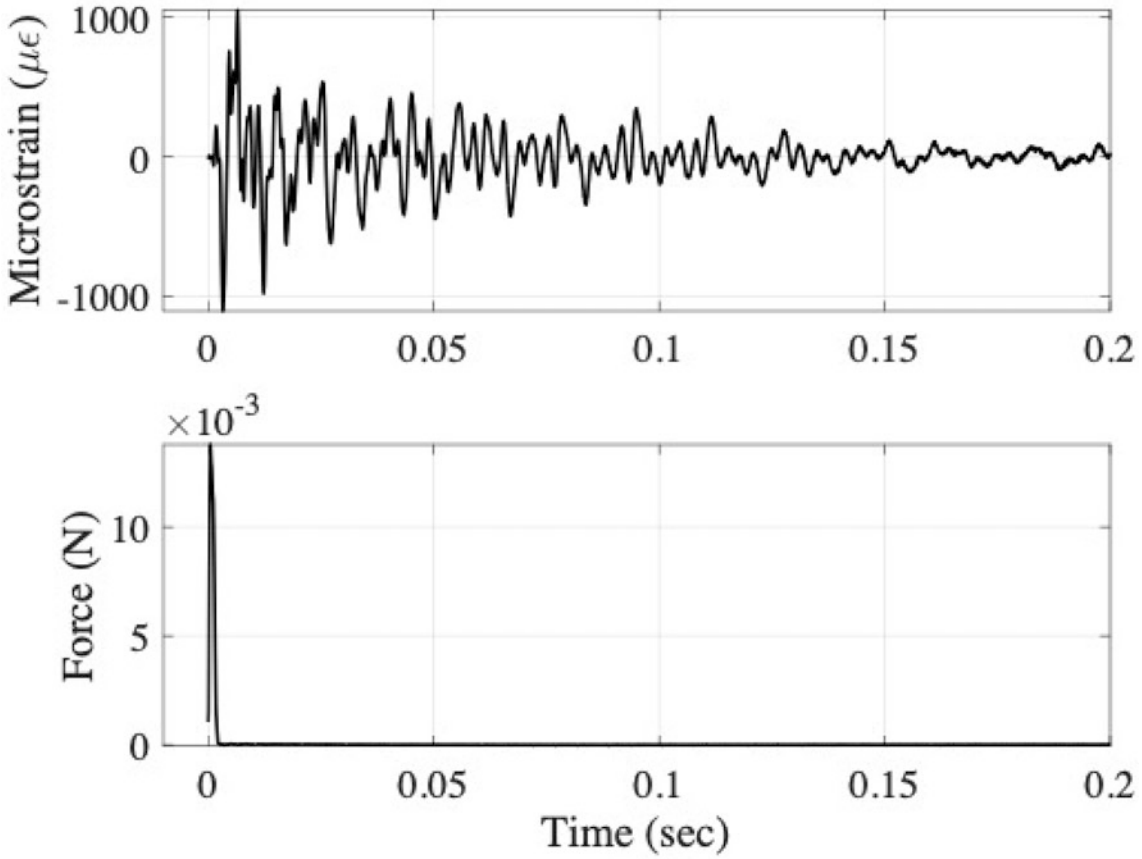

Fig. 17.6 Time histories of measured impact and strain, after low-pass filtering

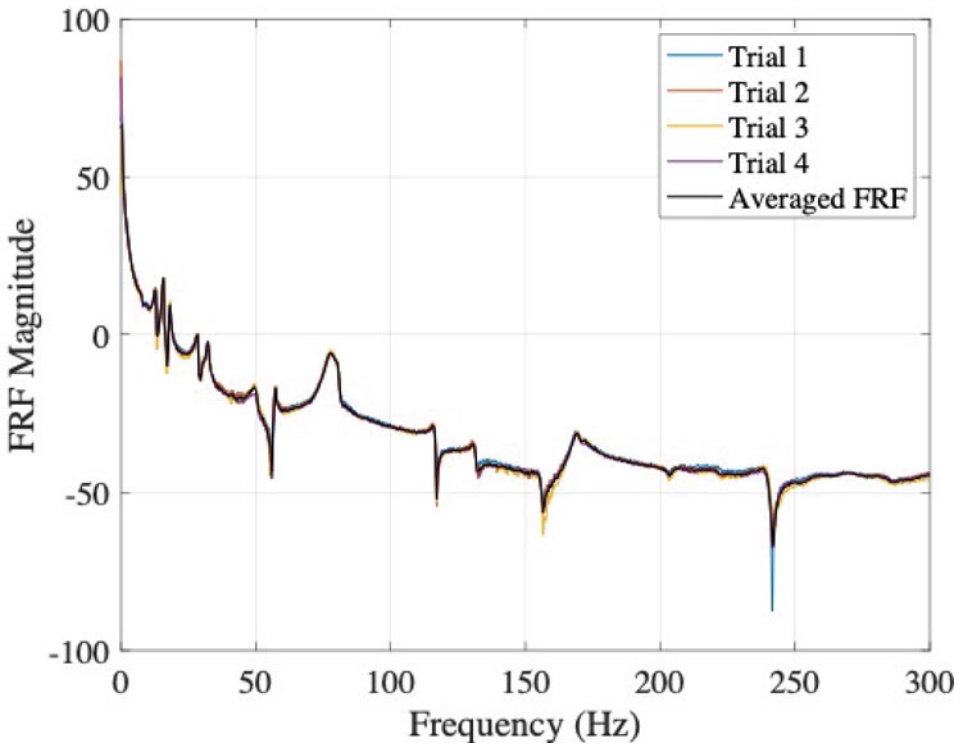

Fig. 17.7 Example of frequency response functions for multiple impacts

Table 17.2 Comparison of measured and calculated natural frequencies

Nat. frequency (FEA) [Hz]	Nat. Frequency (Experiment) [Hz]	% diff.
28.5	28.7	0.7
71.6	75.8	5.7
119.8	116.4	2.8
163.2	167.4	2.5

Acknowledgments This work was supported by AFOSR grant FA9550-21-1-0089 under the NASA University Leadership Initiative (ULI), with Dr. Sarah Popkin as program manager.

References

1. Bellini, A., Güçeri, S.: Mechanical characterization of parts fabricated using fused deposition modeling. Rapid Prototyping J. **9**, 252–264
2. Garg, A., Bhattacharya, A.: An insight to the failure of FDM parts under tensile loading: finite element analysis and experimental study. Int. J. Mech. Sci. **120**, 225–236 (2017)
3. Xue, F., Robin, G., Boudaoud, H., Cruz Sanchez, F.A., Daya, E.M.: Effect of process parameters on the vibration properties of PLA structure fabricated by additive manufacturing. In: 2021 International Solid Freeform Fabrication Symposium, University of Texas at Austin, 2021
4. Mohammed, R.N., Babu, K., Palaniappan, P.L., RajeshKannan, P., Venkatramanan, N.S.: Effect of FDM process parameters in ABS plastic material. Int. J. Mech. Prod. Eng. (2017) 895–903.
5. Klock, R.J.: Efficient numerical simulation of aerothermoelastic hypersonic vehicle. Ph.D. Thesis, University of Michigan (2017)
6. SensuronLLC.: Strain measurements comparison between distributed fiber optic sensing and strain gauges. https://www.sensuron.com/
7. Sadd, M.H.: Elasticity: Theory, Applications and Numerics, 4th edn. Elsevier, Amsterdam (2021)

Chapter 18
Improving Dynamic Characteristics of Strain Gauge Load Cells Using Additive Manufacturing

M. Vanali, S. Pavoni, A. H. Lanthaler, and D. Vescovi

Abstract Additive manufacturing is becoming more popular in the rapid prototyping of sensors, even for force transducers like load cells. These transducers are largely used in static or quasi-static measuring but their dynamic performances are of a certain interest too. Therefore, the enhancement of their dynamic properties is getting higher and higher attention. In this paper, an improvement in the dynamic characteristics of a strain gauge load cell is proposed with the redesign of the force transducer relying on additive manufacturing possibilities. The response characteristics of the force transducers built with both additive and conventional manufacturing methods are evaluated by analyzing the frequency response function estimated with an impulsive method. Dynamic parameters from both transducers have been evaluated and compared. The possibilities offered by the additive manufacturing technology led to an increase in the measurable frequency band of the considered transducer.

Keywords Load Cell · Dynamic calibration · Additive manufacturing · Bandwidth enhancement

18.1 Introduction

The innovation in new measurement components and sensors with higher performances is constantly increasing over the years. Additive manufacturing (AM) or 3D printing is becoming more popular in the rapid prototyping of components [1] or the development of new sensors [2], even for force transducers like load cells. This technique allows the development and investigation of new sensor geometries and the improvement of certain features through design engineering. For example, in [3], an additive manufacturing prototype of a load cell with embedded strain gauges made using polyurethane thermoplastic and a conductive PLA is proposed.

Strain gauge load cell is one of the most used force transducer kind due to its cheap cost and simple application. Since these transducers are becoming more and more employed in measuring dynamic forces, different techniques have been developed to provide a faster response in the measurement of forces. In [4], an adaptive shaper-based filter has been implemented to shorter the measurement time of a load cell. Unfortunately, this strategy relies on the post-processing of the load cell signal only. Other approaches are based on the enhancement of transducers' bandwidth changing the mechanical properties of the components.

The bandwidth of this type of transducer is strictly related to its natural frequency and damping ratio: the higher the natural frequency and damping factor are, the larger the bandwidth of the transducer will be. To increase these two dynamic properties, the improvement of the related transducer's characteristics is fundamental. The first strategy to improve the dynamic response of force transducers is to increase the damping ratio by applying damping materials inside or on the surface of the component: This approach requires an impressive growth in damping that has a number of practical drawbacks (installation, materials, etc.). Another strategy is to increase the first natural frequency of the transducer with the increment of the stiffness or the decrement of the mass. The increase of the stiffness of the component, keeping unchanged the geometry, is possible only with the employment of another material with a higher Young's modulus and will affect the overall sensitivity of

M. Vanali (✉) · S. Pavoni · A. H. Lanthaler
Dipartimento di Ingegneria e Architettura, University of Parma, Parma, Italy
e-mail: marcello.vanali@unipr.it

D. Vescovi
LAUMAS Elettronica s.r.l, Montechiarugolo, PR, Italy

M. Allen et al. (eds.), *Special Topics in Structural Dynamics & Experimental Techniques, Volume 5*,
Conference Proceedings of the Society for Experimental Mechanics Series, https://doi.org/10.1007/978-3-031-37007-6_18

the transducer. The removal of the mass, where it is unnecessary, can improve the dynamic response of the force transducers. In this particular field, additive manufacturing can be an important step forward in strain gauge load cell design.

In this paper, an enhancement of the dynamic characteristics of a strain gauge load cell is proposed with the redesign of the force transducer relying on additive manufacturing techniques. A prototype of a load cell has been produced through the fused deposition modeling (FDM) method and tested. The response characteristics of additive manufacturing and conventional manufacturing load cells with the same geometry have been evaluated by analyzing the frequency response function (FRF) estimated with an impulsive method. Finally, results obtained from both load cells have been compared. In the next section, the redesign of the load cell with additive manufacturing is presented.

18.2 Design of the Load Cell Prototype

The prototyping of the additive manufacturing load cell started from a transducer already present on the market. The force transducer is a classic single-point load cell produced by the company LAUMAS Elettronica S.r.l. which is a worldwide weighing systems supplier. The transducer is an FTP75 [5] model load cell with a 75 kg capacity and AISI 420 stainless steel as material. The peculiarity of this load cell is that the strain locations of the component are concentrated in small areas of the transducer's surface.

Since the aim of this work is the removal of the mass where it is unnecessary, the first step has been to implement a finite element method (FEM) model of the traditional load cell. The FEM model is fundamental as it allows us to understand the distinction between the principal areas under stress, where the load cell should maintain its properties, from those not stressed, where material can be removed.

The FEM analysis in Fig. 18.1 illustrates the stress behavior of the load cell at full load (750 N): the stress regions, computed through the Von Mises criterion, are concentrated in 4 narrow zones of the load cell where the central hole leaves a thin thickness with external edges. In fact, these are the surfaces where commonly strain gauges are applied, since the maximum strain of the component has to be measured. Furthermore, the FEM analysis reveals that the remaining part of the component is not under stress at all, but it has purely a structural role. Hence, a prototype of the additive manufacturing load cell has been designed taking into account these properties.

The additive manufacturing technology choice has fallen on the atomic diffusion additive manufacturing (ADAM) technique which is an FDM method [6] based on a filament composed of metal powders encased in thermoplastic polymeric binders. After material extrusion through a nozzle similar to the fused filament fabrication (FFF), the procedure consists of an initial solidification followed by washing (removal of polymeric parts) and sintering (fusion of metal powders) treatments [7]. The ADAM process begins importing a .STL file which is shown in Fig. 18.2, where the filament pattern of the procedure is set.

The load cell regions under stress have been designed to keep the component full of material, thanks to the thickness of external layers. The remaining part where mass can be removed presents a classic triangular 20% infill pattern with a thickness of 1 mm. This infill architecture, which is particularly helpful due to its high mass–strength ratio, allows material reduction preserving the structural resistance [8].

The prototype has been made with stainless-steel 17-4 PH, a high resistance and hardness material with an ultimate tensile strength of 1250 MPa, yield strength of 1100 MPa, and a tensile modulus of 170 GPa. The employment of the ADAM technology and the 17-4 PH steel as production material is particularly advantageous since the cost of the procedure is extremely cheap compared to others, and the precision of the final component is highly accurate [9].

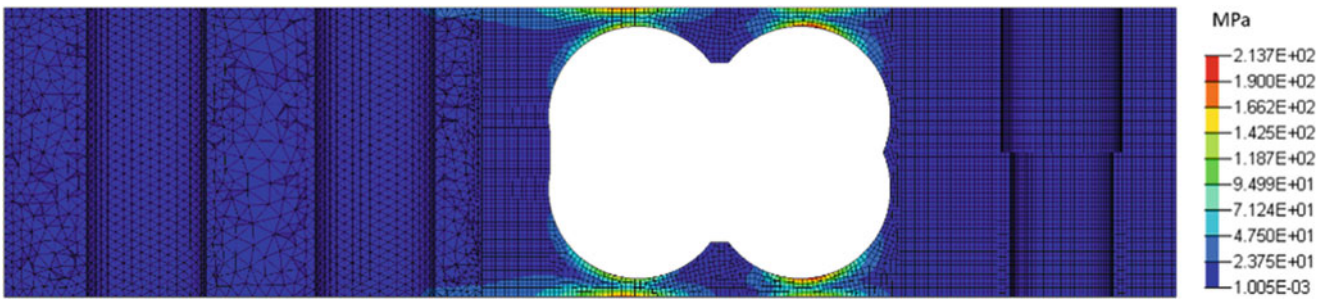

Fig. 18.1 Load cell stress locations from finite element model analysis

Fig. 18.2 Filament pattern of the additive manufacturing load cell prototype

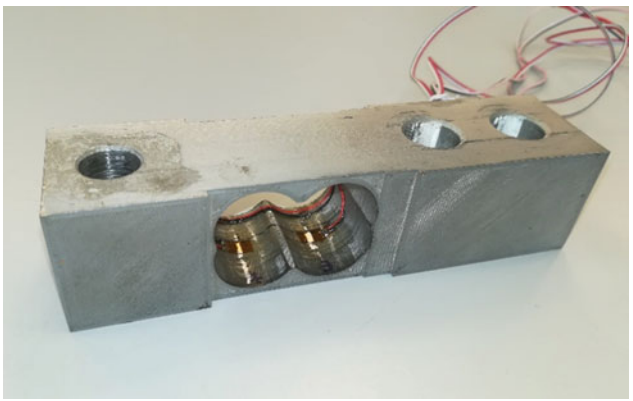

Fig. 18.3 Additive manufacturing load cell prototype

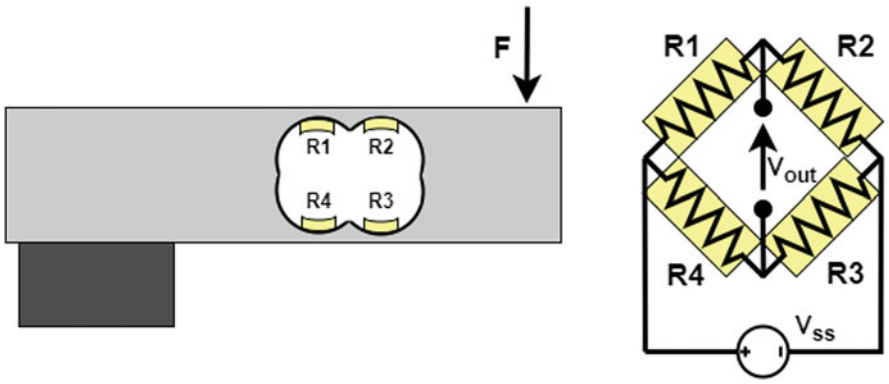

Fig. 18.4 Strain gauges layout on the additive manufacturing load cell

Figure 18.3 shows the load cell prototype made with the additive manufacturing technique mentioned before. The load cell prototype presents a consistent reduction of the material, since the component mass has been reduced from 700 g of the conventional load cell to 294 g.

Four strain gauges with a resistance of 120 Ω and a gauge factor of 2.1 have been applied on the stressed surfaces as on the conventional load cell, and connected each other with a traditional Wheatstone full bridge circuit layout as in Fig. 18.4. In the next section, the first tests performed on the prototype specimen are introduced.

18.3 Static Calibration

One of the fundamental prerogatives for the proposed prototype is the maintenance of the static performances of the original transducer; thus, a static calibration has been evaluated. The procedure has been performed at the LAUMAS laboratory with a compression testing machine, EASYDUR model AURA 10 TON, which has the INRIM [10] requirements for the

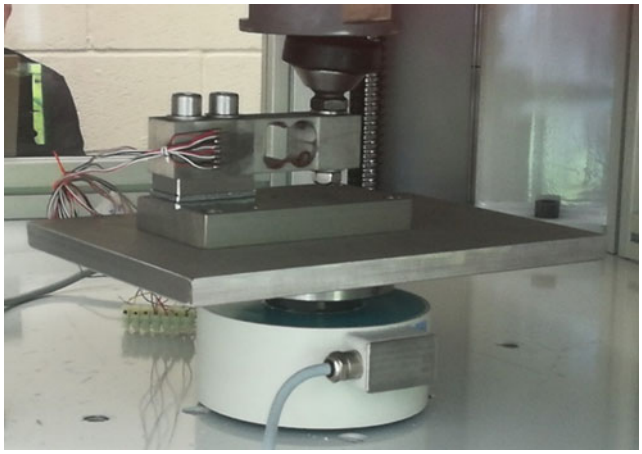

Fig. 18.5 Calibration of the prototype

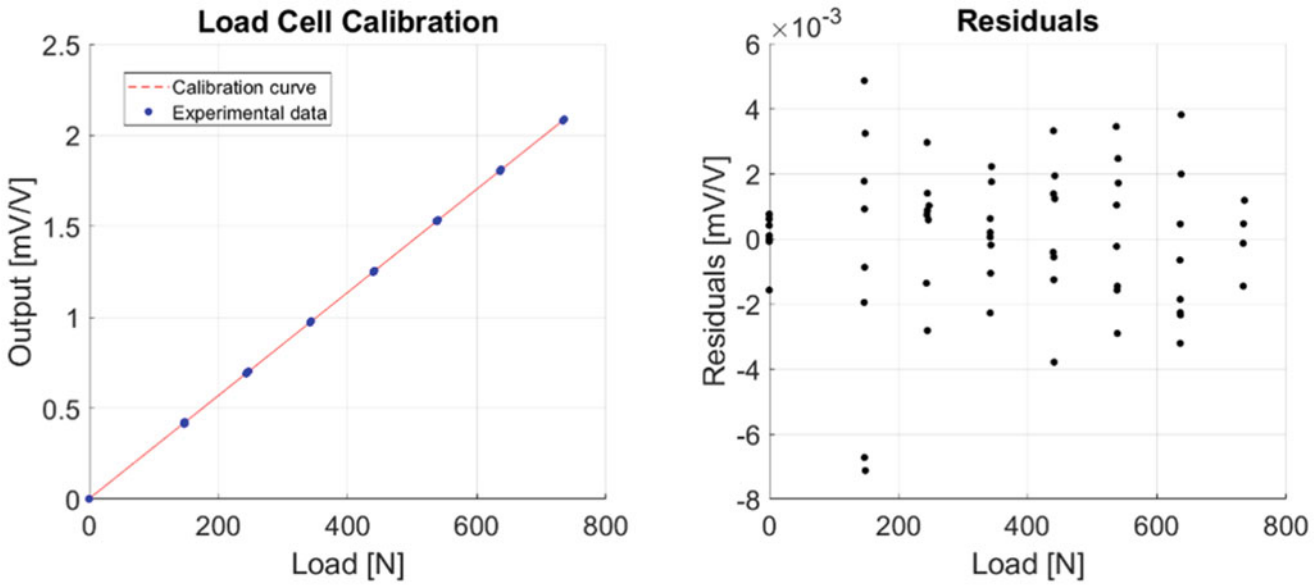

Fig. 18.6 Calibration diagram and residuals of the prototype load cell

calibration of force transducers. The calibration procedure is given in ISO standard 376: transducers have to be calibrated by a process with stepwise loading and unloading forces after three preloads at the full capacity of the load cell. A number of four increasing-decreasing cycles have been used to have a sufficient number of experimental points for the calibration. The weighing transducer regulation for static calibration suggests the employment of increasing–decreasing cycles with force increments of 20, 40, 60, 80, and 100 percent of the rated capacity of the force transducer: The force values correspond to 150, 300, 450, 600, and 750 N. To evaluate a higher number of experimental points, a denser series of loads have been used for the prototype calibration: Steps employed in the loading forces are 150, 250, 350, 450, 550, 650, and 750 N. In Fig. 18.5, a detail of the calibration procedure of the additive manufacturing load cell is shown.

The data acquisition has been performed with a National Instruments system that consists of a NI 9218 board, which simultaneously provides the supply voltage (2 Volt) and measures the output of the circuit, and an analog-to-digital converter NI compact DAQ that can be connected to a PC through a USB cable. The effective load on the transducer is measured and provided by the calibration machine itself. The sampling frequency of measurements has been set to 2048 Hz; thus, it has been possible to perform an averaging to remove the noise from each step of the loading cycle.

The calibration in Fig. 18.6 shows a perfect linear behavior of the prototype; thus, a linear regression function has been estimated for the characterization of the additive manufacturing load cell. The distribution of residuals and the linear correlation coefficient ($R^2 = 0.99$) shows that the linear model for the regression can be appropriate. The relationship between the measurand and the output of the prototype can be represented as follows:

$$\text{Load } [N] = 353.77 \left[\frac{\text{N}}{\frac{\text{mV}}{\text{V}}} \right] \cdot \text{Output } \left[\frac{\text{mV}}{\text{V}} \right]$$

The calibration results reveal a sensitivity of the prototype of 2.12 mV/V at full load, which is very similar to the conventional manufacturing one (about 2.00 mV/V). The instrumental uncertainty has been evaluated as the standard deviation of experimental points, having a value of 0.77 N which is 0.1% of the transducer full scale. The slight difference between the two values is probably due to a different tensile modulus (170 GPa of the prototype against the 210 GPa of the original transducer). However, it is possible to assert that the static properties of the additive manufacturing load cell preserve the same features of the traditional manufacturing load cell. Once the static characteristics of the prototype have been verified, in the next section the experimental setup of the load cell dynamic characterization is presented.

18.4 Dynamic Characterization Experimental Setup

The main purpose of this paper is the improvement of dynamic characteristics of load cells using additive manufacturing. Thus, an experimental test has been performed to evaluate the dynamic parameters from both load cells. An impulsive method has been implemented using an impact hammer. The idea of the impulsive strategy is that such excitation is limited to an extremely narrow time interval and allows the observation of the free response of the transducer under test. In such a manner, it has been possible to evaluate the forcing and the response of the transducers and determine the transfer functions.

The load cells have been excited in the load application point with an impact hammer, PCB 086C03 type, having a sensitivity of 2.25 mV/N, connected to a National Instruments input voltage board NI 9234. The response of transducers has been recorded with a National Instruments full bridge input board NI 9218. The board simultaneously provides the supply voltage (2 Volt) and measures the output of the bridge. Both boards have been included in an analog-to-digital converter NI compact DAQ connected to a PC with a USB cable. Previous tests have demonstrated that the typical resonance frequency of this kind of transducer reached up to 600 Hz; therefore, the dynamic experiment has been performed with a sampling frequency of 2048 Hz. Since the response should not be influenced by external dynamics, load cells have been fixed to a 1000 kg mass with two screws: The mass stiffness allows to not influence the dynamic behavior of the force transducers. The experimental layout is shown in Fig. 18.7.

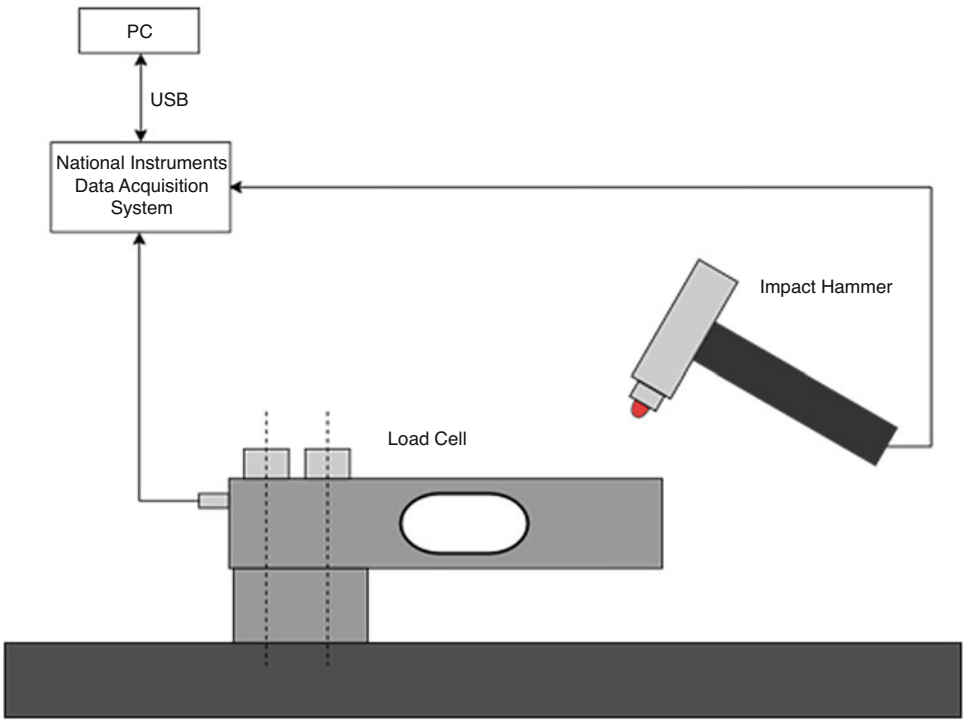

Fig. 18.7 Experimental setup of the dynamic characterization test

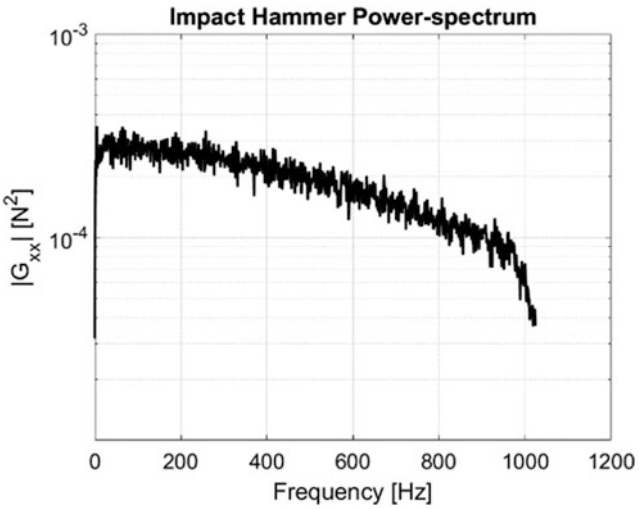

Fig. 18.8 Power spectrum of the impact hammer

The forcing of the additive manufacturing load cell without making a double hit has not been possible due to the incredibly fast comeback movement of the component. Therefore, the impulsive method for the estimation of the transducer FRF has been carried out using a series of randomly spaced impacts. A total number of 25 5 seconds windows have been processed to perform averaging in the frequency domain to reduce the uncorrelated noise that in the case of strain gauges are higher than the one usually found in accelerometer measurements.

The FRF has been evaluated using the H1 estimator as follows:

$$H_1(f) = \frac{G_{\mathrm{xy}}(f)}{G_{\mathrm{xx}}(f)}$$

where $G_{\mathrm{xy}}(f)$ is the cross-spectrum between load cell response and hammer, and $G_{\mathrm{xx}}(f)$ is the power spectrum of the hammer [11]. Results and parameter estimation are shown in the next section.

18.5 Dynamic Characterization Results

In Fig. 18.8, the power spectrum of the force impulses generated by the impact hammer is shown. The reduction of −20 dB in the impact hammer response sets the acceptable frequency range of the analysis. Since the impact hammer power spectrum does not present a level reduction of −20 dB, the entire frequency range of the spectrum from 0 to 1000 Hz has been considered suitable for the procession of dynamic parameters.

The frequency response function (FRF) between the impact hammer and the transducer has been calculated for both additive manufacturing and conventional manufacturing load cells. In Fig. 18.9, the magnitude (above) and the phase (below) of FRFs from both load cell responses are shown (conventional manufacturing in blue and additive manufacturing in green). It is possible to notice the tolerable level of the coherence functions until the resonances of the two systems are reached (conventional manufacturing in red and additive manufacturing in yellow); hence, dynamic parameter estimation from these functions is considered reliable.

The natural frequencies for both FRFs have been evaluated in correspondence of the maximum value of the magnitude. Critical damping ratios have been estimated with the half-power method on each resonant peak. The estimation of modal parameters for both transducers is shown in Table 18.1.

Results prove an increase in the natural frequency of the prototype with respect to the conventional load cell of 246 Hz. The reduction of the mass in strategic areas of the transducer has led to a 43.1% growth in the first resonance frequency. Once achieved an increment of the natural frequency of the transducer, the next step has been the examination of the bandwidth in order to establish a real improvement of the dynamic characteristics of the load cell.

The bandwidth of transducers has to be estimated in the low frequency range, close to the static sensitivity. However, results from the FRFs show a significant influence of the noise in the initial range of the transfer functions. Furthermore, the impact hammer at very low frequencies is not able to provide enough energy for a correct estimation of the FRF, providing

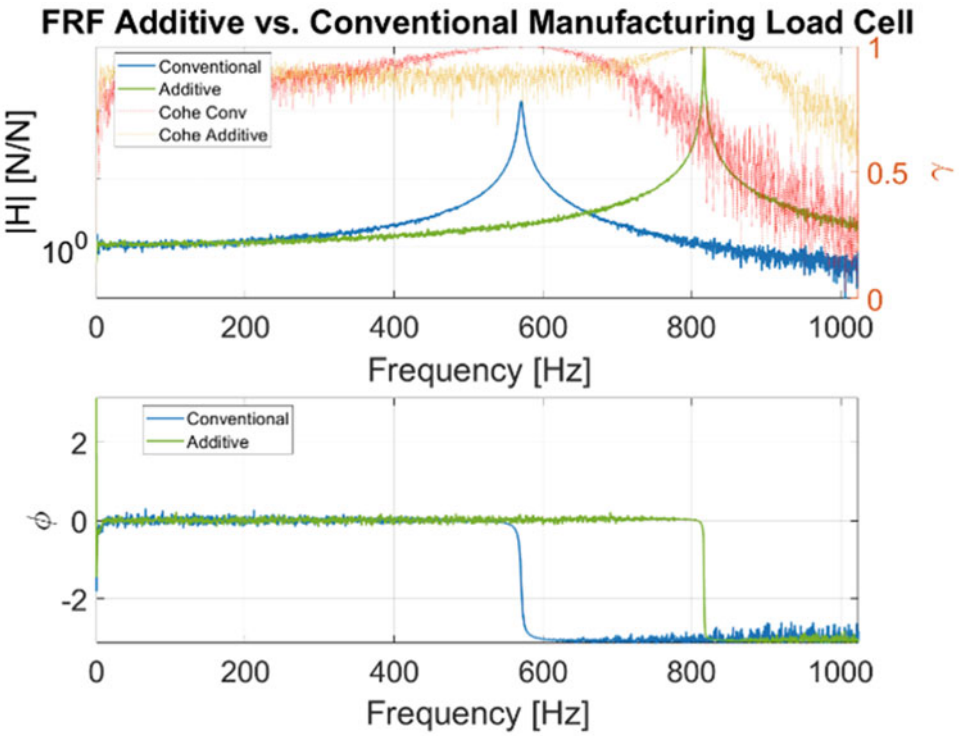

Fig. 18.9 FRF comparison between additive and conventional manufacturing load cells

Table 18.1 Natural frequencies and critical damping ratios estimated from FRFs of additive and conventional manufacturing load cells

	Natural frequency [Hz]	Critical damping ratio [%]
Additive manufacturing	817	0.10
Conventional manufacturing	571	0.67

an erroneous value of the static sensitivity. The effect is noticeable in the power spectrum of the impact hammer in Fig. 18.8 where the hammer energy quickly drops to zero at 0 Hz. Therefore, it is fundamental to elaborate a model able to describe properly the load cell behavior in the initial range of the transfer function.

For this particular frequency response function, a single-degree-of-freedom model with high modes residues has been fitted with a least-square method to the experimental FRF, in order to estimate the bandwidth of transducers. The model is the following:

$$H(f) = \frac{S}{1 - \left(\frac{f}{f_\mathrm{n}}\right)^2 + 2j\zeta\left(\frac{f}{f_\mathrm{n}}\right)} + R_\mathrm{H}$$

where S is the static sensitivity (which should be a unity), f_n is the natural frequency and ζ is the damping of the load cell, and R_H is the higher frequency modes contribution.

In Fig. 18.10, the modeling of the two FRFs is shown, proving an excellent similarity between the experimental functions and the reconstructed model. It is reasonable to affirm that the elaborated model is able to synthesize accurately the trend of the FRFs at low frequencies. Thus, bandwidth for both transducers can finally be estimated.

The bandwidth of transducers is computed starting from the magnitude value of the reconstructed FRF at 0 Hz, which represents the static sensitivity, establishing a tolerance range. The tolerance ranges have been suggested by the load cell supplier: 1%, 5%, and 10%. Therefore, three different bandwidths have been evaluated for each transducer depending on the error level. In Fig. 18.11, the evaluation of the three different bandwidths is shown, starting from the reconstructed FRF of the additive manufacturing load cell.

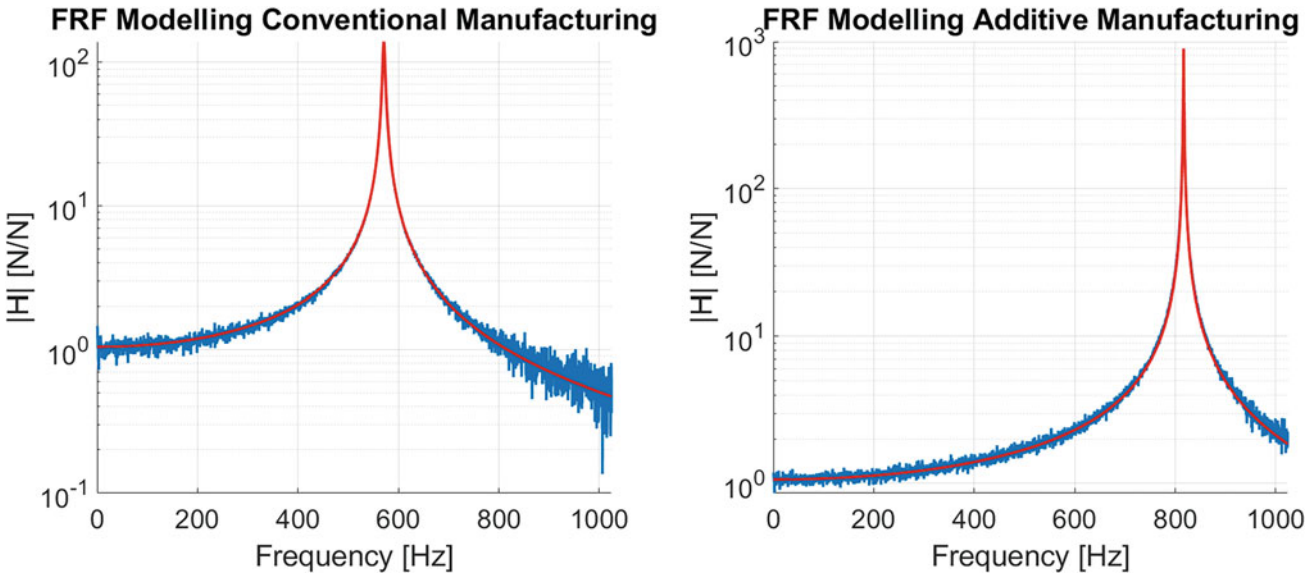

Fig. 18.10 Modeling of the two load cells FRFs

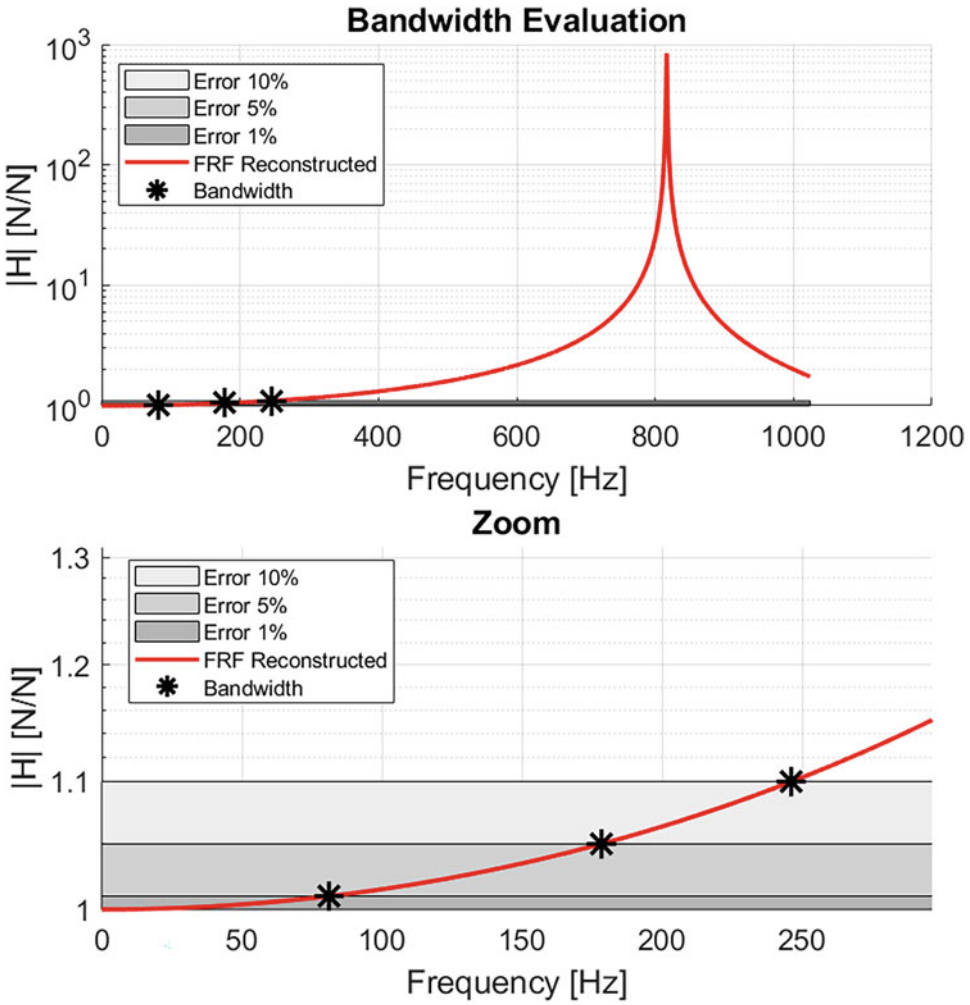

Fig. 18.11 Bandwidth evaluation for the additive manufacturing load cell

Table 18.2 Bandwidth estimated from load cell measurements analysis

	High cutoff freq [Hz]		
	1%	5%	10%
Additive manufacturing	81	178	246
Conventional manufacturing	57	125	170

Finally, a comparison between bandwidths from both load cells has been evaluated in order to understand properly an eventual enhancement of the dynamic characteristics. In Table 18.2, results computed from the transducers' bandwidth identification are shown.

Results prove an increase in bandwidth of the prototype with respect to the conventional load cell of respectively 24 Hz for 1% error, 53 Hz for 5% error, and 76 Hz for 10% error. The redesign of the transducer with additive manufacturing has led to a 43.1% average growth in bandwidth.

18.6 Conclusion

The aim of the research has been the enhancement of load cell dynamic characteristics relying on additive manufacturing. A classic single-point strain gauge load cell has been redesigned with ADAM technology, removing material, where it is unnecessary. Static calibration of the prototype has proved that the static properties of the original transducer have been preserved and the additive manufacturing load cell can be employed in traditional applications. An impulsive method has been performed with an impact hammer to evaluate the dynamic properties of both additive manufacturing and conventional manufacturing load cells. The impulsive method relied on a series of randomly spaced impacts measuring both forcing and response. Natural frequencies from FRFs have been evaluated for both transducers and compared, revealing a 43% increment in the resonance frequency value to the benefits of the additive manufacturing load cell. A single-degree-of-freedom model has been evaluated for a better estimation of the FRFs, especially at low frequencies, where functions are particularly affected by noise and bandwidths are estimated. Finally, bandwidths have been processed starting from the reconstructed FRFs values at 0 Hz with three different range tolerances. Bandwidth results proved an enhancement of dynamic characteristics to the benefits of the additive manufacturing load cell too, showing a 43.1% increment in bandwidth frequencies.

The redesign of the strain gauge load cell with additive manufacturing technique improved the dynamic characteristics of the transducer, thanks to mass removal in areas where the transducer is not under stress. The bandwidth has been enhanced despite a lower critical damping ratio. Therefore, a further strategy to increase the dynamic features of the AM load cell could be the increment of the damping ratio through the application of damping materials inside or on the surface of the AM transducer. Such strategies are going to be investigated in future works.

Acknowledgments The authors would like to express their deep gratitude to LAUMAS Elettronica S.r.l., which provided technical and economic support, disposability in the employment of their equipment, and useful suggestions for the development and analysis of the additive manufacturing load cell.

References

1. Kruth, J.-P., Leu, M.C., Nakagawa, T.: Progress in additive manufacturing and rapid prototyping. CIRP Ann. **47**(2), 525–540 (1998). https://doi.org/10.1016/S0007-8506(07)63240-5
2. Stano, G., Bottiglione, F., Percoco, G.: Fused filament fabrication for one shot additive manufacturing of capacitive force sensors. Procedia CIRP. **110**, 168–173 (2022). https://doi.org/10.1016/j.procir.2022.06.031
3. Stano, G., di Nisio, A., Lanzolla, A., Percoco, G.: Additive manufacturing and characterization of a load cell with embedded strain gauges. Precis. Eng. **62**, 113–120 (2020). https://doi.org/10.1016/j.precisioneng.2019.11.019
4. Richiedei, D.: Adaptive shaper-based filters for fast dynamic filtering of load cell measurements. Mech. Syst. Signal Process. **167**, 108541 (2022). https://doi.org/10.1016/j.ymssp.2021.108541
5. https://www.laumas.com/en/catalog/load-cells-and-mounting-kits-product-catalog-electronic-format-pdf/
6. Singh, S., Ramakrishna, S., Singh, R.: Material issues in additive manufacturing: a review. J. Manuf. Process. **25**, 185–200 (2017). https://doi.org/10.1016/j.jmapro.2016.11.006
7. Enrique, P.D., DiGiovanni, C., Mao, N., Liang, R., Peterkin, S., Zhou, N.Y.: Resistance is not futile: the use of projections for resistance joining of metal additively and conventionally manufactured parts. J. Manuf. Process. **66**, 424–434 (2021). https://doi.org/10.1016/j.jmapro.2021.04.035

8. Bachhav, C.Y., Sonawwanay, P.D.: Numerical comparison of additive manufacturing of ABS material based on infill design subjected to tensile load. Mater. Today Proc. **62**, 6727–6733 (2022). https://doi.org/10.1016/j.matpr.2022.04.806
9. Lavecchia, F., Pellegrini, A., Galantucci, L.M.: Comparative study on the properties of 17-4 PH stainless steel parts made by metal fused filament fabrication process and atomic diffusion additive manufacturing. Rapid Prototyp. J. **29**, 393 (2022). https://doi.org/10.1108/RPJ-12-2021-0350
10. https://www.inrim.it/en
11. Brandt, A.: Noise and Vibration Analysis. Wiley (2011). https://doi.org/10.1002/9780470978160

Chapter 19
Niceclick: A New Frontier for Haptic Technologies

Elvio Bonisoli, Luca Dimauro, Simone Venturini, Salvatore Paolo Cavallaro, and Flavio Cerruti

Abstract The use of touch screens and displays is quickly increasing in the automotive industry, especially for supercars. Touchscreen commands are affected by the problem of feedback to drivers, i.e. the driver cannot look at the touch display; indeed, he needs to understand if the required command is received from the car. Haptic surfaces represent the solution to this problem; hence, touch screens with embedded actuators are suitable to switch from mechanical vibrations to human feeling. This paper focuses on an innovative electromechanical device called Niceclick. It is a compact and powerful actuator able to modulate the haptic surface vibrations. After an overview of the tactile perception, measurement systems, human sensibility to vibrations, and psychophysical compliance are analysed to define the parameters of an ideal actuator suitable to create some specific signals, the related frequency bandwidth, and the associate energy profile. The tailored tool, appropriate to get these goals, is described, modelled, and experimentally tested coupled to the fundamental co-system where it is applied. A comparison between rigid and deformative coupled structures is considered to define performance and aims.

Keywords Electromechanical device · Haptic feedback · Tactile perception · Human body vibration frequency · Sensibility

19.1 Introduction

The increment in the number and complexity of command and settings on vehicles led the automotive OEMs to find suitable solutions and technologies [1, 2]. Perhaps, the massive use of touch screens in all everyday devices, particularly in the main interface in vehicles cab, represents a critical issue about the driver safety. In fact, the actuation of a virtual switch on a touch screen does not give any feedback to the driver, which must visually check the correctness of the desired command, diverting the attention from the road. Instead, when a driver interacts with an analogical switch, he receives both tactile and audible feedbacks. The differences in the two sensations are not negligible, and the tactile stimulus is the main feedback.

The human machine interfaces (HMIs) were deeply investigated in the last decade to combine a pleasant driver perception and the desired innovative design aspects [3, 4]. The evolution of automotive HMIs is strictly related to the human tactile perception [3, 5], specifically in haptic surfaces [6]. The haptic surface is a complex interface that includes one or more actuators producing a tactile response [7]. In the state of the art, several attempts have been done in finding a reliable and effective technology for this application, from electrostatic to ultrasonic actuation [6], employing varied system dynamics [8].

The driver population is wide and varied; hence, the preferred vehicle interface style is subjective, due to the different sensitivity to tactile stimuli. Therefore, the interfaces are commonly designed by analysing the typical user characteristics and calibrating button pression feedback on statistical information. Nevertheless, user feedbacks are not objectified in the design process. Using simple devices, researchers are trying to deceive the human perception, creating fictitious sensations.

In this scenario, this paper focuses on an innovative haptic device called Niceclick, a compact and powerful actuator able to modulate the haptic surface vibrations. The device is calibrated on objectified parameters to generate some specific

E. Bonisoli · L. Dimauro · S. Venturini (✉) · S. P. Cavallaro
Politecnico di Torino, Department of Mechanical and Aerospace Engineering, Torino, Italy
e-mail: simone.venturini@polito.it

F. Cerruti
Trama Engineering, Alba, CN, Italy

M. Allen et al. (eds.), *Special Topics in Structural Dynamics & Experimental Techniques, Volume 5*,
Conference Proceedings of the Society for Experimental Mechanics Series, https://doi.org/10.1007/978-3-031-37007-6_19

feedback patterns with the associate energy profile. A tailored tool called tactilometer has been developed to experimentally characterise tactile perception and to orient design choices in Niceclick development.

The paper is organised as follows: in Sect. 19.2, the state of the art on human tactile perception is presented before introducing the innovative Niceclick device in Sect. 19.3, which is proposed with the application of tactilometer. After that, results of experimental test are presented from both static and dynamic point of views in Sect. 19.4 to describe Niceclick dynamic behaviour. Finally, in Sect. 19.5, remarks about the performed activity and considerations on future developments are depicted.

19.2 State of the Art on Tactile Perception

The human tactile perception is allowed by tactile receptors in human fingertips. The tactile receptors are usually modelled as a four degrees of freedom (DoF) system [9] in which each DoF corresponds to a different fibre-type mechano-receptor sensitive to a defined frequency range. These different corpuscles, described in Table 19.1, are subdivided into slowly adapting (SA) and rapidly adapting (RA) receptors.

The differences in frequency sensitivity of the four corpuscles make the human threshold to vibrations perception frequency dependent, as shown in Fig. 19.1. Moreover, the receptor distribution in the skin determines a dependence on the contact area [11]. The contact area has a double effect on the vibration perception due to the spatial distribution of receptors: if the contact area is up to a 0.1 cm^2, the vibration perception is linearly dependent on the contact, because an increasing number of receptors is involved; for larger contact areas, the probability to involve the low-threshold receptors increases and experienced threshold becomes lower [9].

The perception of a vibrational signal can be even masked by the presence of other vibrations. This mechanism has been experienced recording the perception threshold of a test signal on the index fingertip while a masking signal was exerted on the thenar eminence [12]. A relevant masking effect is observed within the RA-II Pacinian corpuscle and only if both the test and the masking signals activate this type of receptors. An enhancement effect is present too. A signal produces an enhancement in the perception of another signal, belonging to the same frequency range and thus activating the same receptors, if they are separated by a time interval up to 500 ms. Any interaction between different receptors type has not been noticed. As the same, adaptation occurs when a conditioning signal is present in the same frequency range of the test signal.

Table 19.1 Human finger tactile receptors [10]

Corpuscle	Channel	Frequency range [Hz]	Peak sensitivity [Hz]
SA-I Merkel receptor	NP III	0.4÷30	20÷30
SA-II Ruffini corpuscle	NP II	20÷500	200÷400
RA-I Meissner corpuscle	NP I	1÷300	30÷50
RA-II Pacinian corpuscle	P	5÷1000	200÷300

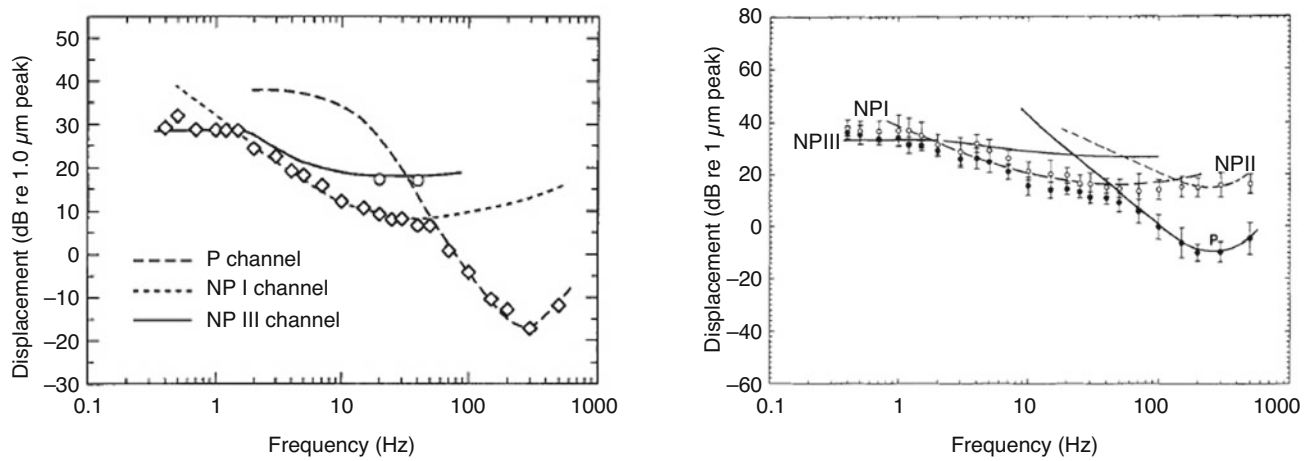

Fig. 19.1 Average threshold, function of stimulus frequency [9, 10]

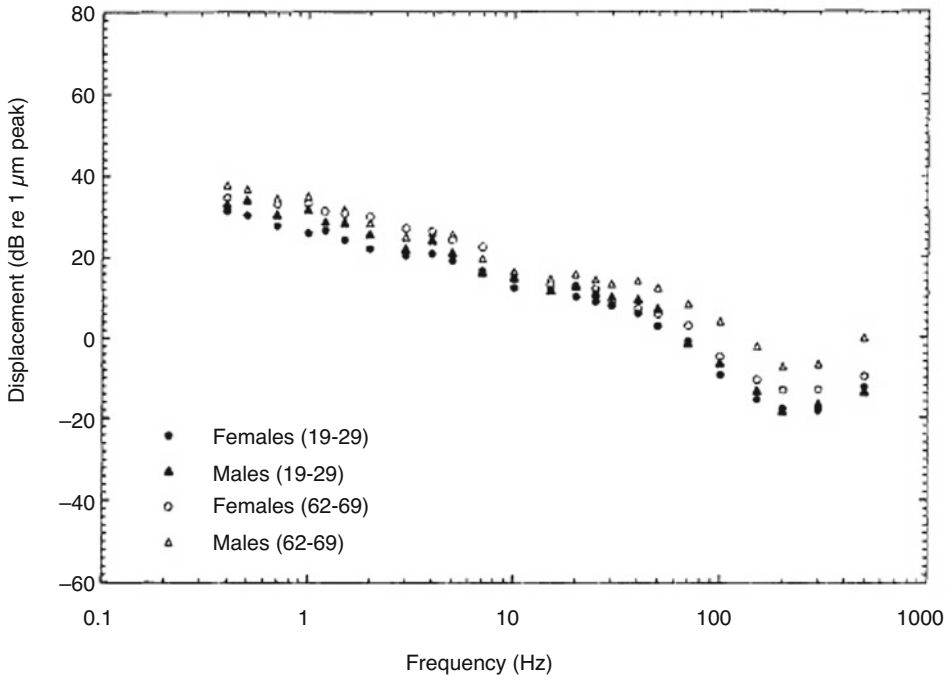

Fig. 19.2 Effect of ageing on sensitivity threshold [10]

Again, the effect is present only within the receptor family [12]. Considering the application of a vibrating haptic surface on a vehicle, the environmental vibration presence must be analysed.

Finally, the tactile perception is affected by subjective characteristics: the age is the most important one, as shown in Fig. 19.2. Experimental tests [10] have shown that the perception thresholds generally increase with the age and even more drastically over 65 years and mostly for RA-II Pacinian channel activating frequencies (above 100 Hz).

Moreover, females have been noticed to generally have a better sensitivity than males. The perception subjectivity enforces the need of a tunable interface. Besides, the same subjectivity brings out the absence of a reliable system for measuring and objectively describing the human tactile perception.

Another tactile aspect that has been investigated is the sense of compliance. This kind of perception is due to SA receptors. Experimental tests demonstrated that the passive perception of objects compliance is referred to the skin deformation sensed by SA-I laying in the sides of the finger pad [13] (in literature, it is referred as "lateral force"). Another important cue is the variation in contact area that clearly identifies a soft surface. Concerning the influence of active pressing, kinaesthetic force does not determine the perception, but can influence it increasing the sense of hardness. This effect is due to the mechanical properties of the fingertip that shows a nonlinear compliance [14]. The perception is function of both finger and object compliances and activated by cutaneous (90%) and kinaesthetic (10%) cues. Analysing the two channels, it came out that in case they are in conflict, an intermediate perception is experienced [15]. This statement opens the possibility to give a displacement illusion of a rigid surface through the stimulation of cutaneous receptors [16] When a surface is deformed by a finger touch, the sensation experienced is due to the friction forces exchanged by skin and surface: this can be effectively reproduced by a vibration that varies with the force exerted, in order to actively feedback a properly tuned reaction simulating hardness or softness. Even if the best and most realistic way to reproduce a sense of compliance is through both kinaesthetic and cutaneous cues [17], haptic devices showed how a tactile stimulus very close to one of real button can be reproduced by a finely tuned vibration.

19.3 Niceclick Device

The Niceclick is a device that recalls an energy harvesting [18–20] in its structure. The Niceclick has been developed by Trama Engineering, in order to get a wide vibrational tuning range, related to the different excitation conditions. It is a linear

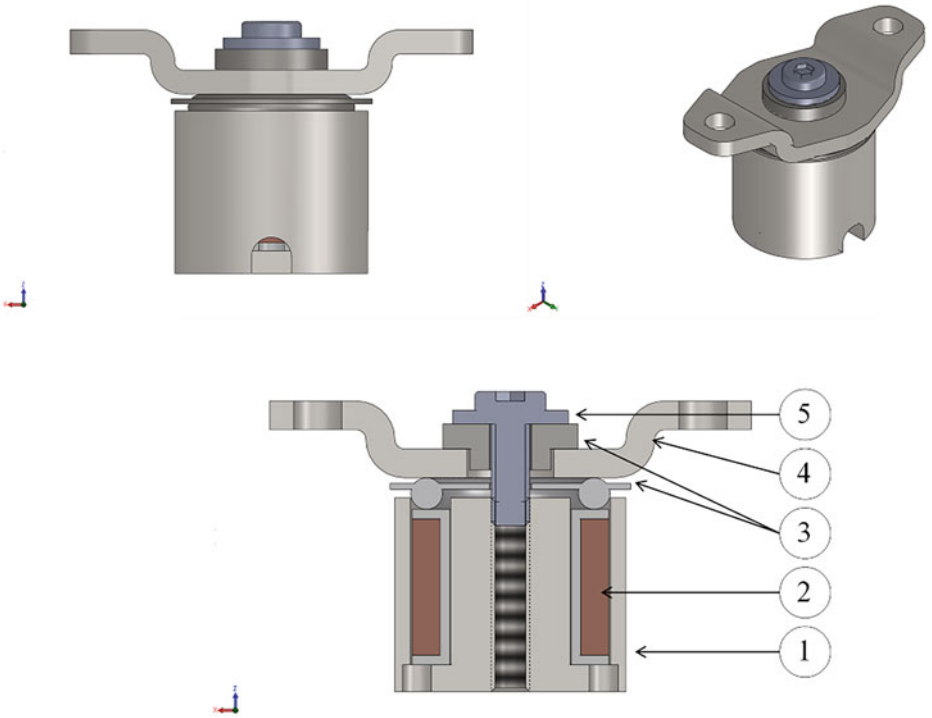

Fig. 19.3 Niceclick in details

actuator, driven by a specific software, that is able to generate a finely tuned vibrating motion as response of an external force input. The three views in Fig. 19.3 show the device in detail; its components are listed below:

1. Metallic body
2. Coil and plastic body
3. Upper and lower elastic elements
4. Omega pad
5. Preload screw

When a current is provided to the coil by a specific driver, the metallic body attracts the omega pad towards itself, compressing the lower elastic element. When no current is applied, the spring pushes upwards the pad: the system, having a single degree of freedom, starts to oscillate at a frequency which is function of the spring elastic coefficient and the mass of the pad. Thanks to the high frequency of current control that the interface allows, the user can generate a completely customised vibration, within a reasonable range of frequency, given by the system dynamics.

As a source, one or more Niceclick can excite a surface, even with a complex geometry, and generate precise and defined sensations on a human finger by working coordinately, although each Niceclick has an independent vibrational behaviour. The different but coordinated Niceclick responses are guaranteed by the innovative device feature that allows to perceive the amount of force acting on the surface and to tune, through the software, their respective vibrational output contributions that together create a properly tuned tactile stimulus, as shown in Fig. 19.4. Furthermore, the control interface allows to set the duration of the semi-period of the push and release phases simulated by vibrational outputs that can be properly tuned by a customisable signal as reported in Fig. 19.5.

As previously mentioned, the two features described above, working together, are fundamental to create a wide range of customisable tactile perceptions, moreover with applications that involve the use of more than just one Niceclick, making this innovative device a new interesting haptic tool.

The next chapter will focus on a higher application of this device, the definition of a standard measurement for vibrational stimuli sensed by a human finger.

Fig. 19.4 Niceclick cooperative functioning

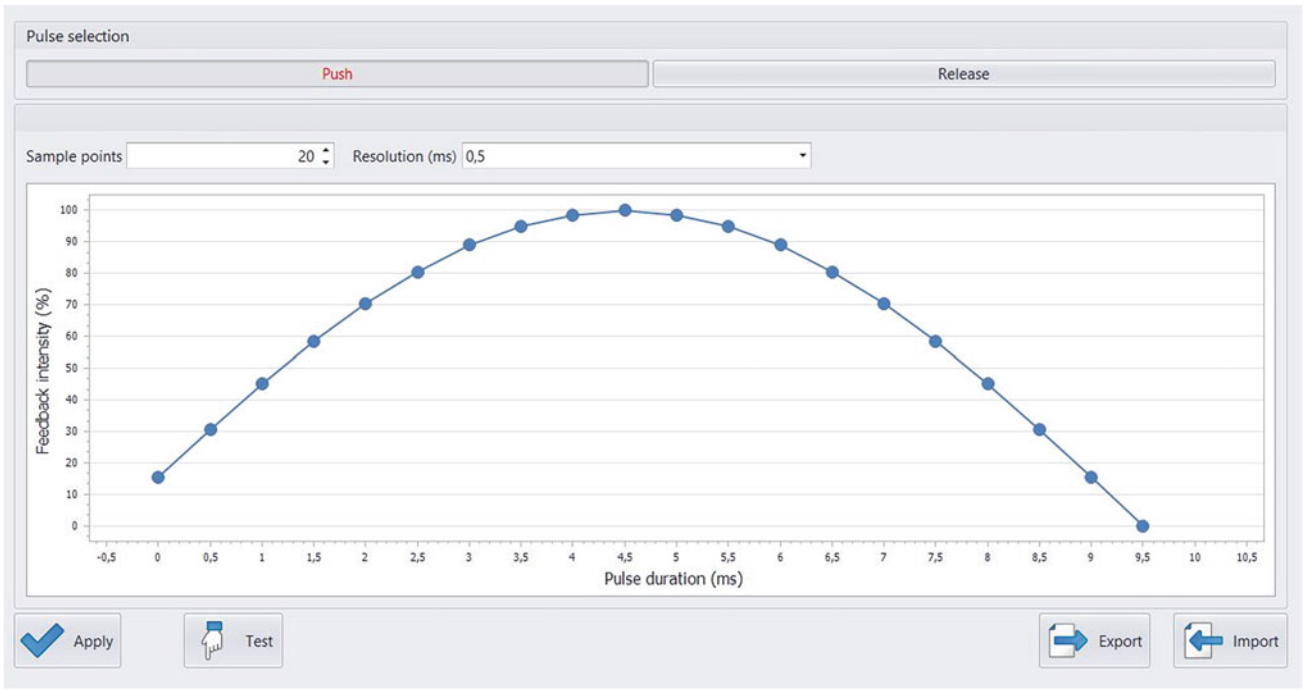

Fig. 19.5 Niceclick signal customisation

19.3.1 The Tactilometer

The Tactilometer is a mechanical measuring system, composed by an aluminium supporting structure, a Niceclick, and a pivoting aluminium plate; Fig. 19.6 reports three views of the prototype.

A programmable electronic circuit provides the current to the Niceclick. It is set up to produce two kinds of signal: a continuous vibration and a short actuation, repeated every second. The two are then divided into two level of intensity: the barely sensible and the most pleasant (as suggested by the results of an internal statistical investigation). As can be noticed, on the plate there is a scale, reporting the value of acceleration, expressed in [g], that is sensible in a certain point when the standard signal is sent.

Fig. 19.6 Tactilometer device

19.4 Experimental Tests

The Tactilometer has been used as a test rig for analysing the Niceclick static and dynamic behaviours. Two theoretically identical devices provided by the producer, named "Niceclick 1" and "Niceclick 2", have been tested. For measuring the plate vertical accelerations and displacements, we used a Siemens SCADAS Mobile, three Keyence lasers, and a monoaxial PCB accelerometer. Figure 19.7 reports a setup photograph.

Figure 19.8 displays in detail the three measured points. The accelerometer was placed exactly on the Niceclick projection on the plate upper surface, named "P". The three lasers were used for measuring the displacements of three points: one for the accelerometer upper surface (as the Niceclick vertical motion), one for the barycentre projection on the plate upper surface, "G", and one for a point out of the plane xz, "Q", at the same distance from the hinge as the barycentre.

19.4.1 Static Analysis

The Niceclick static properties have been tested by indirectly measuring the device vertical deformation when a known load was applied in the point "A", shown in Fig. 19.8, positioned in the median point between "G" and "P".

A set of masses, ranging from 10 to 200 gr and shown in Fig. 19.9, was used for the test. The setup allowed to place on point "A" from 10 to 140 gr with fix steps of 10 gr, then 200 gr, as reported by Table 19.2. The load on the Niceclick was composed by the aluminium plate, the omega pad with the two screws connecting it to the plate and the additional load. The elastic element also sustains its weight force. The omega pad mass has been evaluated equal to 2.76 gr, while the two screws can be reasonably assumed to be 1.5 gr together. The m_Ω column includes screws and omega pad. The equivalent load on the Niceclick has been evaluated for every configuration considering the system geometry. Being point "A" in the middle of the distance between "P" and "G", each configuration has the following load distribution on the Niceclick:

$$F_{\text{Niceclick}} = \left(\frac{1}{2}m_{\text{plate}} + \frac{3}{4}m_{\text{load}} + m_\Omega\right) g \tag{19.1}$$

The sum of force constraints balances the mass weight force, corresponding to:

$$F_{\text{hinge}} + F_{\text{Niceclick}} = \left(m_{\text{plate}} + m_\Omega + m_{\text{load}}\right) g \tag{19.2}$$

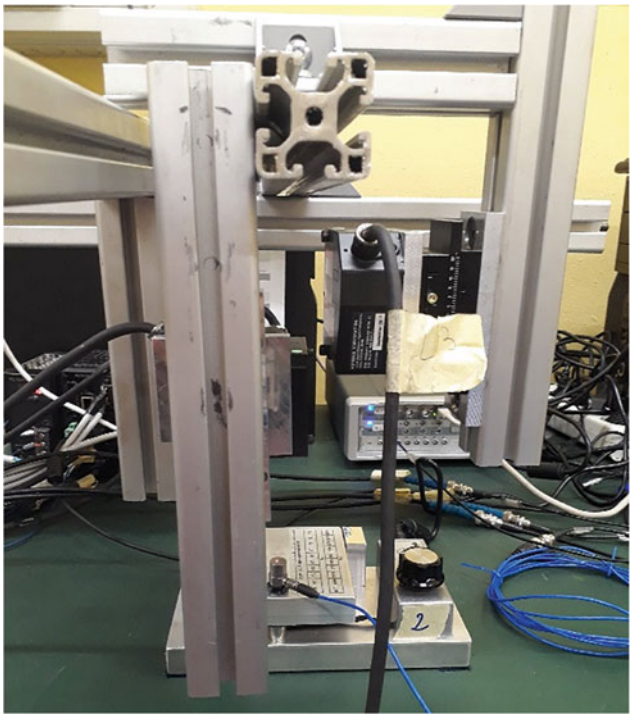

Fig. 19.7 Experimental setup

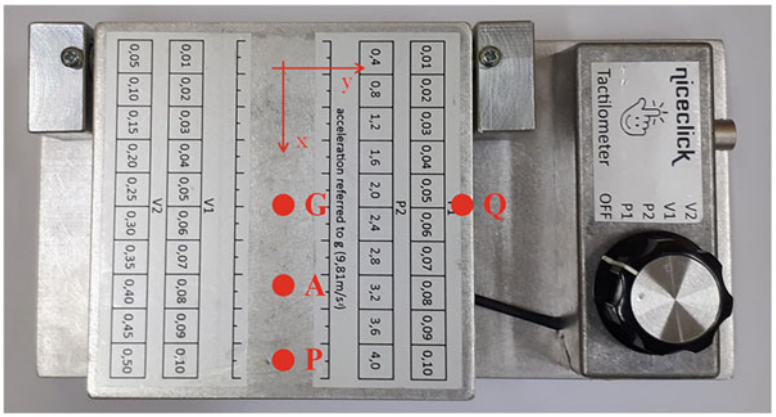

Fig. 19.8 Reference system and measured points

Fig. 19.9 Set of masses for the static loading conditions

Three measures were performed for each configuration, following two up-down cycles. The results for Niceclick 1 are reported only. In Fig. 19.10, the Force-Displacement curves at point "P" are shown.

Table 19.2 Loads evaluation

Configuration	m_{plate} [gr]	m_{Ω} [gr]	m_{load} [gr]	F_{hinge} [N]	$F_{Niceclick}$ [N]
1	550	4.26	10	2.72	2.81
2	550	4.26	20	2.75	2.89
3	550	4.26	30	2.77	2.96
4	550	4.26	40	2.80	3.03
5	550	4.26	50	2.82	3.11
6	550	4.26	60	2.84	3.18
7	550	4.26	70	2.87	3.25
8	550	4.26	80	2.89	3.33
9	550	4.26	90	2.92	3.40
10	550	4.26	100	2.94	3.48
11	550	4.26	110	2.97	3.55
12	550	4.26	120	2.99	3.62
13	550	4.26	130	3.02	3.70
14	550	4.26	140	3.04	3.77
15	550	4.26	200	3.19	4.21

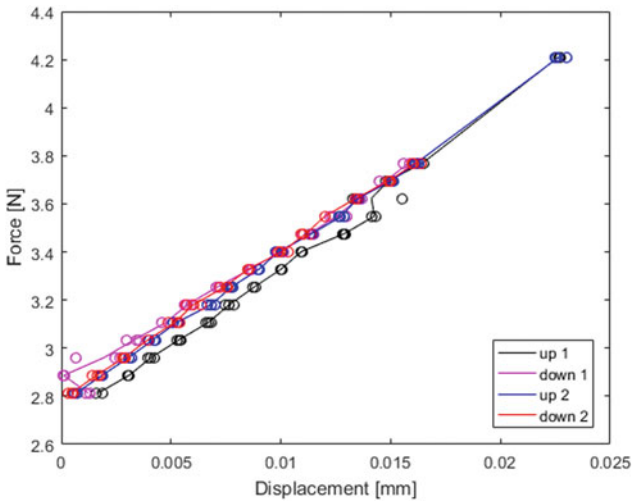

Fig. 19.10 Displacement curves at point "P"

Two interpolation techniques were adopted for trying to describe the elastic properties, a linear and a cubic one, respectively resumed by the following equations:

$$F_{\text{interp}} = k_0 + k_1 x \tag{19.3}$$

$$F_{\text{interp}} = k_0 + k_1 x + k_2 x^2 + k_3 x^3 \tag{19.4}$$

The error was evaluated as well, defined as the mean of the square difference between the experimental and the interpolated values:

$$\text{Eps}^2 = \frac{1}{n} \sum_{j=1}^{n} \left(F_{\text{exp},j} - F_{\text{interp},j} \right)^2 \tag{19.5}$$

The two function coefficients are reported in Tables 19.3 and 19.4; the plots of interpolated values are shown in Fig. 19.11, for linear (left) and cubic (right) interpolation, respectively.

Considering the results, the elastic element stiffness can be roughly considered linear; however, the more precise description provided by the cubic interpolation highlights a hardening behaviour, visible in the right part of the plots. This characteristic is probably due to the element deformation.

Table 19.3 Linear interpolation coefficients and errors

	k_0 [N]	k_1 [N/m]	Eps^2 [N^2]
Up 2	2.767	$62.72\ 10^3$	$1.234\ 10^{-4}$
Down 2	2.793	$61.36\ 10^3$	$1.106\ 10^{-4}$
Up&Down 2	2.778	$62.41\ 10^3$	$6.662\ 10^{-5}$

Table 19.4 Cubic interpolation coefficients and errors

	k_0 [N]	k_1 [N/m]	k_2 [N/m^2]	k_3 [N/m^3]	Eps^2 [N^2]
Up 2	2.767	$65.57\ 10^3$	$-4.992\ 10^8$	$1.825\ 10^{13}$	$7.218\ 10^{-5}$
Down 2	2.775	$70.36\ 10^3$	$-9.747\ 10^8$	$2.914\ 10^{13}$	$7.870\ 10^{-5}$
Up&Down 2	2.770	$67.83\ 10^3$	$-7.133\ 10^8$	$2.293\ 10^{13}$	$2.408\ 10^{-5}$

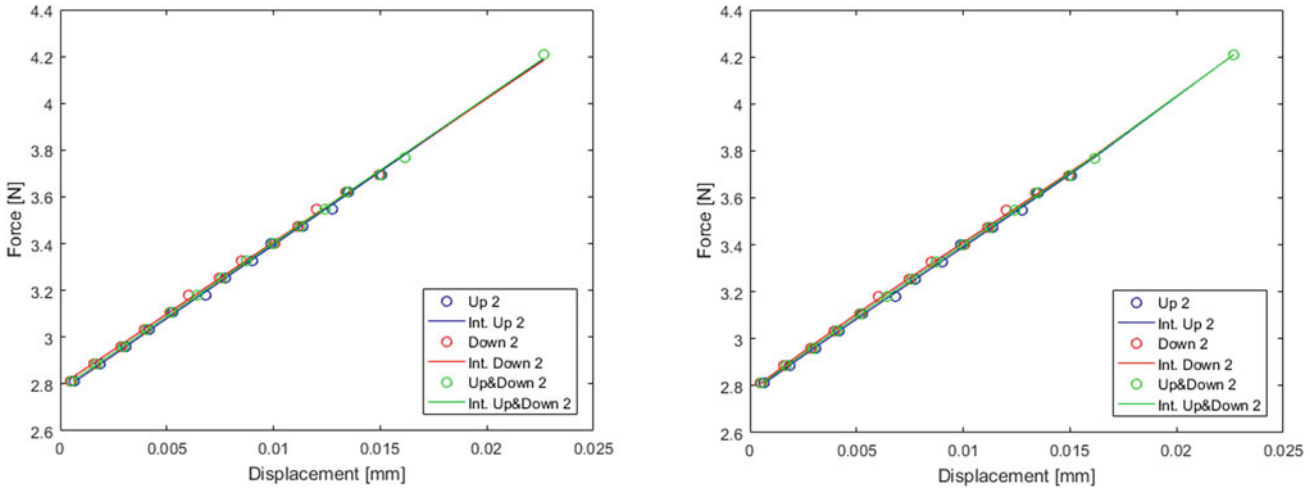

Fig. 19.11 Linear (left) and cubic (right) interpolation

19.4.2 Dynamic Analysis

An impact test was performed for evaluating the system dynamic properties. Because of the complex measuring setup, the only available point on the plate surface was "A"; for reference, see Fig. 19.8. A PCB instrumented hammer was used, together with the three lasers and the monoaxial accelerometer, positioned as described above. Several measurements were performed for each Niceclick, but only the Niceclick 1 results are reported.

Figure 19.12 shows an analytical representation of the system, with the free body diagram of the plate. The dynamic behaviour is expressed by (19.6), where I_O is the plate moment of inertia referred to the hinge, k is the Niceclick stiffness, $l = 80$ mm is the distance between the points "O", and "P" and ϑ is the plate rotational angle (considered very small) around the hinge axis.

The value of I_O was obtained by the following equation:

$$I_O = \frac{1}{12} m L^2 + m\overline{OG}^2 = 1.36 \cdot 10^{-3}\ \text{kg} \times \text{m}^2 \tag{19.6}$$

where $L = 100$ mm is the plate length, $m = 550$ gr is the plate mass, and $OG = 40$ mm is the distance between the barycentre and the rotational axis.

The resonance frequency of the system can be evaluated by the following equation:

$$f = \frac{1}{2\pi}\sqrt{\frac{kl^2}{I_O}} \tag{19.7}$$

Considering as a reliable value of stiffness the Up&Down k_1 coefficient from Table 19.4, the system resonance frequency results:

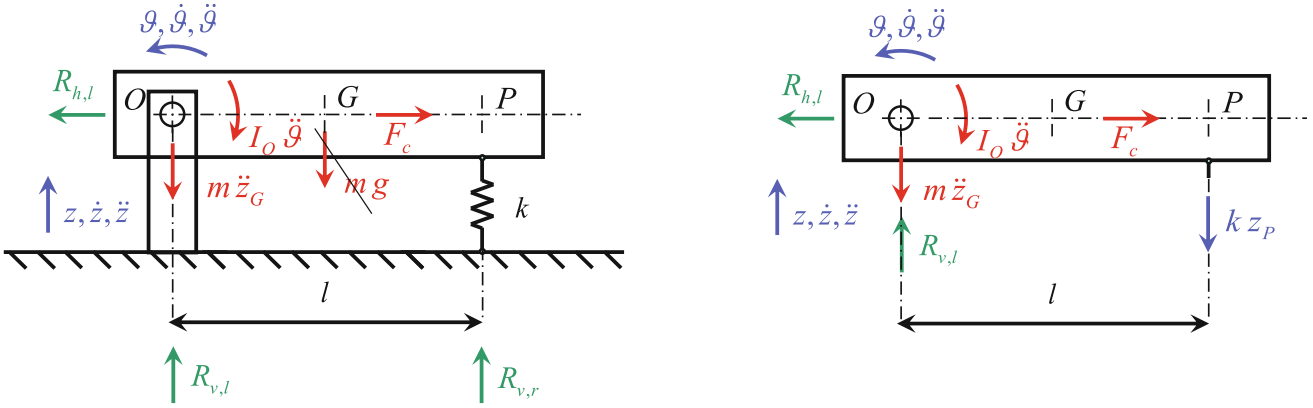

Fig. 19.12 Whole-system representation (left) and plate free body diagram (right)

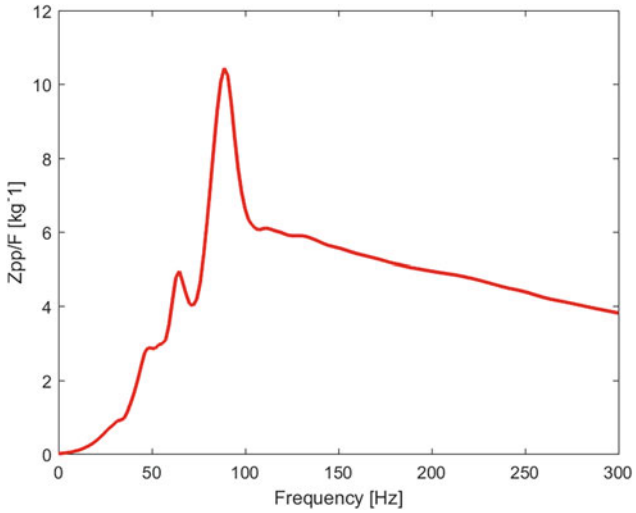

Fig. 19.13 Inertance FRF

$$f = \frac{1}{2\pi}\sqrt{\frac{kl^2}{I_O}} = \frac{1}{2\pi}\sqrt{\frac{67830 \cdot 0.08^2}{1.36 \cdot 10^{-3}}}\ \text{Hz} = 89.96\ \text{Hz} \tag{19.8}$$

The data from the impact test were analysed and the inertance FRF (evaluated in point "P") of Fig. 19.13 was obtained. The system resonance, that is represented in the plot by the highest peak, occurs at a frequency of 88.80 Hz, a value very close to the one in (19.8), calculated from the interpolation coefficient of the static test results.

Finally, the Niceclick dynamic analysis confirmed that the device specifics are perfectly suitable for the haptic applications since his reactiveness and dynamic response cover a very wide accelerometer range that goes beyond the human tactile perception frequency spectrum whose peak is around 250 Hz.

19.5 Niceclick Applications in Haptic Interfaces and Conclusions

The Niceclick is a very powerful haptic device in HMI application. For example, the most used interface on a vehicle is the steering wheel set of buttons, that includes, in certain cases, not only the infotainment system but even lights and screen wipers switches and the gearshift paddles [21]. Therefore, the simple, rectangular shapes are quite an exception. In the paper, the developed tools for developing the feedback patterns are depicted, showing the versatility of the device in different applications. An ad hoc measuring tool is developed to characterise the static and dynamic behaviour of the system.

The characterisation was performed on stiffness of the system showing a linear behaviour for extremely large displacement range, making the Niceclick quite interesting in automotive field. Moreover, it is objectified the state-of-the-art sensation evaluation through calculation of tactilometer natural frequency, which demonstrates the Niceclick suitability for industrial applications.

In the future, it will be studied the effect of the device inside a complex mechanical system, such as a steering wheel haptic interface, to evaluate the prototype performance and to define a methodology for optimal haptic device placement.

Acknowledgements Authors fully acknowledge Dr. Flavio Cerruti, CEO of Trama S.r.l., for all the suggestions, experience, deep knowledge, and enthusiasm in driving the project.

References

1. Akamatsu, M., Green, P., Bengler, P.: Automotive technology and human factors research: past, present and future. Int. J. Veh. Technol. **3**, 1–27 (2013). https://doi.org/10.1155/2013/526180
2. Kern, D., Schmidt, A.: Design space for driver-based automotive user interfaces. In: Proceedings of 1st International Conference on Automotive User Interfaces and Interactive Vehicular Applications, Essen, Germany, pp. 3–10 (2009). https://doi.org/10.1145/1620509.1620511
3. Gaspar, J., Fontul, M., Henriques, E., Silva, A.: Haptics of in-car radio buttons and its relationship with engineering parameters. Int. J. Ind. Ergon. **59**, 29–45 (2017). https://doi.org/10.1016/j.ergon.2017.03.005
4. François, M., Osiurak, F., Fort, A., Crave, P., Navarro, J.: Automotive HMI design and participatory user involvement: review and perspectives. Ergonomics. **60**(4), 541–552 (2017). https://doi.org/10.1080/00140139.2016.1188218
5. Gaspar, J., Fontul, M., Henriques, E., Ribeiro, A., Silva, A., Valverde, N.: Psychoacoustics of in-car switch buttons: from feelings to engineering parameters. Appl. Acoust. **110**, 280–296 (2016). https://doi.org/10.1016/j.apacoust.2016.03.037
6. Altinsoy, M.E., Merchel, S.: Audiotactile feedback design for touch screens. In: 4th International Conference on Haptic and Audio Interaction Design, Dresden, Germany, pp. 136–144 (2009). https://doi.org/10.1007/978-3-642-04076-4_15
7. Basdogan, C., Giraud, F., Levesque, V., Choi, S.: A review of surface haptics: enabling tactile effects on touch surfaces. IEEE Trans. Haptics. **13**(3), 450–470 (2020). https://doi.org/10.1109/toh.2020.2990712
8. Xu, H., Klatzky, R.L., Peshkin, M.A., Colgate, J.E.: Localised rendering of button click sensation via active lateral force feedback. In: 2019 IEEE World Haptics Conference, Tokyo, Japan, pp. 509–514 (2019). https://doi.org/10.1109/WHC.2019.8816158
9. Gescheider, G.A., Bolanowsky, S.J., Pope, J.V., Verrillo, R.T.: A four-channel analysis of the tactile sensitivity of the fingertip: frequency selectivity, spatial summation, and temporal summation. Somatosens. Mot. Res. **19**(2), 114–124 (2002). https://doi.org/10.1080/08990220220131505
10. Gescheider, G.A., Bolanowski, S.J., Hall, K.L., Hoffman, K.E., Verrillo, R.T.: The effects of aging on information-processing channels in the sense of touch: I. Absolute sensitivity. Somatosens. Mot. Res. **11**(4), 345–357 (1994). https://doi.org/10.3109/08990229409028878
11. Verrillo, R.T.: Effect of contactor area on the vibrotactile threshold. J. Acoust. Soc. Am. **35**(12), 1962–1966 (1963). https://doi.org/10.1121/1.1918868
12. Verrillo, R.T.: Psychophysics of vibrotactile stimulation. J. Acoust. Soc. Am. **77**(1), 225–232 (1985). https://doi.org/10.1121/1.392263
13. Bisley, J.W., Goodwin, A.W., Wheat, H.E.: Slowly adapting type I afferents from the sides and end of the finger respond to stimuli on the center of the fingerpad. J. Neurophysiol. **84**(1), 57–64 (2000). https://doi.org/10.1152/jn.2000.84.1.57
14. Srinivasan, M.A., LaMotte, R.H.: Tactual discrimination of softness. J. Neurophysiol. **73**(1), 88–101 (1995). https://doi.org/10.1152/jn.1995.73.1.88
15. Bergmann Tiest, W.M., Kappers, A.M.L.: Cues for haptic perception of compliance. IEEE Trans. Haptics. **2**(4), 189–199 (2009). https://doi.org/10.1109/toh.2009.16
16. Kildal, J.: 3D-press: haptic illusion of compliance when pressing on a rigid surface. ICMI-MLMI. **21**, 1–8 (2010). https://doi.org/10.1145/1891903.1891931
17. Scilingo, E.P., Bianchi, M., Grioli, G., Bicchi, A.: Rendering softness: integration of kinaesthetic and cutaneous information in a haptic device. IEEE Trans. Haptics. **3**(2), 109–118 (2010). https://doi.org/10.1109/TOH.2010.2
18. Tornincasa, S., Repetto, M., Bonisoli, E., Di Monaco, F.: Energy harvester for vehicle tires: nonlinear dynamics and experimental outcomes. J. Intell. Mater. Syst. Struct. **23**(1), 3–13 (2012). https://doi.org/10.1177/1045389X11430739
19. Tornincasa, S., Repetto, M., Bonisoli, E., Di Monaco, F.: Optimization of magneto-mechanical energy scavenger for automotive Tyre. J. Intell. Mater. Syst. Struct. **23**(18), 2055–2064 (2012). https://doi.org/10.1177/1045389X11430741
20. Tornincasa, S., Bonisoli, E., Di Monaco, F., Moos, S., Repetto, M., Freschi, F.: Chapter 30: Nonlinear dynamics of an electro-mechanical energy scavenger. In: Modal Analysis Topics, Vol. 3, Proceedings of the 29th IMAC, A Conference and Exposition on Structural Dynamics Conference Proceedings of the Society for Experimental Mechanics Series 2011., 578 pp., pp. 339–349. Springer (2011). https://doi.org/10.1007/978-1-4419-9299-4_30
21. Galvagno, E., Dimauro, L., Mari, G., Velardocchia, M., Vella, A.D.: Dual Clutch Transmission vibrations during gear shift: a simulation-based approach for clunking noise assessment. In: 2019 SAE Noise and Vibration Conference and Exhibition, June 10–13, 2019, Grand Rapids, Michigan, SAE Technical Paper 2019-01-1553, pp. 1–12 (2019). https://doi.org/10.4271/2019-01-1553

Chapter 20
Simultaneous Passive Vibration Attenuation and Energy Harvesting on a Fan-Folded Piezometaelastic Structure

Leticia H. Maki, Paulo S. Varoto, Elvio Bonisoli, Luca Dimauro, and Make S. V. Paredes

Abstract Simultaneous passive vibration suppression and energy harvesting through piezoelectric materials have been raising growing interest in the general area of structural dynamics. In the vibration isolation context, metastructures composed of multiple unit cells have played a major role in the design of suitable structures for the generation of frequency bandgaps, capable of mitigating structural vibration signals in a given frequency range. Additionally, concurrent energy harvesting in a given megastructure is possible through adequate positioning of piezoelectric layers on strategic locations along the metastructure geometric configuration. This work presents numerically simulated and experimental results of a study carried out on a given metastructure composed of a host beam with multiple resonators attached to it. Each resonator is designed from the arrangement of multiple beams forming a fan-folded structure that will significantly affect both, the vibration suppression as well as the capability of harvesting energy. Numerically simulated results are obtained through finite element modeling and a lumped parameter modeling methodology. Experimental results are gathered on a test prototype to verify the numerical results. Interesting results are obtained from multiple configurations of the individual fan-folded resonators as well as the total number of resonators positioned on the host beam.

Keywords Vibration attenuation · Vibration mitigation · Local resonators · Piezoelectric energy harvesting · Bandgap formation

20.1 Introduction

The field of smart structures has seen great developments in the topic of piezoelectric energy harvesting, especially in the last decade. More recently, investigations on passive energy absorption techniques using metamaterials have been attracting significant attention. This work aims to perform a numerical and experimental work on concurrent energy generation and absorption in a system composed of a main host beam-type structure and individual vibration absorbers composed of multiple beams forming a fan-folded structure.

When dealing with passive vibration attenuation using metastructures, one of the main concerns is the bandgap formation, more specifically in which frequency bandwidth they are formed in order to mitigate a give vibration amplitude, generally in the vicinity of a natural frequency of the host structure. It is known that structures with periodic nature exhibit a unique dynamic characteristic of acting as mechanical filters for wave propagation. Nouh [1] has studied periodic cells with local resonances, similar to most cases that the base structures contain cavities which house resonating masses connected to the cavity wall by springs. In the same vein, [2] has also investigated the dynamic of a lumped analytical model, an array of small resonators connected to a host structure in order to mitigate vibration within a desired frequency band. Together, these studies conclude that bandgap formation is associated to the absorbers periodicity.

However, the addition of oscillators is not the unique solution to obtain vibration suppression. Surveys such as conducted by Sugino and Erturk [3] have provided a fundamental understanding of bandgap formation in locally resonant electromechanical metastructures where the resonators are piezoelectric layers, that differs from purely mechanical

L. H. Maki · P. S. Varoto (✉) · M. S. V. Paredes
Department of Mechanical Engineering, University of Sao Paulo, Sao Carlos, Brazil
e-mail: leticia.maki@usp.br; varoto@sc.usp.brmsvalencia@usp.br

E. Bonisoli · L. Dimauro
Department of Mechanical and Aerospace Engineering, Politecnico di Torino, Torino, Italy
e-mail: elvio.bonisoli@polito.it; luca.dimauro@polito.it

M. Allen et al. (eds.), *Special Topics in Structural Dynamics & Experimental Techniques, Volume 5*,
Conference Proceedings of the Society for Experimental Mechanics Series, https://doi.org/10.1007/978-3-031-37007-6_20

metastructures with vibration absorbers attached to a main host structure. Alternatively, the periodic distribution of PZT patches over a beam allows the bandgap formation. Their work points out that, in this case, the bandgap in metastructures formation is associated with a frequency-dependent modal stiffness term, unlike the frequency-dependent modal mass term in mechanical structures.

An additional and important concern is that for many engineering applications, it is desired to control vibration at relatively low frequency ranges without using large structures. Thus, most researches involving periodic structures have two competing goals in common: (i) minimize natural frequencies and (ii) minimize mass and/or volume. The consideration of small structures with natural frequencies in the low frequency bands plays a relevant role for vibration mitigation. Numerous researches have examined bandgaps generation at high frequencies band, but a key aspect of this case is to suppress vibration at frequencies near to those from fundamental mode of vibration, which are, usually, in the low frequency band and typically result in the highest magnitude response. As a solution, dynamic absorbers are used.

A single resonator may have very little effect on the host structure; however, the collective dynamics of many oscillators has been shown to have significant vibration suppression capabilities. According to Yamaguchi [4], the use of multiple dynamic absorbers may be more effective than a single one coupled to the main structure. Moreover, as also studied by [5], the system response improves as more absorbers are used, but to a certain extent the addition of more resonators will provide only a marginally better performance, and an optimal number of resonators depends on the specific structure under consideration [6]. In summary, previous discussions suggest that there is no single configuration that is suitable for all applications, but the analysis of the system and its parameters is important in order to mitigate undesirable vibrations.

Undesirable vibrations are not necessarily unpleasant; when looking through another point of view, it can be converted and used for other purposes. There is a large volume of published papers studying many applications about energy harvesting as an isolated process; the most common are the ones that convert environmental signals into useful electrical energy. There are several geometric configuration types investigated. For example L-shaped [7, 8] design, or the presence of folds or creases through the beam as done by [9, 10], or foldable configurations as studied by [11] and [12]. All of them contribute to energy generation that can replace or supplement conventional batteries.

A more recent approach suggests an increasing interest in the study of the combination of energy harvesting and vibration attenuation in metastructures. As it is in a state of the art, a considerable amount of literature has contemplated the investigation of discrete systems where the resonators are usually attached to a host beam, and, the dimension of the bandgap is controlled by the added stiffness to the lumped system. The use of discrete oscillators with one degree of freedom has been an object of research by [13] and [14]. Another important contribution investigates metastructure where resonators consist of cantilever beam with tip mass modeled as a discrete system [15]. As previously discussed, many previous researches have used lumped model to study systems, but none have addressed the continuous theory for both, especially to the resonators model.

The main goal of this paper is to study a fan-folded structure in the context of piezoelectric energy harvesting and passive vibration attenuation. The fan-folded geometry under study can be seen in Fig. 20.1 in isometric and side views, respectively. Previous investigations [11, 12, 16] have already assessed the dynamics of such a structure with a different number of connecting beams. For the investigation concerning the passive vibration attenuation, the structure shown in Fig. 20.2 will be considered. A host beam carrying a certain number of fan-folded structures will be considered. The metastructure will be modeled by two different modeling strategies: a finite element model and a parametric lumped parameter methodology [17] in order to provide a comparison basis for the finite element results. In both, the fan-folded and metastructure studies experimental tests are conducted in order to obtain data from prototypes. The experimental data is confronted with the numerically simulated results in order to verify the models used.

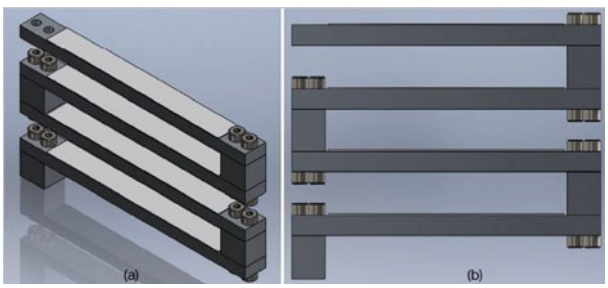

Fig. 20.1 Geometric configuration of fan-folded energy harvesters: (**a**) isometric; (**b**) lateral view

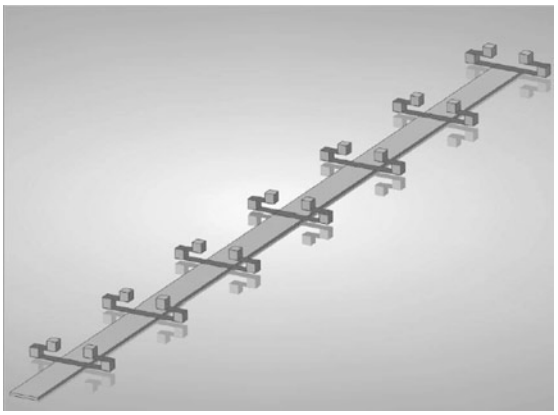

Fig. 20.2 Metastructure with two beam fan-folded vibration absorbers

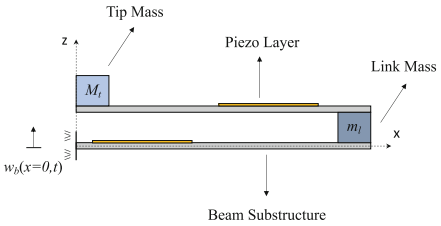

Fig. 20.3 Metastructure with 14 fan-folded of two beams

20.2 Theory Review

This section presents a theory review of the continuous model developed for the fan-folded energy harvester. Further details of the derivation of the equations can be found in [11, 12, 16]. The development employs the kinematics diagram, shown in Fig. 20.3, that represents a two beam fan-folded structure with a single connecting lumped mass m_l, an end mass M_t, and segmented piezoelectric layers on one of the surfaces of each beam according to the unimorph configuration [18]. The system is driven by an input vertical harmonic motion $w_b(x = 0, t)$ that is applied to the boundary of the first beam.

The partial differential equation of motion for the i^{th}-beam in a general fan-folded energy harvester such as shown in Fig. 20.3 employs the well-known Euler-Bernoulli beam model [19] and can be shown as [11, 12]

$$\rho A \frac{\partial^2 w_{\mathrm{r}}(x,t)}{\partial t^2} + EI \frac{\partial^4 w_{\mathrm{r}}(x,t)}{\partial x^4} = -\alpha \left[\frac{d\delta(x)}{dx} - \frac{d\delta(x-L)}{dx} \right] v(t)$$
$$- \left[\rho A + M_l \delta(x - x^*, i-k) + M_t \delta(x - x_{end}, i-n) \right] \frac{d^2 w_b(t)}{dt^2} \tag{20.1}$$

As can be seen, Eq. 20.1 does not account for dissipation terms, which can be introduced according to the model of damping used, namely, viscous or strain rated (or both) [18]. The right-hand side of Eq. 20.1 contains two terms that correspond respectively to the electrical voltage generated in the piezoelectric layer, and the external loading, assumed to be in the form of an acceleration imposed on the boundary of the first beam. Due to the application of this base-imposed motion-type input, Eq. 20.1 is written as a function of the relative displacement $w_r(x, t)$ to the base motion of the system. The index i denotes the ith beam of the *fan-folded*.

The modal model of the system shown in Fig. 20.1, which is composed of the undamped natural frequencies and eigenfunctions, can be found by solving the associated homogeneous equation of motion, obtained from Eq. 20.1 with appropriate boundary and interface boundary conditions. The solution for the free vibration is obtained from the [19] method of separation of variables, and the displacement $w(x, t)$ is expressed as follows:

$$w_i(x,t) = \sum_{j=1}^{\infty} \phi_{ij}(x) T_j(t) \tag{20.2}$$

$\phi_{ij}(x)$ represents the part of the solution that is a function of the spatial variable x and represents the eigenfunction or undamped mode shape. Function $T_j(t)$ represents a function in the time domain. These are respectively given as

$$T_j(t) = D_j cos(\omega_{nj} t) + E_j B sen(\omega_{nj} t) \tag{20.3}$$

$$\phi_{ij}(x) = A_{ij} cos(\beta_j x) + B_{ij} sen(\beta_j x) + C_{ij} cosh(\beta_j x) + D_{ij} senh(\beta_j x) \tag{20.4}$$

The indexes in Eqs. 20.3 and 20.4 can be read as the jth mode shape of the ith beam. Also, constants A_{ij}, B_{ij}, C_{ij}, and D_{ij} depend on the boundary conditions and are different constants in each case. Variable ω_n is the *n-th* undamped natural frequency of the whole system, given by

$$\omega_n = \beta_n^2 c \tag{20.5}$$

c is a constant that depends on the bending stiffness EI and the geometrical and material properties ρ and A, and is given as a function of the corresponding eigenvalue β_n

$$c = \sqrt{\frac{EI}{\rho A}} \tag{20.6}$$

Due to the continuous nature of the system, j can vary from zero to infinity modes of vibration but for research purpose, it goes to n finite modes. Thus, it is worth noting that for each vibrating mode, there is a corresponding value of natural frequency associated, as well as a corresponding value of β_j, which are the eigenvalue of the characteristic function. Moreover, for each beam and for each mode, there is an associated $\phi_{ij}(x)$. As previously pointed out, the undamped natural frequencies and eigenfunctions can be found by defining the boundary conditions for the system under study. For the case of a fan-folded composed of multiple beams, two boundary conditions are defined, one at $x = 0$, or at the boundary of the first beam, and the second at the end of the last beam, where the lumped tip mass M_t is located. Hence, a total of four equations define these boundary conditions, and they are given as

$$\phi_{1j}(x) = 0 \tag{20.7}$$

$$\phi'_{1j}(x) = 0 \tag{20.8}$$

$$EI\phi''_{nj}(x) \pm (-I_t \phi'_{nj}(x)\omega_{nj}^2) = 0 \tag{20.9}$$

$$EI\phi'''_{nj}(x) \pm (-M_t \phi_{nj}(x)\omega_{nj}^2) = 0 \tag{20.10}$$

The first two equations above establish zero deflection and slope for the $x = 0$ for the first beam, whereas the last two equations establish moment and force equilibrium between the beam and the tip mass for the last beam of the fan-folded arrangement. Additional interface equilibrium conditions between two consecutive beams are needed in order to solve for the modal properties

$$\phi_{ij}(x) = \phi_{(i+1)j}(x) \tag{20.11}$$

$$\phi'_{ij}(x) = \phi'_{(i+1)j}(x) \tag{20.12}$$

$$EI\phi''_{ij}(x) = -EI\phi''_{(i+1)j}(x) \pm (-I_l \omega_{nj}^2 \phi'_{(i+1)j}(x)) \tag{20.13}$$

$$EI\phi'''_{ij}(x) = -EI\phi'''_{(i+1)j}(x) \pm (-M_l \omega_{nj}^2 \phi_{(i+1)j}(x)) \tag{20.14}$$

As shown in [11, 12, 16], application of Eqs. 20.8–20.10 and 20.11–20.14 to Eq. 20.4 leads to the determination of the eigenvalues and eigenfunctions of the fan-folded energy harvester. The eigenvalues β_n and corresponding undamped natural frequencies are obtained from the solution of the system's characteristic equation whereas the coefficients A_{ij}, B_{ij}, C_{ij}, D_{ij} for the eigenfunctions are obtained from the solution of a system of homogeneous equations, for a given eigenvalue.

Once the natural frequencies and eigenfunctions for the system under study are determined, the next step is to derive expressions for the electromechanical frequency response functions for the fan-folded energy harvester. For this purpose, Eq. 20.1 must be solved for the harmonic input driven motion. Due to the multi-physical nature of the piezoelectric material, a suitable electrical configuration is required. In the present case, the piezoelectric layer is assumed to be an electrical current source connected in parallel with an equivalent capacitance and a load resistance. The differential equation for the electric circuit is give as [12]

$$P_i C_p \dot{v}(t) + i_i(t) = -2b_s d_{31} E_p \frac{t_p + t_s}{2} \sum_{j=1}^{\infty} \frac{dT_j(t)}{dt} [\phi'_{ij}(Ls) - \phi'_{ij}(0)] \tag{20.15}$$

with the internal capacitance C_p given as

$$C_p = 2\varepsilon_{33}^s \frac{L_s b_s}{t_p} \tag{20.16}$$

ε_{33}^s is the permittivity of the piezoelectric material. In Eq. 20.15, $i_i(t)$ represents the current, d_{31} the piezoelectric coupling coefficient. Note that this modeling assumes that the entire length of the piezoelectric layer covers the beam. By employing modal analysis principles for harmonic forced motion in combination with the electrical model given by Eq. 20.15, it can be shown that the following expressions for the system's FRF can be found [12]:
Voltage FRF with respect to the input acceleration:

$$\frac{v(\omega)}{a_b(\omega)} = \frac{\sum_{j=1}^{\infty} \frac{j\omega\chi_j\gamma_j}{\omega_{nj}^2 + 2\zeta\omega_{jn}\omega - \omega^2}}{\frac{1}{R} + j\omega C_p + \sum_{j=1}^{\infty} \frac{j\omega\chi_j^2}{\omega_{nj}^2 + 2\zeta\omega_{nj} j\omega - \omega^2}} \tag{20.17}$$

FRF of the total electrical power can be easily obtained from the voltage FRF

$$\frac{p(\omega)}{a_b^2(\omega)} = \frac{v^2(\omega)}{R} = \frac{1}{R} \left(\frac{\sum_{j=1}^{\infty} \frac{j\omega\chi_j\gamma_j}{\omega_{nj}^2 + 2\zeta\omega_{jn}\omega - \omega^2}}{\frac{1}{R} + j\omega C_p + \sum_{j=1}^{\infty} \frac{j\omega\chi_j^2}{\omega_{nj}^2 + 2\zeta\omega_{nj} j\omega - \omega^2}} \right)^2 \tag{20.18}$$

FRF of the relative acceleration to the base acceleration:

$$\frac{a_r(\omega)}{a_b(\omega)} = -\omega^2 \frac{w(\omega)}{a_b(\omega)} = -\omega^2 \left(\sum_{j=1}^{\infty} \frac{-1}{\omega_{nj}^2 + 2\zeta\omega_{nj} j\omega - \omega^2} \right) \left(\chi_j \frac{\sum_{j=1}^{\infty} \frac{j\omega\chi_j\gamma_j}{\omega_{nj}^2 + 2\zeta\omega_{nj} j\omega - \omega^2}}{\sum_{j=1}^{\infty} \frac{j\omega\chi_j^2}{\omega_{nj}^2 + 2\zeta\omega_{nj}^2 j\omega - \omega^2}} + \gamma_j \right) \phi_{ij}(x) \tag{20.19}$$

Equations 20.17, 20.18, and 20.19 are the frequency response functions of the fan-folded generator studied in this work. These equations will be further used in numerical simulations.

20.3 Fan-Folded Model Verification

This section describes numerically simulated and experimental results obtained for a two beam fan-folded system which properties are shown in Tables 20.1 and 20.2. The numerically simulated data was obtained by employing the FRF equations shown in the previous section and also by using finite element simulations. For the experimental data, the experimental arrangement shown in Fig. 20.4 was used.

As shown in Fig. 20.4, the two beam fan-folded structure is mounted on the vibration table of an electromagnetic vibration exciter for the base driven tests. A broadband random signal is used to drive the exciter through its power amplifier. The input acceleration signal is measured by a piezoelectric accelerometer conveniently positioned on the vibration exciter table. Output signals are composed of the piezoelectric voltage from a single piezoelectric layer that is first introduced into a resistance box that is adjusted to provide a load resistance of $R_l = 100\,\text{k}\Omega$. Then, resulting acceleration and voltage signals are fed into the spectrum analyzer for FRF determination using standard signal processing techniques [20, 21].

Figures 20.5 depicts numerically simulated and experimental results for two configurations of the fan-folded energy harvester. In both cases it can be seen a good agreement between numerical and experimental results.

The result for a fan-folded composed by a single beam shown in Fig. 20.5 is actually the traditional cantilever beam with a tip mass and corresponds to the acceleration transmissibility FRF considering the output acceleration at the tip mass with respect to the base acceleration. This result shows a single resonant frequency around 78 Hz in the entire frequency range.

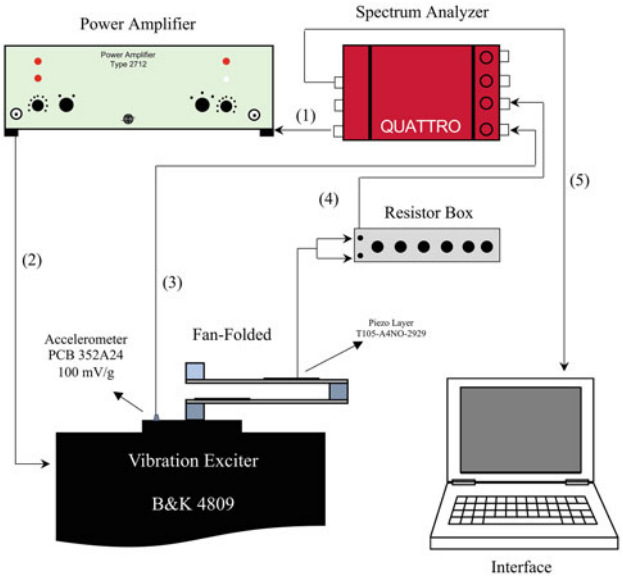

Fig. 20.4 Experimental setup for fan-folded transmissibility tests

Table 20.1 Geometric parameters of two beam fan-folded harvester

Parameter	Beam	Link mass	Tip mass	PZT
Length (mm)	140	12.7	12.7	50
Width (mm)	12.7	12.7	25.4	12.7
Thickness (mm)	3.2	12.7	12.7	0.26

Table 20.2 Material and electromechanical properties of fan-folded harvester

Property	Substructure	Link mass	Tip mass	PZT
Young Modulus (GPa)	72	72	72	66
Density (kg/m^3)	2770	2770	2770	7800
Permittivity, ϵ (nF/m)	–	–	–	13.3
Resistance (Ω)	–	–	–	500×10^3
Capacitance (nF)	–	–	–	0.48911

The second result shown in Fig. 20.5 also shows the acceleration FRF except that now a two beam fan-folded is considered. By adding a second beam, the system now shows two resonant peaks in the frequency range, the first in the vicinity of 49 Hz and the second at approximately 80 Hz. In both cases an excellent agreement is seen to occur between the numerical and experimental results. As seen in [12], as the number of beams increases, the number of resonant peaks present in the same frequency range also increases, thus allowing energy to be harvested at lower frequencies, as it is usually the case for environmental vibration signals.

Figure 20.6 shows the corresponding voltage electromechanical FRF results for a single and two beam fan-folded, respectively. Similarly to the case of the purely mechanical FRF, a good agreement is seen to occur for the voltage FRF for both configurations of the fan-folded energy harvester.

20.4 Fanfolded Metastructure Analysis

This section describes numerically simulated and experimental results obtained from the analysis of the metastructure composed of a host aluminum and two beam fan-folded sub-systems as resonators, as shown in Fig. 20.2. For the experimental analysis the setup shown in Fig. 20.7 is used. Figure 20.7a shows the experimental apparatus arrangement for the FRF measurements while Fig. 20.7b shows an image of the actual test. The host aluminum beam is attached to the vibrating table of a long stroke APS 113 vibration exciter that is driven by a random signal provided by the Dp QUATTRO

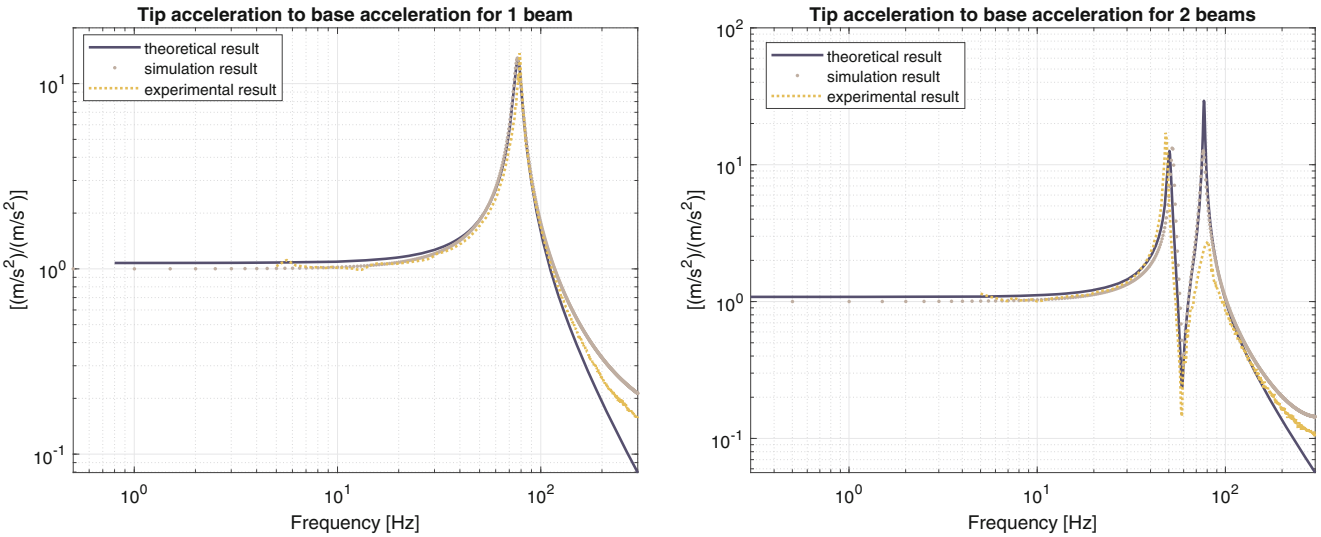

Fig. 20.5 Free end acceleration to base acceleration FRFs

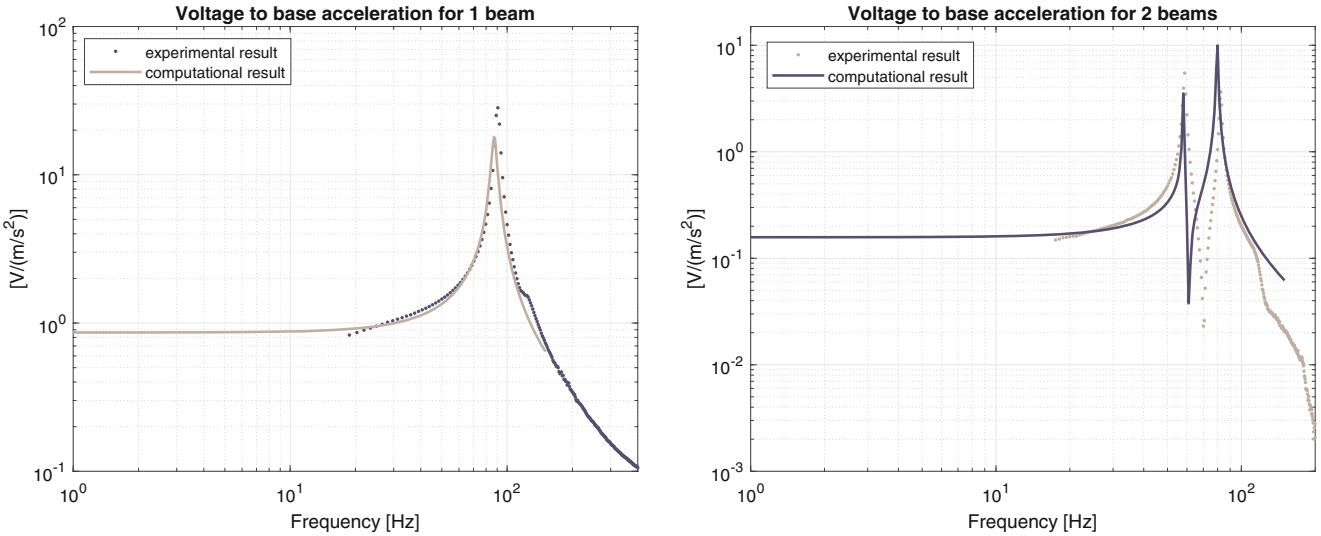

Fig. 20.6 Voltage to base acceleration FRFs

spectrum analyzer. Mechanical transmissibility FRF are measured by two miniature accelerometers, one positioned at the free end of the host beam and the second mounted on the clamping device in order to get the input driven acceleration signal.

Table 20.3 shows the dimensions that compose the metastructure. The host beam is made of aluminum with dimensions $1000 \times 32 \times 3.2$ mm. Each resonator contains two beams made of spring steel and dimensions of $35 \times 0.25 \times 10$ mm. The lumped masses that are used in connecting the individual beams of the fan-folded are square blocks of 10 mm, and they are made of aluminum. Attachment of the fan-folded resonators on the host beam is made with M3 bolts at holes equally spaced on each side of the host beam. The full configuration of the metastructure comprises up to 20 resonators on each side of the host beam, thus giving a total of 40 resonators. Intermediate testing configurations are obtained by placing a smaller number of resonators, not necessarily evenly spaced on the host beam.

For the numerical simulations, in addition to finite element modeling of multiple configurations of the metastructure, a parametric model of the fan-folded metastructure has been realized using Lupos software [22, 23]. 1D Timoshenko beams are used for modelling all the structure geometric characteristics. Due to its parametric implementation, it is possible to choose the number of added fan-folded beams, and their type to realize one, two, or three beam fan-folded configurations. The family of models covers a range from 912 to 24672 dofs.

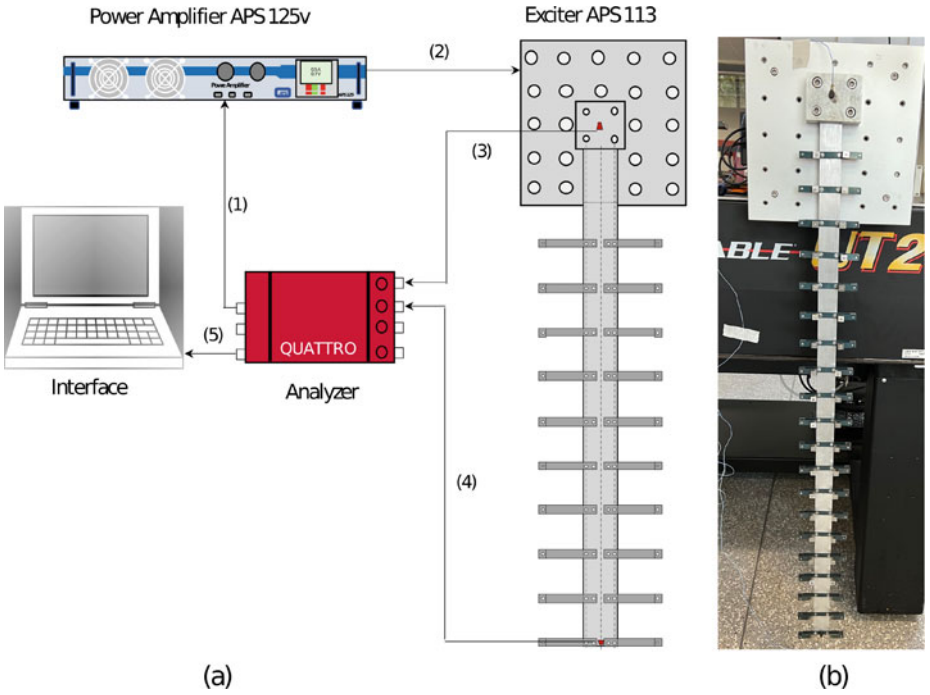

Fig. 20.7 Experimental setup for test with metastructure composed of fan-folded and host beam: (**a**) apparatus; (**b**) actual test

Table 20.3 Metastructure parameters

Parameter	Host beam	Link mass	Tip mass	Fan-folded beam
Length (mm)	1000	10	10	30
Width (mm)	32	10	10	10
Thickness (mm)	3	10	10	0.25

An example of increasing complexity of the structure is reported in Fig. 20.8, where a metastructure up to 20 resonators composed up to three levels is realized. It is possible to compute the dynamic properties of the structure, evaluating mode shapes, and their natural frequencies. A mode-shape tracing method, called Dynamic Modal for Assembly (DMA) [17, 24, 25], is performed to analyze the frequency trend of the host beam global modes. Crossing phenomena happen between torsional mode shapes (labelled 1t, 2t) and the corresponding transversal bending modes (labeled 2_{xy}, 3_{xy}) in the frequency range 0–500 Hz. For details about crossing and veering dynamic phenomena in parametric structures, see [24, 26–28].

In Fig. 20.9 a comparison of host beam global mode shapes increasing the level of 10 resonators is taken into account. MAC index [29, 30] is used to evaluate the auto-correlation when one, two, or three levels of fan-folded beams are added. In Fig. 20.10, the same MAC index is used to evaluate the cross-correlation between host beam global modes when one, two, or three levels of fan-folded beams are added. Some transversal bending modes show coupling with the first torsional having quite large distance in frequency. The main effect due to the fan-folded beams is to have packages of their bending modes at similar frequencies that can be coupled with the host beam dynamics.

According to the fact that the added fan-folded beams are secondary additional structures attached to the main structure, the host beam can have more or less coupled mode shapes with a multiplicity due to the number of added secondary beams [24]. In Fig. 20.11 a transparency parameter is used to transform the host beam alone with the three possible levels of fan-folded beams. The choice of material density and geometry (length, width, and thickness) of the added beams and the additional masses can be tuned to have more significant interactions with respect to the global mode shapes of the host beam.

As shown in [24], the ratio between Young modulus and density of the added components is maintained constant in changing the transparency between the single host beam (transparency of 1%) and the full system (transparency of 100%), while the density of the added beams is progressively increased. It is evident that the weight of these additional components can interact with the main host beam producing a wider frequency bandwidth of interaction.

Also a variation of the MAC index [27, 30] can be used to underline the similarities and couplings of the multiplicity of the fan-folded beam modes. Always taking into account the case of 10 resonators made of multiple fan-folded multi-beam,

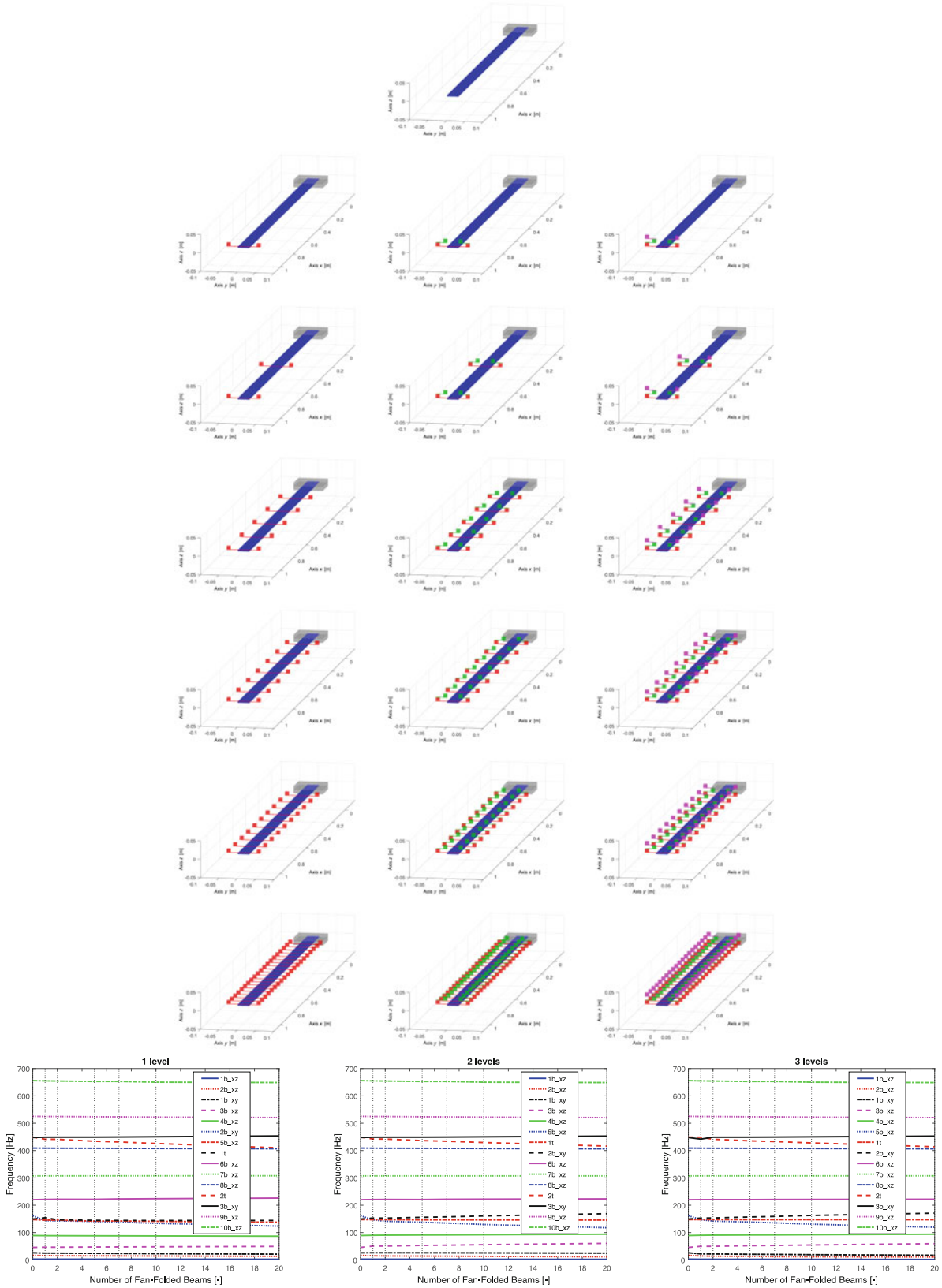

Fig. 20.8 DMA analysis with structure composed by host beam + from 1 to 20 fan-folded beams for each side (from up to down), from 1 to 3 levels of fan-folded beams (from left to right)

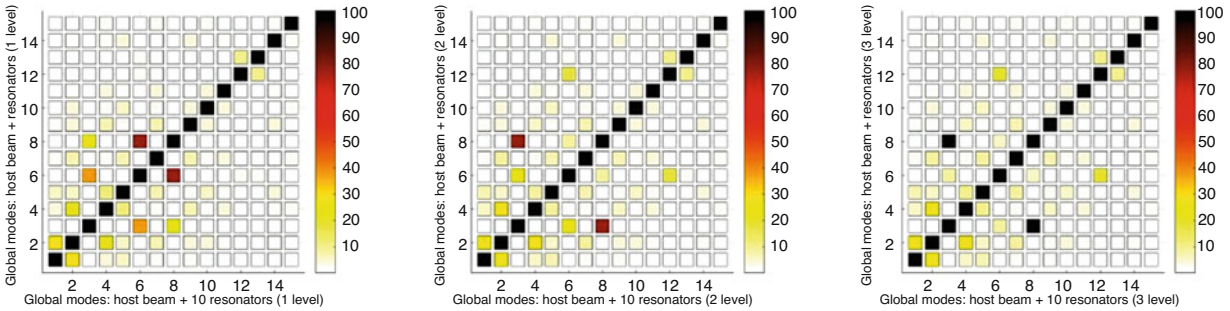

Fig. 20.9 AutoMAC for global modes of the host beam + 10 resonators with 1 level (left), 2 levels (centre), 3 levels (right)

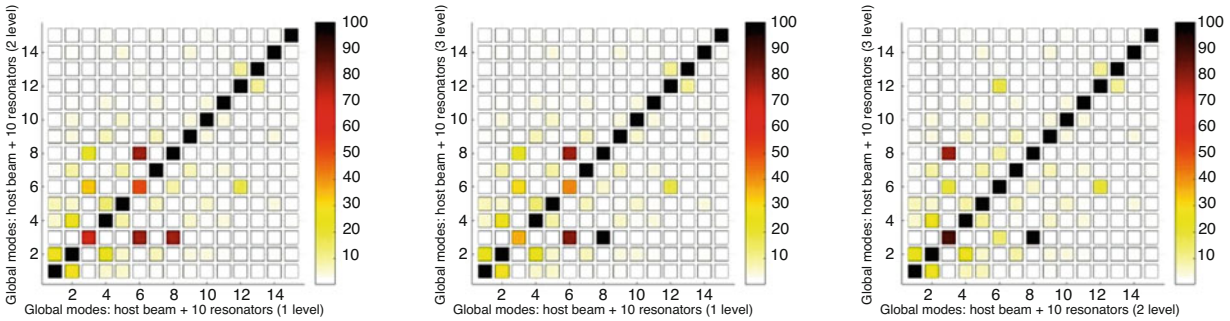

Fig. 20.10 CrossMAC for global modes of the host beam + 10 resonators between 1?2 levels (left), 1?3 levels (centre), 2?3 levels (right)

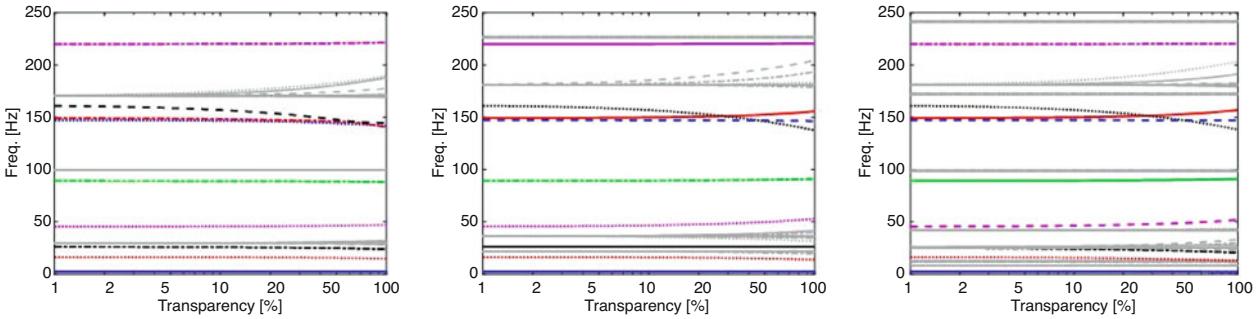

Fig. 20.11 On the left, DMA analysis with structure composed by host beam + 10 resonators (1 level). In the middle (2 levels). On the right (3 levels)

in Fig. 20.12 the frequency distance between modes is adopted to show the frequency gaps and the similarities of modes far from the main diagonal.

Assuming a constant damping ratio $\zeta = 0.5\%$, the numerical transmissibility in z direction between host beam constraint and host beam free end is compared increasing the number of resonator in Fig. 20.13. Considering that energy harvesting technique with multiple PZT patches can be installed on the structure as in [28], an interesting increment of frequency bandwidth is detected in the resonator regions. Also a large anti-resonance bandwidth is detected between 35 and 50 Hz, corresponding to in-phase and out-of-phase mode shapes of all the resonators. It is also interesting to note that the increment of resonators on the host beam can produce a predictable decrement of the corresponding natural frequencies for some bending modes along z direction, while other bending modes increase, as in the range 55 Hz and 90 Hz.

In order to obtain a better understand about the dynamic behavior of metastructure, finite element frequency response analysis was performed varying not only the type of resonators but also the number of them distributed in the host beam. Some configurations studied are shown in Fig. 20.13, on the left of the picture there are 40 cantilever beams resonators attached to the host, and on the right side, there are 14 two beams fan-folded. These structures were used to acquire experimental data of free end acceleration to base acceleration.

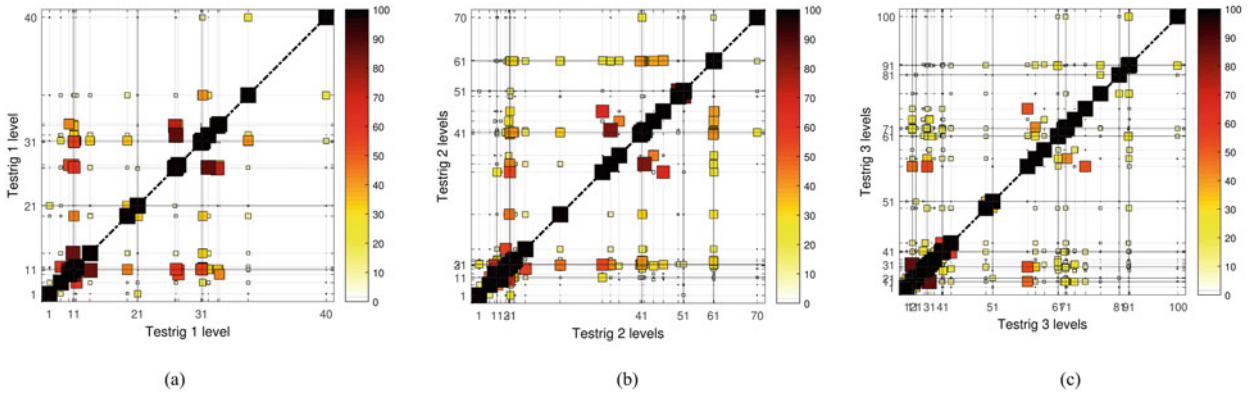

Fig. 20.12 MAC analysis with structure composed by host beam + 10 resonators: single fan-folded beams (1 level, left), two fan-folded beams (2 levels, center), three fan-folded beams (3 levels, right)

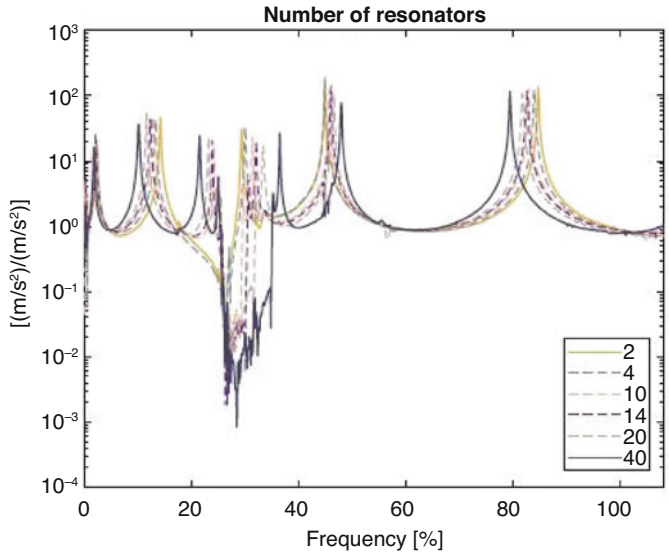

Fig. 20.13 Varying the number of resonators

Figure 20.13 aims to investigate the influence of number of resonators on the bandgap generation. The minimum number of them that can be attached is 2 (one for each side), and the maximum amount is 40 (20 for each side). According to the result, as the number of resonators increases, the bandgap becomes wider in the frequency range. So, the minimum configuration is enough to have a bandgap formation. However, the addition of more connections can be useful depending on the application. It enhances significantly the bandgap width; in this case, the full configuration increased the bandwidth in more than 85% related to the case with only two fan-folded resonators.

Such as in the previous section, experimental tests were carried out for several configurations of the metastructure. Since another major concern is related to vibration attenuation, it is important not only to determine the dynamic behavior when there are many resonators coupled, but also, when the host has no resonators attached to it. This test is fundamental in order to assess the bare host natural frequencies, to further decide which resonant peak is to be mitigated by the addition of the fan-folded resonators. Figure 20.14 shows numerical and experimental acceleration transmissibility FRF for the host beam. As it can be seen, the first five natural frequencies fall in the 0–150 Hz frequency range, and their values are: (i) 2.5 Hz; (ii) 15.8 Hz; (iii) 44 Hz; (iv) 86.3 Hz and (v) 142.6 Hz.

Subsequently, comparisons can be done in order to verify the vibration attenuation phenomenon. Figure 20.15 shows finite element numerically simulated and experimental results for different configuration of the metastructure. The difference between the different configurations relies on the number of two beam fan-folded resonators used in each configuration. The experimental result for the host beam acceleration transmissibility FRF is plotted, and it can be shown that the bandgap

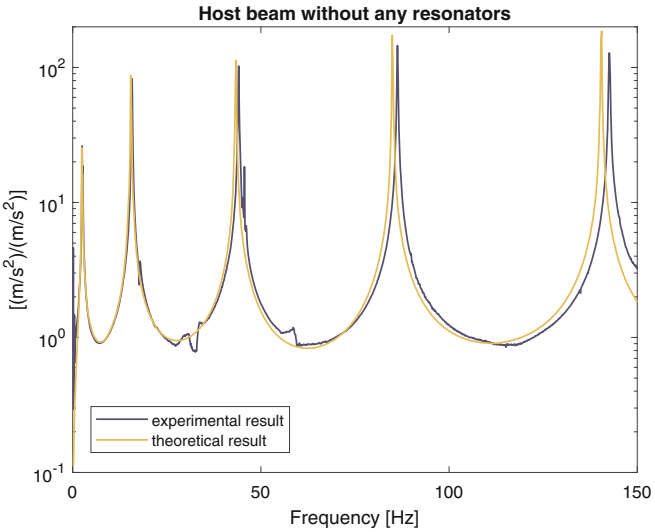

Fig. 20.14 Host beam acceleration transmissibility FRF. Output location, beam free end; input location, beam clamping device

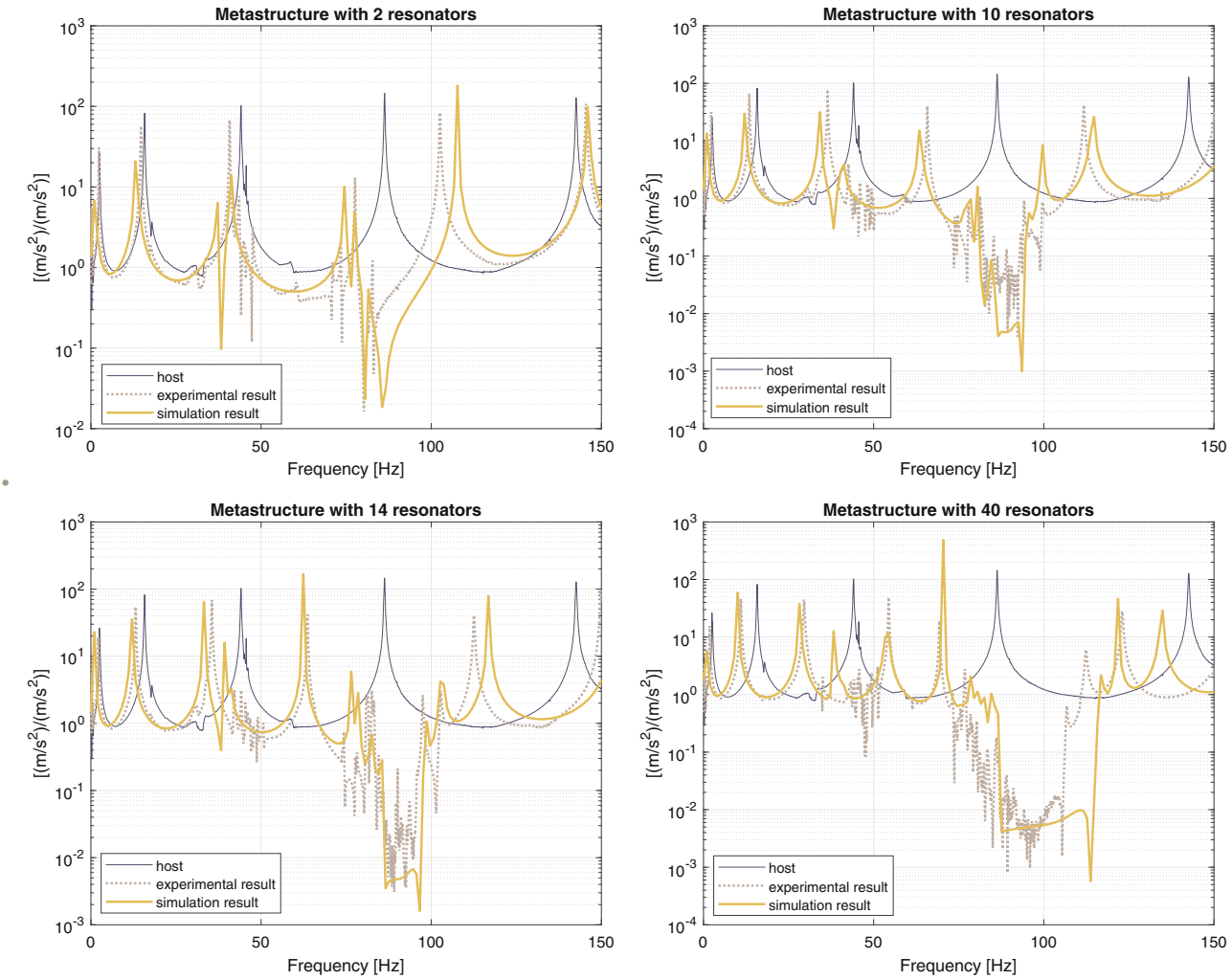

Fig. 20.15 Vibration attenuation for different metastructure configurations for the two beam fan-folded resonator

formation occurs in the vicinity of the fourth natural frequency of the host beam. Also, there is a reasonable coherence between experimental and simulation, especially in terms of natural frequency and the bandgap location.

20.5 Conclusion

This paper has discussed the use of a fan-folded structure in both contexts, as a harvester in energy harvesting and as a resonator in a metastructure. In order to achieve the goal, analytical model, experimental tests, and simulations were performed. Results have shown that fan-folded can be used in both functionalities, and specially, when it comes to metastructure, it is important to consider that when bandgaps are generated. A parametrically lumped model of the metastructure was formulated using LUPOS and proved to be very efficient in capturing the main characteristics of the metastructure dynamics. Therefore, Multi-Level Modal Analysis is definitely a suitable method to apply in the future more complex examples and to be developed as an improvement of the classical Finite Element software. For the purpose of this paper, its use addressed the efficiency in terms of accuracy and time consuming. Finallly, the combination of metastructures and energy harvesting areas shows to be relevant and clearly demonstrates a promising research field in the area, since it has been supported by the current findings with a good agreement in the results obtained.

Acknowledgments Authors fully acknowledge all support received from the Mechanical Engineering Department, Sao Carlos Engineering School (EESC-USP)—Brazil, CNPq (Official funding agency of the state of Sao Paulo, grant Nr. 131342/2020-7) and from the Department of Mechanical and Aerospace Engineering, Politecnico di Torino—Italy. This paper is dedicated the memory of Prof. Elvio Bonisoli, a friend and a mentor, who sadly is no longer with us. Elvio cooperated with passion, curiosity and enthusiasm in this research work, where his beloved structural dynamics and his love for energy harvesting find their perfect combination.

References

1. Nouh, M., Aldraihem, O., Baz, A.: Vibration characteristics of metamaterial beams with periodic local resonances. J. Vib. Acoust. **136**(6), 061012 (2014)
2. Hobeck, J.D., Laurent, C.M.V., Inman, D.J.: 3d printing of metastructures for passive broadband vibration suppression (2015)
3. Sugino, C., Leadenham, S., Ruzzene, M., Erturk, A.: An investigation of electroelastic bandgap formation in locally resonant piezoelectric metastructures. Smart Mater. Struct. **26**(5), 055029 (2017)
4. Yamaguchi, H., Harnpornchai, N.: Fundamental characteristics of multiple tuned mass dampers for suppressing harmonically forced oscillations. Earthquake Eng. Struct. Dyn. **22**(1), 51–62 (1993)
5. Reichl, K.K., Inman, D.J.: Lumped mass model of a 1d metastructure for vibration suppression with no additional mass. J. Sound Vib. **403**, 75–89 (2017)
6. Sugino, C., Xia, Y., Leadenham, S., Ruzzene, M., Erturk, A.: A general theory for bandgap estimation in locally resonant metastructures. J. Sound Vib. **406**, 104–123 (2017)
7. Harne, R.L., Sun, A., Wang, K.W.: Leveraging nonlinear saturation-based phenomena in an l-shaped vibration energy harvesting system. J. Sound Vib. **363**, 517–531 (2016)
8. Liu, D., Al-Haik, M., Zakaria, M., Hajj, M.R.: Piezoelectric energy harvesting using l-shaped structures. J. Intell. Mater. Syst. Struct. **29**(6), 1206–1215 (2018)
9. Pydah, A., Batra, R.C.: Beam-based vibration energy harvesters tunable through folding. Am. Soc. Mech. Eng. **141**(1), 011003 (2018)
10. Su, W.-J., Zu, J.W.: Modeling of v-shaped beam-mass piezoelectric energy harvester: impact of the angle between the beams. Am. Soc. Mech. Eng. (2012)
11. Ansari, M.H., Karami, M.A.: Modeling and experimental verification of a fan-folded vibration energy harvester for leadless pacemakers. J. Appl. Phys. **119**(9), 094506 (2016)
12. Maki, L.H., Valencia, M.S., Varoto, P.S.: Dynamic performance and uncertainty analysis of a piezometaelastic structure for vibration control and energy harvesting. In: Special Topics in Structural Dynamics & Experimental Techniques, Volume 5, pp. 215–231. Springer, Berlin (2021)
13. Basta, E.E., Ghommem, M., Emam, S.A.: Vibration suppression and optimization of conserved-mass metamaterial beam. Int. J. Non-Linear Mech. **120**, (103360) (2020)
14. Hu, G., Tang, L., Das, R.: Metamaterial-inspired piezoelectric system with dual functionalities: energy harvesting and vibration suppression. In: Active and Passive Smart Structures and Integrated Systems 2017, vol. 10164, pp. 425–434. SPIE (2017)
15. Khattak, M.M., Sugino, C., Erturk, A.: Concurrent vibration attenuation and low-power electricity generation in a locally resonant metastructure. J. Intell. Mater. Syst. Struct. **33**(15), 1990–1999 (2022)
16. Paredes, M.S.V.: Coletor piezeletrico de vibracoes estruturais com geometria sanfonada: Analise teorica e experimental. Master's Thesis, Escola de Engenharia de Sao Carlos, Universidade de Sao Paulo, 2020
17. Bonisoli, E., Lisitano, D., Dimauro, L.: Detection of critical mode-shapes in flexible multibody system dynamics: the case study of a racing motorcycle. Mech. Syst. Signal Process. **180**, 109370 (2022)
18. Erturk, A., Inman, D.J.: Piezoelectric Energy Harvesting, 1st edn. Wiley, New York (2011)

19. Rao, S.: Vibrations of Continuous Systems,. 1st edn. Wiley, New York (2007)
20. McConnell, K.G., Varoto, P.S.: Vibration Testing: Theory and Practice, 2nd edn. Wiley, New York (2008)
21. Ewins, D.J.: Modal Testing: Theory, Practice and Applications, 1st edn. RSP (2000)
22. Bonisoli, E.: Lupos: LUmped Parameters Open Source FEM code. Politecnico di Torino, Department of Mechanical and Aerospace Engineering, Italy
23. Venturini, S., Bonisoli, E., Dimauro, L. (eds.): Lupos: Open-Source Scientific Computing in Structural Dynamics. Lecture Notes in Computer Science, Austin, Texas. Proceedings of the 41th IMAC
24. Bonisoli, E., Marcuccio, G., Rosso, C.: Crossing and veering phenomena in crank mechanism dynamics. In: Topics in Model Validation and Uncertainty Quantification, vol. 5, pp. 175–187. Springer, Berlin (2013)
25. Bonisoli, E., Marcuccio, G., Venturini, S.: Interference fit estimation through stress-stiffening effect on dynamics. Mech. Syst. Signal Process. **160**, 107919 (2021)
26. Bonisoli, E., Delprete, C., Esposito, M., Mottershead, J.E.: Structural dynamics with coincident eigenvalues: modelling and testing. In: Modal Analysis Topics, vol. 3, pp. 325–337. Springer, Berlin (2011)
27. Bonisoli, E., Brino, M., Delprete, C.: Numerical-experimental comparison of a parametric test-rig for crossing and veering phenomena. Mech. Syst. Signal Process. **128**, 369–388 (2019)
28. Varoto, P.S., Bonisoli, E., Lisitano, D.: Parametric analysis and voltage generation performance of a multi-directional MDOF piezoelastic vibration energy harvester. In: Sensors and Instrumentation, Aircraft/Aerospace, Energy Harvesting & Dynamic Environments Testing, vol. 7, pp. 85–95. Springer, Berlin (2021)
29. Allemang, R.J.: A correlation coefficient for modal vector analysis. In: Proc. 1st Int. Modal Analysis Conference, pp. 110–116 (1982)
30. Allemang, R.J.: The modal assurance criterion–twenty years of use and abuse. Sound Vib. **37**(8), 14–23 (2003)

Chapter 21
Induction Motor Diagnostics Using Vibration and Motor Current Signature Analysis

Suri Ganeriwala

Abstract Diagnostics of an induction motor is a serious issue for improving plant reliability. Induction motors are workhorse of the world today. Motor current signature analysis (MCSA) and vibration data are commonly used for diagnosing induction motor problems. However, the fault signatures are complicated and lack consensus. The problem is further complicated by the loading effects of the defect signatures. This paper will present a comparison of vibration and motor current signals for induction motor subjected to different levels of torque, unbalance, and misalignment loadings. Experiments were performed on intentionally faulted motor with varying degrees of electro-mechanical defects. Different levels of mechanical torque, unbalance, and misalignment loadings were applied to the rotor side. The data were analyzed using both vibration and motor current sensors. Results indicate motor current signature provides better indication of certain electrical faults such as airgap eccentricity and broken rotos bars, and vibration signature is better indicator of mechanical defects. The results suggest that both motor current and vibration measurements are required for more complete diagnostics of induction motors.

Keywords MCSA · diagnostics · vibration analysis · motor current signature analysis · induction motors

21.1 Introduction

Diagnostics and condition monitoring in industrial rotating machinery can avoid machine downtime and save time and money. Faults in rotating equipment can generate vibration of mechanical parts or change the power quality of the motor. Also, electrical faults in induction motor can change the behavior of the motor reflecting in motor currents. Motor current signature analysis (MCSA) techniques process motor currents to diagnose the machine. Therefore, a comprehensive study of motor current/voltage and vibration response under faults is needed for such diagnostics. Induction motors are critical components of many industries and are considered to be the 'power horses' of the industry. This paper focuses on the application of motor current signature analysis (MCSA) to diagnose faults in three-phase induction motors. MCSA has the advantages of non-invasive and online monitoring techniques [1]. A review of publications in the field of MCSA reveals inverse relationship between fault detection ease and importance to the user of that fault detection [2]. Also, the amount of literature available on the application of MCSA on broken rotor bars is considerably high compared to the other faults.

This work studies effects of induction motor faults on machine vibration and motor current spectrum. Four major faults including (1) bearing faults, (2) static rotor airgap eccentricity, (3) mechanical imbalance, and (4) broken rotor bars have been introduced to the machinery fault simulator (MFS). For each fault, 16 channels of data including vibration, voltages, currents, and tachometer signals were recorded. Each channel has been analyzed, and the results of channels with distinct aberrations are presented. Results can be used for detection, isolation, and assessment of induction motor faults. First, induction motors fundamental equations and fault components for each fault are introduced. Experiment setup is detailed. For each fault, vibration signals are investigated first. Then, motor current signals are studied in time and frequency domain to find fault components. Results associated with each fault are presented in terms of graph and tables.

S. Ganeriwala (✉)
Spectra Quest Inc., Richmond, VA, USA
e-mail: suri@spectraquest.com

M. Allen et al. (eds.), *Special Topics in Structural Dynamics & Experimental Techniques, Volume 5*,
Conference Proceedings of the Society for Experimental Mechanics Series, https://doi.org/10.1007/978-3-031-37007-6_21

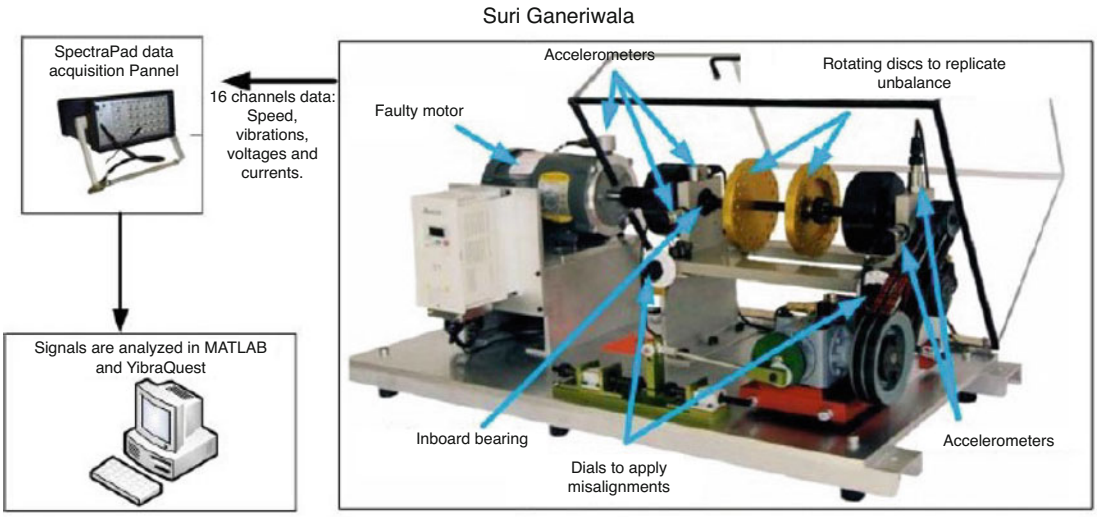

Fig. 21.1 Machinery fault simulator (MFS) and SpectraPad data acquisition system

Table 21.1 Experiment parameters and specifications

Parameter	Value	Parameter	Value
Induction Motor, Marathon	0.5 HP	Rolling element bearings	MB ER-10K
Number of rotor bars	34	Number of balls	9
Number of stator slots	24	Ball Dia. [mm]	7.94
Shaft diameter [in]	0.625	Outer race Dia. [mm]	31.38
Shaft length [in]	21	Inner race Dia. [mm]	47.26
Rotor bearings span [in]	14.1	Bearing pitch Dia. [mm]	39.32

21.2 Experimental Setup

Experiments were performed on a machinery fault simulator (MFS). MFS is a comprehensive testbed for rotating machinery experiments and for in-depth studies of the most common machinery faults. MFS consists of an induction motor coupled to the main shaft supported by two rolling element bearings (Fig. 21.1). Table 21.1 shows the specification of the MFS.

Vibrations of the motor, inboard bearing, and outboard bearing were measured. Shaft speed was measured with tachometer. Voltages and currents were measured with the V/I transducer made by Spectra Quest. For each fault, machine started up from rest and reached steady state and 16 channels of data were acquired simultaneously using the SpectraPad DAQ board at a sampling rate of 5120 Hz (Table 21.2).

21.3 Results and Discussion

21.3.1 Rolling Element Bearing Faults

Bearing faults (ORF, IRF, BF) were introduced at the inboard bearing. Vibration and currents signals were measured for each case and results are presented here. For comparison in time domain, Kurtosis value of the bearing vibration in vertical direction, k, and RMS of the current in steady state, I_{ss}, are calculated and presented in Table 21.3. For frequency analysis, fault components should be calculated. The induction motor with two poles and line frequency of 60 Hz has the synchronous speed of $f_s = 60$ (Hz). Bearing multipliers, M, running speed and bearing frequency components, $M.f_r$, are obtained for each case and shown in Table 21.3.

Kurtosis values, a measure of the 'peakedness' of the vibration data, and motor currents are plotted in Fig. 21.2 for each fault. Bearing faults generate periodic impacts in bearings which increase Kurtosis values. Also, as shown in Fig. 21.2, motor

Table 21.2 Experiments design

Faults	Description	16 Channels
Rolling element bearing faults	Inner Race Fault (IRF) Outer Race Faults (ORF) Ball Faults (BF) Combined Faults (CF)	Tachometer Acceleration of motor, vertical Acceleration of motor, horizontal Acceleration of inboard bearing, vertical Acceleration of inboard bearing, horizontal Acceleration of outboard bearing, vertical Acceleration of outboard bearing, horizontal Acceleration of gearbox, axial Acceleration of gearbox, vertical Acceleration of gearbox, horizontal Currents (3 phase) Voltages (3 phase)
Airgap eccentricity faults	Level I: 25% Level II: 50% Level III: 75% Level IV: 100%	
Mechanical imbalance	Static imbalance Coupled imbalance	
Broken rotor bars	3 broken bars, load 0.5 lb-in 3 broken bars, load 10 lb-in 6 broken bars, load 0.5 lb-in 6 broken bars, load 10 lb-in	

Table 21.3 Effect of bearing faults on motor current

	f_r [Hz]	M	$M.f_r$ [Hz]	K	I_{ss} [A]
Baseline	59.626	–	–	2.90	1.881132
ORF	59.609	3.052	181.92	3.31	1.893456
IRF	59.571	4.948	294.76	6.19	1.904126
BF	59.602	3.984	237.45	8.71	1.906715

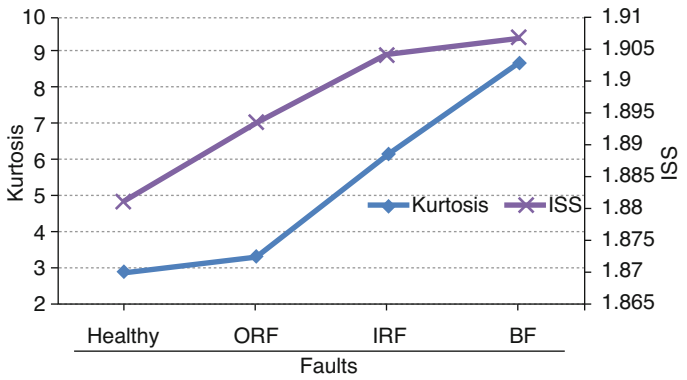

Fig. 21.2 Bearing faults increase both vibration Kurtosis and motor startup currents

currents are slightly increased with presence of faults. Figure 21.3 shows bearing vibrations for different faults. Increase in the level of vibration due to bearing faults is clearly observed.

Frequency spectra of bearing vibrations (Fig. 21.4a) reveal fundamental frequencies for each fault. However, changes in motor current signals due to bearing fault are not as clear as changes in vibration signals. Bearing faults can affect motor currents either by changing the rotational load or changing the airgap. Changes in rotational load due to faults are very small, compared to the total load. Also, the effect of bearing faults on motor airgap is very small since these bearings are not motor bearings.

In the current spectrum, sidebands of line frequency around center frequency harmonics of $M.f_r$ are expected. Figure 21.4b plots frequency spectrum of motor currents for different faults. Line frequency harmonics are clearly observed through the spectrum. However, the fault components, f_{bg}, are not clear. For few cases, sidebands of 60 Hz are observed around center frequency harmonics of $M.f_r$ which are highlighted in Fig. 21.4.

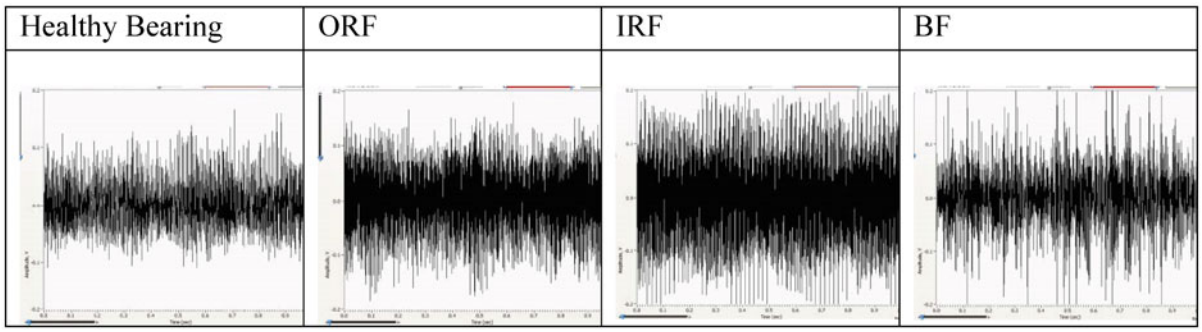

Fig. 21.3 Bearing vibrations due to bearing faults

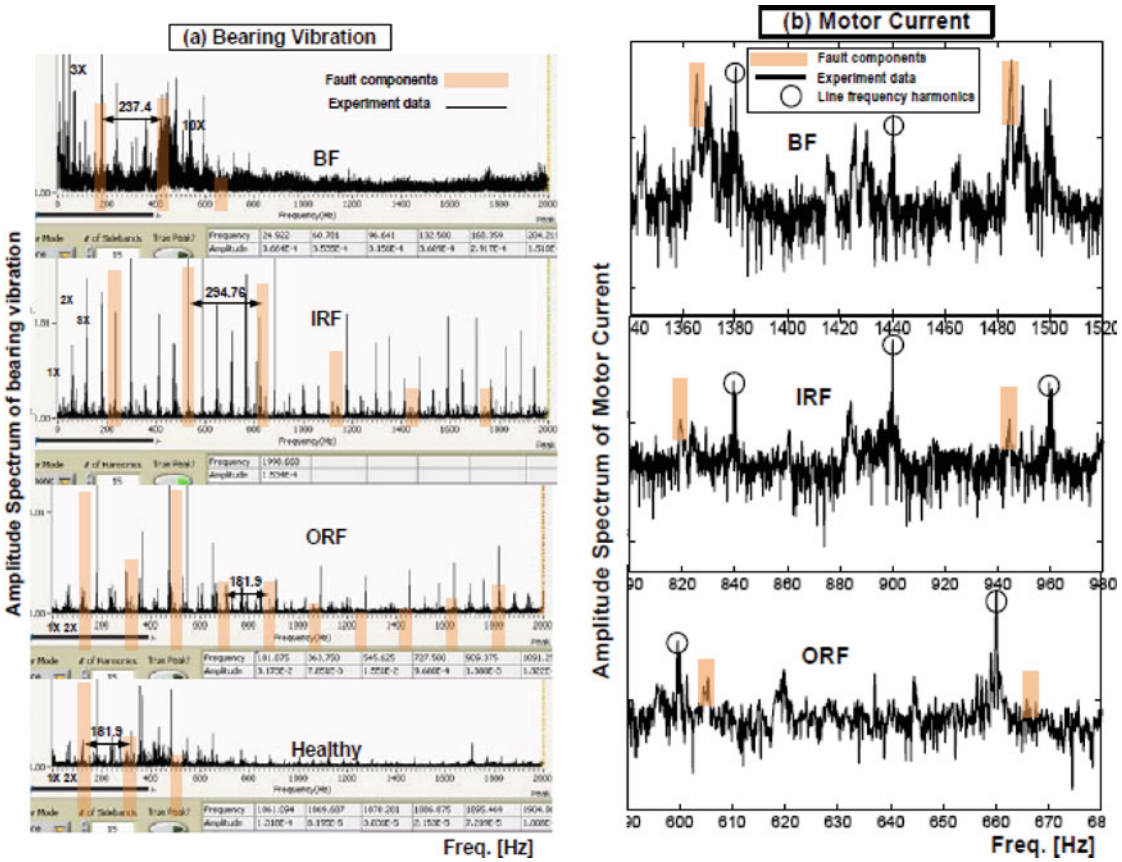

Fig. 21.4 Frequency spectrum of vibration signals (**a**), and frequency spectrum of motor currents (**b**) for different bearing faults

21.3.2 Motor with Airgap Eccentric Rotor

Table 21.4 shows motor running speed, slip speed, rms values of motor vibration, rising time, and motor current values as obtained from experiments with different levels of motor static eccentricity. These results are plotted in Fig. 21.5. As the severity of eccentricity increases, motor slip and motor vibration increase. However, bearing vibration levels are not increased much compared to the motor vibration. This effect can be used in can be used for the fault isolation. Also, eccentricity faults in induction motors increase motor rising time as well as motor running currents as shown in Fig. 21.6.

Figure 21.6 plots frequency spectrum of motor currents for different severity levels of eccentricity faults. The sidebands of $\pm vf_1$ around center frequency of $R.f_r$ in motor current spectrum are expected for faulty motor. These sidebands are clearly observed in the spectrum as fault components. However, the magnitude of fault components is not affected by the fault, and even in the healthy case, the fault components are observed. Therefore, the results of this study cannot validate expected fault components in motor current spectrum.

Table 21.4 Effect of static rotor eccentricity faults on motor parameters

	f_r [Hz]	S [Hz]	Motor Vibration, RMS	I_{max} [A]	T_r [sec]	I_{ss} [A]
Baseline	58.95	1.047	0.069	5.66	2.05	2.64
Eccentric rotor, Level I	58.99	1.006	0.068	5.73	2.08	2.60
Eccentric rotor, Level II	59.00	1.000	0.070	5.55	2.15	2.59
Eccentric rotor, Level III	58.89	1.114	0.072	5.59	2.33	2.67
Eccentric rotor, Level IV	58.27	1.726	0.163	5.55	2.43	3.07

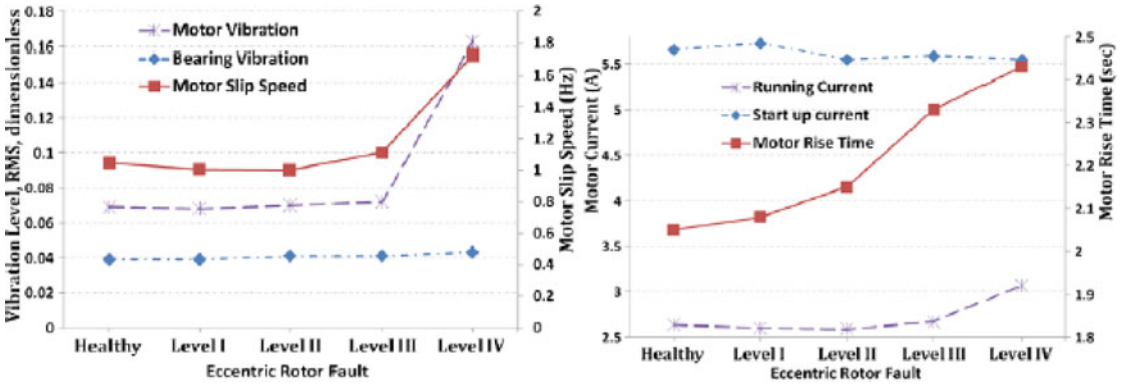

Fig. 21.5 Effect of eccentricity on vibration and motor slip speed

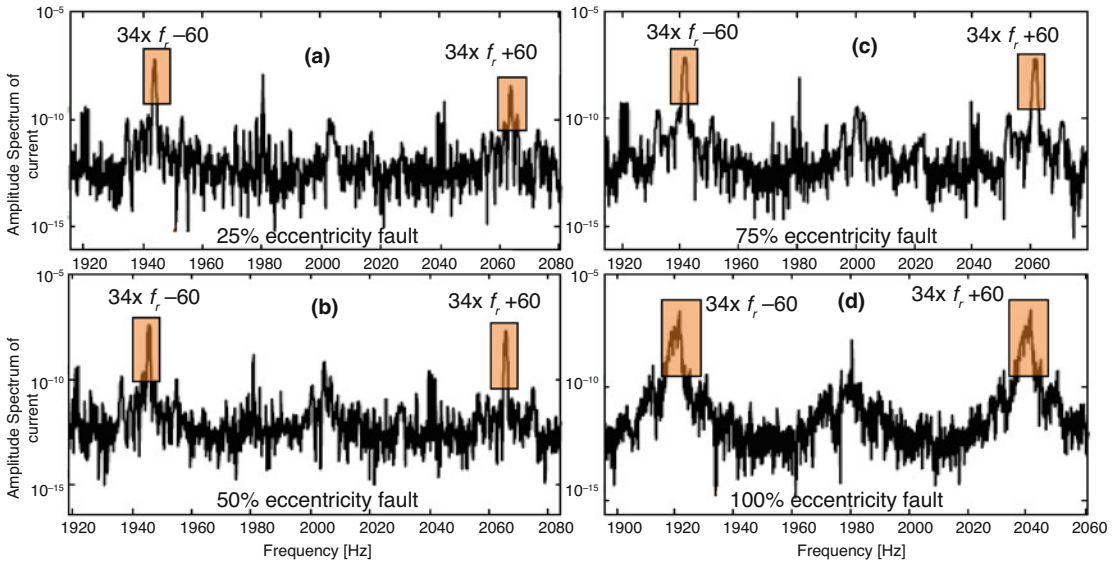

Fig. 21.6 Current spectrum of motor with eccentricity faults. (**a**) 25% eccentricity, (**b**) 50% eccentricity, (**c**) 75% eccentricity, (**d**) 100% eccentricity

21.3.3 Mechanical Imbalance

The effect of mechanical imbalance on the machine vibration is very strong and significant. The level of vibration is increased in unbalanced machine as shown in Fig. 21.7a, the slip speed of the motor is increased as shown in Fig. 21.7, and 1X frequency component of vibration is significantly increased as shown in Fig. 21.7c.

As described before, mechanical imbalance can cause lateral movement of the shaft or bending of the rotor of the motor (Fig. 21.8). In the case of bending, mechanical imbalance is treated as dynamic eccentricity faults in MCSA, and fault components are expected in current spectrum. Figure 21.9a plots frequency spectrum of the motor current I1, and three portions of the spectrum containing fault components are zoomed in Fig. 21.9b–d. Also, each plot is overlaid with baseline

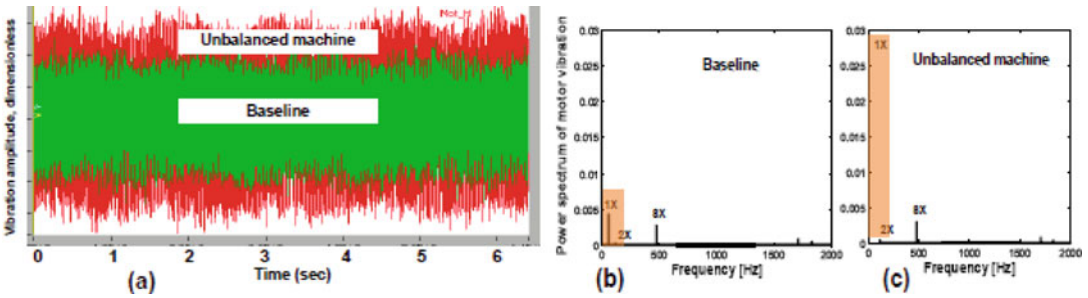

Fig. 21.7 Effect of rotor imbalance on motor vibration (**a**) vibration time signals: baseline vs. imbalance, (**b**) spectrum: baseline, (**c**) spectrum: unbalanced machine

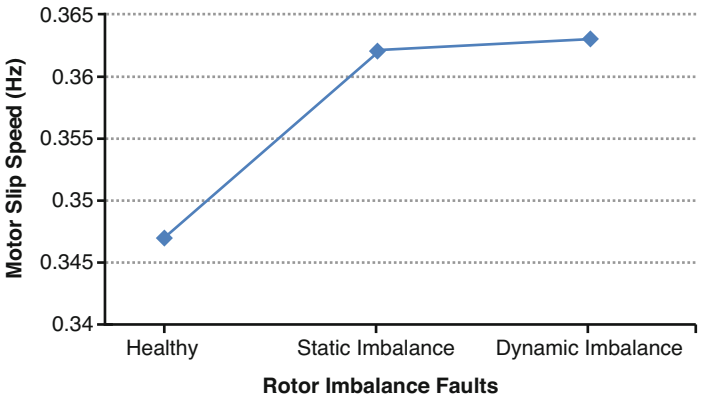

Fig. 21.8 Motor slip is slightly increased when rotor imbalance is introduced

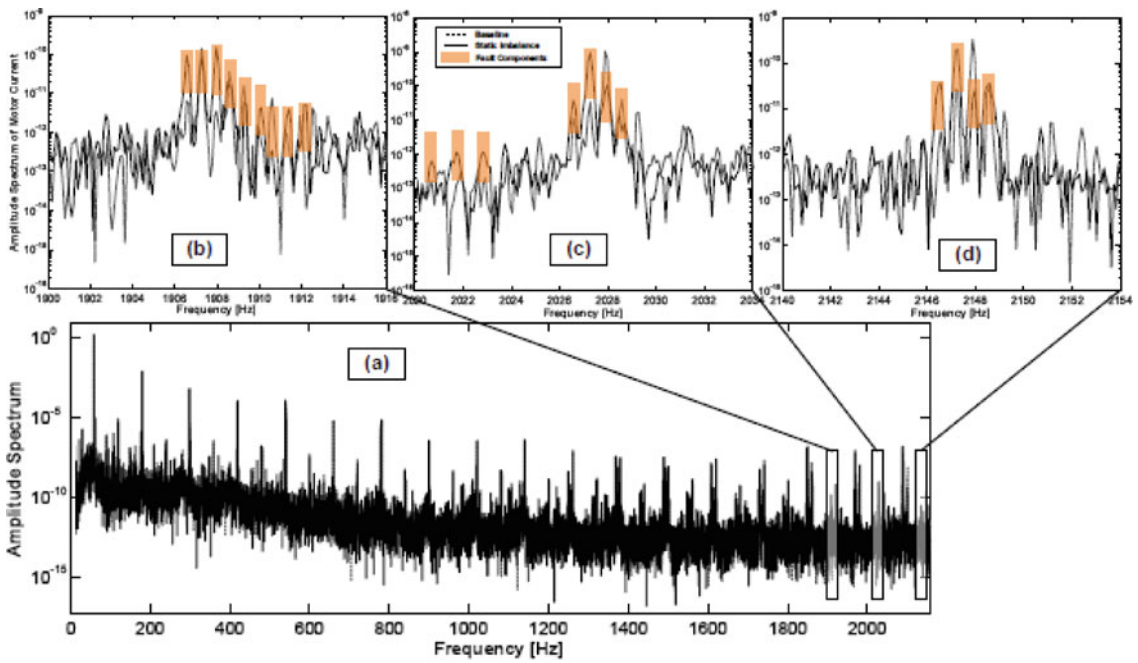

Fig. 21.9 Frequency spectrum of motor current I1 for healthy motor and motor with mechanical imbalance faults. (**b**), (**c**), and (**d**) are magnified portions of the plot (**a**)

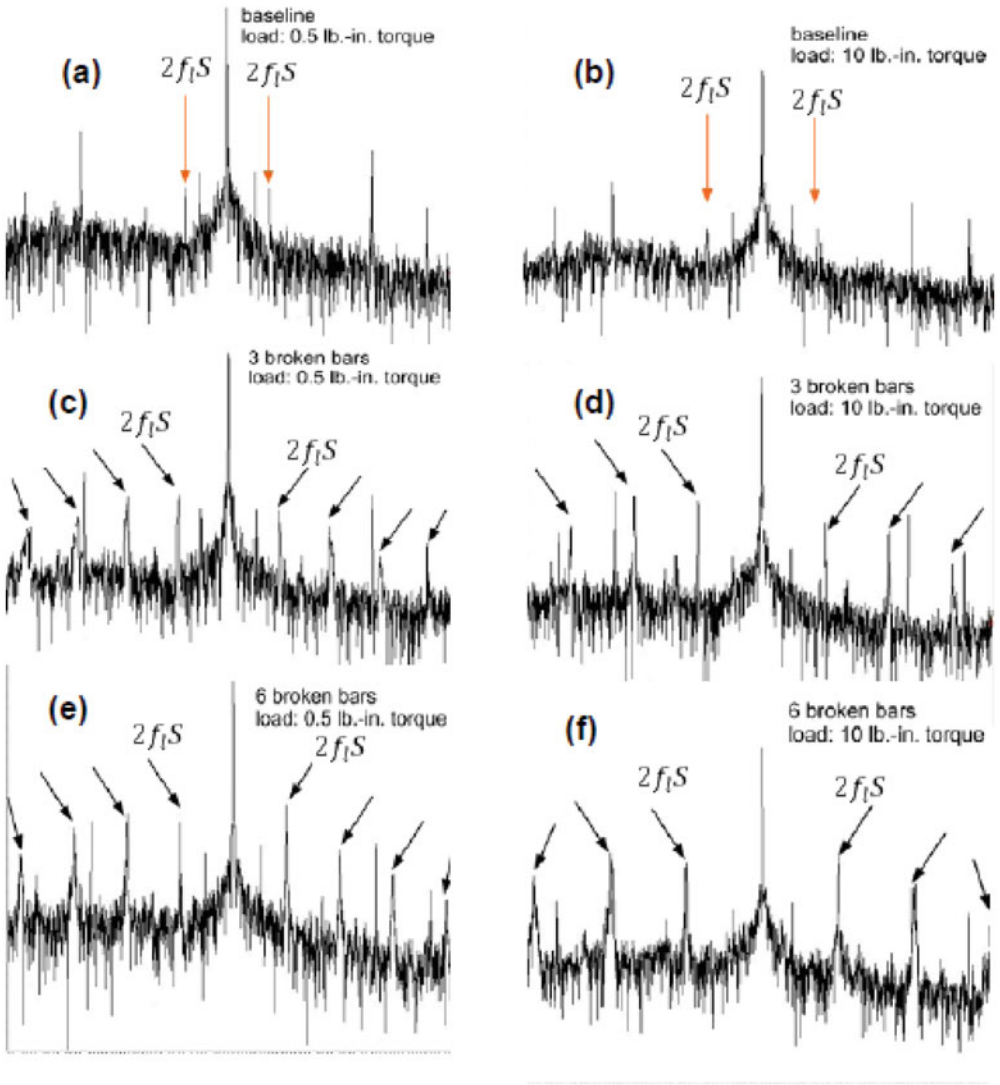

Fig. 21.10 Current spectrum of (**a**) healthy motor under load of 0.5 lb-in, (**b**) healthy motor under load of 10 lb-in, (**c**) motor with three broken rotor bars under load of 0.5 lb-in, (**d**) motor with three broken rotor bars under load of 10 lb-in, (**e**) motor with six broken rotor bars under load of 0.5 lb-in, and (**f**) motor with six broken rotor bars under load of 10 lb-in

plots for the comparison. Fault components are slightly increased with introducing the faults. However, these components are observed even in the baseline spectrum showing the presence of dynamic eccentricity in the healthy motor.

21.3.4 Motor with Broken Rotor Bar

Broken rotor bar experiments were conducted for three cases (1) healthy motor, (2) motor with three broken bars, and (3) motor with 6 broken bars. From the line frequency, which was set to 35 Hz, and tachometer readings, slip speed was obtained for each case. To investigate the effect of load on current signatures, load was increased in two levels of 0.5 lb-in and 10 lb-in using a torque loader connected to the output gear shaft.

Diagnosis of broken rotor bars requires detection of twice slip frequency bands around the supply frequency component. Figure 21.10 plots power spectrum of motor currents for different load and fault conditions. As noticed in Fig. 21.10a, b, the twice slip frequency sidebands appear even in the case of a healthy motor. However, there are no clear harmonics of twice slip sidebands. In case of broken bar faults, the amplitude of the twice slip sidebands increases with the number of

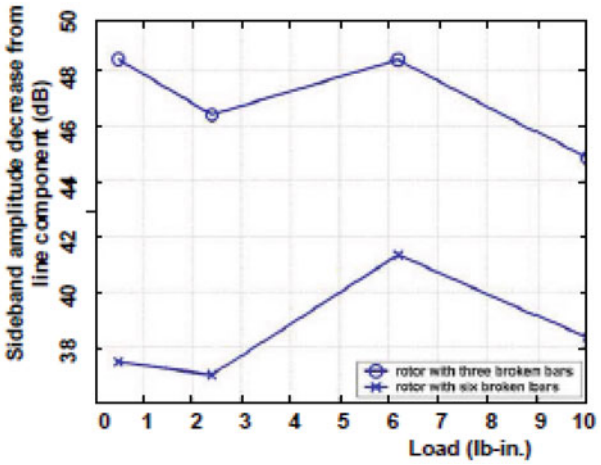

Fig. 21.11 Effect of load on amplitude decrease between slip sideband and line frequency

broken bars. Load increases motor slip and the sideband values of $2sf_1$ as shown in Fig. 21.10. However, the effect of load on amplitude spectrum for the load range tested here is difficult to trend (Fig. 21.11).

References

1. El Hachemi benbouzid, M.: A review of induction motors signature analysis as a medium for faults detection. IEEE Trans. Ind. Electron. **47**(5), 984–993 (2000)
2. Nandi, S., Toliyat, H.A., Li, X.: Condition monitoring and fault diagnosis of electrical motors –a review. IEEE Trans. Energy Convers. **20**(4), 719 (2005)
3. Nakhaeinejad, M., Bryant, M.D.: Measurements of faulty and healthy rolling element bearings. In: ASME/STLE International Joint Tribology Conference, Memphis, TN, 2009
4. Penrose, H.W.: Practical motor current signature analysis taking the mystery out of MCSA. In: All-Test Pro Inc. Tech Note, Saybrook, CT
5. Schlensok, C., van Riesen, D., Hameyer, K.: Structure-dynamic analysis of an induction machine with eccentric rotor movement. In: 17th International Conference on Electrical Machines, ICEM (2006)
6. Panadero, R.P., Llinares, J.P., Alarcony, V.C., Sánchez, M.P.: Review of diagnosis methods of induction electrical machines based on steady state current
7. Thomson, W.T.: Keep motors turning via motor current signature analysis. In: IMC-2003, the 18th International Maintenance Conference, Clearwater, FL
8. Thomson, W.T.: On-line MCSA to diagnose shorted turns in low voltage stator windings of 3-phase induction motors prior to failure. In: Proceedings of IEEE Conference on Electrical Machines and Drives (IEMDC), Boston, 2001
9. Thomson, W.T.: A review of on-line condition monitoring techniques for three-phase squirrel-cage induction motors - past, present, and future. In: IEEE Symposium on Diagnostics for Electrical Machines, Power Electronics and Drives, pp. 3–18, Gijon (1999) (opening keynote address)
10. Thomson, W.T., Frenger, M.: Current signature analysis to detect induction motor faults. IEEE Ind. Appl. Mag. **7**, 26 (2001)
11. Spectra Quest Tech Note: Diagnostics of induction motor with broken bars using motor current signature analysis (MCSA), January 2006

Chapter 22
Application of Synchronous Averaging for Detecting Defects of a Gearbox

Suri Ganeriwala

Abstract Condition monitoring of gearboxes in industrial settings is often based on trending vibration levels at gearmesh frequencies and sideband frequencies associated with matting shaft rotational speeds. However, it is debated on the vibration levels for setting different alarms related to the gearbox health. Another issue of controversy is what an indicator of fault severity; is it energy in gearmesh frequencies or the energies in sidebands . In this work, we analyzed vibration signature caused by gear tooth seeded faults of different levels. The data are analyzed in both time and frequency domains. The experimental study is conducted on a Machinery Fault Simulator ™ (MFS). The pinion gear in the gearbox is intentionally faulted with increasing severities, and vibration signal was collected for each case using IEPE accelerometers. Data are also obtained using a high-resolution encoder. Signals are analyzed using time synchronous averaging and traditional spectrum analysis. The results indicate that the vibration signature of a faulted bevel gear tooth is a pulse in time domain. Because of this impulse signal, strong sidebands arise in the spectrum around the mesh frequency. And the energy inside bands are better indicator of tooth defect severity.

Keywords Gearbox · Time Synchronous Averaging · Spectra · Gearmesh · Side bands

22.1 Introduction

Gearboxes are very commonly used in industry as well as in vehicles for transferring motion and power from shaft to another shaft. During their extended service lifetimes, gear teeth will inevitably be worn, chipped, or even missing under high load. Therefore, effective diagnostic methods are required in order to enhance the reliability of the entire machine before any unexpected catastrophic consequences occur. The vibration-based techniques are the most widely used since it is easy to obtain the acceleration signals using accelerometers. The gear diagnostic parameters include RMS value, crest factor, kurtosis, energy ratio, and other metrics [1]. They are all statistical methods. Standard vibration analysis is based traditional spectral analysis examining gearmesh frequencies and associated shaft speed-related sidebands.

Typically, the data are averaged using RPM averaging technique [2–4]. The RPM averaging smooth the variation about the mean but mean stays the same. Once a gearbox wears, its noise floor goes up. This makes it difficult to analyze the defects and its severity. In this work, we used time synchronous averaging to study the gearbox faults and the degradation. It is observed that when a faulted bevel gear tooth enters meshing, it produces an impulse-like signal in the time domain and the amplitude of the impulse increase with the damage. In the frequency domain, the amplitudes of pinion sidebands also increase with the severity level.

S. Ganeriwala (✉)
Spectra Quest Inc., Richmond, VA, USA
e-mail: suri@spectraquest.com

M. Allen et al. (eds.), *Special Topics in Structural Dynamics & Experimental Techniques, Volume 5*,
Conference Proceedings of the Society for Experimental Mechanics Series, https://doi.org/10.1007/978-3-031-37007-6_22

22.2 Test Setup

The experiment is conducted on a Machinery Fault Simulator ™ (MFS). The MFS and the position of the gearbox in the MFS are illustrated in Fig. 22.1.

The gearbox details are shown in Fig. 22.2a. The transmission ratio is 1.5:1. There are two straight bevel gears in the gearbox and they are shown in Fig. 22.2b. The number of teeth on the pinion is 18. The gearbox input shaft is connected to a sheave and driven by a V belt drive. The gearbox output shaft is connected with a variable brake loader. Torsional loading is applied to the gearbox using a magnetic particle brake. This is driven by a double belt drive connected to the motor shaft. The speed ratio of 2.56 was configured as a reducer. Belt tension can be adjusted using dowel tell mechanism or by pushing the lower part of the belts with a turnbuckle system. The tachometer is installed on the rotor deck with a bracket and used to measure the speed of the belt sheave connected with gearbox input shaft as illustrated in Fig. 22.3.

The vibration data were collected by a tri-axial accelerometer installed on the top of the gearbox. The accelerometer is also shown in Fig. 22.3. The frequency limit is set to 5 KHz in the data acquisition. During the test, the motor speed was kept at 1000 RPM and the brake loader was set to 2.5. First, the baseline gearbox vibration data are collected. Then, the gearbox is disassembled, and the pinion gear is taken out. The surface of a pinion tooth on the meshing side is milled with a drill mill. After the damage is done, the pinion gear is put back into the gearbox. Vibration data are collected again with all the other running conditions kept the same (speed and load). The data were processed using traditional RMP averaging and time synchronous averaging.

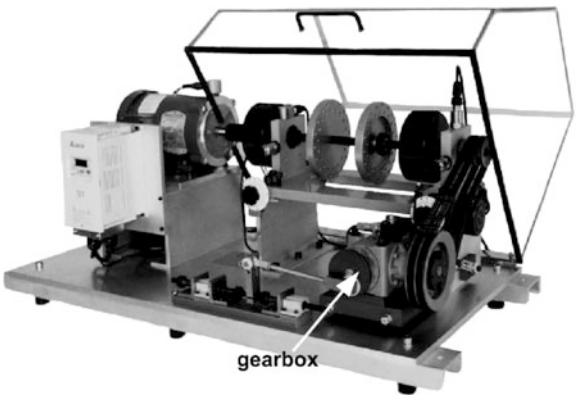

Fig. 22.1 Machinery fault simulator and gearbox in MFS

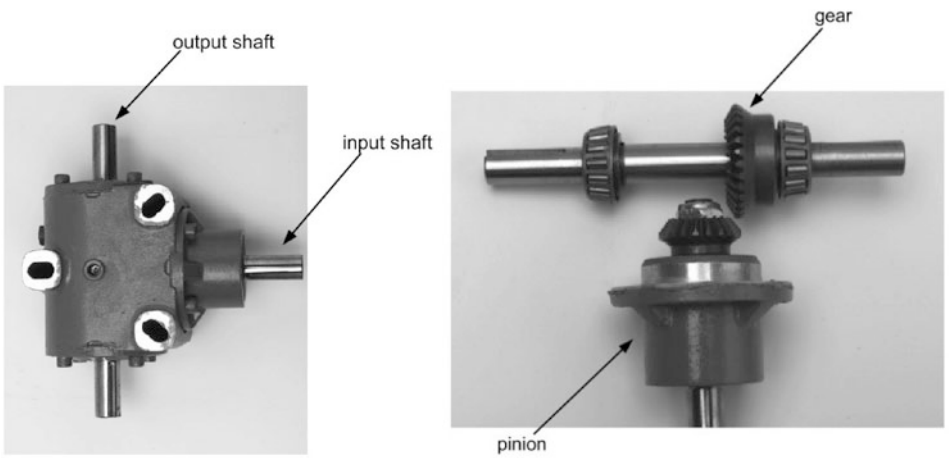

Fig. 22.2 Gearbox. (**a**) Gearbox. (**b**) Pinion and gear

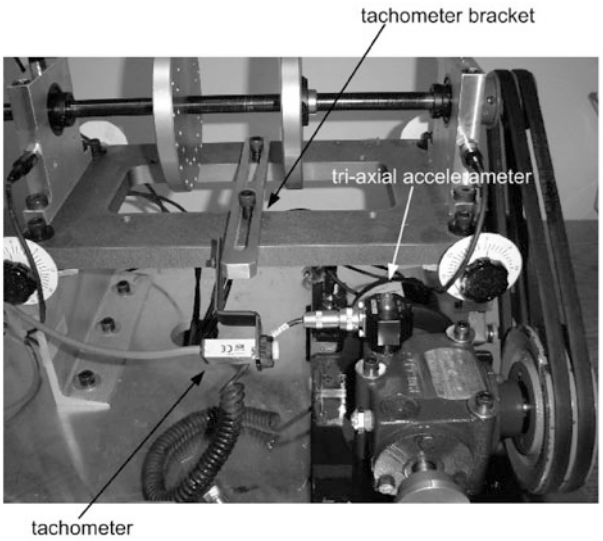

Fig. 22.3 Installation of tachometer on the gearbox

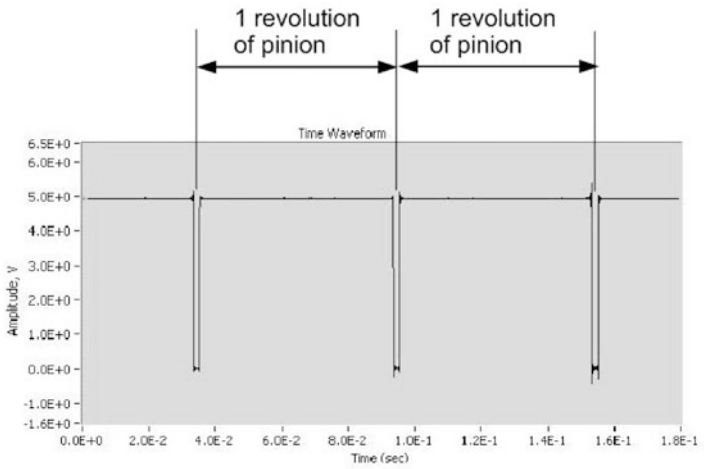

Fig. 22.4 Baseline signals in time domain

22.3 Test Results

22.3.1 Time Domain

The baseline waveforms illustrated in Fig. 22.4a, b are the tachometer signal and gearbox acceleration in the axial direction, respectively. The time between two successive pulses in the tachometer signal is the rotation period of the pinion. The time scales on these two figures show the identical time range.

The waveform for damaged pinion is illustrated in Fig. 22.5. Comparing of Fig. 22.5 with Fig. 22.4b, it can be noticed that there are impulses appearing in Fig. 22.5.

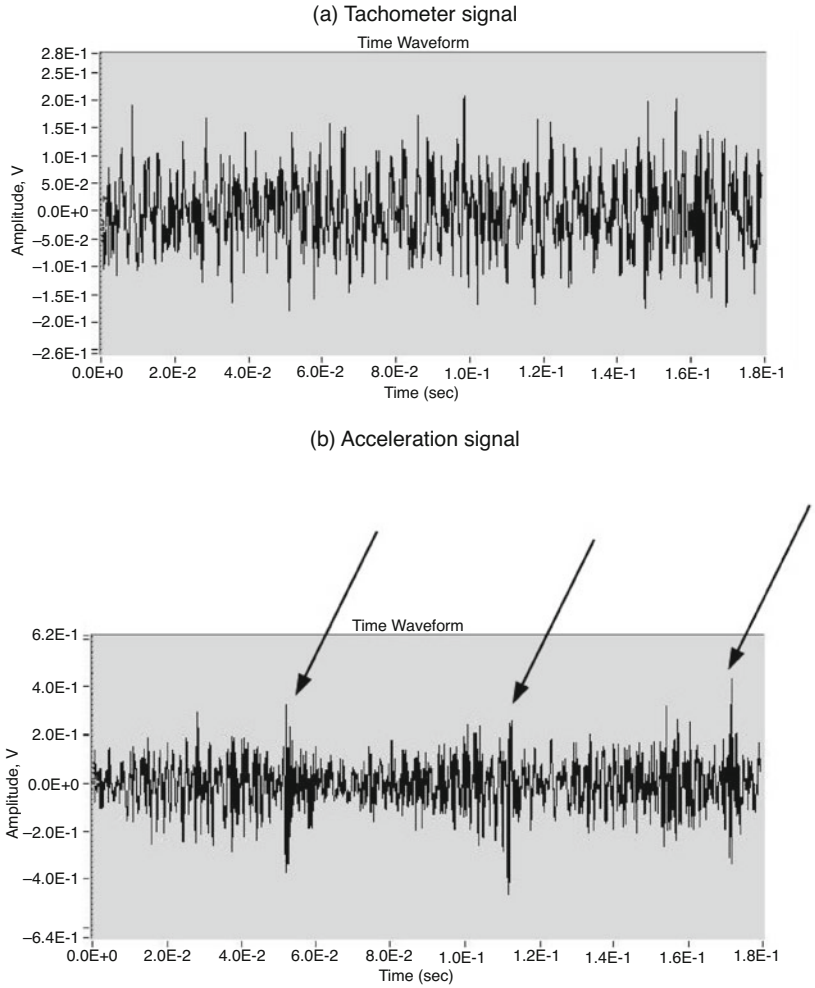

Fig. 22.5 Time acceleration signal Signals of damage pinion. (**a**) Tachometer signal. (**b**) Acceleration signal

22.3.2 Frequency Domain

The spectrum of the baseline vibration data is illustrated in Fig. 22.6. Figure 22.6a is the spectrum in the baseband spectrum, and Fig. 22.6b is the spectrum around the mesh frequency with frequency range from 250 to 350 Hz (the mesh frequency is around 300 Hz, 1000 RPM/60*18 = 300 Hz). The mesh frequency and its harmonics are illustrated clearly in Fig. 22.6b. Figure 22.6b reveals that there is pinion rotation modulation sideband around mesh frequency component. However, the sideband is not dominant [2].

The spectrum for worn gearbox with RMS spectral average is shown in Fig. 22.7 and that with time synchronous averaging about motor tachometer is illustrated in Fig. 22.8. The spectrum data in Fig. 22.7 are caused by random vibration due to gears and bearing looseness and wear resulting in raised floor. The spectrum in Fig. 22.8 is time synchronously averaged about the gearbox tachometer. This operation brings mean down and enhances spectral peaks associated the Gearmesh frequency and side bands [4, 5]. Figure 22.9 shows time synchronously averaged about the motor shaft tachometer [2]. Since belt drive ration is non-integer multiple of the input shaft, the spectra associated with gearbox is averaged out when time synchronous averaging performed about the motor shaft.

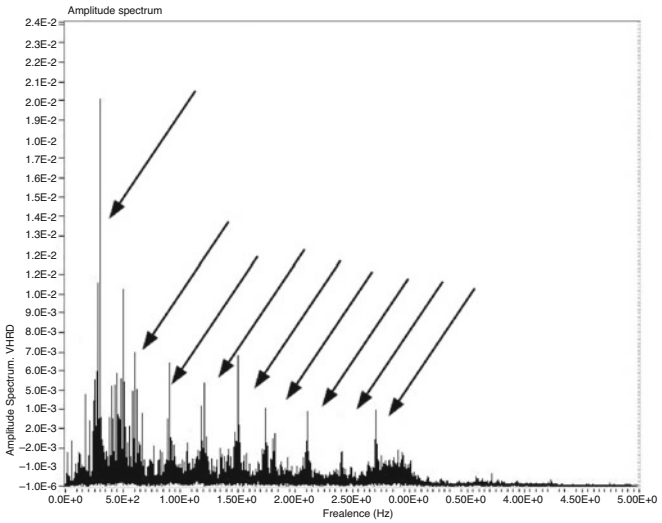

Fig. 22.6 Baseline vibration signal spectrum

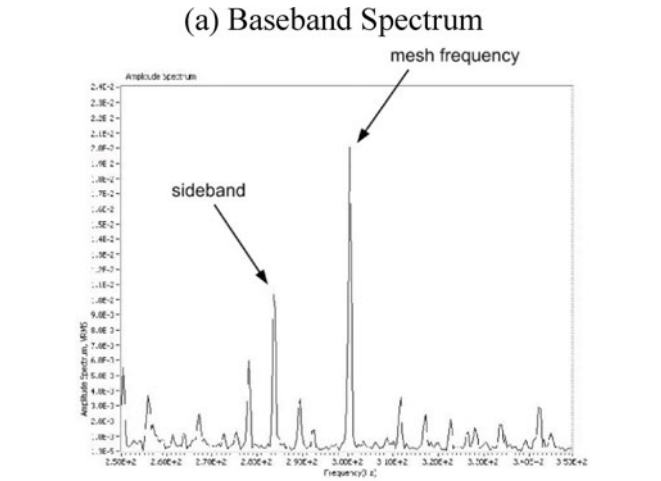

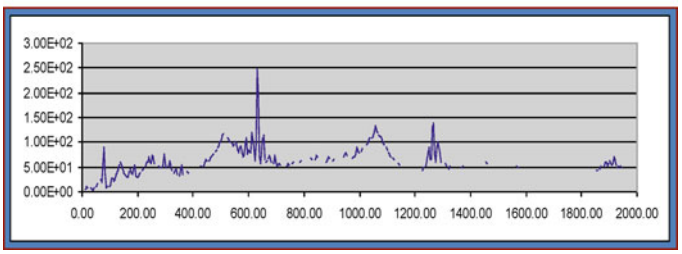

Fig. 22.7 Vibration signal spectrum of a worn gearbox with RMS spectral averaging. (**a**) Baseband spectrum. (**b**) Spectrum around mesh frequency component

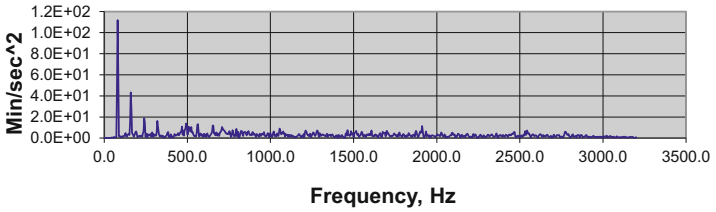

Fig. 22.8 Vibration signal spectrum of a worn gearbox with time synchronous averaging about the motor shaft tachometer

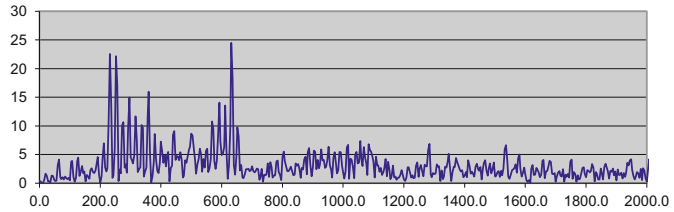

Fig. 22.9 Vibration signal spectrum of a worn gearbox with time synchronous averaging about the gearbox tachometer

22.4 Summary and Remarks

In this test, vibration signature caused by bevel gear tooth seeded fault is studied in the time and frequency domains. The pinion gear in the gearbox is intentionally faulted with increasing severities and vibration signal is collected for each case. The signal is analyzed in time and frequency domain. Frequency domain was analyzed using conventional RMS and time synchronous averaging about motor shaft and the gearbox shaft, respectively. Time synchronous averaging clearly shows Gearmesh frequency and gear/pinion-associated side bands. The results clearly illustrate the advantage of using two tachometers for in-depth analysis of gear damage. When a faulted bevel gear tooth enters meshing, it creates an impact pulse in the time domain vibration signal. The amplitude of impulse increases with damage.

References

1. http://mfpt.org/Archive%20Old%20Pages/mfpt_geardiagnosticparam.html
2. Analyzing gearbox degradation using time-frequency signature analysis, Spectra Quest Tech Note, March 2006
3. “Vibration signal analysis of fan rotors”, Spectra Quest Tech Note, March 2007
4. Randall, R.B., Sawalhi, N., Coats, M.: A comparison of methods for separation of deterministic and random signals. Int. J. Condit. Monit. **1**(1), 11–19 (2011)
5. McFadden, P.D., Smith, J.D.: An explanation for the asymmetry of the modulation sidebands about the tooth meshing frequency in epicyclic gear vibration. Proc. Institut. Mech. Eng. **199**(C1), 65–70 (1985)

Chapter 23
A Time-Variant/Invariant Equivalence for the Transient Response of Rotor Blades in Resonance Crossing

Vincent Denoël and Luigi Carassale

Abstract The transient response of a time-varying oscillator under a chirp loading is considered in this paper. It is assumed that the natural frequency of the system changes with time during sweeping. Numerical simulations indicate that the maximum response amplitude and the apparent damping ratio are both higher than in the case without time-varying natural frequency. These two specificities of the time-varying problem are caused by the prolongated locking of the excitation frequency to the natural frequency. An asymptotic solution of the problem is derived and demonstrates that, at leading order, the time variant system responds like a time invariant system subjected to another sine sweep, having a slightly lower frequency rate. This suggests a simple equivalence. Previous studies of the time invariant problem indicate that a decrease in the sweeping rate results in increased amplification and apparent damping. This shows that the proposed equivalence is able to capture the main feature of the transient response of the time variant problem.

Keywords Resonance crossing · Transient · Dynamic amplification · Rotating machinery · Perturbation

23.1 Introduction

Resonance crossings are important features in the dynamic response of rotor components. They happen when a multiple of the rotation frequency of the rotor momentarily matches a natural frequency (or a family of natural frequencies) of the rotor assembly during the machine run-up or run-down. On the one hand, the transient response due to resonance crossing is a concern for designers as it may induce high-cycle fatigue, e.g., [1]. On the other hand, it is often exploited for system identification purpose during validation and monitoring activities, e.g., [2]. When rotor components are flexible like for the case of blades in turbomachinery, their geometric stiffness induced by the centrifugal force can be comparable with their elastic stiffness, making the natural frequencies changing with the rotor speed and therefore with time. In these conditions, the rotor components behave as Linear Time-Varying (LTV) systems, e.g., [3]. In this paper, we show that it is possible to treat the LTV problem as an equivalent Linear Time Invariant (LTI) system subject to a modified rotor acceleration. This result can be employed, on the design side, to simplify calculations, but it may be even more useful on the identification side as it provides an analytic response to be used in data fitting.

23.2 Mathematical Model

We consider a rotor disk of a turbomachinery having a resonance crossing the Engine Order (EO) r at the time t_0 with a vibration mode whose circular frequency is ω_0. In the neighborhood of this resonance crossing, the rotor speed is $\Omega(t)$ and its acceleration is $\dot{\Omega}$, while the natural frequency is $\omega(t)$ and its time derivative is $\dot{\omega}$. Assuming that the considered mode is isolated, the equation of motion of its generalized coordinate can be written in the form

V. Denoël
Structural & Stochastic Dynamics, University of Liège, Liège, Belgium
e-mail: v.denoel@uliege.be

L. Carassale (✉)
Department of Mechanical Engineering, University of Genova, Genova, Italy
e-mail: luigi.carassale@unige.it

M. Allen et al. (eds.), *Special Topics in Structural Dynamics & Experimental Techniques, Volume 5*,
Conference Proceedings of the Society for Experimental Mechanics Series, https://doi.org/10.1007/978-3-031-37007-6_23

$$\ddot{q} + 2\xi\omega(t)\,\dot{q} + \omega^2(t)\,q = \frac{p_0}{m}\,\mathrm{e}^{\frac{\mathrm{i}}{2}r\dot{\Omega}t^2} \tag{23.1}$$

where m is the generalized mass, ξ the viscous damping ratio, p_0 the force amplitude assumed as a constant, and i the imaginary unit. In large rotating machinery, the rotor acceleration $\dot{\Omega}$ and rate of variation of the natural frequency $\dot{\omega}$ change slowly with time (in terms that needs to be specified); thus, to obtain an analytic formulation valid in the neighborhood of a resonance crossing, we assume $\dot{\Omega} = const$ and $\dot{\omega} = const$. Considering a single resonance, this assumption can be extended everywhere, i.e.,

$$\Omega(t) = \dot{\Omega}t \quad ; \quad \omega(t) = \omega_0 + \dot{\omega}(t - t_0) \tag{23.2}$$

Assuming the rotor at rest at $t = 0$, the time of the resonance crossing t_0 is given as $t_0 = \omega_0/r\dot{\Omega}$. For calculation purpose, it is convenient to introduce a shifted time t' such that the resonance crossing appears at $t' = 0$. With this substitution Eq. (23.1) becomes

$$\ddot{q} + 2\xi\left(\omega_0 + \dot{\omega}t'\right)\dot{q} + \left(\omega_0 + \dot{\omega}t'\right)^2 q = \frac{p_0}{m}\,\mathrm{e}^{\frac{\mathrm{i}}{2}r\dot{\Omega}t'^2}\,\mathrm{e}^{\mathrm{i}r\dot{\Omega}t_0t'}\,\mathrm{e}^{\frac{\mathrm{i}}{2}r\dot{\Omega}t_0^2} \tag{23.3}$$

A dimensionless version of the governing equation is obtained by introducing the dimensionless time $\tau = \omega_0 t'$ and nondimensional response

$$q\left[t(\tau)\right] = \frac{p_0}{2\,\varepsilon\,\mathrm{i}\,m\,\omega_0^2}q(\tau) \tag{23.4}$$

where the small parameter $\varepsilon = \xi$ is introduced for the subsequent perturbation analysis. After substitutions and simplifications, the governing equation yields

$$x'' + 2\left(1 + \kappa\,\alpha\varepsilon^2\tau\right)\varepsilon x' + \left(1 + \kappa\,\alpha\varepsilon^2\tau\right)^2 x = 2\,\varepsilon\,\mathrm{i}\,\mathrm{e}^{\mathrm{i}\tau}\mathrm{e}^{\frac{\mathrm{i}}{2}\kappa\,\varepsilon^2\tau^2}\mathrm{e}^{\mathrm{i}\Phi_0} \tag{23.5}$$

where the symbol $\cdot'$ represents the derivative respect to τ, $\Phi_0 = \omega_0 t_0$ is a constant phase angle, while κ and α are nondimensional parameters representing, respectively, the rotor acceleration and the rate of increment of the natural frequency. The choice of a proper definition for this parameter is not straightforward and is based on the solution of the time-invariant problem studied in [4].

$$\kappa = \frac{\dot{\Omega}}{\xi^2\omega_0^2} \quad ; \quad \alpha = \frac{\dot{\omega}}{\dot{\Omega}} \tag{23.6}$$

According to this definition, the parameter κ indicates whether or not the rotor acceleration is large enough to trigger transient effects (i.e., transient effects are negligible if $\kappa \ll 1$ [4]). The parameter α indicates the sensitivity of the natural frequency respect to the rotor speed. In practice, α may be considered as bounded in the range $[0, 1)$. The value $\alpha = 0$ represents the case of time invariant system, while slightly negative values are possible, but are rare for rotor blades.

23.3 Multiple Scales Solution of the Problem

The time invariant problem ($\alpha = 0$) has already been solved with a multiple scales technique [4]. It is based on recognizing the existence of a slow timescale $T = \varepsilon\tau$ and a fast timescale τ. It is possible to show that the response reads, at leading order for small ε, $x = A(\varepsilon\tau)\mathrm{e}^{\mathrm{i}\tau}$, where the slow envelope $A(T)$ is the solution of $A'(T) + A(T) = \exp\left(\frac{\mathrm{i}}{2}\kappa T^2\right)$. It is therefore expressed by

$$A(T) = \int_{-\infty}^{T} \mathrm{e}^{\frac{\mathrm{i}}{2}\kappa s^2 - (T-s)}\mathrm{d}s = \mathrm{e}^{-T}\mathcal{D}(T;\kappa) \tag{23.7}$$

with $\mathcal{D}(T;\kappa) = \int_{-\infty}^{T} \mathrm{e}^{\frac{\mathrm{i}}{2}\kappa s^2+s}\mathrm{d}s = \sqrt{\frac{\mathrm{i}\pi}{2\kappa}}\mathrm{e}^{\frac{i}{2\kappa}}\mathrm{erfc}\left[\mathrm{e}^{-\mathrm{i}\frac{\pi}{4}}\frac{\mathrm{i}-\kappa T}{\sqrt{2\kappa}}\right]$. Although (23.7) does not admit a simple exact analytical solution, the time variant problem can be tackled with the same approach. Following the perturbation technique described in [4], it is possible to show that the leading order solution still is $x = A(\varepsilon\tau)\mathrm{e}^{\mathrm{i}\tau}$, but where $A(T)$ now satisfies

$$A'(T) + (1 - \mathrm{i}\kappa\,\alpha\,T)\,A(T) = \mathrm{e}^{\frac{\mathrm{i}}{2}\kappa T^2}. \tag{23.8}$$

This linear (slow) time variant problem admits the solution

$$A(T) = \mathrm{e}^{-T}\mathrm{e}^{\frac{\mathrm{i}}{2}\kappa\,\alpha T^2}\mathcal{D}\left(T;\hat{\kappa}\right). \tag{23.9}$$

where $\hat{\kappa} = \kappa\,(1-\alpha)$.

23.4 Discussion and Illustration

Equation (23.9) generalizes (23.7) to cases where $\alpha \neq 0$. The comparison of these two equations shows that the time-varying nature of the system manifests in two ways : (i) a change of phase in the envelope of the response, but this is not noticeable in terms of amplitude, since $\left|\mathrm{e}^{\frac{\mathrm{i}}{2}\kappa\,\alpha T^2}\right| = 1$; (ii) more importantly, a change of the second argument in $\mathcal{D}\left(T;\hat{\kappa}\right)$. But in terms of magnitude of the response envelope, this simple analytical solution demonstrates that, at leading order for small ε, the time variant problem with parameters κ and α has the same solution as a time invariant problem with an equivalent dimensionless rotor acceleration $\kappa\,(1-\alpha)$. In the time-varying problem, both the natural frequency and the rotor speed increase with time. As a result, they remain longer closer to each other, relatively speaking. This explains why the equivalent rotor acceleration is smaller than in the time-varying problem, $\hat{\kappa} \leq \kappa$.

Figure 23.1 illustrates these findings. Figure 23.1a is a simple graphical illustration of the equivalence principle. In particular, it illustrates that the equivalent (LTI) dimensionless rotor acceleration is always smaller than the actual one (LTV). Figure 23.1b shows the exact solution of the original problem with the numerical values reported in the figure caption. It compares the exact solution (in blue) to the solution that would have been obtained by neglecting $\dot{\omega}$ (in gray) and to the solution of the equivalent problem with reduced rotor acceleration ($\dot{\Omega}_{\text{equiv}} = \dot{\Omega}\,(1-\alpha) = 1.1\,\text{rad/s}^2$). The time shift introduced in Sect. 23.1 makes it such that resonance crossing happens around $t_0 = 300\,\text{s}$ for the first two solutions and around $t_0/(1-\alpha) = 545.45\,\text{s}$ in the equivalent model. Despite this unimportant time shift in the solution, a shifted representation of the solutions in Fig. 23.1c shows that the proposed equivalence actually yields an almost perfect match with the solution of the initial time variant problem, while the other solution (constant frequency) clearly underestimates the response envelope.

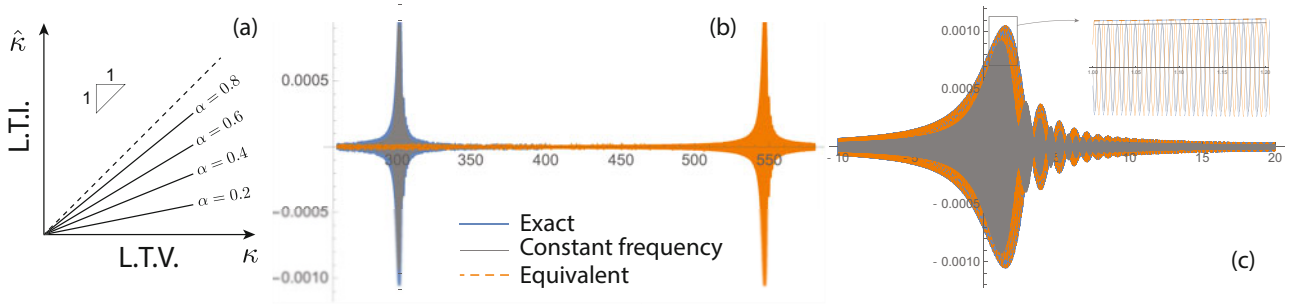

Fig. 23.1 (**a**) Illustration of the equivalence principle; (**b–c**) Response of the initial problem (blue), of the same problem but neglecting $\dot{\omega}$ (gray) and of the proposed equivalent problem. Numerical values : $\bar{\omega} = 600$ rad/s, $\dot{\omega} = 0.9$ rad/s^2 $\dot{\Omega} = 2$ rad/s^2, $\xi = 0.1\%$ ($\alpha = 0.45$, $\kappa = 5.56$)

23.5 Conclusion

With a standard perturbation technique, we could determine the leading order approximation of the response of a rotating blade with varying natural frequency subjected to a sine sweep. We found that the envelope of the response coincides, at leading order, to the envelope of a blade with constant natural frequency but subjected to a chirp with smaller rotor acceleration.

References

1. Srinivasan, A.V.: Flutter and resonant vibration characteristics of engine blades. J. Eng. Gas Turbines Power **119**(4), 742–775 (1997)
2. Hackenberg, H.-P., Hartung, A.: An approach for estimating the effect of transient sweep through a resonance. J. Eng. Gas Turbines Power **138**(8), 082502 (2016)
3. Carassale, L., Marrè-Brunenghi, M. and Patrone, S.: Wavelet-based identification of rotor blades in passage-through-resonance tests. Mech. Syst. Signal Process. **98**, 124–138 (2018).
4. Carassale, L., Denoël, V., Martel, C., Panning-von Scheidt, L.: Key features of the transient amplification of mistuned systems .J. Eng. Gas Turbines Power **143**(3), 031016 (2021)